COMPARISON OF DIRECT STRESS FATIGUE WITH ROTATING BENDING FATIGUE AND ITS RELEVANCE TO THE FATIGUE MECHANISM

A THESIS

PRESENTED FOR THE

DEGREE OF DOCTOR OF PHILOSOPHY

IN THE

DEPARTMENT OF MECHANICAL ENGINEERING,

UNIVERSITY OF CANTERBURY,

CHRISTCHURCH, NEW ZEALAND.

LIM KEN HUAT

MARCH, 1978.

SYNOPSIS.

Accumulated data suggests that the fatigue limit obtained with rotating bending testing is higher than that obtained by reversed direct stress testing. An average value of the ratio

$$\frac{\text{rotating bending fatigue limit}}{\text{direct stress fatigue limit}} = 1.18$$

appears to be in accordance with the published results. The issue is further complicated by the "size effect" in rotating bending fatigue tests.

To date, several theories have been advanced to account for the variation in the fatigue strength under these two different modes of fatigue loading, but none of these theories could offer a complete explanation for all the fatigue properties generally observed in plain and notched fatigue specimens.

With the increasing demand for more efficient and economic components in today's design, the understanding of the exact mechanisms that are operating under these two different modes of fatigue cycling is thus of vital importance.

In this investigation, steels with two different levels of active nitrogen and varying grain sizes were chosen for rotating bending and reversed direct stress fatigue tests. A special high nitrogen-low carbon steel was also used to reveal the plastic deformation accumulated during fatigue cycling. These tests were supplemented by the metallographic examination, microhardness surveys, temperature monitorings on specimens tested in direct stress fatigue and tensile tests on specimens fatigued under direct stress loading.

The results indicate that the dynamic yield stress of low carbon steels is below the direct stress fatigue limit. Under rotating bending loading, where the applied maximum surface

stress is above the direct stress fatigue limit of the material, dynamic yielding of the maximum stressed outer fibre after prolonged cycling, results in stress redistribution. The formation of a plastic layer after dynamic yielding thus increases the load carrying capacity (hence, the fatigue strength) of the rotating bending member.

A minimum depth of this plastically deformed layer is necessary before propagating cracks can develop under rotating bending loading. The existence of this critical depth of plastic zone also explains the size effect in rotating bending testing and other fatigue properties of notched specimens.

ACKNOWLEDGEMENTS.

My grateful thanks go to my supervisor, Dr. L.A. Erasmus, Reader in the Department of Mechanical Engineering, University of Canterbury, for the help and guidance he has always so freely given.

Many members of the technical staff of the Department of Mechanical Engineering assisted with this research programme and with the preparation of the thesis. In particular the valuable assistance of Messrs. D. Somerville, M. Flaws and Mrs. Jill Ritchie is acknowledged. My grateful thanks to all those who gave so willingly of their time, and to Mrs. June Ritchie for her meticulous typing.

I should also like to acknowledge the continual encouragement and interest of my family, and the understanding and sacrifice given by my wife.

Materials for this research programme were kindly donated by Pacific Steel Ltd., Auckland, New Zealand.

CONTENTS.

LIST OF FIGURES.

LIST OF TABLES.

NOMENCLATURE.

SYMBOL.	DEFINITION.	1st EQUATION.
A	Cross-sectional area	4.1
A_o	Original cross-sectional area	4.3
C_2	Constant	3.15
E	Modulus of elasticity	4.15
H	Constant	3.14
I	Moment of inertia	
K	Strength coefficient	4.6
K_c	Concentration equilibrium constant	6.3
K_f	Fatigue strength reduction factor	2.5
K_s	Solubility product	6.4
K_t	Theoretical stress concentration factor	2.5
L	Elementary block	
M	Equivalent elastic modulus	3.5
M	Bending moment	5.15
M_e	Elastic bending moment	5.17
M_p	Plastic moment	5.16
M_p	Fully plastic moment	
M_T	Total bending moment	5.14
N	Number of stress or strain cycles	1.1
N_E	Stress cycles at S_E	
P	Load	4.1
P_e	Load corresponds to σ_e	
P_p	Fully plastic load	
Q	Constant	3.8
Q	Activation energy	6.5
R	Proportional constant	3.2
R	Radius	5.8

SYMBOL.	DEFINITION.	1st EQUATION.
R	Gas constant	6.5
S_E	Endurance limit at N_E	
T	Absolute temperature (^oK)	3.14
T_r	Ambient temperature (^oK)	3.14
LCF	Low cycle fatigue	
HCF	High cycle fatigue	
a	Constant	1.1
b	Burger's Vector	3.6
d	Mean grain diameter	3.2
f	Constant	3.7
h	Plastic deformation zone (rotating bending)	
h_e	Plastic deformation zone (etching)	
h_m	Plastic deformation zone (microhardness survey)	
l	Length	4.2
l_o	Original length	4.2
m	Constant	3.10
n	Strain hardening exponent	4.6
n_o	n at $d^{-\frac{1}{2}} = 0$	4.17
q	Constant	3.8
q	Notch sensitivity index	2.5
r	Length to nearest dislocation source	3.2
r	Plastic zone as fraction of specimen's radius = h/r_1	
r_1	Radius of specimen	
r_c	Critical depth of plastic deformation zone	9.2
r*	Radius where $\sigma = \sigma_e$	5.10
t	Time at elevated temperature	3.14
t_r	Time at ambient temperature	3.14

SYMBOL.	DEFINITION.	1st EQUATION.
v	Average dislocation velocity	3.6
ε	True strain	4.2
$\dot{\varepsilon}$	Tensile machine strain rate	3.4
$\dot{\varepsilon}_e$	Elastic strain rate	3.4
ε_o	Total strain at σ_o	4.13
ε_p	Plastic true strain	4.13
ε'_p	Equivalent plastic true strain	4.12
$\dot{\varepsilon}_p$	Plastic strain rate	3.4
ε^*_p	Fatigue saturation strain	9.1
$\Delta\varepsilon$	Strain amplitude	1.1
θ	Integration constant	6.5
λ	Constant	5.22
γ	Stacking-fault energy (S.F.E.)	
γ	Constant	5.22
ρ	Dislocation density	3.7
ρ	Hole radius	5.2
ρ	Notch root radius	9.10
ρ_o	Initial dislocation density	3.8
σ	True stress	4.1
σ_a	Stress amplitude	9.1
σ_{app}	Applied stress from elastic theory	
σ_c	Stress to create dislocations	3.2
σ_e	Dynamic yield stress	
σ_e	Yield stress for ideal elastic-plastic material	5.1
σ_i	Friction stress on dislocations	3.2
$\sigma_i{}^*$	Temperature independent friction stress	4.11
$\sigma_i{}^o$	Temperature dependent friction stress	4.11
σ_n	Nominal stress	5.2
σ_o	Equivalent friction stress	4.16

SYMBOL.	DEFINITION.	1st EQUATION.
σ_y	Lower yield stress	3.3
σ_A	Anelastic limit	
σ_E	Elastic limit	
σ_L	Fatigue limit	3.15
σ_{DS}	Direct stress fatigue limit	
σ_{RB}	Rotating bending fatigue limit	
σ_1	Fatigue limit at $d^{-\frac{1}{2}} = 0$	3.15
σ_{max}	Maximum stress at notch root	9.10
τ	Shear stress	3.1
τ_c	Shear stress to create dislocations	3.2
τ_i	Friction stress on dislocations	3.2
δ	Change in length	

CHAPTER 1.

INTRODUCTION.

1.1 SCOPE OF THESIS:

Fatigue failures can be regarded as the progressive failure of parts under repeated loading. These failures usually occur at stresses which under static loading conditions should give infinite lives. It has been a problem faced by the engineers for a long time, and has hampered their freedom of design. As early as 1840, Rankine[1] had noted the characteristic "brittle appearance" of parts broken under repeated loading, and systematic investigation of fatigue was carried out over a hundred years ago on iron and steel by Wohler[2]. Since then extensive study has been carried out on a wide range of materials. However, despite the fact that a large amount of experimental data has been accumulated, fatigue failure is still by far the most common cause of service failure in machinery and structures operating at or close to room temperature.

There are three common test methods whereby a specimen can be subjected to a zero-mean-load cyclic loading, that is, a stress cycle varying from a maximum nominal tensile stress to a numerically equal nominal compressive stress, they are:- rotating bending, reversed direct stress and reversed plane bending, which will be referred to simply as direct stress and bending respectively in this thesis. It has long been known that the fatigue strength of similar material tested under these three different modes of loading may be different.

It is generally recognised that the fatigue strength

under rotating bending is greater than that under direct stress loading, and rotating bending fatigue limit to direct stress fatigue limit ratio of 1.35 to 1 has been reported[3,4]. It has been suggested that this discrepancy is mainly due to the experimental difficulties in obtaining perfect alignment for the direct stress testing[5,6,7]. However, many researchers[8,9,10,11,12] have consistently reported that the fatigue strength under rotating bending is higher than that under direct stress loading, and this has been observed over a wide range of materials, e.g. wrought iron[8], aluminium alloys[9], magnesium alloy[10], stainless steel[11] and carbon steels[12]. Hence, this phenomenon cannot be associated to any particular material, but the two different modes of cyclic loading. It has, however, been observed that the ratio of rotating bending fatigue limit to direct stress fatigue limit approaches unity for materials of high strength.

The issue is further complicated by the "Size Effect" in bending or rotating bending type fatigue testings. That is, the fatigue limit obtained from bending or rotating bending type fatigue testings generally decreases with increasing specimen diameter. By contrast, the fatigue limit obtained from direct stress testings remains fairly constant over a wide range of specimeter diameter.

With the increasing demand for more efficient and economic components (e.g. higher operating speed and minimum weight design) in today's design, the understanding of the exact fatigue mechanisms that are operating under these two different modes of fatigue cycling is thus of vital importance.

In low carbon steels, it is generally accepted that strain ageing can affect the fatigue strength to a certain extent[13,14,15]. In fact, some researchers[16,17] have attributed the

presence of the fatigue limit to the ability of these materials to strain age dynamically during the course of fatigue loading. This strain ageing process, as occurs under the normal service conditions, i.e. at operating temperatures below 150°C, has been shown[12] to be due to the presence of interstitial nitrogen in steels.

Fatigue properties of low carbon steels are also affected by the polycrystalline grain size[15,18,19]. Klesnil et al[19] presented metallographic evidence that grain boundaries hinder the growth of slip bands produced during the early stages of fatigue damage. They also showed that the dependency of fatigue limit on grain size follows the Hall-Petch relationship. Hence, in order to examine fully the differences in the fatigue mechanisms that are operating under these two different modes of fatigue loading (i.e. direct stress and rotating bending) in low carbon steels, it seems necessary to examine specimens with varying grain size and strain age propensity.

1.2 CHARACTERISTICS OF FATIGUE FRACTURE SURFACES:

All surfaces produced by fatigue have certain common features. Depending on the material, environment and loading conditions, some of these features may not be revealed clearly. Generally, the fatigue fracture surface can be divided into two parts; the fatigue area A and the final rupture area B, see fig.1.1.

The fatigue area is generally comparatively smooth and flat, indicating an absence of any appreciable amounts of gross plastic deformation. This fatigue area will also

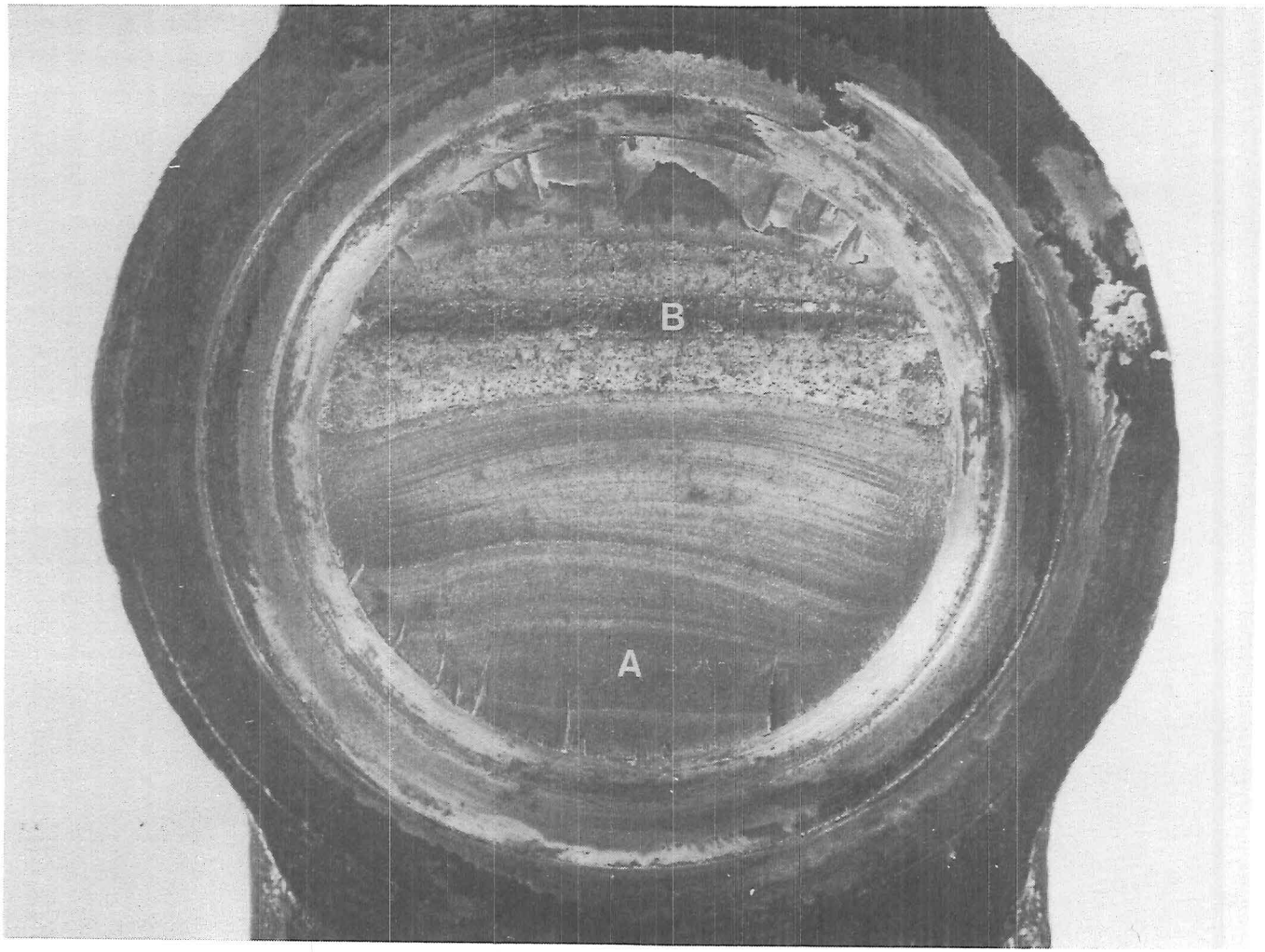

A = fatigue area; B = final failure area.

Fig. 1·1 FATIGUE FRACTURE SURFACE OF A VEHICLE STUB AXLE.

contain the fatigue crack origin(s), and other features which indicate the rate and direction of the crack growth at any particular stage in its history. For components under service failures occurring over a long period of time, the fracture surfaces usually contain crack arrest marks (crescent-shaped markings) perpendicular to the direction of crack propagation, and usually referred to as "tide marks" or "clam shell markings." These markings are thought to have occurred by corrosion or oxidation of the crack surfaces during the crack arrest periods, as no similar markings can be found for specimens tested with simple sinusoidal load under laboratory conditions.

Radial marks on the fatigue fracture surfaces are ledges, they result from crack fronts advancing on different levels, i.e. with jogs, and are usually regions of ductile fracture.

The final rupture area is rougher in texture and may have occurred under tension, bending or torsion. This area will also show evidence of any plastic deformation occurring before final separation.

1.3 THE S-N CURVE AND THE FATIGUE STRENGTH:

The most important factor determining the fatigue life of a material is the magnitude of the applied cyclic stress or strain amplitude. The most frequently used method of presenting this relationship is to test a number of identical specimens at various stress (or strain) levels, and to plot the resultant lives on a graph of stress (or strain) amplitude against life to failure, see fig.1.2. Such a graph usually shows considerable "scatter" in resultant points. The scatter is usually broader at the lower stress levels, i.e. during high cycle fatigue.

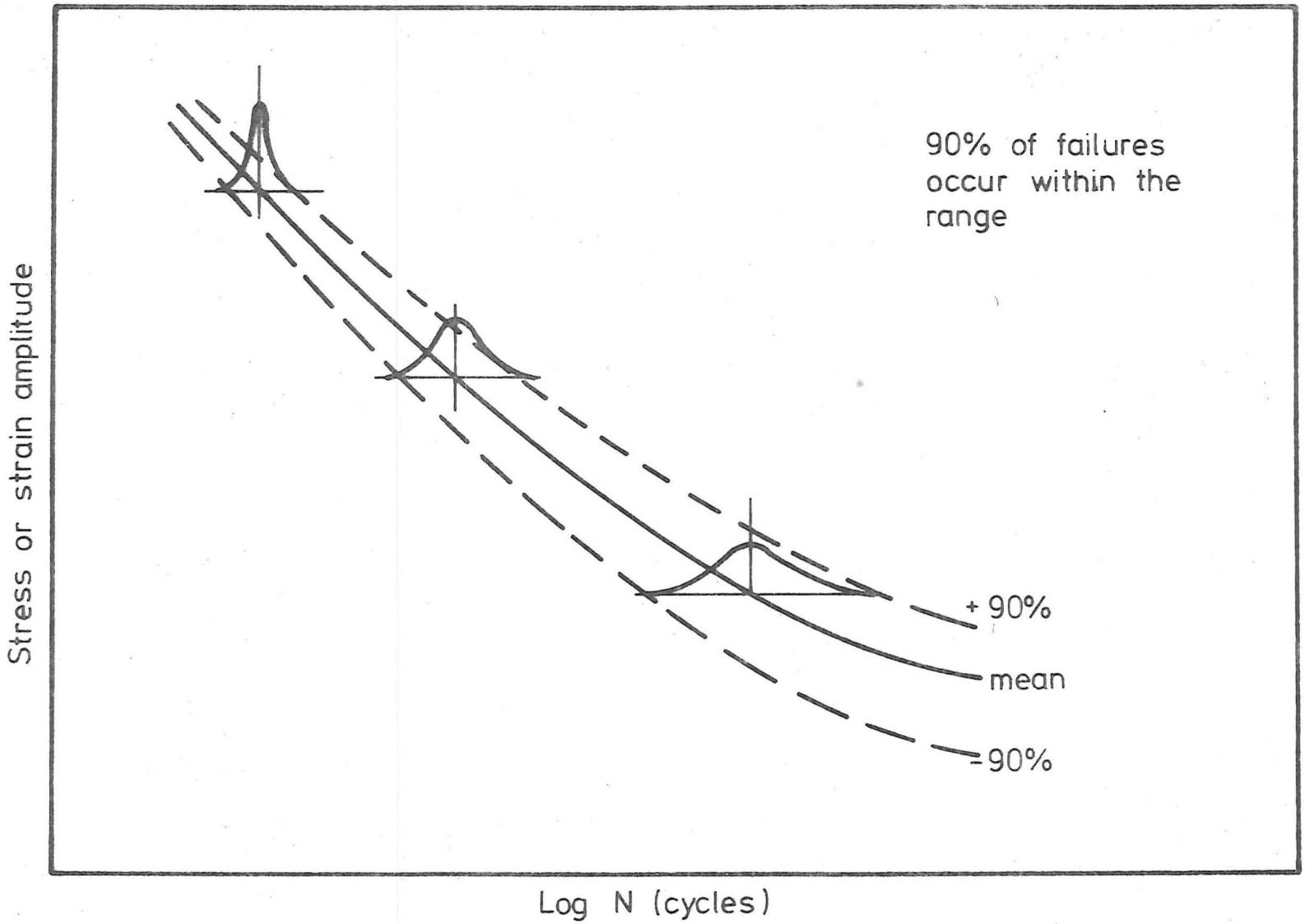

Fig. 1·2 FATIGUE CURVE, SHOWING FATIGUE "SCATTER"

This scatter in fatigue life is thought to be inherent in the material and is due mainly to the critical dependence of crack initiation on the maximum localised stress and the microscopic properties of the material. In high stress (strain)-low endurance regions, where the life is dominated by the crack propagation process, the amount of scatter is usually much reduced[20], as the crack propagation stages are usually independent of the material properties.

A comprehensive study of structural changes on the free surface of copper specimens by Wood et al[21] has led to the now acceptable division of the stress (strain)-log N curve into three basic regions, where N is the number of stress or strain cycles, see fig.1.3. The division into H, F and S regions is based on the slope of the curve and the type of damage produced at various load levels. In the H region, the high strain reversal breaks down each grain into small regions of different lattice orientation and cell structures are formed. This is also the region where significant macroscopic plastic deformation is usually involved, and the Manson-Coffin relationship is found to apply in this region[22]:-

i.e. $N^a \Delta\varepsilon$ = constant eqn. 1.1

where N = number of stress or strain cycles

$\Delta\varepsilon$ = strain amplitude

a = constant.

Testing within this region should ideally be done under constant strain cycling, however, it can be shown that, provided the strain cycle is well within the elastic limit of the material, it is acceptable to measure the stress amplitude instead of the strain amplitude.

The transition from H to F generally occurs at around 10^5

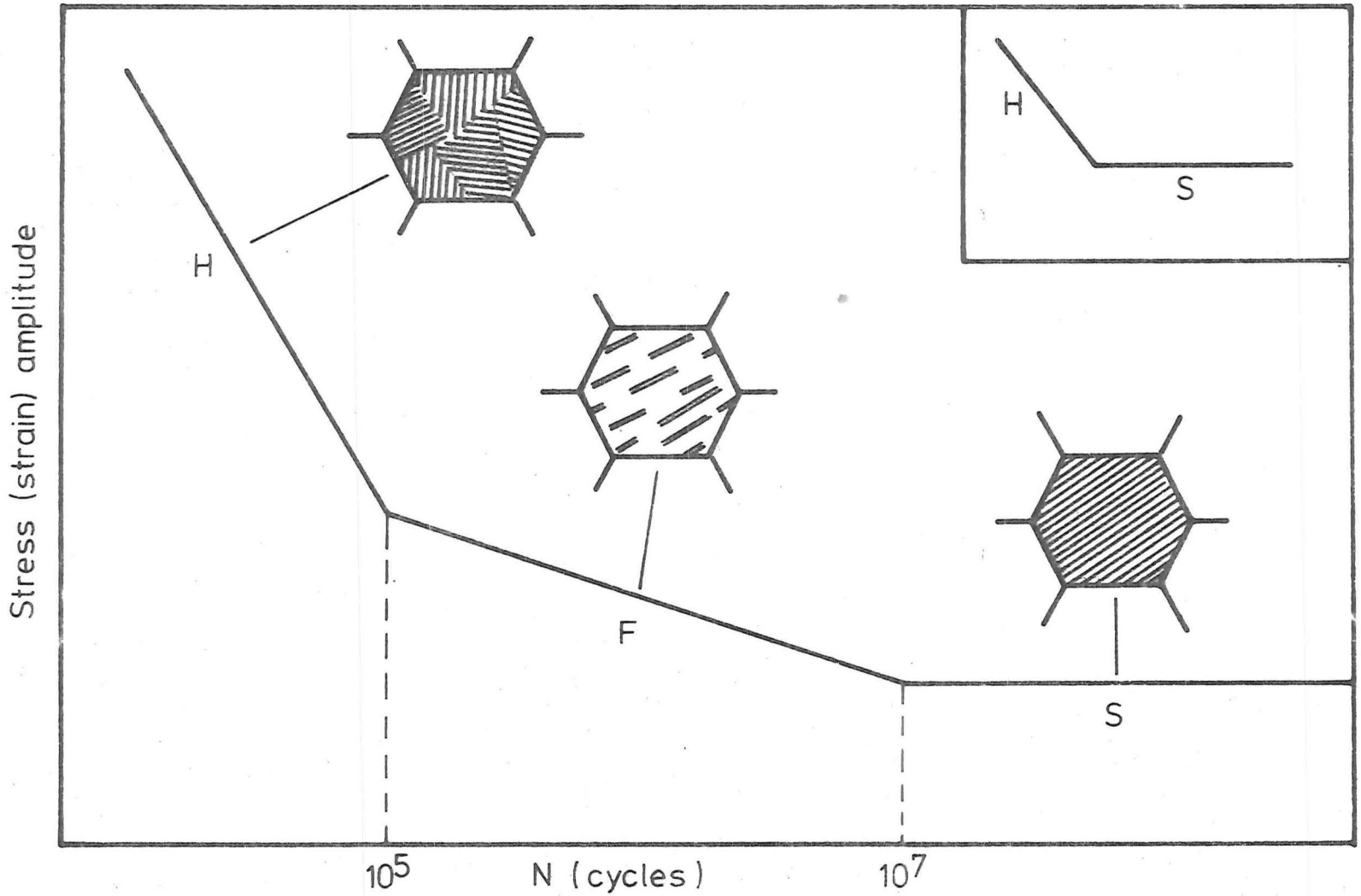

Fig. 1·3 IDEALISED S-N CURVE OF WOOD et al. (Ref. 21)

cycles. In the F region, the grains are able to accommodate the smaller strains without rumpling and disorienting them significantly. Slip movements tend to continue on and about the slip planes where they begin. As a result, the slip movements are concentrated in bands[21] and the fatigue cracks eventually nucleated from these bands.

The transition of F to S mode behaviour occurred at approximately 10^7 cycles. The S region is thought[21] to be the "pseudo-safe" region. The slip movement no longer concentrated in bands, but instead appears to be widely dispersed, and fatigue cracks are rarely nucleated in this region[21]. Some bands may develop after prolonged cycling, but they tend to be very few and therefore harmless.

There is general agreement that for metals two kinds of fatigue (S-N) curves exist, as illustrated in fig.1.4. For materials such as cast iron and low carbon steels, there exists a stress level below which the material is able to withstand an infinite number of loading cycles ($>10^8$) without failure. This limiting stress is defined as the fatigue limit σ_L of the material, see fig.1.4a. By contrast, most non-ferrous metals such as gold, silver and most aluminium alloys, do not show any fatigue limit. For these materials, the term endurance limit S_E is used to define the stress amplitude required to cause fatigue failure in a specific number of stress cycles N_E, see fig.1.4b.

Wood et al[23] suggested that the apparent difference in the two basic curves is due to the absence of the intermediate structural change, i.e. the F region, for materials which exhibit a fatigue limit.

Contradicting views on the occurrence of a fatigue limit

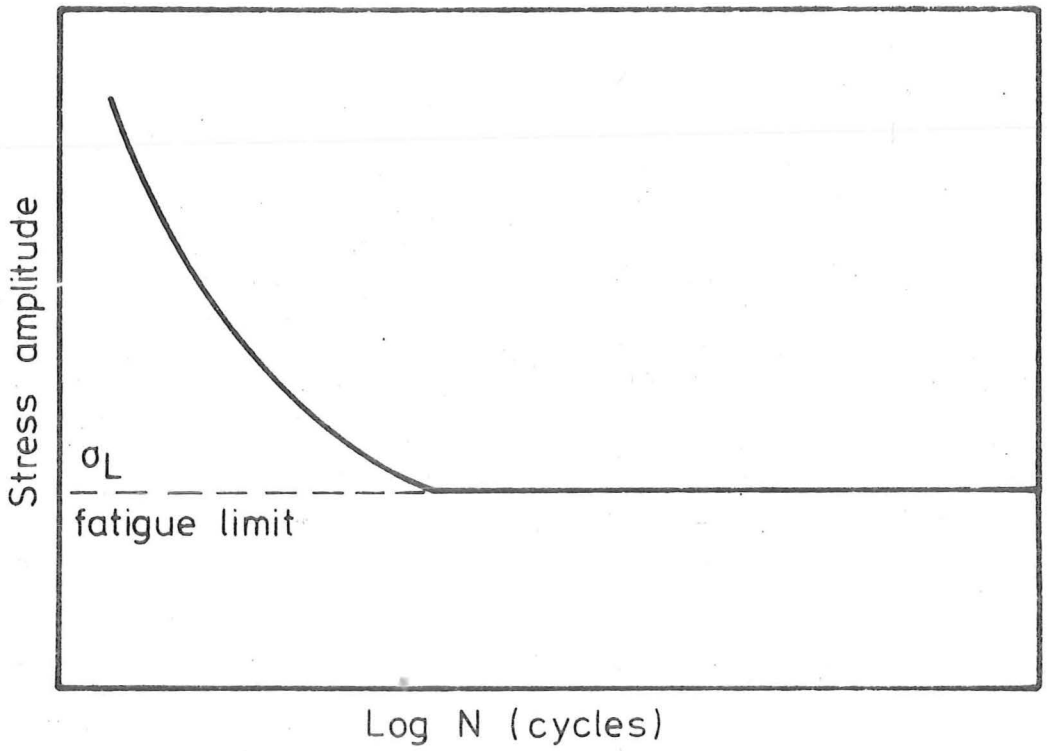

(a) ferrous materials

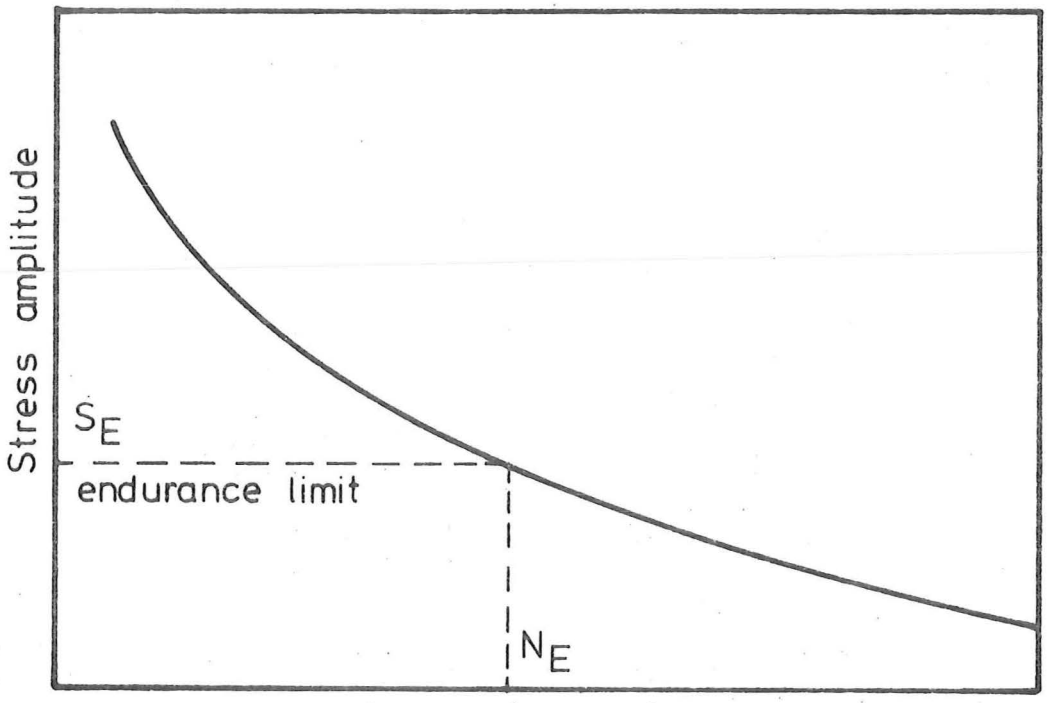

(b) non-ferrous materials

Fig. 1·4. SCHEMATIC FATIGUE CURVES

in low carbon steels have also been reported. Levy[16] attributed the presence of fatigue limit in these steels to their ability to strain age dynamically at room temperature. However, the work of Erasmus[12] showed that, although dynamic strain ageing due to interstitial nitrogen does occur in steels, it has little if not negligible effect on the fatigue limit, and suggested that the main contribution towards the formation of a fatigue limit in low carbon steels is the result of the initial low density of mobile dislocations in these materials.

1.4 THE PROCESS OF FATIGUE DAMAGE:

Since the review of Wadsworth and Thompson[24] in 1958, many subsequent papers[25,26,27] have also been published to give a comprehensive review of the process of fatigue damage. It is now well known that fatigue crack initiation in smooth specimens of ductile crystalline materials often occur in slip bands (or slip markings). However, in engineering components or structures, where geometric effects such as notches and machining marks are present, plastic deformation is often localised in these positions on the free surface and fatigue cracks are almost without exception nucleated at these regions of high localised strain.

It is now accepted that the fatigue process can be divided into a number of stages. Each stage may involve different mechanisms or be governed by different stress criteria. Generally, failure by fatigue consists of the following four stages:- (i) crack initiation, (ii) Stage I crack growth along planes of high shear stress, (iii) Stage II crack growth on planes of high tensile stress, and (iv) final separation by cleavage or microvoid coalescence.

Crack Initiation:- As with unidirectional straining, the main factors affecting the internal sub-structure (i.e. types of dislocation arrangement) are strain amplitude, stacking-fault energy and temperature. High value of these factors will promote cross-slip and increase the tendency of a continuous cellular formation. The formation of sub-grain structures (i.e. cell formation) under the action of cyclic stressing was first observed microscopically by Forsyth[28] in pure aluminium and aluminium alloys, and indirectly using X-ray technique by Wood et al[29]. More recently, with the advent of transmission electron microscopy, the formation of sub-grain structures in low carbon steels and other materials has been studied in great detail[19,30,31,32,33,34].

Under high strain (low cycle, $N<10^5$) fatigue condition, sub-grain structures similar to those formed under uniaxial tension are formed, but the cell size is usually larger and characterised by narrow boundaries similar to the cell structures appearing after polygonization[19,30]. The cell walls generally consist of clusters of dislocations surrounding areas of essentially dislocation-free material[35]. As cycling progresses, the sub-grain boundaries sharpen and the average sub-grain volume decreases to a limiting volume[26]. For aluminium the limiting sub-grain volume is about 2 cu μ[26].

For cyclic stressing at low strain amplitude, i.e. the high cycle fatigue condition, the cellular structure as observed under low cycle fatigue is not created, instead prismatic loops are formed. These loops are found to be heterogeneously distributed. However, in copper and aluminium, discontinuous dislocation arrangements have been found to be superseded by a cellular structure on increasing the cyclic strain amplitude, suggesting that the discontinuous dislocation

arrangement formed under low cyclic strain is simply a poorly developed form of the cellular structure[27].

The effect of stacking-fault energy (S.F.E.)γ of a material on cell formation during fatigue cycling may be seen from the following example. Polycrystalline aluminium ($\gamma \simeq 200$ ergs/cm^2), when subjected to cyclic strains giving fatigue lives of 2×10^6 cycles, will possess a sub-grain structure[36]. Copper ($\gamma \simeq 40$ ergs/cm^2) will do so at cyclic strains giving fatigue lives of about 10^5 cycles. However, with copper - 7.5% aluminium, which has a very low S.F.E. ($\gamma \simeq 2$ ergs/cm^2), cell structure cannot be observed at lifetimes as short as 10^4 cycles.

The effect of temperature on the dislocation distribution induced by fatigue cycling is not as marked as that of strain amplitude or S.F.E. The net result is usually an alteration in the scale of the dislocation arrangement.

As the usual outcome of cyclic deformation is the production of changes in surface topography in the form of persistent slip bands, intrusions and extrusions, it is important to relate these changes to the dislocation structures of the immediate sub-surface. Persistent slip bands on the surface as observed in the F range of the fatigue curve shown in fig.1.3 have been shown to be associated with broad bands of dislocations. To date, such correlation has been achieved for many materials[19,33,37]. However, a contradicting report is that of Lukas et al[38], who examined foils both parallel and non-parallel to the specimen surface, and revealed a three dimensional dislocation arrangement associated with the persistent slip bands. They suggested that areas of high dislocation density seen when viewing planes parallel to the surface are actually linked below the surface. The band is

composed of regions of high dislocation density forming the walls of irregular cylindrical cells, the axes of which are perpendicular to the primary slip plane.

Most of the researchers have also suggested that the sub-surface regions between the persistent slip bands are essentially dislocation-free. However, Wilson[39] and Klesnil et al[33] suggested that persistent slip bands formed "channels" below the surface. Wilson[39] reported that these channels have a very low dislocation density by comparison with regions between channels, whereas Klesnil et al[33] found that the channels in their low carbon steels were sandwiched between zones of very high dislocation density, the combined zones fell within one persistent slip band.

The study of "fatigue damage" within the bulk of the specimen as discussed above generally involves the preparation of foils for observation by electron microscopy. Although the overall dislocation arrangement as observed under the electron microscope seems likely to be representative of the arrangement existing in the bulk of the specimen, it is unlikely to give an absolute estimation of the dislocation density. This is because large numbers of dislocations (as many as 50%) are usually lost during the thinning process[32,40]. Further complication is likely for fatigue specimens tested at low temperatures, as they have to be warmed up to the electropolishing temperatures during the thinning process. It has, however, been suggested that with a foil thickness of greater than 2000^{o}A, a representative distribution will be retained[41]. This should only give problem to materials with very low electron transparency. Another important point in thin foil microscopy is the exact position in the specimen from which the foil is taken, especially when the specimen has been subjected to inhomogeneous

fatigue cycling, for example, rotating bending, torsional and reversed plane bending.

So far, the discussion has been restricted to the changes in the internal sub-structure within the specimen under the process of fatigue cycling. Changes in the surface topography are, however, a major part in the process of fatigue damage, and fatigue cracks are usually nucleated from the active slip bands on the free surface. The phenomenon of persistent slip bands and the importance of free surface in fatigue crack initiation have been reported in the early work of Thompson et al[42]. They reported that, with the periodic removal of about 30 μm from their direct stress specimen surface, the lives of their copper crystals were extended indefinitely. Similar results have also been reported for other materials subjected to other forms of fatigue loading. The importance of the free surface cannot therefore be associated with any particular material or type of fatigue loading.

Test atmosphere has also been shown to have an important role in fatigue damage. Wood et al[43] reported that an argon atmosphere extended the lives of their copper specimens more than five times over those tested in air. The beneficial effect of a vacuum is that some rebonding of the freshly created surfaces at the crack tip can occur. Also, the absorption of gas at the freshly created surfaces will lower the binding energy of the atoms.

Crack Propagation:- The precise point at which a slip band can be regarded as a Stage I crack has been a matter of contention, and physical distinction is obviously difficult. It has, however, been shown that fatigue damage may be annealed out and the specimen restored to its original condition, provided that

the treatment is carried out before the onset of saturation hardening. Cracking can thus be regarded to be coincidental with the exhaustion of work-hardening capacity, which coincides with the concentration of slip in a few bands[27].

The fatigue crack propagation can be divided into two consecutive stages[37]. Stage I crack propagation occurs on crystallographic slip planes in single crystals, and on macroscopic surfaces of maximum resolved shear stress in polycrystalline materials and is usually described as shear mode propagation. In severely notched brittle specimens tested at high stress amplitude, the Stage I crack may be absent. In unnotched specimens, Stage I crack may be fully developed in less than 10% of the fatigue life for pure metals, and may involve up to 90% of the total life in some alloys under low strain fatigue loading conditions[25]. The distance covered by Stage I cracks is usually of the order of a few grain diameters, even though it may occupy up to 90% of the total life[25]. However, under favourable loading conditions, for example torsional fatigue and corrosive environment, extensive Stage I crack growth has been reported.

The major obstacles to the understanding of the mechanisms of Stage I fatigue crack growth are the general lack of features on the Stage I fracture surfaces and its slow rate of propagation (of the order of angstroms per cycle).

As Stage I crack propagates from the free surface into the interior of the specimen, the ratio of shear stress to tensile stress at the crack tip progressively decreases, and propagation subsequently changes its plane of growth from one at about 45^{o} to the tensile axis to that at 90^{o}. For polycrystalline materials, this transition usually occurs at a grain boundary, and this mode of crack growth is termed Stage II propagation by

Forsyth[37]. This Stage II crack growth process generally produces by far the largest area of a fatigue fracture surface, although it may occupy only a very small percentage of the specimen's life, sometimes as little as 10%. Depending on the stress levels, specimen's geometry and the material properties, Stage II cracks may occupy from 10 to 100% of the specimen's fatigue life.

Under normal service failures, the Stage II fracture surfaces usually contain the classic macroscopic crack progression markings, that is, tide marks, clam shell markings or crack arrest marks. For specimens tested under laboratory conditions, microscopic fatigue striations running parallel to the crack front usually cover the surface. Two different types of fatigue striations have been reported by Forsyth et al[44], namely:- type A or "ductile" striations and type B or "brittle" striations. The spacing of both types of striations generally increases with the stress at crack tip. Fatigue striations have also been shown[45,46] to have a one to one relationship with stress cycles.

Many mechanisms have been proposed for the formation of fatigue striations, these include the plastic blunting (or plastic relaxation) theory of Laird[25], the intersecting slip processes of Hertzberg[47] and the cleavage fracture-plastic deformation sequences of Forsyth and Ryder[45]. Laird's[25] plastic blunting theory suggested that striation is formed by crack tip extension during the tensile part of the stress cycle followed by re-sharpening of the tip during the compression half cycle, whereas Hertzberg[47] suggested that crack extension also occurs during the compression half cycle and Forsyth[45] proposed that crack propagation takes place by cleavage fracture ahead of the crack tip and the elevation forming the striation

occurs by ductile necking. The plastic blunting theory of Laird[25] however, appears to be more acceptable in explaining the formation of fatigue striations[46]. However, Meyn[48] has reported that fatigue striations are not formed when the fatigue crack propagation test is performed in vacuum. This observation would destroy the validity of the plastic blunting theory. Pelloux[49] also suggested that fatigue striations are the result of an environment factor and not created by plastic blunting as suggested by Laird (at least for low growth rates), and the mechanism of crack extension is by alternating shear.

Attempts have also been made to correlate the striations on the fatigue fracture surface to the dislocation sub-structure beneath the fracture surface. Grosskreutz and Shaw[50] concluded from their work on aluminium and aluminium alloys that no such correlation exists. Klesnil and Lukas[51] however, observed cell formation near the fracture surface and smaller striation spacing which is the result of lower rate of crack growth, generally resulted in larger cell size. Awatani et al [52] examined foils containing sharp cracks taken from fatigued α-iron specimens concluded that tangled dislocations of very high density are formed within the zone immediately ahead of the crack tips, and cell structures are created ahead of this zone. In the areas near the crack sides, they observed fine cell formation, and the cell size increases with increasing distance from the crack side. They also suggested that the high density of tangled dislocations at the crack tips re-arrange into cell structures in a very short space of time after the passage of the crack tip.

The fatigue striation patterns formed on the low carbon steels' fatigue fracture surfaces (especially under high strain-low cycle conditions) are generally of irregular appearance

jagged and unequally spaced, as compared to the generally well defined striation patterns formed on the aluminium or aluminium alloys' fatigue fracture surfaces. It appears that there are fundamental differences between the crack growth processes in these two materials, however, the work of Koterazawa et al[53] showed that the striation spacing in low carbon steels (where most of the fracture surface is covered by irregular "quasi-striations") generally agreed very well with the macroscopic crack growth rate in the same way as the aluminium alloys (which have regular striations over most of their fracture surfaces), and they concluded that "quasi-striations" in low carbon steels do not have a primary role in the crack growth process, and there is not much difference between the crack growth processes of these two materials.

CHAPTER 2.

EFFECT OF STRESS GRADIENT AND NOTCH ON THE FATIGUE PROPERTIES.

2.1 VARIATION BETWEEN DIRECT STRESS AND ROTATING BENDING FATIGUE LIMITS, AND THE SIZE EFFECT:

Accumulated data suggests that the fatigue limit under bending testing or rotating bending testing is higher than that under direct stress testing, a ratio of

$$\frac{\text{rotating bending fatigue limit}}{\text{direct stress fatigue limit}}$$

of 1.35 has been reported, and an average value of 1.18 appears to be in accordance with the published results. Table 2.1 summarises data which compares the rotating bending and direct stress fatigue (endurance) limits of some materials.

Although it is generally accepted that the higher fatigue strength obtained under bending or rotating bending is mainly due to the stress gradient associated with the bending or rotating bending type of loading, and the greater volume of material subjected to the maximum stress in the direct stress loading, it has also been suggested that this discrepancy is mainly due to the difficulties in obtaining perfect alignment in direct stress fatigue testings[5,6,7]. Indeed, Irwin[5,6] carried out direct stress testings where the specimens were carefully aligned in the testing machine, and reported no variation in the fatigue limits between rotating bending loading and direct stress loading. However, many researchers have consistently reported that the fatigue strength under rotating bending is higher than that under direct stress loading, and this has been observed over a wide range of materials, for example, wrought iron[8], aluminium alloy[9], magnesium alloy[10]

TABLE 2.1

COMPARISON BETWEEN ROTATING BENDING AND REVERSED DIRECT STRESS FATIGUE (ENDURANCE) LIMITS FOR PLAIN SPECIMENS.

MATERIAL	REF.	FATIGUE LIMIT		FATIGUE RATIO σ_{RB}/σ_{DS}
		DIRECT STRESS	ROTATING BENDING	
		MN/M^2	MN/M^2	
Wrought Iron	8	165	214	1.30
0.45% C Steel, Normalised	8	183	247	1.35
0.45% C Steel, Q & T	8	315	318	1.01
0.85% C Steel, Normalised	8	207	275	1.33
0.85% C Steel, Q & T	8	411	412	1.00
0.5% C Steel	9	340	385	1.13
15% Cr Steel	9	340	380	1.12
4½% Cu-Al Alloy	9	125	145	1.16
2% Zn-Mg Alloy	10	90	100	1.11
13% Cr Stainless Steel	11	415	540	1.30
Mild Steel	12	-	-	1.19
Mild Steel	55	185	225	1.22
0.24% C Steel at 400°C	57	260	280	1.08
0.17% C Steel	57	216	262	1.21
PR 58 Al Alloy at 200°C	57	43	54	1.26
Mild Steel	115	201	294	1.46

stainless steels[11] and low carbon steels[12]. Hence, this phenomenon cannot be associated with any particular material, but the two different types of fatigue loading. It has, however, been observed that the ratio of

$$\frac{\text{rotating bending fatigue limit}}{\text{direct stress fatigue limit}}$$

decreases to unity with increasing material strength.

This issue is further complicated by the "size effect" in bending or rotating bending fatigue loading, that is, the fatigue limits obtained under bending or rotating bending tend to vary with specimen diameter, this is illustrated in table 2.2. The results show that in general the fatigue limits under rotating bending testing decrease with increasing specimen diameter, for example, the rotating bending fatigue limits of 0.45% C steel[54] specimens of 7.5 mm, 38 mm and 150 mm diameter were 226 MN/m^2, 193 MN/m^2 and 120 MN/m^2 respectively. By contrast, the fatigue limits of steels tested under direct stress can be seen to remain fairly constant over a wide range of specimen diameter.

The type of surface finish also affects the fatigue limits of some materials. Table 2.3 summarises the results of Frost and Denton[55]. It can be seen that hardening the surface layer of mild steel has the effect of increasing the fatigue limit of rotating bending specimens, the increase is however not as significant for specimens tested under direct stress loading. This illustrates the importance of surface layer in rotating bending fatigue loading.

The work of Irwin[5,6] unfortunately did not indicate the type of surface finish or the size of the rotating bending specimens, and it is therefore difficult to assess to what extent his rotating bending results were influenced by the size of the

TABLE 2.2

EFFECT OF SPECIMEN SIZE ON THE FATIGUE LIMIT OF PLAIN SPECIMENS.

MATERIAL	REF.	SPECIMEN DIAMETER	FATIGUE LIMIT	TESTING METHOD
		mm	MN/M^2	
0.45% C Steel	54	7.5	226	Rotating Bending
		38.0	193	"
		150.0	120	"
1% Ni Steel	116	5.0	334	Rotating Bending
		20.0	318	"
		100.0	220	"
0.37% C Steel	117	4.0	270	Rotating Bending
		8.0	256	"
		16.0	242	"
0.37% C Steel	117	4.0	236	Reversed Direct Stress
		8.0	246	"
		16.0	232	"
0.07% C Steel	118	4.8	187	Reversed Direct Stress
		4.8	204	"
		8.4	204	"
		25.0	203	"
		25.0	177	"
		35.0	201	"
EN 26 Steel	118	4.8	594	Reversed Direct Stress
		8.4	572	"
		12.7	603	"
		25.0	571	"

TABLE 2.3

EFFECT OF SURFACE FINISH ON FATIGUE LIMIT OF NORMALIZED MILD STEEL (REF.55)

SPECIMEN CONDITION	FATIGUE LIMIT	
	DIRECT STRESS	ROTATING BENDING
	MN/M^2	MN/M^2
Mechanically polished and stress-relieved	178	190
Mechanically polished	185	225
Surface-rolled	190	240
Through-hardened to same hardness as surface of mechanically polished specimens	-	240
Through-hardened to same hardness as surface of surface-rolled specimens	-	295

specimens or the fatigue limits affected by the surface finish.

An attempt has been made by Forrest and Tapsell[56,57] to correlate the rotating bending and direct stress fatigue strengths on the basis that the maximum fibre stress in rotating bending is calculated from the theoretical applied bending moment, assuming ideal elasticity. Whereas when the maximum fibre stress is higher than the dynamic elastic limit, the surface layer will deform plastically and the true surface stress is lower than the calculated stress. They derived the dynamic stress-strain curves by measuring the hysteresis loop at various stress levels in direct stress machine and, when replacing the nominal stress (calculated ideal elastic stress) value in rotating bending test by the corresponding true surface stress, obtained rotating bending S/N curves coinciding with those obtained in direct stress loading. Their analysis is, however, strictly applicable only in the case of plane bending. In plane bending, the stress at the two extremities of a horizontal strip element of the cross-section is the same and this is not the case in rotating bending, as the stress at one extremity is increasing to its maximum value, while that at the other extremity is decreasing to its minimum value, depending on the direction of rotation. Also, the dynamic stress-strain curves as obtained by their experimental procedure are questionable as the stress-strain curves were derived by measuring the strain of one test piece for increasing values of stress amplitude. This procedure can only give a true dynamic stress-strain curve if previous cyclic stressing at lower stress levels has no appreciable effect on the stress-strain behaviour at higher stress levels. This may be so, as the saturation hardness values of most materials are only dependent on the cyclic stress amplitudes and are independent of the previous cyclic

history[58], but sufficient stress cycles are necessary before this saturation value can be achieved. This can be a major problem at stresses above the direct stress fatigue limit of the material, as stress cycles larger than the fatigue lives of the material may be necessary to achieve the necessary saturation values. Another objection to the stress distribution theory as suggested by Forrest and Tapsell is that this theory suggests a critical surface stress for all specimen sizes so that all should give the same fatigue strength. Since there is undoubtedly a "size effect" in bending or rotating bending type fatigue testings, this theory as such is inadequate.

Apart from the stress redistribution theory discussed above, other theories have also been advanced to account for the size effect in bending and rotating bending testings. Most of these theories are linked directly or indirectly with the stress gradient in the specimen. Some of these theories are summarised below:-

(a) The inherent flaw theory[59]:- This theory suggests that all materials contain internal discontinuities or stress concentrations. If the flaws are randomly distributed within the specimen, and assuming that the presence of a flaw above a certain critical size would cause failure, it is then possible to assume that the strength of the specimen would depend on the surface area subjected to the maximum stress, hence the size of the specimen. However, this theory also suggests a size effect in direct stress type of fatigue loading, and as many published results have indicated that there is little variation in the fatigue strength with specimen size under direct stress loading, see table 2.2, this theory as now understood is therefore not adequate.

(b) The elementary block concept of Neuber[59] :- The theoretical elastic stress distribution suggests that the maximum stress occurs only at a point or a line on the specimen surface, the material however cannot be sub-divided indefinitely without affecting the mechanical properties of the material. This elementary block concept suggests that fatigue failure is not governed by the maximum stress, but by the average stress across an elementary block of finite size L, measured from the surface inwards. Higher maximum stress can therefore be withstood with a high stress gradient (or, for the same maximum surface stress, this means a smaller specimen diameter). This concept was first introduced by Neuber[60]. Several formulas based on Neuber's formula have since been derived. One of these is that of Moore and Markovin[61] who considered that inherent defects are randomly distributed within the specimen and set up stress concentrations, thus weakening the material. Surface defects are considered to be more damaging than the internal defects, each defect was assumed to be equivalent of a circumferential semicircular notch of radius R'. The corresponding theoretical stress concentration factor K'_t depends on the specimen size. Applying Neuber's formula, they arrived at equation 2.2.

Neuber's formula -

$$K'_a = 1 + \frac{K'_t - 1}{1 + \sqrt{(a/R')}} \qquad \text{eqn 2.1}$$

from which

$$\sigma_b = \left\{\frac{1 + \sqrt{(a/R')}}{K'_t + \sqrt{(a/R')}}\right\} \sigma_p \qquad \text{eqn 2.2}$$

where

$$K'_a = \frac{\text{Unnotched fatigue strength for hypothetical material without defects } (= \sigma_p, \text{ say})}{\text{Fatigue strength of plain material with defects } (= \sigma_b)}$$

K_t' = Theoretical stress concentration factor for semicircular notch or defect of constant radius R'

a = A constant representing an elementary structure unit of the material.

This theory, like the inherent flaw concept, suggests a size effect in direct stress loading.

(c) Stress gradient concept[59]:- Under bending or rotating bending type of testings, if the lower stressed grains remote from the surface layer are regarded as giving support to the higher stressed grains near the specimen surface by restricting their deformation, then the steeper the stress gradient, the greater the supporting effect would be. Two possible relationships have been formulated based on this concept, they are:-

$$\sigma_b = \sigma_B + \left(a \frac{d\sigma}{dx}\right)^b \qquad \text{eqn 2.3}$$

and $$\sigma_b = \sigma_B \left\{1 + \left\{\frac{a}{\sigma_b} \frac{d\sigma}{dx}\right\}^b\right\} \qquad \text{eqn 2.4}$$

where

σ_b = Calculated surface stress or fatigue limit as obtained from elastic theory, i.e. $M = \sigma I/n$

σ_B = Stress or fatigue limit for very large diameter specimen as obtained from elastic theory.

$\frac{d\sigma}{dx}$ = The maximum stress gradient at the point of maximum stress.

$\frac{1}{\sigma_b} \frac{d\sigma}{dx}$ = Relative stress gradient at the point of maximum stress.

a and b are constants.

This concept, however, could not explain the increase in fatigue strength after coaxing or understressing for materials which do not strain age dynamically, for example, the coaxing results from a commercially pure aluminium of Erasmus[12].

2.2 EFFECT OF NOTCHES ON FATIGUE STRENGTH:

Most of the engineering components or structural members contain some form of discontinuity such as keyway, fillet, hole or external groove. Any of these discontinuities can be generally referred to as a notch. To date, considerable testing has been carried out on notched fatigue specimens, and Heywood [59] and Frost et al [62] have collected and summarised most of the available data.

The presence of a notch in a member under fatigue loading reduces the fatigue strength of the member, and the ratio of the plain fatigue limit to the corresponding notched fatigue limit is termed the fatigue-strength reduction factor, denoted by K_f:- that is,

$$K_f = \frac{\text{plain fatigue limit}}{\text{notched fatigue limit}}$$

This fatigue-strength reduction factor K_f is generally smaller than the corresponding stress concentration factor K_t of the notch, or the notched fatigue strength is usually larger than the theoretical notched fatigue strength σ of the material, where $\sigma = \frac{\text{plain fatigue limit of the material}}{K_t}$

For a small value of K_t, K_f may equal K_t, but for a large value of K_t, K_f is always very much smaller than K_t. Table 2.4 summarises some of the published results.

Tests have also been carried out to determine the effect of specimen size on the K_f value for geometrically similar notched specimens, that is, having the same K_t. This is illustrated in table 2.5. Unlike the plain specimens, notched fatigue specimens exhibit size effect in both direct stress and rotating bending, that is, notch fatigue strength decreases with increasing specimen diameter in both direct stress and rotating

TABLE 2.4

RELATIONSHIP BETWEEN K_f AND K_t (REF.62).

(a) Rotating bending fatigue data for circumferentially vee notched specimens 10 mm outside diameter.

NOTCH DETAILS				K_f		
INCLUDED ANGLE (DEGREES)	DEPTH (mm)	ROOT RADIUS (mm)	K_t	BS 6L1 4% Cu-Al ALLOY	DTD 683 5½% Zn-Al ALLOY	Z 3 Z MAGNESIUM ALLOY
20	1.0	0.25	2.9	1.9	2.0	2.7
30	1.0	0.25	2.9	2.5	1.7	2.6
45	1.0	0.25	2.9	2.1	1.8	2.5
60	1.0	0.25	2.9	2.1	2.0	2.5
80	1.0	0.25	2.9	2.1	1.9	2.5
100	1.0	0.25	2.9	2.0	1.7	2.1
60	0.5	0.25	2.9	1.9	1.9	2.7
60	1.0	0.25	2.9	2.1	2.0	2.5
60	1.5	0.25	2.9	2.3	1.9	2.9
60	2.0	0.25	2.7	2.6	1.7	3.3
60	2.5	0.25	2.6	3.1	2.4	3.9
60	1.0	0.25	2.9	2.1	2.0	2.5
60	1.0	0.5	2.3	2.0	1.7	2.1
60	1.0	0.89	1.9	1.5	1.4	1.9
60	1.0	1.0	1.9	1.6	1.1	1.6

(b) Reversed direct stress fatigue data for tests on 64 mm wide sheet specimens 2 mm thick.

NOTCH DEPTH (mm)	K_t	K_f		
		245-T3 Al ALLOY	755-T6 Al ALLOY	SAE 4130 STEEL (.4% C)
9.5	2	1.8	1.9	1.7
0.24	4	2.0	2.4	2.4
9.5	4	3.1	4.0	3.5
3.3	4	3.0	3.0	3.6
9.5	5	3.4	5.0	4.7

TABLE 2.5

RELATIONSHIP BETWEEN K_f AND SPECIMEN SIZE.

(a) Rotating bending fatigue data for geometrically similar specimens containing circumferential hyperbolic groove, $K_t = 3.3$ (ref.116)

SPECIMEN DIAMETER (mm)	K_f		
	0.18% C STEEL	0.37% C STEEL	NICKEL-MOLYBDENUM ALLOY STEEL
5	1.7	2.1	2.4
10	1.9	2.2	2.5
20	2.4	2.3	3.0
100	2.6	2.3	3.3

(b) Reversed direct stress fatigue data for geometrically similar specimens containing a transverse hole of diameter 1/6 the outside diameter of the specimen $K_t = 2.8$ (ref.118)

SPECIMEN DIAMETER (mm)	HOLE DIAMETER (mm)	K_f	
		MILD STEEL	NICKEL-CHROMIUM ALLOY STEEL
4.8	0.8	1.80	2.55
8.4	1.4	1.55	2.25
14.2	2.4	1.65	2.40
24.9	4.0	1.95	2.75
43.0	7.1	2.15	2.75

bending. Published results have also indicated that K_f is a function of polycrystalline grain size, with K_f generally decreasing with increasing grain size[63].

In notched specimens, the proportion of life spent in crack initiation and propagation generally varies with material, notch geometry, specimen size and stress level. Cracks develop quickly in sharp notched specimens, and crack propagation may occupy the major part of the life. Indeed, for many sharp notched specimens, it is possible that cracks develop very early in life and fail to propagate to failure, that is, remain non-propagating. Thus, an unbroken notched specimen does not necessarily imply that the material near the notch root is uncracked. These non-propagating cracks have been observed over a wide range of materials, and are generally observed at stresses between the notch fatigue limit and plain fatigue limit divided by K_t, where K_t is the theoretical stress concentration factor.

Many attempts have also been made to explain the variation between K_f and K_t, and to formulate relationships between K_f and K_t, so that the value of K_f may be predicted from the known value of K_t. Some of these theories are briefly summarised below:-

(a) Inherent flaw concept[59,62]:- As discussed in the previous section, this theory suggests that all materials contain inherent defects which are randomly distributed within the specimen. If there are many flaws in the specimen, the introduction of a notch of similar size as the flaws will have little effect on the fatigue strength of the material, K_f will then tend to unity. If, on the other hand, the size of the notch is very large in comparison to the flaws, there will be a number of flaws within the notch root, that is, at the maximum stressed region, this will weaken the member consider-

ably, and in this case, K_f will approach K_t.

(b) Changes in notch root radius[62] :- This theory suggests that under maximum tensile stress, the notch root radius increases due to the increase in the arc length at the notch root, thus the actual stress concentration factor is less than the theoretical stress concentration factor, hence the lower value of K_f in comparison to K_t.

(c) Notch sensitivity index q[62] :- For some materials, the notched fatigue limits are either equal to or not far from the corresponding value of plain fatigue limits divided by K_t, but for other materials, the notched fatigue limits are very much larger than the corresponding plain fatigue limits divided by K_t. These are referred to as notch sensitive and notch insensitive respectively. This theory suggests that the ratio of the increase in actual stress $K_f\sigma_n$ (where σ_n is the nominal stress at the notched fatigue limit) over the nominal stress σ_n to the increase in the theoretical stress $K_t\sigma_n$ over the nominal stress σ_n is a material constant, termed the Notch Sensitivity Index q:-

that is $$q = \frac{K_f\sigma_n - \sigma_n}{K_t\sigma_n - \sigma_n}$$

or $$q = \frac{K_f - 1}{K_t - 1} \qquad \text{eqn 2.5}$$

When K_f approaches unity, q approaches zero, the material is then said to be fully notch insensitive, and when K_f approaches K_t, q approaches unity, the material is said to be fully notch sensitive.

It has been suggested[64] that notch sensitivity index q is not only dependent on the material, but is a function of notch geometry and specimen size. Thus the q value determined from one batch of notched specimens may give misleading results

if it is used in another batch of notched specimens with different notch geometry or specimen size.

(d) Elementary block concept of Neuber[59,62]:- This concept was first used in an attempt to explain the size effect in rotating bending type of testing, see section 2.1. This theory suggests that fatigue failure is not governed by the maximum stress at the notch root, but by the average stress over an elementary block of finite size L.

(e) Plasticity or the stress redistribution effect:- This theory was first put forward by Forrest[65,66]. This plastic theory suggests that, if the plain fatigue limit of a material is higher than the dynamic elastic limit, specimens tested at the plain fatigue limit can develop a hysteresis loop, that is to say, the material can deform plastically without causing failure. This would mean that the actual nominal stress just sufficient to cause a maximum stress greater than the plain fatigue limit at the notch root is greater than that calculated from the elastic theory[66]. That is, the ratio of the maximum stress to this nominal stress is less than K_t, and can be considered as a plastic stress concentration factor K_{tpl} which the experimentally determined value K_f cannot exceed. Dynamic stress-strain curves as discussed in section 2.1 are used to determine the maximum stress at the notch root. Fairly good correlation between K_{tpl} and K_f were achieved for many materials [66] and it was suggested[62] that this plasticity effect does account for some of the discrepancy between K_f and K_t. But, as has been mentioned in section 2.1, for geometrically similar notched specimens, redistribution of stress due to dynamic yielding should be the same for all specimen diameters, hence, the fatigue strength should be the same for all specimen

diameters. However, published results have indicated that there is a definite size effect for notched specimens under both direct stress and rotating bending testings, see table 2.6, this theory as such is therefore not adequate.

TABLE 2.6

"SIZE EFFECT" IN NOTCHED FATIGUE SPECIMENS (REF.59).

(a) "Size effect" in notched direct stress specimens.

MATERIAL	SPECIMEN DIAMETER (mm)	K_t	K_f	FATIGUE LIMIT MN/M^2	
				PLAIN (dia.mm)	NOTCHED
EN 36 Steel	10.0	1.36	1.20	371	309
0.14% C	32.8	1.36	1.22	371	305
3.12% Ni, 0.91% Cr	6.7	1.76	1.41	371	263
0.48% Mn, 0.25% Si	22.2	1.76	1.60	371	232
0.07% C Steel	4.8	2.81	1.75	203	116
	8.3	2.81	1.56	203	130
	14.3	2.81	1.66	203	122
	24.8	2.81	1.97	203	103
	43.0	2.81	2.16	203	94

(b) "Size effect" in notched rotating bending specimens.

MATERIAL	SPECIMEN DIAMETER (mm)	K_t	K_f	FATIGUE LIMIT MN/M^2	
				PLAIN (dia.mm)	NOTCHED
SAE 1020	3.7	2.01	1.28	194(25.4)	152
0.22% C	7.4	2.01	1.41	194(25.4)	138
0.46% Mn	14.7	2.01	1.58	194(25.4)	123
0.2% Si	29.5	2.01	1.63	194(25.4)	119
	54.7	2.01	1.76	194(25.4)	110
SAE X4130	3.7	2.01	1.65	439(38.1)	266
0.31% C	7.4	2.01	1.71	439(38.1)	257
1.08% Cr	14.7	2.01	1.78	439(38.1)	247
0.55% Mn	29.5	2.01	1.84	439(38.1)	239
0.2% Mo	51.6	2.01	1.83	439(38.1)	240

CHAPTER 3.

EFFECT OF STRAIN AGEING AND GRAIN SIZE ON THE FATIGUE LIMIT OF LOW CARBON STEELS.

3.1 THE YIELD POINT IN LOW CARBON STEELS:

When polycrystalline annealed low carbon steels are deformed in tension, the stress-strain curves generally show a localized heterogeneous transition from elastic to plastic deformation, see fig.3.1, instead of the normal flow curve with a gradual transition common to other metals and alloys. The stress at which the sudden drop occurs is known as the upper yield stress σ_u, and corresponds to the stress where the transition from elastic to plastic deformation occurs. At this upper yield point σ_u, localised plastic instability results in the formation of a discreet band of plastically deformed metal (known as the Luder band) which propagates along the specimen gauge length, resulting in a decrease in stress to an approximately constant stress known as the lower yield stress σ_y.

Luder bands are formed at approximately 45^o to the tensile axis, and their propagations along the specimen gauge length at the lower yield stress result in the yield point elongation. As each plastically deformed Luder band strain hardens, and as the applied load increases, further yielding and band propagation occur until the Luder bands have spread down the whole gauge length of the test-piece.

The plastic deformation accumulated at the lower yield stress is termed Luders strain or the yield point elongation, and is dependent on chemical composition, grain size and other metallurgical variables.

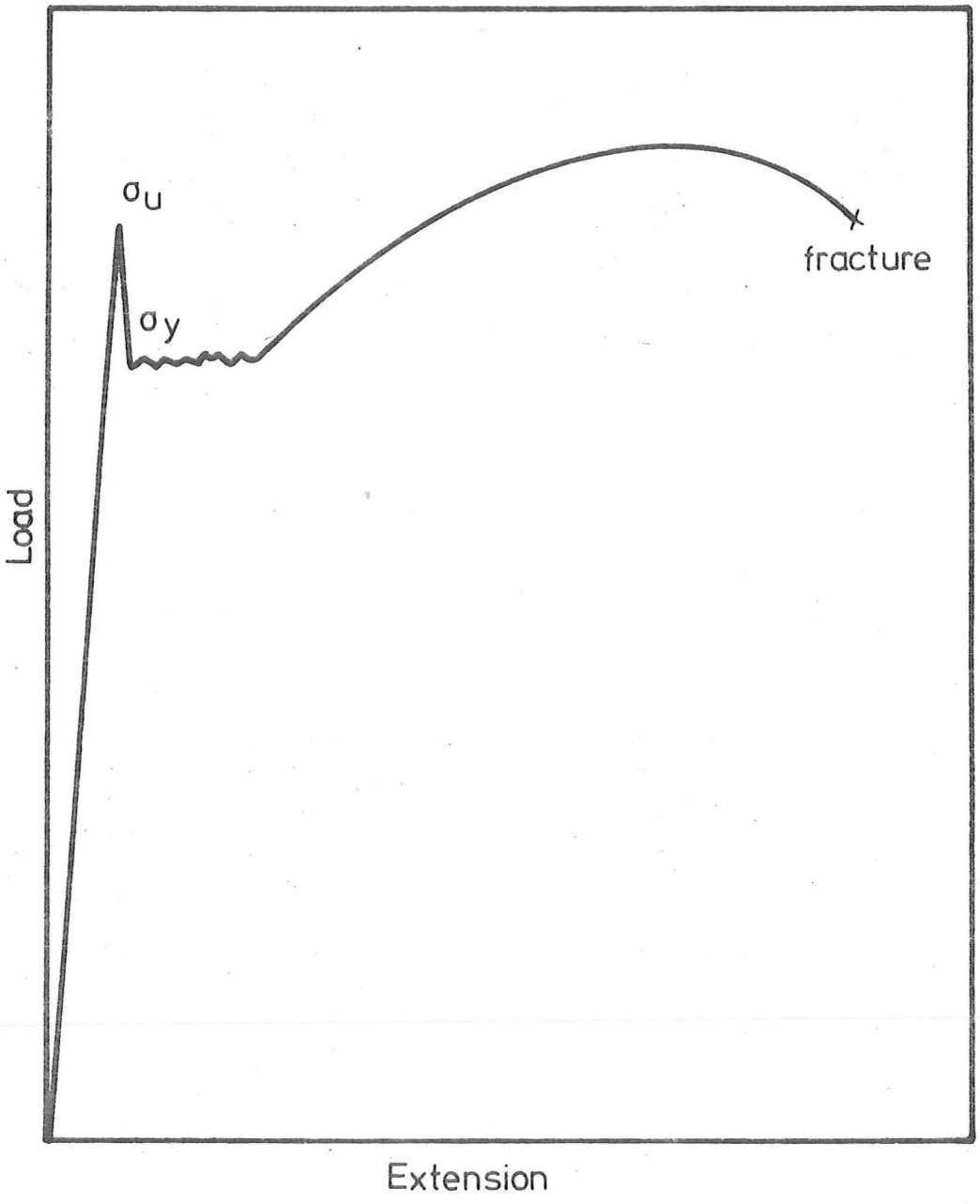

Fig. 3·1 LOAD EXTENSION TENSILE CURVE FOR A TYPICAL LOW CARBON STEEL.

After the Luders strain, the stress increases again and the test-piece continues to elongate uniformly and normal strain hardening occurs. A number of factors such as machine stiffness, axiality of the applied force, strain rate and surface finish may affect the value of upper and/or lower yield point, and have been summarised elsewhere[67].

The critical dependent of the discontinuous yielding in low carbon steels on the amount of carbon and nitrogen has been known since early this century, and the earliest theory attempting to explain the yield point phenomenon was that of Dalby[68]. He suggested that the ferrite grains were surrounded by an invisible film of cementite, which enabled the mass to support a stress well above that for ferrite crystals themselves, and consequently, plastic deformation was restricted until a certain critical stress was reached, that is, the upper yield point. At this point, the film broke down, and nucleation of first Luder band began.

Dalby's theory was later surpassed by that of Cottrell and Bilby[69] who suggested that interstitial atoms of carbon and nitrogen in solid solution in the ferrite segregated to dislocations and locked them in position. The interstitial atoms of carbon and nitrogen at ambient temperature occupy the interstitial sites in the ferrite matrix, which are too small for them. This strain energy can be relieved by the diffusion of these interstitial atoms to the tensile side of edge dislocations, where the lattice is itself dilated. Cottrell and Bilby estimated this binding energy to be about 0.5 eV per atom plane, and that a concentration of about 10^{-6} wt % C was sufficient to place one carbon atom on each dislocation per atom plane, assuming the normally accepted dislocation density of 10^{8} lives cm^{-2}. For yielding to occur, the applied strain energy,

assisted by thermal activation, has to exceed this binding energy, then the dislocations break away from their atmospheres, multiply and so form the first Luders band.

If these dislocations pile up against a grain boundary, they will produce a concentration of stress in the nearby parts of the adjoining grain. Therefore, a blocked slip band of length l can be considered to transfer a force of $(\tau - \tau_i)$ to the next grain, see fig.3.2, where

τ = applied shear stress

τ_i = the friction stress which opposes the glide of a dislocation in the slip band.

By analogy between a slip band and a crack, it can be shown from the elastic theory that the applied stress is increased by a factor of $\{l/(4r)\}^{\frac{1}{2}}$ at a distance r ahead of the blocked slip band. If r is assumed to be the average distance between the blocked slip band and the nearest locked dislocation sources in the next grain, and if it is further assumed that -

(a) l is directly proportional to the grain diameter d so that $l = R.d$;

(b) there is a critical shear stress value τ_c required to create dislocations from the locked sources;

the pile-up stress can make the neighbouring grain yield if

$$\tau_c = (\tau - \tau_i) \left(\frac{l}{4r}\right)^{\frac{1}{2}} \qquad \text{eqn 3.1}$$

Assuming that the applied shear stress is equal to the lower yield shear stress, and converting all shear stresses to the equivalent tensile stresses, equation 3.1 can be rewritten as

$$\sigma_c = (\sigma_y - \sigma_i) \left(\frac{Rd}{4r}\right)^{\frac{1}{2}} \qquad \text{eqn 3.2}$$

or $$\sigma_y = \sigma_i + K_y\, d^{-\frac{1}{2}} \qquad \text{eqn 3.3}$$

where $K_y = 2\sigma_c \left(\frac{r}{R}\right)^{\frac{1}{2}}$

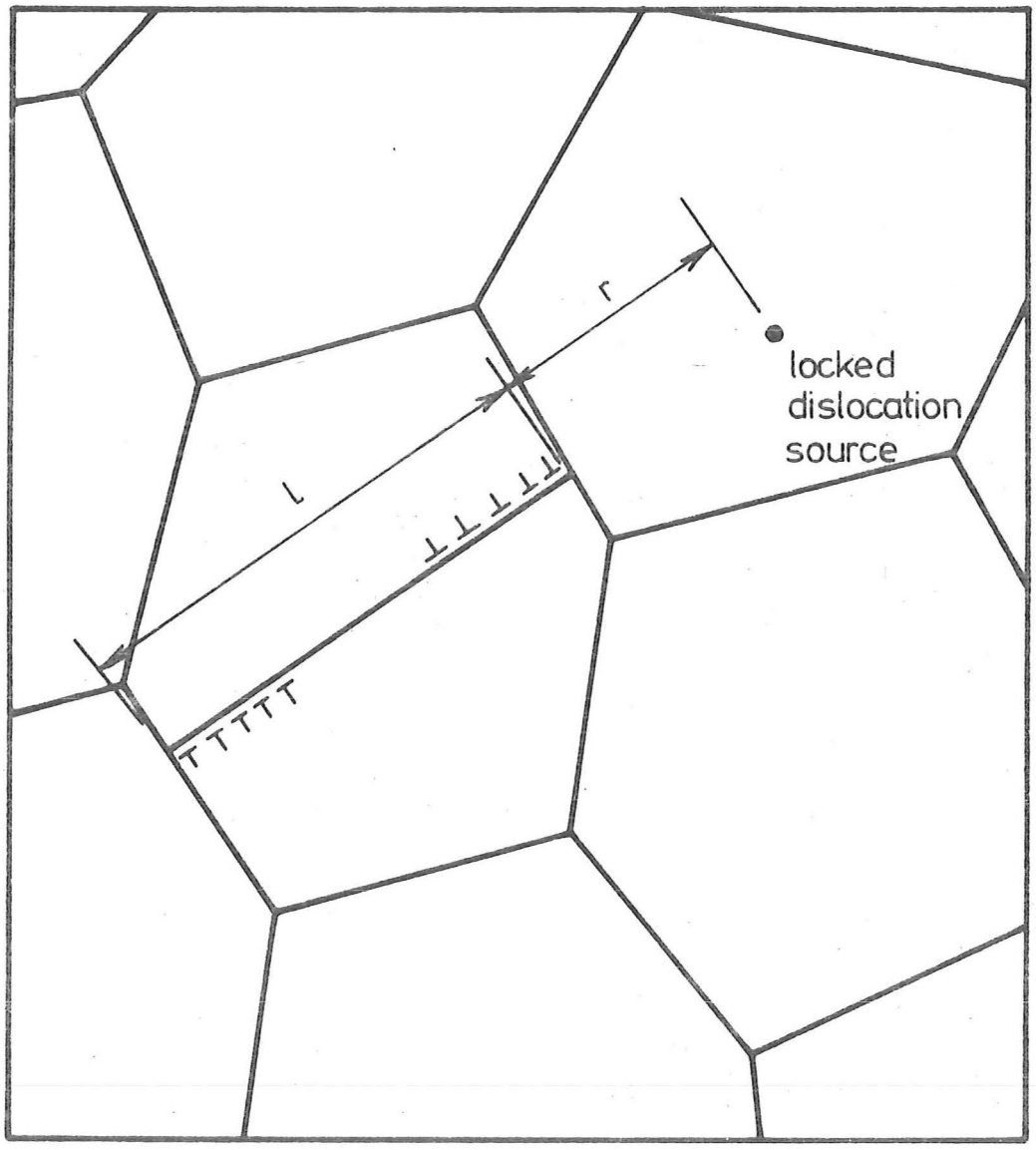

Fig. 3·2 DISLOCATION PILE UP AGAINST GRAIN BOUNDARY

σ_i and K_y are constants for a particular material, where K_y is considered as a measure of the contribution of grain boundaries to the strength of the polycrystalline metals, and is known as the grain boundary strengthening coefficient. Equation 3.3 is known as the Hall-Petch equation.

The Cottrell-Bilby theory has been criticised by some workers[70], who suggested that when a dislocation is locked by a precipitate, it would be permanently locked. On straining such a specimen, yielding would have to occur by the generation of new dislocations, which would multiply rapidly under the applied stress, and possibly produce a situation where these dislocations can continue to move under a lower stress, that is, at the lower yield stress. A mathematical model based on this line of argument is that of Hahn[71]. In this model, the strain rate imposed by the machine in a tension or compression test $\dot{\varepsilon} = d\varepsilon/dt$, must be matched by the elastic strain rate, $\dot{\varepsilon}_e = d\varepsilon_e/dt$, and the plastic strain rate $\dot{\varepsilon}_p = d\varepsilon_p/dt$.

or $$\dot{\varepsilon} = \dot{\varepsilon}_e + \dot{\varepsilon}_p \qquad \text{eqn 3.4}$$

The elastic strain rate $\dot{\varepsilon}_e$ can be described in terms of the stress σ and the modulus M, which describes the net elastic response of the test piece, grip and the testing machine,

or $$\dot{\varepsilon}_e = \frac{1}{M}\frac{d\sigma}{dt} \qquad \text{eqn 3.5}$$

The plastic strain rate $\dot{\varepsilon}_p$ can be described in terms of the Burgess vector b, the total length of the dislocation line in motion per unit volume L, and the average velocity of the dislocations v

or $$\dot{\varepsilon}_p = 0.5\ bLv \qquad \text{eqn 3.6}$$

where 0.5 b is the contribution of a single dislocation of unit length and unit velocity moving in a direction close to the maximum resolved shear stress.

As a first approximation, the quantity L is assumed to be a fixed fraction f of the dislocation density ρ,

i.e. $L = f\rho$ eqn 3.7

Also, dislocation multiplication and straining can be described by parabolic relationship of the form

$$\rho = \rho_o + Q\,\varepsilon_p^{\,q} \qquad \text{eqn 3.8}$$

The stress dependence of dislocation velocity can be described by the relationship,

$$v = \left(\frac{\tau}{\tau_o}\right)^n \qquad \text{eqn 3.9}$$

where τ is the resolved shear stress and is approximately equal to $\sigma/2$, and τ_o is the resolved shear stress corresponding to unit velocity.

Now, let $\Delta\sigma$ be the stress increment needed to maintain a given dislocation velocity, and assuming a simple linear strain hardening law such that

$$\Delta\sigma = m\varepsilon_p \qquad \text{eqn 3.10}$$

where m is a constant,

then, it follows that

$$v = (2\tau_o)^{-n}\,(\sigma - m\varepsilon_p)^n \qquad \text{eqn 3.11}$$

By combining equations 3.4, 3.5, 3.6, 3.7, 3.8 and 3.11, an expression for the relation between flow stress, plastic strain and strain rate is obtained:-

$$\dot{\varepsilon} = \frac{1}{M}\frac{d\sigma}{dt} + 0.5\,bf\,(\rho_o + Q\varepsilon_p^{\,q})\,(2\tau_o)^{-n}\,(\sigma - m\varepsilon_p)^n \qquad \text{eqn 3.12}$$

If the contribution of elastic strain is neglected, then the equation can be simplified to:-

$$\sigma = m\varepsilon_p + 2\tau_o\left[\frac{\dot{\varepsilon}}{0.5\,bf\,(\rho_o + Q\varepsilon_p^{\,q})}\right]^{\frac{1}{n}} \qquad \text{eqn 3.13}$$

This model is not elastic, but totally rigid under these conditions, and a finite yield stress dictated by ρ_o and $\dot{\varepsilon}$ is assumed the instant the test begins.

The model suggests that abrupt yielding of ordinary cubic structure metal will occur if[71]:-

(a) the initial density of mobile dislocations is sufficiently low,

(b) the internal stress opposing dislocation motion is sensitive to dislocation velocity, and

(c) rapid dislocation multiplication can occur.

Annealed polycrystalline low carbon steels generally satisfy all of the above requirements. This model, however, does not make allowances for the effect of grain size, temperature and other metallurgical factors. The omission of the effects of grain size in this "dynamic" yielding theory is very important as the grain-size dependence of the lower yield stress at ambient temperature has been well established. On the other hand, the grain boundary barrier theory (equation 3.3) does not provide for the yield points displayed by single crystals[71].

3.2 STRAIN AGEING IN LOW CARBON STEELS:

Strain ageing manifests itself chiefly by an increase in the yield or flow stress after ageing. This increase in yield or flow stress is the most universal indication of strain-ageing.

Referring to fig.3.3, the stress-strain curve of low carbon steel takes the form of curve (a). If the specimen is strained to a point A beyond the lower yield extension, unloaded and immediately retested, the stress-strain curve will follow the same curve (a). If, however, the specimen is unloaded at A and allowed to age for a period of time, the discontinuous yielding behaviour returns and the stress strain curve follows a curve such as (b). The yield point is now higher than the flow stress at the end of pre-strain.

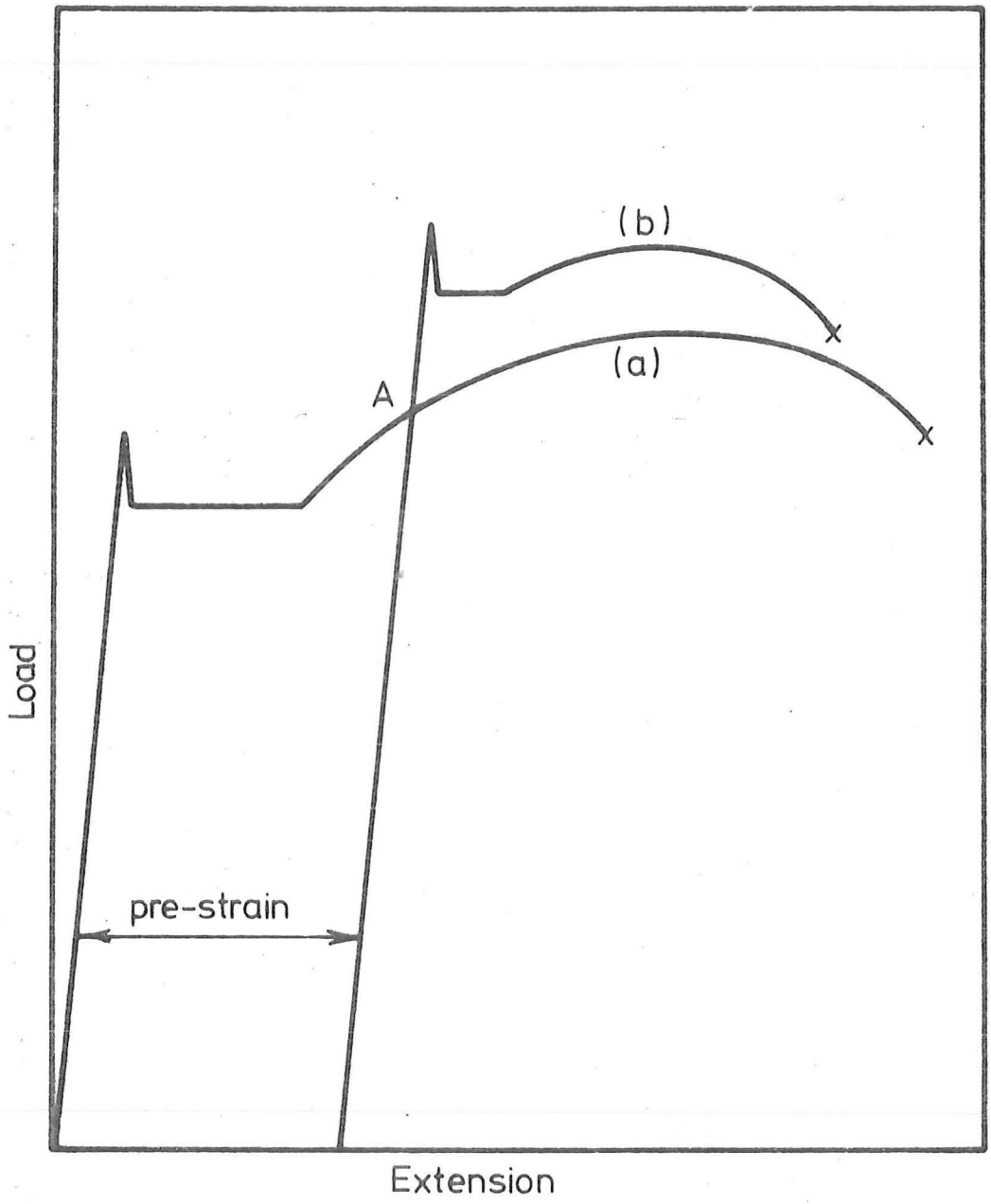

Fig. 3·3 EFFECT OF STRAIN AGEING ON THE TENSILE CURVE OF STEEL.

Other properties may also change during strain ageing; for example, increase in tensile strength; rise in the ductile-brittle transition temperature and the decrease in ductility.

Previous investigators have firmly established that strain ageing in steels is caused largely by the interstitial atoms of carbon and nitrogen. There is also considerable evidence to show that natural ageing (ageing at ambient temperature) after straining in low carbon steels or artificial ageing at temperatures below about 150°C is different in character from ageing at a higher temperature, e.g. above 200°C. It is now believed that strain ageing (both static and dynamic) below about 150°C is predominantly due to the presence of interstitial nitrogen, so that when the nitrogen is tied up by a strong nitride former such as titanium, aluminium, boron and vanadium, the steel shows negligible ageing below 150°C. At higher temperatures, the role of interstitial carbon cannot be ignored, and ageing due to carbon may be observed even in steels containing strong nitride formers.

Recent theories divide strain-ageing processes into two stages - where only "atmosphere" formation takes place, and where atmosphere formation is succeeded by the precipitation on the dislocations.

In steels containing no strong nitride formers, the first stage of strain ageing is consequently due to the formation of "Cottrell-atmospheres" which lock the dislocations. Below about 150°C, these atmospheres consist predominantly of nitrogen atoms, but at higher temperatures, considerable amounts of carbon atoms may be present. The first stage of strain ageing is characterised by the return of the yield stress and Luder strain on subsequent testing. The basic flow curve is not affected, since on straining beyond the yield point extension, the

"atmospheres" formed on the dislocations are dispersed.

In the second stage of strain-ageing, continued segregation of interstitial solutes to dislocations after the formation of "atmospheres" will result in the formation of precipitates (iron nitride at low ageing temperatures, and iron carbide at high ageing temperatures) on the dislocations, and raise the basic flow stress curve, hence, the lower yield point and the ultimate tensile strength. The corresponding increase in the strain hardening rate results in a decrease in elongation and the reduction of area.

As ageing is critically dependent on the diffusion rate of interstitial nitrogen and carbon atoms, the "degree" of ageing at different temperatures will be different, and Hundy[72] had formulated the following equation correlating strain ageing at ambient temperature and elevated temperatures.

$$\log \frac{t_r}{t} = H\left(\frac{1}{T_r} - \frac{1}{T}\right) - \log \frac{T}{T_r} \qquad \text{eqn 3.14}$$

where

t_r = ageing time at ambient temperature T_r (^oK)

and t = ageing time at elevated temperature T (^oK).

The constant H is equal to 4,400 for the diffusion of carbon atoms and 4,000 for the diffusion of nitrogen atoms.

Equation 3.14 suggests that the diffusion rate of carbon and nitrogen atoms to dislocations should be approximately the same, consequently, there is no reason why nitrogen atmospheres should form preferentially to carbon atmospheres on the dislocations during ageing at low temperatures. However, the solubility of nitrogen in ferrite is higher than that for carbon (0.10 wt % as compared to 0.022 wt %), and because of the low equilibrium solubility temperature of the iron nitrides Fe_4N and $Fe_{16}N_2$, these precipitates have a lower stability than the

iron carbides. The resolution of iron nitrides therefore takes place much more rapidly and gives a steady supply of interstitial nitrogen atoms for dislocation locking.

Only a small amount of interstitial atoms is needed for ageing to occur, and Baird[73,74] estimated that 0.0001 wt % of carbon or nitrogen is sufficient to produce detectable ageing and 0.001 wt % will produce severe ageing.

During normal fatigue testings, it has been established[12] that only interstitial nitrogen atoms are responsible for dynamic strain ageing (if any) in low carbon steels, consequently in this investigation, only steels with different levels of active (or free) nitrogen will be investigated as far as the aspect of strain ageing is concerned.

3.3 EFFECT OF DYNAMIC STRAIN AGEING AND COAXING ON THE FATIGUE LIMIT OF LOW CARBON STEELS:

Alloys which are known to process a definite fatigue limit generally have two other characteristics in common; they usually show a sharp yield point and can be strengthened by strain ageing. Published results have, however, shown that there is no close relationship between the static yield strength and fatigue strength[7]. Instead, better correlation between the fatigue limit and the tensile strength is generally observed, which suggests that strength after plastic deformation is important in fatigue.

Many attempts have also been made to establish the effect of dynamic strain ageing on the fatigue properties of materials, and the concept of the formation of a knee in the S-N curve, hence, the existence of a fatigue limit due to dynamic strain ageing, that is, ageing during the course of fatigue cycling, was first suggested by Levy[13,16]. This theory suggests that

fatigue damage and strengthening due to dynamic strain ageing are competitive processes, and cyclic stresses above the fatigue limit are necessary to develop damage sufficiently rapidly to outpace the progressive strengthening process due to ageing.

Referring to fig.3.4, it was postulated that the fatigue curve for the material, were it by some means prevented from strain ageing during testing, would be the smooth curve A-A'. If on the other hand, the material is strengthened fully by strain ageing before the test, the curve would be represented by another smooth curve X-X'. Both curves are smooth because no strain ageing is allowed to occur during the test. Since in practice strain ageing does occur, as it is a diffusion process which will inevitably follow after plastic deformation, which is known to be associated with the fatigue damage. It was argued that there would be a consequent increase in strength and the actual S-N curve will fall between A-A' and X-X', say along P_1P_2 at stresses S_1 and S_2. However, at a lower stress S_3, the conditions of stress, time and temperature may be such that sufficient strain ageing has taken place to convert the material to that represented by the curve X-X' before the specimen can fracture at K. If S_3K does not intersect X-X', fracture cannot occur and the observed fatigue curve will be P_1P_2KR with a knee at K.

Many workers have attempted to remove the knee of the fatigue curve of low carbon steels by the removal of interstitial nitrogen and carbon atoms, their results are, however, contradictory. Lipsitt and Horne[17] who compared the S-N curves given by a low carbon steel before and after decarburisation showed that a virtually smooth curve was obtained after decarburisation, and their result is often quoted

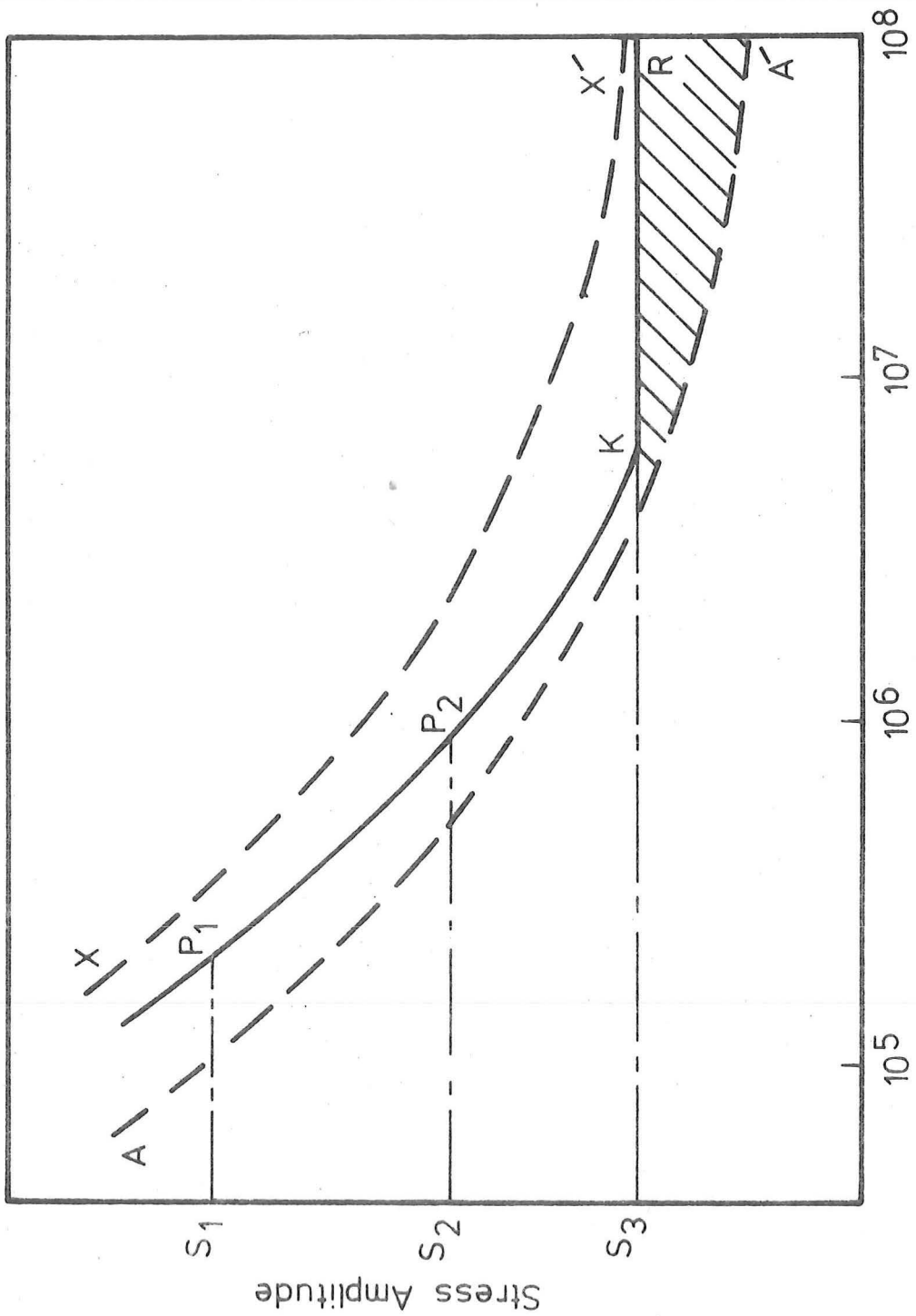

Fig. 3·4 EFFECT OF STRAIN AGEING OCCURRING DURING FATIGUE TEST. (Ref. 13)

in support of the strain ageing theory. On the other hand, Bishop et al[75] showed that a definite fatigue limit was retained even at a very low temperature of -196°C for two steels. At this low temperature, strain ageing, which depends on the diffusion process, is expected to be ineffective. Ferro and Montalenti[76] have also claimed that iron containing insufficient interstitial solute to allow strain ageing effects still retains a fatigue limit, and they suggested that fatigue limit is an intrinsic characteristic of the iron structure. The work of Erasmus[12] on three sets of steels having different strain age propensity showed conclusively that the effect of dynamic strain ageing (if any) in low carbon steels during normal fatigue testings is due solely to the interstitial nitrogen atoms, and steels containing negligible amounts of active nitrogen also retain a well defined fatigue limit. He further suggested that the main contribution towards the formation of a fatigue limit in low carbon steels is the result of the low initial free dislocation density in these materials.

Oates and Wilson[15] attempted to differentiate the role of dynamic strain ageing and initial dislocation locking present before cyclic stressing. In their investigation, evidence of dislocation relocking or dynamic strain ageing was only found in their coarse grained steel, where the yield stress/U.T.S. ratio was low, and cyclic stresses which were sufficient to cause general plastic deformation were not necessarily sufficient to cause fatigue failure. In their fine grained steel, where the yield stress/U.T.S. ratio was high, it was suggested that initial dislocation locking played an important role by limiting the spread of plasticity, and hence the fatigue damage. As a result, cyclic stresses which were sufficient to

cause general plastic deformation were also sufficient to cause fatigue failure.

As has been pointed out by Erasmus[12], the above theory as such would suggest a curve of fatigue limit versus grain size of the form as shown in fig.3.5, that is, a curve showing two regions of different slope. Section AB, i.e. the coarse grained region, is dependent on strain ageing after plastic deformation and should have a much gentler slope as compared to BC - the fine grained region, which is dependent on initial dislocation locking and consequently should have a slope similar to that of the yield stress[12]. Published results, however, do not show such a relationship and a continuous line of constant slope is generally obtained[19,77,78] such that:-

$$\sigma_L = \sigma_1 + C_2 d^{-\frac{1}{2}} \qquad \text{eqn 3.15}$$

It is well known that the fatigue limit of many common engineering materials is not a fixed quantity, but may be affected by the previous cyclic stress history. Understressing (i.e. cyclic loading at stresses below the fatigue limit) and coaxing (the process of understressing, followed by a procedure of gradually increasing the applied load in small increments and allowing a large number of stress cycles to occur after each load increment) have been shown to increase the fatigue limit of some metals considerably. In an extensive study of the coaxing behaviour of a selection of materials (ingot iron, in both unstrained and strain aged conditions, two carbon steels, 70/30 brass and an aluminium alloy), having differences in their ability to be strengthened by strain ageing and in their capacity to be strain hardened, Sinclair[14] found that the fatigue strengths of ingot iron and carbon steels were increased considerably by coaxing, but those of other metals showed no improvement.

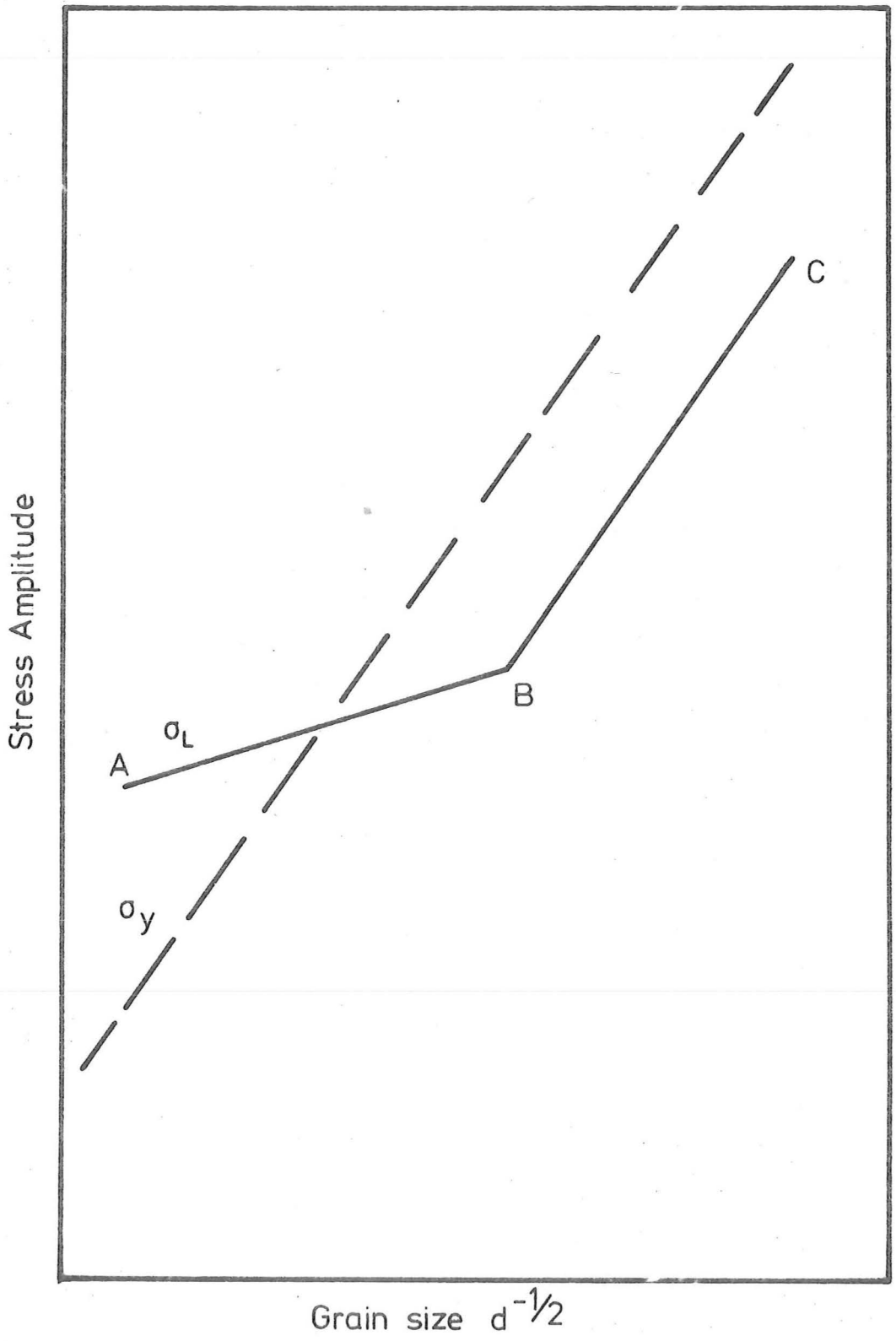

Fig. 3·5 RELATIONSHIP BETWEEN FATIGUE LIMIT AND GRAIN SIZE BASED ON OATES AND WILSON'S RESULTS (Ref. 12)

He concluded that only materials having the ability to be strengthened by strain ageing were capable of being coaxed. Erasmus[12] on the other hand found that steels both with and without active nitrogen, hence, an ability to strain age, were capable of being coaxed to the same degree. In fact, he observed that the fatigue strength of a commercially pure aluminium was coaxed to a much greater degree. He therefore concluded that coaxing is not a strain age hardening process and suggested that a possible explanation for a higher fatigue strength, usually obtained after coaxing or understressing, is due to the stress redistribution of the bending stress gradient, as all of the coaxing results reported were tested under rotating bending conditions.

3.4 THE EFFECT OF GRAIN SIZE ON THE FATIGUE STRENGTHS OF METALS:

Many studies have been carried out on the grain size dependence of mechanical properties of metals, and the Petch's relationship between flow stress (or yield stress) and grain size (equation 3.3) under monotonic tensile test is well known.

The fatigue strength of many metals is also remarkably affected by the polycrystalline grain size, and there are good evidences of increase in fatigue strength due to the reduction in polycrystalline grain size for metals such as low carbon steels[19,78], brass[79,80] and stainless steel[81]. In low carbon steels, the relationship between fatigue limit and grain size is found to follow the Petch type of relationship[19,77], that is:-

$$\sigma_L = \sigma_1 + C_2 d^{-\frac{1}{2}} \qquad \text{eqn 3.15}$$

On the other hand, the fatigue strength for metals such as copper and aluminium is not affected by the polycrystalline

grain size[79,80].

Generally, materials with grain size dependent fatigue lives are also those of difficult cross-slip and where there is no grain size effect, for example, copper and aluminium, cross-slip is relatively easy. The exception is low carbon steels, in which cross-slip is rather easy, but the fatigue lives are also grain size dependent.

Thompson and Backofen[80] investigated the effect of grain size on the high cycle fatigue strength of brass, copper and aluminium, they observed that only brass, which does not cross-slip easily, has its fatigue life affected by the polycrystalline grain size. They also suggested that only stage I crack propagation process is affected by the grain size, whereas the stage II crack propagation and the crack initiation are not generally affected by the polycrystalline grain size.

It was suggested[80] that, in metals which cross-slip easily, cellular sub-structures (which are considerably smaller than the polycrystalline grain size) will develop during fatigue cyclings and mask the grain size. This is because during stage I crack propagation, cracks advance by dislocation motion in the plastic zone at the crack tips, whether the process is by "unslipping" or "plastic blunting". In materials such as copper and aluminium, the cell walls behave much as grain boundaries do, and dislocations cannot penetrate them easily, as a result, most of the dislocations move within the cells, and very few dislocations interact with the grain boundaries. It follows that the deformation required for crack growth is conditioned only by the cell size, i.e. the crack growth is determined only by the applied stress amplitude, as cell size is a function of the stress amplitude, and therefore, grain size variations at constant stress can have little effect on the fatigue lives.

However, for materials such as brass, which does not cross-slip easily, cellular sub-structures are not formed and dislocation structures are in banded or planar arrangements, consequently, dislocation motion will be limited by the grain boundary, and the fatigue strength affected by the polycrystalline grain size.

For low carbon steels, where cross-slip is relatively easy and yet the fatigue strength is dependent on the polycrystalline grain size, Thompson and Backofen[80] suggested that this is due to the availability of grain boundary dislocation sources. Assuming that the dislocation sources per unit grain boundary area are a constant, a reduction in grain size will decrease the number of dislocation sources per grain, and will therefore increase the fraction of grains in which it is difficult to initiate slip.

It has also been suggested[82] that the grain size dependence of the fatigue strength cannot be explained solely by the cross-slip process. Yamada et al[82] examined the effect of temperature on the grain size dependence of the fatigue strength of α-brass and copper, and observed that at 200°C, where cross-slip is expected to be relatively easy, the grain size dependence of the fatigue strength of α-brass is still very remarkable. They subsequently suggested that the ageing effect is important.

Polycrystalline grain size may also affect the shape of the basic S-N curve. It has been shown that the sharpness of the knee in the S-N curve of a soft steel depends on grain size. Fatigue tests[83] on low carbon steel specimens having different grain sizes and varying amounts of carbon and nitrogen, showed that irrespective of the interstitial contents, specimens with finer grain size generally exhibit a much sharper knee than those

given by the specimens with coarser grain size.

CHAPTER 4.

THE RELATIONSHIP BETWEEN FATIGUE STRENGTH AND TENSILE PROPERTIES.

4.1 THE TRUE STRESS - TRUE STRAIN RELATIONSHIP:

The most frequently used method of defining the stress and strain on a member loaded under tension is the so-called nominal or engineering stress and strain, i.e. stress = P/A_o and strain = δ/l_o.

For properties in the elastic range, no serious ambiguity will result from the use of such definitions, as the change in the original area A_o or length l_o is so small as to be almost negligible. However, when dealing with the plastic range, the reduction in area and the strain can become very large, and the nominal stress and strain as defined above cannot be the true stress and true strain in the plastic range, and in many cases become meaningless.

A more realistic definition of stress and strain is the so-called true stress-true strain relationship. True stress is defined as:-

$$\sigma = P/A \qquad \text{eqn 4.1}$$

where A is the actual area of the cross section corresponding to the load P. True strain differs from nominal strain in that each increment of strain is based on the actual length at the time of the increment, instead of on the original length l_o.

i.e. $$\varepsilon = \sum \frac{l_1 - l_o}{l_o} + \frac{l_2 - l_1}{l_1} + \frac{l_3 - l_2}{l_2} + \ldots\ldots + \frac{l_n - l_{n-1}}{l_{n-1}}$$

or $$\varepsilon = \int \frac{dl}{l}$$

$$\therefore \quad \varepsilon = \ln \frac{l}{l_o} \qquad \text{eqn 4.2}$$

For a volume of metal undergoing plastic deformation, the volume may be considered to remain constant, i.e. $A_o l_o = A_1 l_1$, and the true strain may be expressed in terms of either length or area of the member, i.e.

$$\varepsilon = \ln \frac{l}{l_o} = \ln \frac{A_o}{A} \qquad \text{eqn 4.3}$$

True strain can therefore be obtained either by measuring the change in length or diameter on a specimen under tension.

Fig.4.1 compares the true stress-true strain relationship with that of a nominal stress-strain curve. It can be seen that, on a nominal stress-strain curve, a maximum stress (U.T.S.) exists beyond which the stress decreases, there is, however, no such equivalent maximum on a true stress-true strain curve, the stress continues to increase until final fracture.

Despite the dissimilarity between the true stress-true strain curve and the nominal stress-strain curve, it is possible to calculate true stress and true strain values from the nominal stress-strain data:-

because $\sigma A_1 = F A_o$

$$\therefore \quad \sigma = F \frac{A_o}{A_1}$$

but $A_o l_o = A_1 l_1$ (constant volume)

$$\therefore \quad \sigma = F \left(\frac{l_1}{l_o}\right)$$

$$\text{or} \quad \sigma = F \left(\frac{l_o + l_1 - l_o}{l_o}\right)$$

$$\sigma = F (1 + \lambda) \qquad \text{eqn 4.4}$$

$$\text{where } \lambda = \frac{l_1 - l_o}{l_o}$$

also, true strain $\varepsilon = \ln \frac{l_1}{l_o}$ eqn 4.3

$$\text{or} \qquad \varepsilon = \ln (1 + \lambda) \qquad \text{eqn 4.5}$$

But $\ln (1 + x) \simeq x$ for small value of x, therefore, for strain within the elastic range, true strain ε may be approximated by

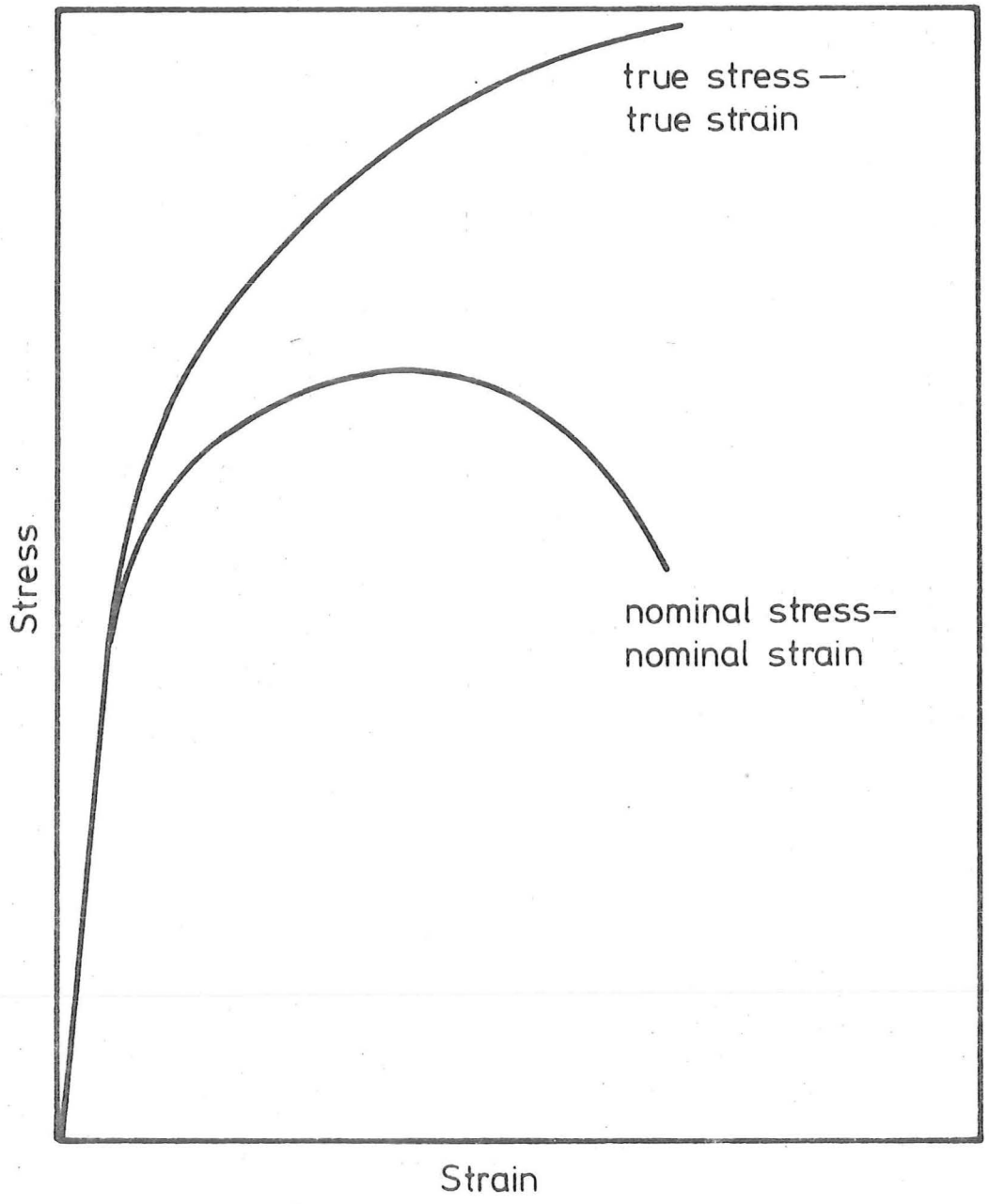

Fig 4·1 TRUE STRESS - TRUE STRAIN CURVE AND NOMINAL STRESS - STRAIN CURVE.

the value λ.

When using the true stress-true strain relationship, the strain hardening portion of the curve for most metals may be approximated by the power function, such that:-

$$\sigma = K\ \varepsilon^{n} \qquad \text{eqn 4.6}$$

where K and n are constants, K is termed the strength coefficient, and is equal to the stress at $\varepsilon = 1$. n is known as the strain hardening exponent. Equation 4.6 may also be expressed by a linear function:-

i.e. $\ln \sigma = \ln K + n \ln \varepsilon$ eqn 4.7

The K and n values may then be determined from a graph of $\ln\sigma$ versus $\ln\varepsilon$.

The rate of strain hardening during plastic deformation for metals which obey equation 4.6 is given by:-

$$\frac{d\sigma}{d\varepsilon} = nK\ (\varepsilon)^{n-1} \qquad \text{eqn 4.8}$$

Now, the point of plastic instability is defined as the point where:-

$\frac{dP}{d\varepsilon} = 0$ where P is the applied load,

but $P = \sigma A_1$

$$\therefore \quad \frac{dP}{d\varepsilon} = A_1 \frac{d\sigma}{d\varepsilon} + \sigma \frac{dA_1}{d\varepsilon}$$

$= 0$ at point of plastic instability,

but from equation 4.3

$$\varepsilon = \ln \frac{A_o}{A_1}$$

$$\therefore \quad A_1 = A_o \exp^{-\varepsilon}$$

and $\frac{dA_1}{d\varepsilon} = -A_1$

or $$\frac{dP}{d\varepsilon} = A_1 \frac{d\sigma}{d\varepsilon} + \sigma(-A_1)$$

$= 0$ at P_{max}

$$\therefore \quad \frac{d\sigma}{d\varepsilon} = \sigma \text{ at } P_{max} \qquad \text{eqn 4.9}$$

that is, the rate of strain hardening at P_{max} is equal to

the true stress at this point. Hence, for metals which strain harden according to equation 4.8,

i.e. $\frac{d\sigma}{d\varepsilon} = nK(\varepsilon)^{n-1}$

then from equation 4.9, $\frac{d\sigma}{d\varepsilon} = \sigma$

$\therefore \quad nK(\varepsilon)^{n-1} = \sigma$

but $\sigma = K\varepsilon^n$ eqn 4.6

$\therefore \quad n(\frac{\sigma}{\varepsilon}) = \sigma$

or $n = \varepsilon$ eqn 4.10

Thus, for metals which obey equation 4.6, the true strain at the point of plastic instability is equal to the strain hardening exponent n of the material.

4.2 THE FRICTION STRESS AND ITS RELATIONSHIP WITH THE FATIGUE LIMIT:

The yield stress of polycrystalline b.C.C. metals in which dislocations are locked by segregation or precipitates is well described by the Hall-Petch's equation:-

$$\sigma_y = \sigma_i + K_y d^{-\frac{1}{2}} \qquad \text{eqn 3.3}$$

The term σ_i is the friction stress, and represents that component of stress necessary to overcome resistance to dislocation movement in a slip band. Cracknell and Petch[84] investigated the effects of interstitial solute atom concentration on the friction stress of low carbon steels and observed that σ_i varied with such heat treatments as nitriding, annealing, sub-critical quenching and ageing. It has also been found that σ_i is markedly sensitive to temperature and strain rate. Heslop and Petch[85] suggested that the friction stress σ_i may be divided into two components:-

i.e. $\sigma_i = \sigma_i^* + \sigma_i^o$ eqn 4.11

where σ_i^* is dependent on composition and is temperature independent, and σ_i^o is the temperature dependent component.

In the Hall-Petch's equation, this friction stress σ_i is assumed to be independent of the polycrystalline grain size, and therefore may be assumed to be the yield stress for a specimen of infinite large grain, i.e. $d^{-\frac{1}{2}} = 0$. Consequently, σ_i may be determined from a plot of σ_y versus $d^{-\frac{1}{2}}$, and extrapolate the straight line to $d^{-\frac{1}{2}} = 0$.

On the true stress-true strain curve, that is, described by $\sigma = K\varepsilon^n$, the strain hardening portion may be extrapolated back to zero plastic strain to determine a stress σ_o on the elastic portion of the curve, see fig.4.2. Rosenfield[86] suggested that this stress σ_o is equivalent to the friction stress σ_i obtained from the Hall-Petch's plot, therefore, the stress $(\sigma_y - \sigma_o)$ is equal to the additional stress $K_y d^{-\frac{1}{2}}$ required to transmit slip across the grain boundaries. This approach has been criticised because of the variation of the parameters K and n in equation 4.6 with polycrystalline grain size[87], and σ_o as such is not equal to σ_i in the Hall-Petch's plot.

Another objection to this approach is that of Erasmus[12], he argued that initial dislocation movement, in the absence of dislocation locking and as the stress is increased above σ_o, will be small, the amount of plastic strain produced will therefore be small, and a smooth transition from elastic to plastic strain should result. Instead, as can be seen from fig.4.2, when the appropriate stress-strain curve is drawn to an extended scale for small strains, there is a discontinuity in the curve at σ_o.

Erasmus[12] suggested another approach to the determination of friction stress. He pointed out that, if the origin of the plastic flow curve were to be shifted away from the true origin by a distance $(\varepsilon_E - \varepsilon_o)$, see fig.4.3, the plastic portion of the

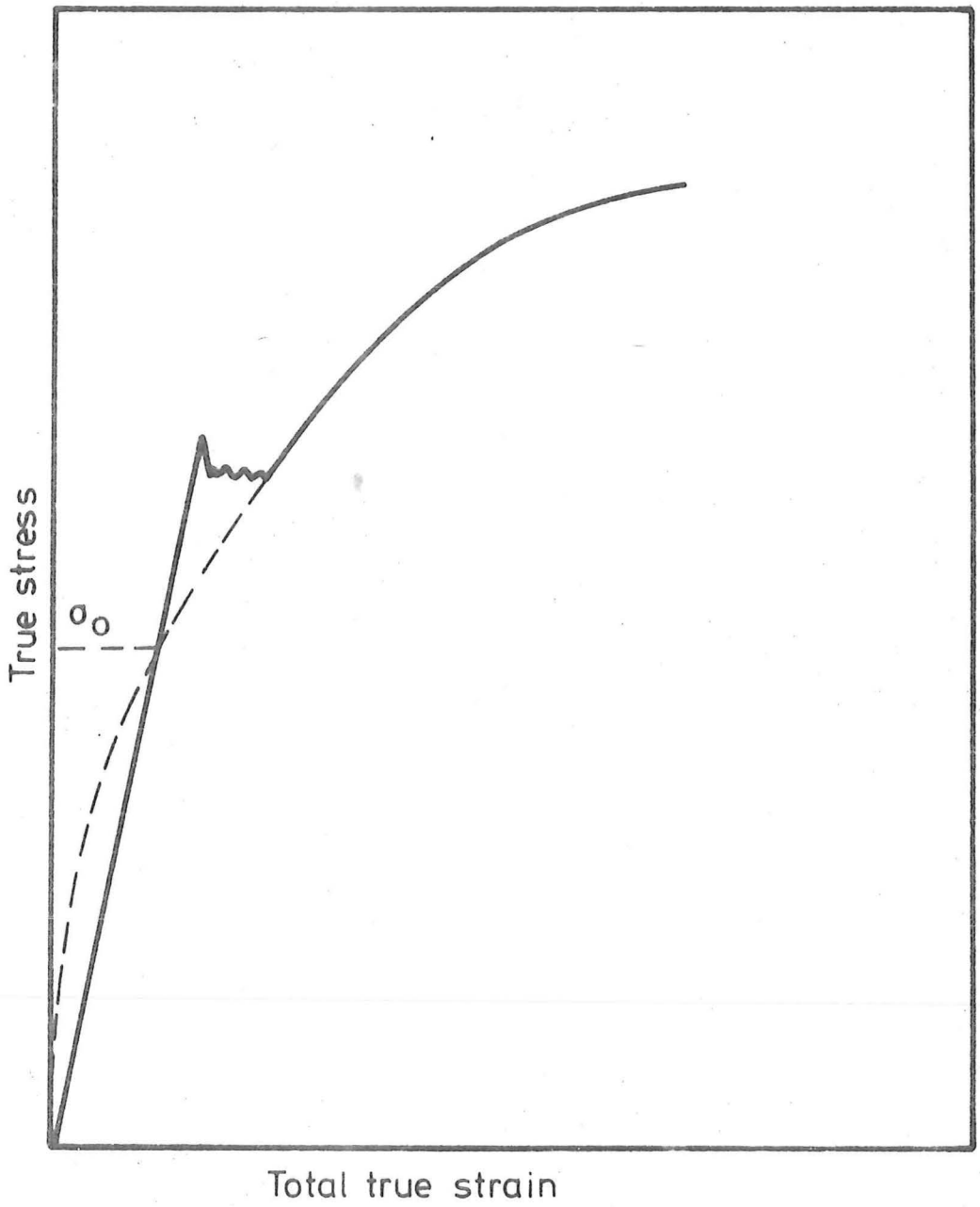

Fig. 4·2. DETERMINATION OF σ_o BY BACK EXTRAPOLATION.

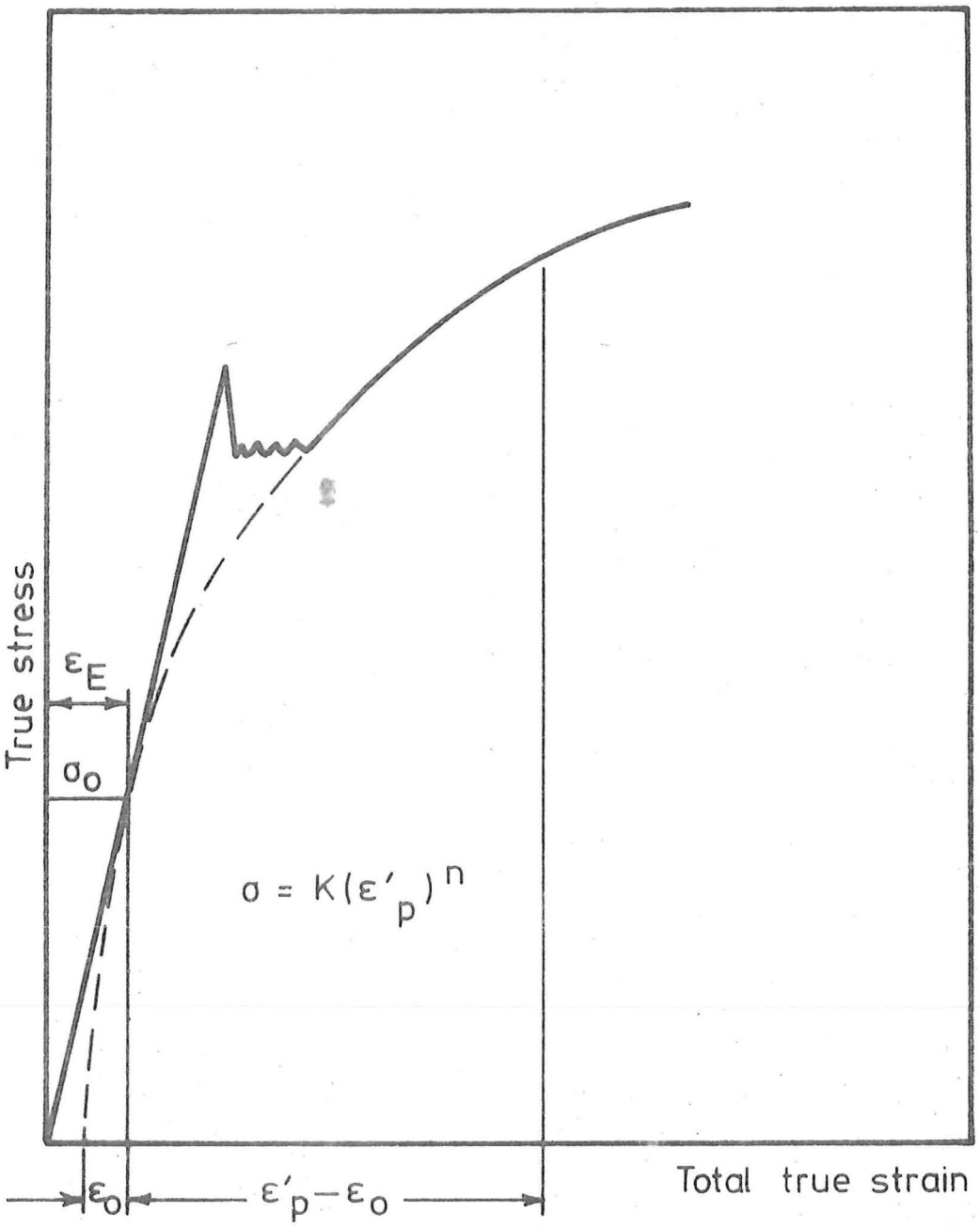

Fig. 4·3 DETERMINATION OF σ_o WITH EQUATION 4·12 (Ref. 12)

stress-strain curve is now assumed to comply with equation 4.6 so that:-

$$\sigma = K(\varepsilon_p')^n \qquad \text{eqn 4.12}$$

where $\varepsilon_p' = \varepsilon_o + \varepsilon_p$ eqn 4.13

The transition from elastic to plastic strain hardening is assumed to occur smoothly and the slope of the plastic flow curve at σ_o is equal to the modulus of elasticity E.

Because $\frac{d\sigma}{d\varepsilon_p'} = n\,K(\varepsilon_p')^{n-1}$ eqn 4.14

at $\varepsilon_p = 0$,

$\frac{d\sigma}{d\varepsilon_p'} = E$, and $\varepsilon_p' = \varepsilon_o$

$\therefore \quad nK(\varepsilon_o)^{n-1} = E$

or $\varepsilon_o = (\frac{nK}{E})^{\frac{1}{1-n}}$ eqn 4.15

but $\sigma = K(\varepsilon_p')^n$ eqn 4.12

$\therefore \quad \sigma_o = K(\varepsilon_o)^n$

or $\sigma_o = K(\frac{nK}{E})^{\frac{n}{1-n}}$ eqn 4.16

Since ε_o is small, i.e. less than ε_E, it was suggested[12] that the parameters n and K may be determined as for equation 4.7, where $\varepsilon = \varepsilon_p' \simeq \varepsilon_p$

σ_o as determined from equation 4.16 is not the true friction stress of the material, this is because the parameters n and K vary with grain size[87]. It was suggested[12] that σ_o may be regarded as an equivalent friction stress which incorporates the grain size component, and affects the absolute value of the friction stress in a metal of any particular grain size.

A recent work of Erasmus[88] on steel with a wide range of grain size showed that the strain hardening exponent n varies linearly with grain size so that:-

$$n = n_o - K_n d^{-\frac{1}{2}} \qquad \text{eqn 4.17}$$

In contrast, the strength coefficient K is independent of grain size, i.e. remains almost constant.

Equation 4.12 can thus be rewritten as

$$\sigma = K(\varepsilon_p')^{n_o - K_n d^{-\frac{1}{2}}} \qquad \text{eqn 4.18}$$

Now, when $\varepsilon_p = 0$, $\varepsilon_p' = \varepsilon_o$ and $\sigma = \sigma_o$.

$$\therefore \quad \sigma_o = K(\varepsilon_o)^{n_o - K_n d^{-\frac{1}{2}}} \qquad \text{eqn 4.19}$$

$$\text{where } \varepsilon_o = \left(\frac{nK}{E}\right)^{\frac{1}{1-n}} \qquad \text{eqn 4.15}$$

$$\text{Also } \sigma_o = K\left(\frac{nK}{E}\right)^{\frac{n}{1-n}} \qquad \text{eqn 4.16}$$

$$\text{and } n = n_o - K_n d^{-\frac{1}{2}} \qquad \text{eqn 4.17}$$

Therefore, at $d^{-\frac{1}{2}} = 0$

$$\sigma_o = K\left(\frac{n_o K}{E}\right)^{\frac{n_o}{1-n_o}} \qquad \text{eqn 4.20}$$

$$= \sigma_o' \quad \text{say}$$

σ_o', which is the proportional limit for a specimen of infinite large grain size, can thus be regarded as the true friction stress of the material, i.e. $\sigma_o' = \sigma_i$ of the Hall-Petch's plot.

Alternatively, the value of σ_o from equation 4.16 may be plotted against $d^{-\frac{1}{2}}$ and extrapolate back to $d^{-\frac{1}{2}} = 0$, where σ_o should again equal σ_i.

As σ_o from equation 4.16 may be considered as the limiting stress below which no plastic deformation can occur, it can therefore be assumed that no fatigue failure should occur at stresses below σ_o, consequently, the direct stress fatigue limit of a material should be greater than or equal to its equivalent friction stress σ_o, or $\sigma_{DS} \geq \sigma_o$.

To date, very few published data on the fatigue limit of steels showed the true stress-true strain data, only the works of Holloman et al[89] and Erasmus[12] included these data.

Erasmus[12] attempted to correlate the fatigue limits with the equivalent friction stress σ_o from the true stress-true strain data of his work and that of Holloman et al, and his analysis is illustrated in fig.4.4. From fig.4.4, it can be seen that the fatigue limits of these materials are not equal to their respective equivalent friction stresses σ_o, and it appears that, for softer materials (i.e. those with low σ_o), stresses above the equivalent friction stress are necessary to cause fatigue failure whereas for harder materials (those with higher values of σ_o), stresses below the equivalent friction stress are sufficient to initiate fatigue failure.

However, the fatigue limits from both Erasmus and Holloman et al were obtained from rotating bending testings, and as has been discussed in section 2.1, the fatigue limits obtained from bending or rotating bending testings are generally higher than the corresponding direct stress fatigue limits. Also, rotating bending fatigue limits are generally affected by the specimen size, and it has also been suggested that the higher fatigue strength of rotating bending testings may be due to the effect of stress redistribution of the maximum stressed outer fibre of the rotating bending specimens. It therefore appears that the more reliable direct stress fatigue limits should be used to correlate the fatigue properties of the materials with their equivalent friction stresses.

As Erasmus[12] did indicate a fatigue ratio

$$\frac{\text{rotating bending fatigue limit}}{\text{direct stress fatigue limit}}$$

of about 1.19 for his work, his fatigue results were subsequently divided by this factor to obtain the corresponding direct stress fatigue limits. Holloman et al, however, did not indicate the fatigue ratio in their work, but as many published results have suggested that (see section 2.1) the fatigue ratio approaches

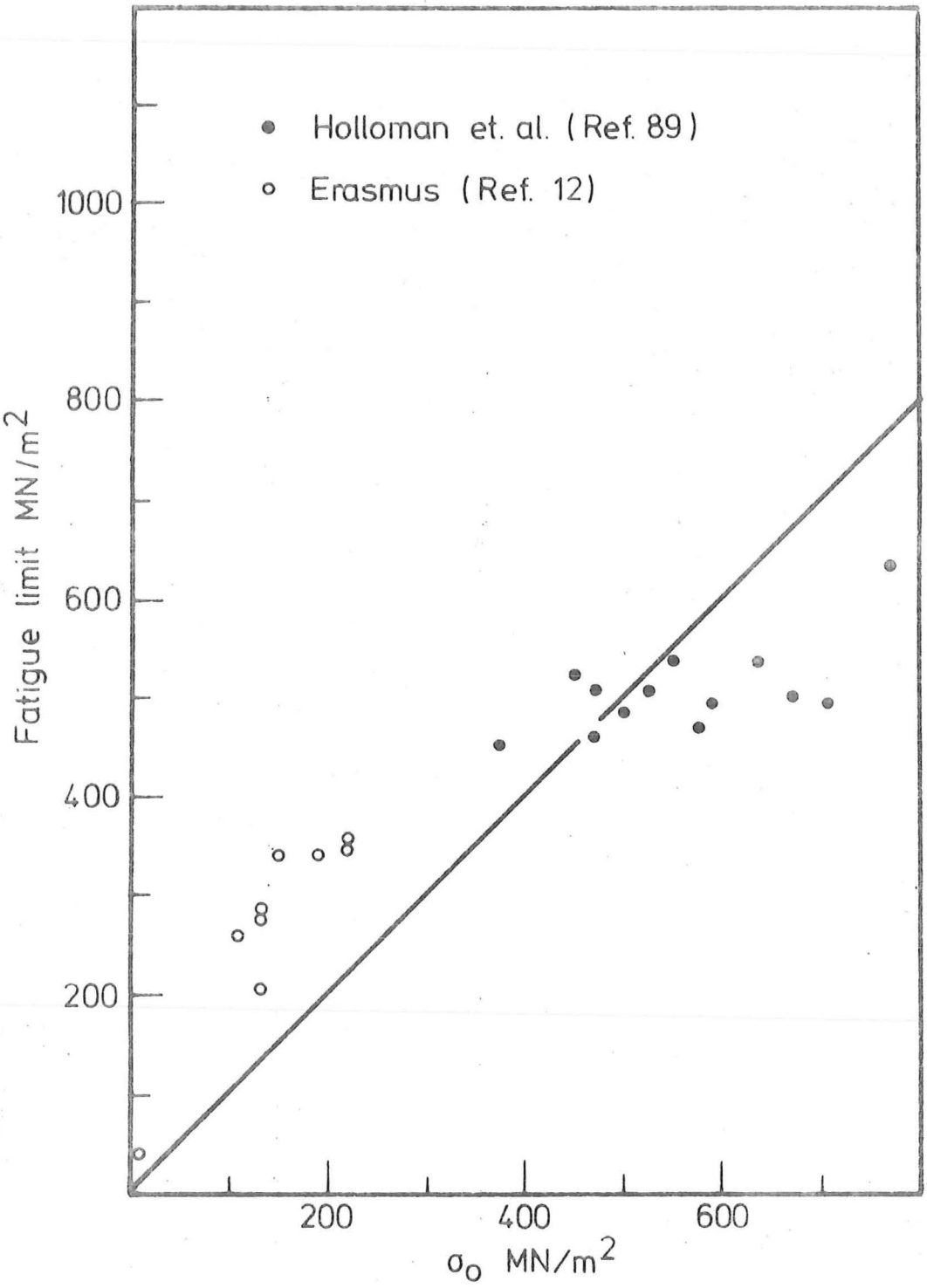

Fig 4·4 RELATIONSHIP BETWEEN FATIGUE LIMIT AND FRICTION STRESS. (Ref. 12)

unity for materials with high strength, and as all the materials used in Holloman et al's work were of very high strength, it seems reasonable to assume that their rotating bending fatigue limits were approximately equal to the direct stress fatigue limits of their materials. These corrected data are shown in fig.4.5, again, it shows that for softer materials, stresses above the equivalent friction stress σ_o are necessary for fatigue failures, or plastic deformation occurs at stresses below the direct stress fatigue limit. For hard materials, it appears that stresses sufficient to initiate plastic deformation are sufficient to cause fatigue failure, as a result, the direct stress fatigue limits are approximately equal to their corresponding friction stresses. For very hard materials, it appears that concentrated localized stress on stress rises such as machining or polishing marks, develops cracks in these positions, and with the aid of chemical activity, results in premature failure. Consequently, the direct stress fatigue limits for very hard materials tend to stresses below the corresponding σ_o.

4.3 THE EFFECT OF CYCLIC PRESTRESS ON THE YIELD POINT OF LOW CARBON STEELS:

An often overlooked aspect of the yielding behaviour is the effect of cyclic prestressing. Several researchers[19,90,91,92,93] have shown that the discontinuous yield behaviour may be substantially altered by cyclic prestressing. The sharp yield drop and the Luders strain can be completely removed, and the limit of proportionality substantially reduced.

Dislocation movement and microplastic strain have been known to occur at stresses well below the static upper yield point[94]. Suit and Chalmers[94], having examined the origin

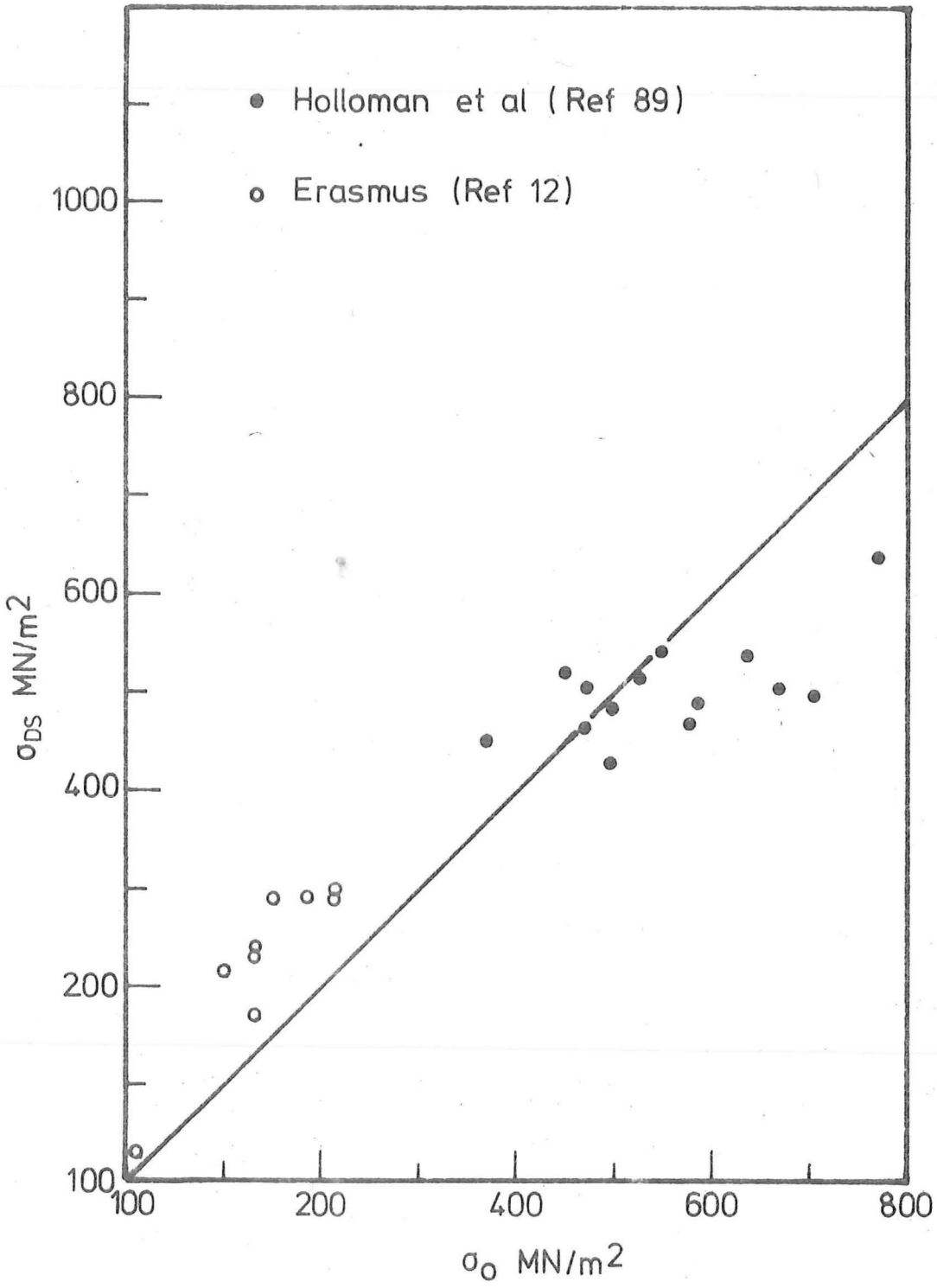

Fig. 4·5. DIRECT STRESS FATIGUE LIMIT vs FRICTION STRESS, CORRECTED DATA FROM REF. 12.

of plastic strain by etching the dislocation in Fe - Si - C alloys, showed that the stress necessary for the initiation of free dislocations and for their movement in slip planes of microvolumes was independent of grain size, and was approximately equal to the friction stress and single crystal yield stress for the silicon iron.

Klesnil et al[19] reported that reversed cyclic stressing of low carbon steel at stresses between the static yield stress σ_y and the direct stress fatigue limit σ_{DS} ($\sigma_y > \sigma_{DS}$), the strain amplitude increased with stress cycles (strain softening) until a maximum value was reached after a relatively large number of stress cycles had been applied, after which the strain amplitude decreased with stress cycles (strain hardening) to a saturation value. They also reported that this cyclic prestress resulted in the gradual removal of the sharp yield drop and the Luder strain with stress cycles. This effect was attributed to the generation of free dislocations and the expansion of the plastically deformed volumes formed during cyclic stressing.

In considering microplasticity, the terminology of Brown et al[95] is commonly used, see fig.4.6. For an annealed or aged α-iron or steel specimen, the stress-strain curve shows an upper and lower yield point followed by a region of plastic flow. Once the specimen has been plastically strained, free dislocations are generated and, upon reloading, a new elastic limit σ_E results. This elastic limit σ_E is the lowest stress determined by a loading-unloading method in tension or compression from which the stress-strain curve upon unloading is not linear, but the hysteresis loop is closed, see fig.4.6. σ_E therefore represents the smallest stress at which the movement of a large number of dislocations can be detected directly, and it was suggested[95] that σ_E truly represents the friction

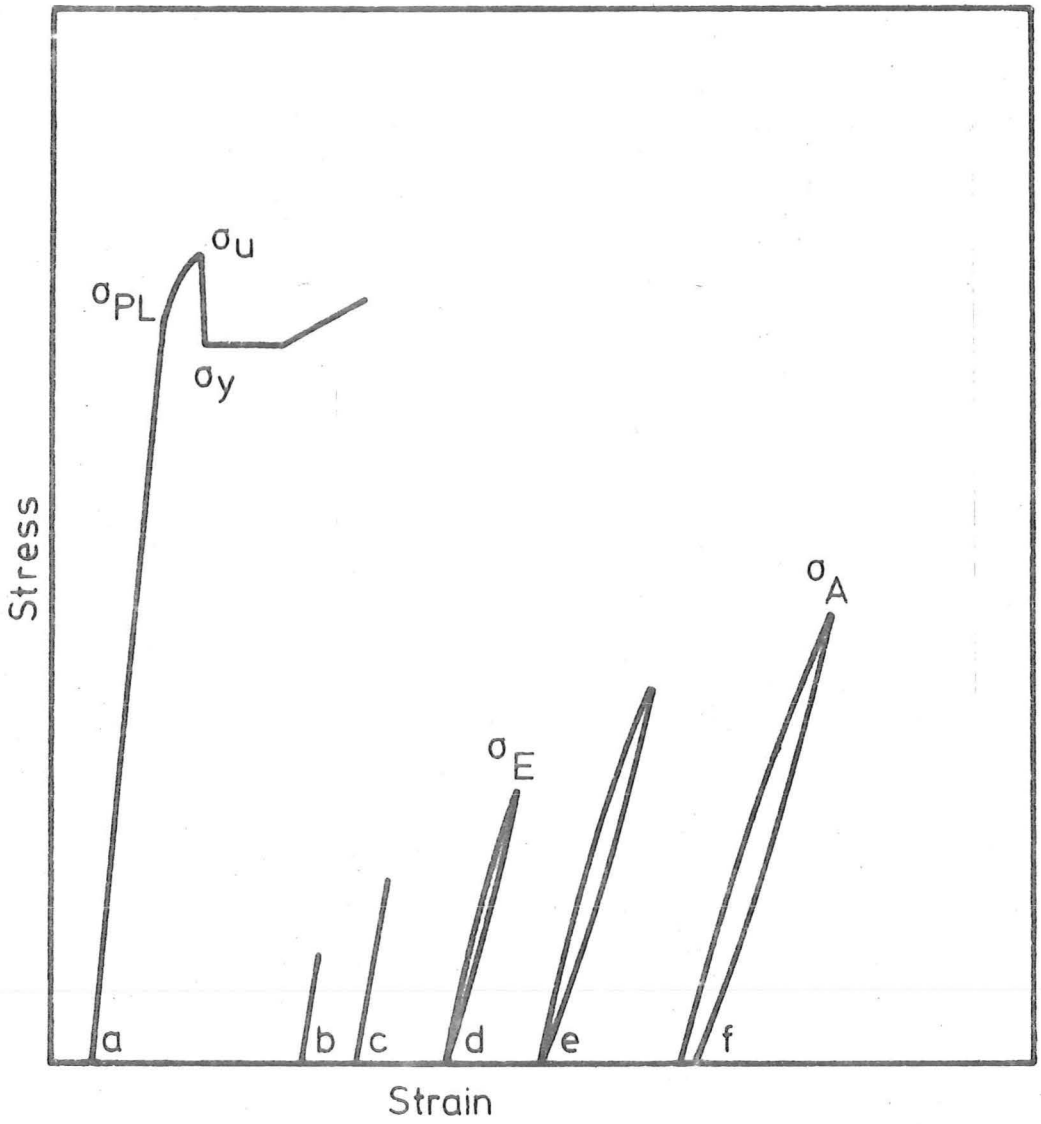

Fig. 4·6 TYPE OF YIELD POINTS IN IRON (Ref. 95)

stress of the material, because it is the stress level which must be exceeded before appreciable dislocation movement is possible. It was also suggested[95] that at σ_E, only the most mobile part of the dislocation array is moved, and most probably only the mobile edge dislocations are involved. The value of σ_E is, however, very much dependent on the sensitivity of the measuring instrument[95].

In a series of loading and unloading tests with increasing stress amplitude, a stress σ_A exists, at which point an open hysteresis loop results, this is termed the anelastic limit of the material. Above σ_A, dislocation movements are irreversible and it was suggested[96] that the movement of screw components results in permanent strain.

Abel and Muir[91] differentiated the mechanisms of micro-yielding in unidirectional cyclic stressing (i.e. cyclic loading in one direction) and that in reversed direct stressing. They observed that, under unidirectional prestress, cyclic stresses around the static lower yield stress were necessary for the suppression of the sharp yield drop, and these stresses were above the anelastic limit σ_A and well above the elastic limit σ_E as obtained by the loading-unloading method described before. However, under reversed direct prestress, the cyclic stresses necessary for the elimination of the sharp yield drop and the Luder strain were well below the static lower yield stress, and very much less than the values of anelastic limit σ_A or the elastic limit σ_E as obtained from the loading-unloading method. It was also suggested that the gradual removal of the discontinuous yield point can be better explained by the "dynamic" dislocation multiplication theory of Johnston and Gilman[70], and Hahn[71].

Abel and Muir[91] suggested that, under unidirectional

cycling, an exhaustion hardening mechanism is operating whereby the supply of the mobile edge dislocations is exhausted, and at cyclic stress below the static lower yield stress, the number of new mobile dislocations generated is very small and is insufficient to satisfy the strain rate imposed by the tensile machine during subsequent tensile tests. At stresses above the static lower yield stress, the normal mechanisms of plastic deformation take over to produce sufficient number of mobile dislocations and result in the suppression of the yield point phenomenon. Under reversed direct stressing, it was suggested [91] that micro-Bauschinger effect is operating, and when an edge segment of a dislocation is forced against a barrier on loading in one direction, its potential to move with the reverse load is increased. Consequently, plastic flow can occur in the compression half-cycle immediately following a tensile half-cycle at a much lower stress than that attained in the preceding half-cycle. It was also suggested that the reverse strain will be larger than the forward strain, and the mobile dislocation density is increased in the process. Sufficient mobile dislocations can consequently be generated to satisfy the strain rate imposed by the tensile machine during subsequent tensile test at cyclic stresses below static yield stress.

As a result of the above finding, Abel and Muir[91] further suggested that the values of anelastic limit σ_A and elastic limit σ_E should be determined from reversed direct cycling (tension-compression) instead of the generally accepted uni-directional cyclic loading (load-unload method) as described previously.

Luther and Williams[93] reported that, under unidirectional cyclic prestress, the yield strength (limit of proportionality) increased progressively with stress cycles, while under reversed

direct prestress, it decreased progressively with stress cycles. The yield strength (limit of proportionality) finally attained for both loadings was equal to the cyclic stress applied. It was suggested that, under reversed direct prestress, cyclic stresses above the direct stress fatigue limit are necessary for the suppression of the discontinuous yield point phenomenon, and micro-Bauschinger effect was also suggested to operate under reversed direct stressing.

Published works have shown that a specific dislocation density is formed at each stress amplitude before fatigue failure, and the dislocation sub-structures under direct stress fatigue loading are very similar to those under tensile loading. These results have led Erasmus[12] to postulate that a fatigue saturation strain ε_p^* is necessary before fatigue failure can occur. If this theory is correct, a finite plastic strain will be accumulated at stresses just below the direct stress fatigue limit, although it may be very small, and if micro-Bauschinger effects, as suggested by Abel and Muir[91], and Luther and Williams[93] are operating under reversed direct stressing at stresses where very small strains are involved, it is reasonable to assume that it should also operate at stresses just below the direct stress fatigue limit, provided that the applied stress is above σ_A (as obtained from tension-compression). The accumulation of mobile dislocations after sufficiently large number of stress cycles should provide enough mobile dislocation density to satisfy the strain rate of the tensile machine during subsequent tensile tests, such that the discontinuous yield point phenomenon is eliminated. It would therefore be interesting to examine if reversed direct stressing at stresses just below the direct stress fatigue limit would suppress the

discontinuous yield point phenomenon of low carbon steels.

CHAPTER 5.

THE INFLUENCE OF SMALL INELASTIC STRAIN ON THE LOAD CARRYING CAPACITY OF MEMBERS.

5.1 INCEPTION AND PROGRESS OF YIELDING:

As has been mentioned in section 4.3, based on the published works on dislocation sub-structure formed during fatigue cycling, Erasmus[12] has postulated that a fatigue saturation strain is needed before fatigue failure can occur under direct stress cycling. Also, the relationship between the direct stress fatigue limit and the equivalent friction stress σ_o as shown in fig.4.5 suggests that general plastic deformation occurs before fatigue failure under direct stress loading, at least for the "soft" materials (i.e. where σ_o is low). It would thus appear that, when a rotating bending or bending specimen is tested at a calculated applied stress σ_{app} (calculated from the elastic theory, $M = \frac{\sigma I}{n}$) above the direct stress fatigue limit σ_{DS}, plastic deformation will occur in the surface layer where $\sigma \geqslant \sigma_{DS}$, provided that sufficient numbers of stress cycles have been allowed. As a result, stress redistribution should occur after the plastic deformation of the surface layer. However, as has been discussed in chapter 2, although the stress redistribution theory accounts for the higher fatigue strength for rotating bending or bending testings compared with direct stress testing, and many fatigue properties of notched specimens, it could not account for the size effect of the rotating bending, bending, and notched fatigue specimens. The stress redistribution theory as such is therefore inadequate and modification to the theory is required.

In order to appreciate fully the effect of a small layer of inelastic strain on the load carrying capacity of a fatigue member, the process of yielding and its influence on the load carrying capacity of members is examined briefly below.

The load P_e or bending moment M_e at which the highest stressed fibre of a tension member or of a beam will just begin to strain inelastically is calculated from the elastic theory

i.e. $P_e = \sigma_e a$, and $M_e = \sigma_e I/r_1$

where σ_e = yield stress of the material

I = moment of inertia

a = area of specimen

r_1 = half width of the beam

It is well known that the load P or the bending moment M required to cause an inelastic strain to spread a small distance is somewhat larger than P_e or M_e respectively.

Referring to fig.5.1, and assuming a case of perfect elastic-plastic material, i.e. one which obeys the stress-strain relationship of fig.5.1 g. Figs.5.1a and 5.1b illustrate the stress distribution in an axially loaded member with a notch and a beam under plane bending. These stress distributions are reached with an applied load P_e or bending moment M_e, such that a maximum stress is just equal to the yield point σ_e (or limit of proportionality) of the material.

If the load P or the bending moment M is increased to a value $P_1 > P_e$, or $M_1 > M_e$, i.e. as shown in figs.5.1c and 5.1d respectively, the members will begin to strain inelastically, and the plastic zones are illustrated by the cross-hatched areas with a depth h, leaving an elastic core of $2(r_1 - h)$. The stress distributions are also shown in figs.5.1c and 5.1d respectively. Within the plastic zone h, the stress remains constant, i.e. equal to σ_e, as the material is assumed to be perfect

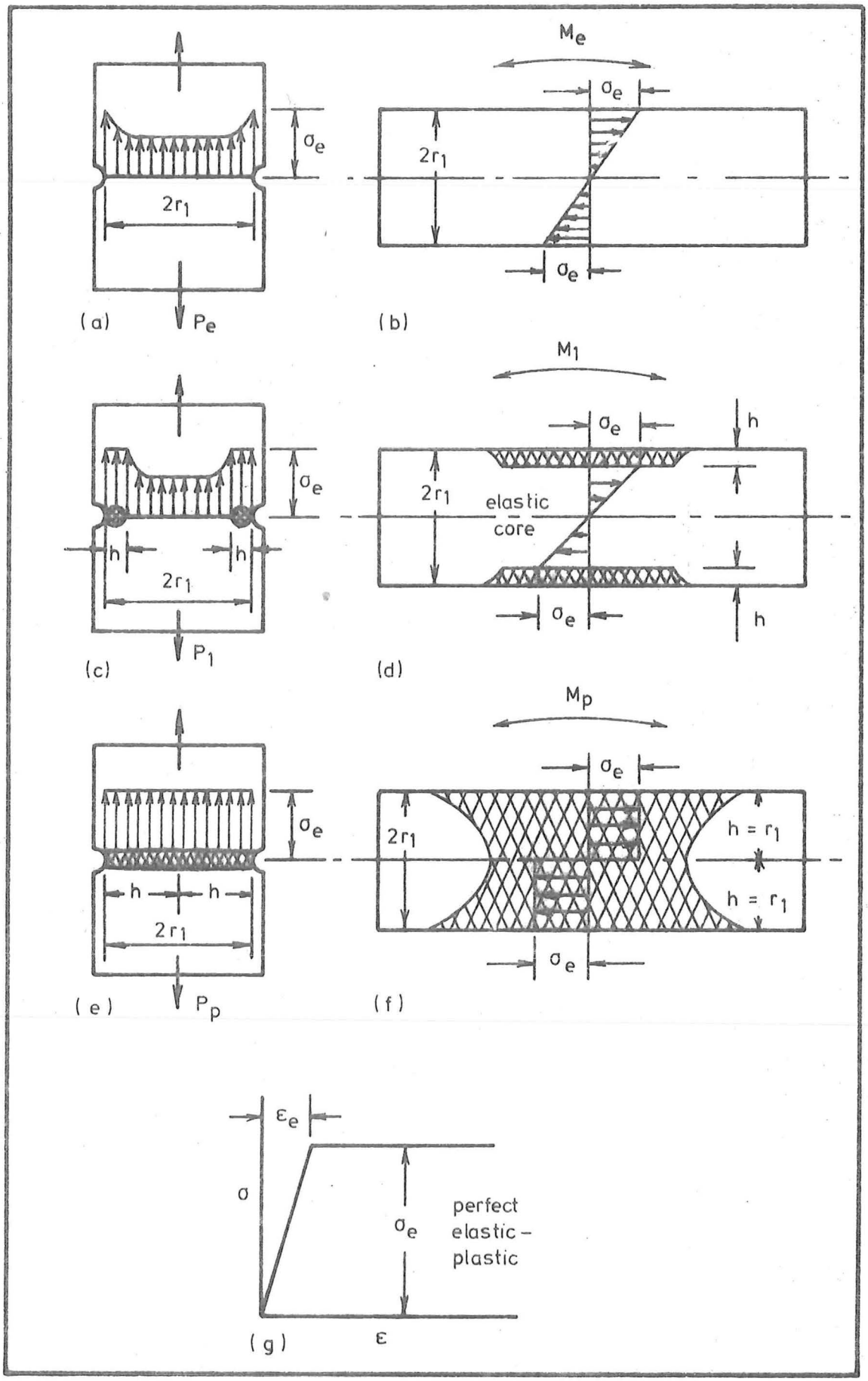

Fig. 5·1. STRESS DISTRIBUTIONS FOR ELASTIC, PARTIALLY PLASTIC AND FULLY PLASTIC CONDITIONS.

elastic-plastic.

If the load P or the bending moment M is increased further, a situation such as shown in figs.5.1e or 5.1f will arise, i.e. plastic strain will spread across the whole cross-section of each member and the load P_p, and the bending moment M_p are known as the fully plastic load and fully plastic moment respectively.

In order to illustrate the effect of a small plastic layer h on the load carrying capacity of a member, a simple case of a circular hole in a plate under uniaxial tension is considered. Fig.5.2a illustrates the stress distribution of a plate containing a hole of radius ρ ($\rho << b$) under axial tension with nominal stress σ_n, such that the yield stress σ_e of the material is just reached at the edge of the hole. The maximum stress will be at the edge of the hole, and since the theoretical stress concentration factor for a circular hole is[64]

$$K_t = 3$$

$$\therefore \quad \sigma_e = 3\sigma_n$$

$$\text{or} \quad P_e = (1/3)\sigma_e a \qquad \text{eqn 5.1}$$

where a = area of the specimen.

The elastic stress distribution around a circular hole can be shown[97] to be

$$\sigma = \frac{\sigma_n}{2}\left(2 + \frac{\rho^2}{x^2} + 3\,\frac{\rho^4}{x^4}\right) \qquad \text{eqn 5.2}$$

Assuming a perfect elastic-plastic material, i.e. as in fig.5.1g, if the load is increased to $P > P_e$, but less than P_p, a plastic deformed layer of depth x_1 will result, and the stress distribution is represented by curve ABC, where AB represents a uniform stress σ_e and BC represents the elastic stress distribution, see fig.5.2b.

The stress distribution around the hole may be approximated

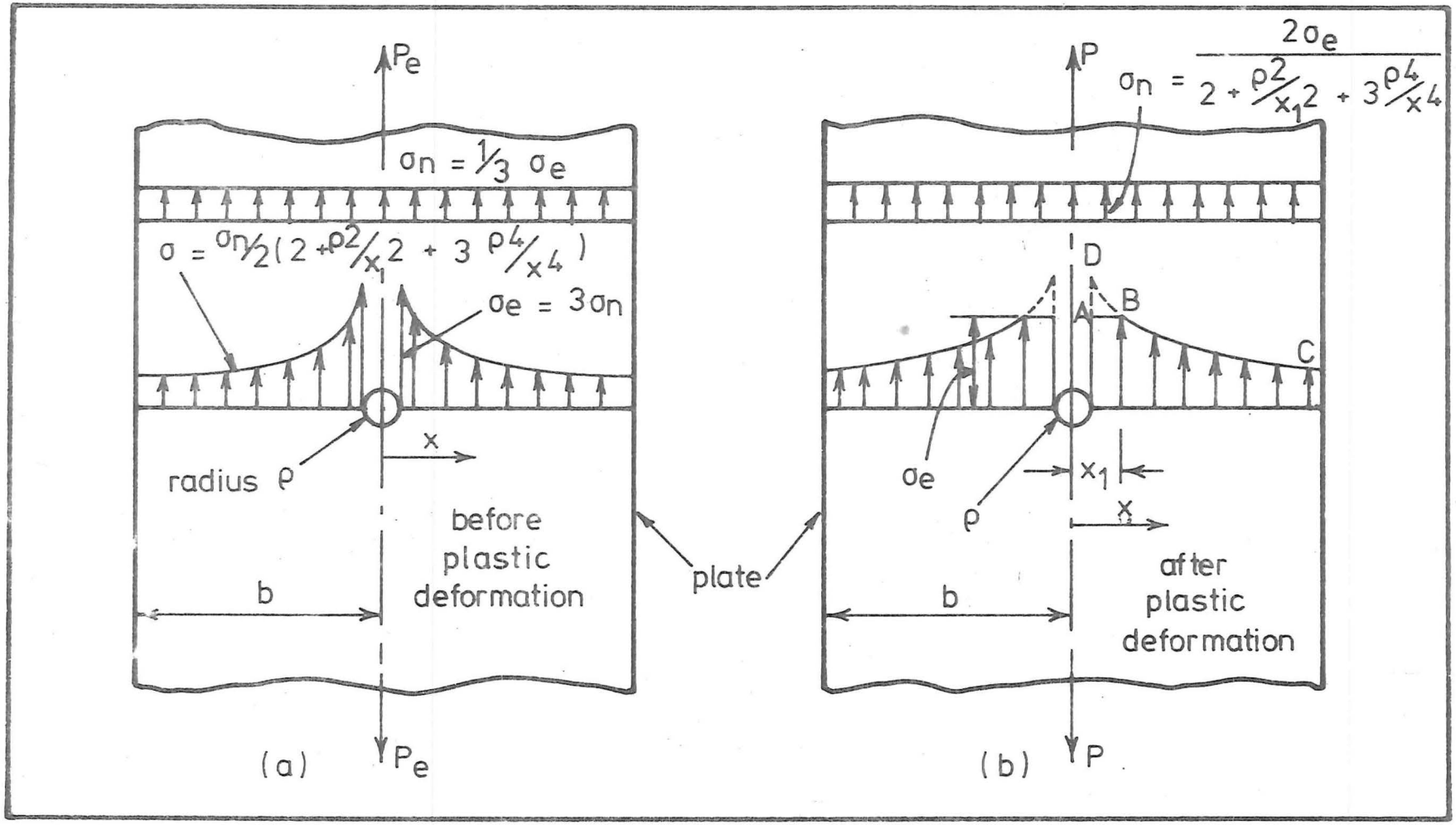

Fig. 5·2 STRESS DISTRIBUTION ON A PLATE CONTAINING A CIRCULAR HOLE BEFORE AND AFTER PLASTIC DEFORMATION.

by an elastic stress distribution (equation 5.2) with only small error provided that[98]

(a) the plate's width is large compared to the hole,

(b) the plastic zone is relatively small.

Therefore the stress distribution around the hole is represented by curve DBC and the stress is

$$\sigma = \frac{\sigma_n}{2}\left(2 + \frac{\rho^2}{x^2} + 3\frac{\rho^4}{x^4}\right) \qquad \text{eqn 5.2}$$

This curve must pass through point B

i.e. $x = x_1$ and $\sigma = \sigma_e$

or $$\sigma_n = 2\sigma_e/(2 + \rho^2/x_1^2 + 3\rho^4/x_1^4) \qquad \text{eqn 5.3}$$

where σ_n represents the nominal stress at some distance from the hole (erroneous) with the assumption that the stresses on the plastic region are represented by ordinates to the curve DB instead of AB, but the error is small, especially when x_1 is small. Therefore, the load P corresponding to a plastic zone x_1 is

$$P = \sigma_n a$$

or $$P = 2\sigma_e a/(2 + \rho^2/x_1^2 + 3\rho^4/x_1^4) \qquad \text{eqn 5.4}$$

but $$P_e = (1/3)\sigma_e a \qquad \text{eqn 5.1}$$

Therefore, the load carrying capacity of the plate with a plastically deformed zone x_1 is

$$P/P_e = 6/(2 + \rho^2/x_1^2 + 3\rho^4/x_1^4) \qquad \text{eqn 5.5}$$

The variation of the load carrying capacity P/P_e as the depth of the plastic zone x_1 increases is shown in fig.5.3. The load carrying capacity P/P_e increases very rapidly from the value $P/P_e = 1$, which corresponds to the load at which inelastic strains are just on the verge of occurring, for example at $x_1 = 1.5\rho$, i.e. $h = 0.5\rho$, the load carrying capacity P/P_e has increased to about 2. This illustrates the importance of an

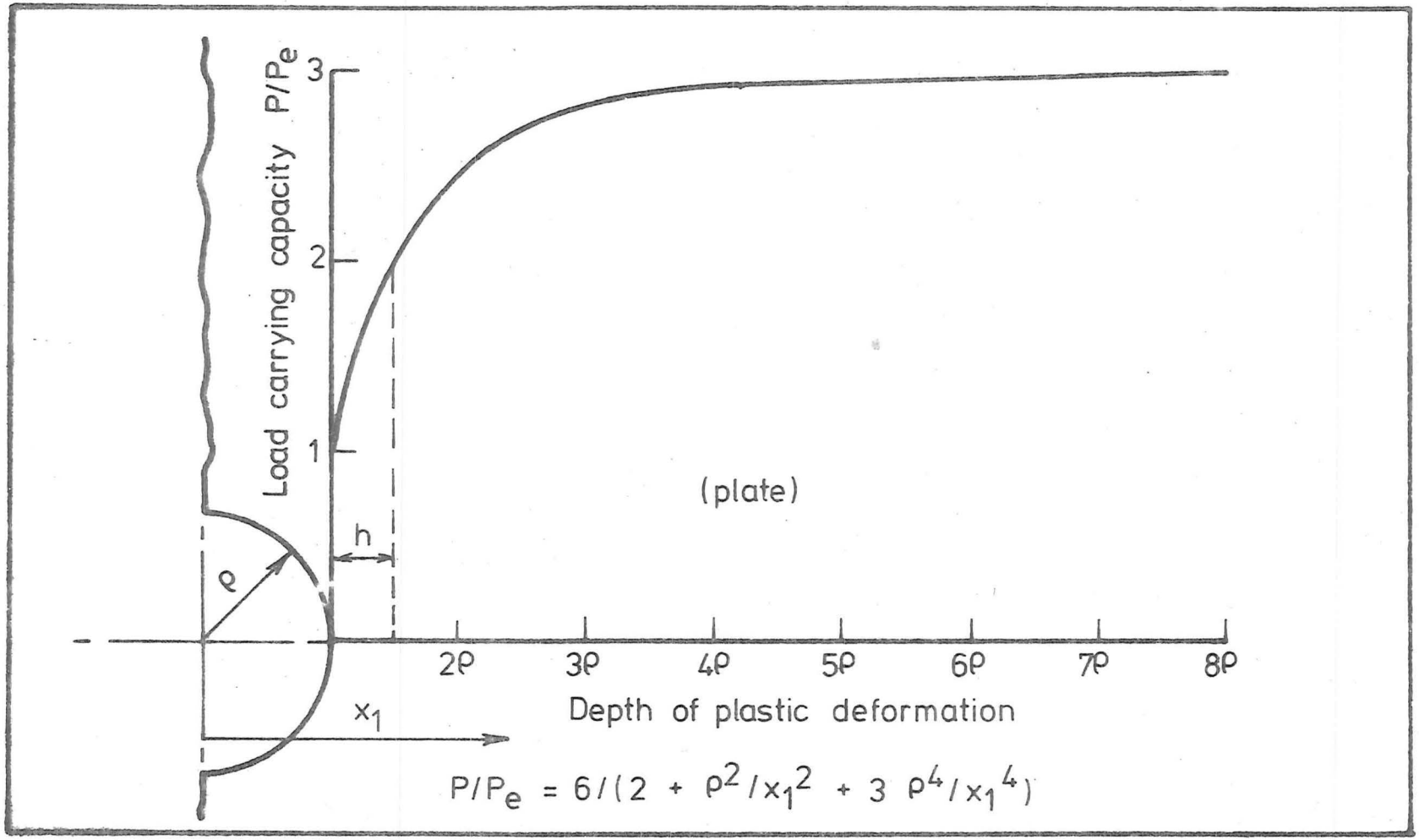

Fig. 5·3 EFFECT OF INELASTIC STRAIN ON THE LOAD CARRYING CAPACITY OF A PLATE CONTAINING A CIRCULAR HOLE.

inelastic layer in determining the load carrying capacity of a member.

5.2 DETERMINATION OF THE PLASTICALLY DEFORMED LAYER OF A ROTATING BENDING MEMBER AFTER STRESS REDISTRIBUTION:

In the previous section, the importance of a small inelastic strain in determining the load carrying capacity of a member subjected to non-uniform stress was illustrated, for example, a plate containing a small hole of radius ρ (ρ << the width of the plate) under uniaxial tension, a plastic zone of depth equal to about 0.5ρ is sufficient to double the load carrying capacity of the member. Consequently, the depth of the plastic layer developed after stress redistribution is an important factor in determining the load carrying capacity (hence, the fatigue strength) of a rotating bending member. It would thus appear that the stress redistribution theory should be considered from the depth of the plastic layer developed after stress redistribution, and not the actual surface stress as suggested by Forrest and Tapsell[56,57].

In order to examine the effect of plastic layer on the load carrying capacity (hence, the fatigue strength) of a rotating bending member, the stress and strain distribution within the cross-section of the specimen has to be understood, so that the depth of the plastic layer developed after stress redistribution can be determined. Let's first assume that:-

(a) there exists a dynamic yield stress σ_e which is below the static lower yield stress σ_y and the rotating bending fatigue limit σ_{RB},

(b) after sufficient number of stress cycles, plastic deformation occurs at surface fibres where $\sigma \geq \sigma_e$.

Fig.5.4a shows the cross section of a rotating bending

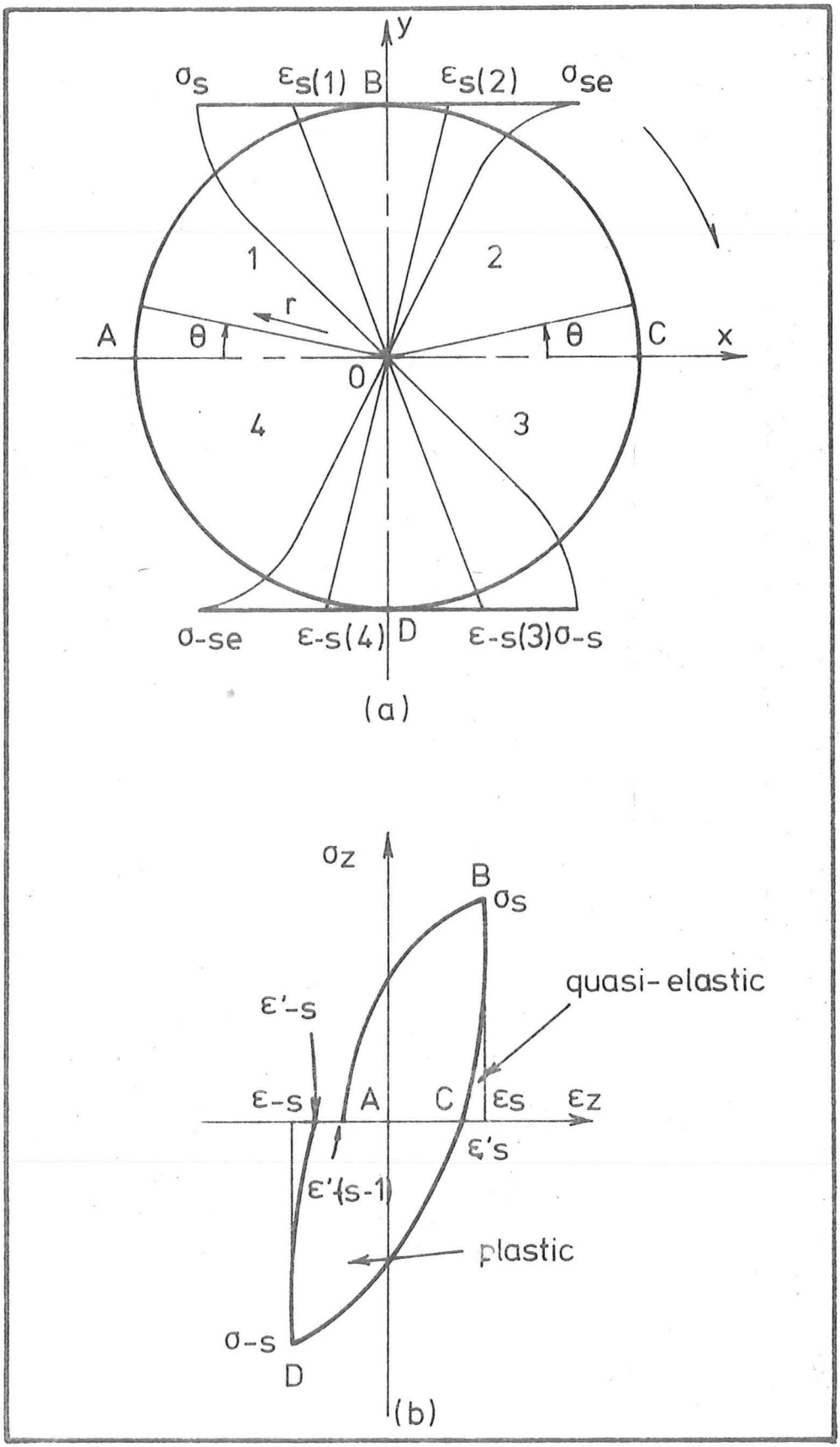

Fig. 5·4. STRESS AND STRAIN DISTRIBUTION FOR A ROTATING BENDING SPECIMEN. (REF. 99)

specimen. The stress-strain relationship for a point A on the specimen surface as it rotates from A→B, B→C, C→D and D→A has been studied by Minamisawa et al[99], and will provide the bases for the following analysis.

It is further assumed that:-

(a) the strain ε on the cross-section of the specimen is directly proportional to the distance from the neutral axis x,

(b) relationship between stress and strain after plastic deformation may be expressed by the relationship

$$\sigma = K \varepsilon_z^n \qquad \text{eqn 5.6}$$

Let the hysteresis curve describing the point A after plastic deformation at S^{th} cycle, as A rotates from A→B, B→C, C→D and D→A be as shown in fig.5.4b. The change in strain as A rotates from:-

$$\text{A→B is } \varepsilon_{s(1)} = \left| \varepsilon'_{-(s-1)} \right| + \left| \varepsilon_s \right| \qquad \text{eqn 5.7a}$$

$$\text{B→C is } \varepsilon_{s(2)} = \left| \varepsilon_s \right| - \left| \varepsilon'_s \right| \qquad \text{eqn 5.7b}$$

$$\text{C→D is } \varepsilon_{-s(3)} = \left| \varepsilon'_s \right| + \left| \varepsilon_{-s} \right| \qquad \text{eqn 5.7c}$$

$$\text{D→A is } \varepsilon_{-s(4)} = \left| \varepsilon_{-s} \right| - \left| \varepsilon'_{-s} \right| \qquad \text{eqn 5.7d}$$

Expressing the strain at any point in the four quadrants by the polar co-ordinates (r, θ), the strain at any point[99] in:-

$$\text{1st quadrant is } \varepsilon_{s.y(1)} = \frac{r}{R} \sin\theta \, \varepsilon_{s(1)} \qquad \text{eqn 5.8a}$$

$$\text{2nd quadrant is } \varepsilon_{s.y(2)} = \frac{r}{R} \sin\theta \, \varepsilon_{s(2)} \qquad \text{eqn 5.8b}$$

$$\text{3rd quadrant is } \varepsilon_{s.y(3)} = \frac{r}{R} \sin\theta \, \varepsilon_{-s(3)} \qquad \text{eqn 5.8c}$$

$$\text{4th quadrant is } \varepsilon_{s.y(4)} = \frac{r}{R} \sin\theta \, \varepsilon_{-s(4)} \qquad \text{eqn 5.8d}$$

where R is the radius of the specimen.

Notes:- (i) Equations 5.8 do not truly express the actual strains, but describe the hysteresis curves AB, BC, etc. with A (or C) at the origin.

(ii) The origin of the angle θ is different in different quadrants.

But within the plastic zone

$$\sigma = K\,\varepsilon_z^{\,n} \qquad \text{eqn 5.6}$$

and substituting equations 5.8 into equation 5.6 yield stresses at any point within the plastic layer[99] :-

$$\text{1st quadrant } \sigma_{s.y(1)} = K_{1s}\left[\frac{r}{R}\sin\theta\;\varepsilon_{s(1)}\right]^{n_{1s}} \qquad \text{eqn 5.9a}$$

$$\text{2nd quadrant } \sigma_{s.y(2)} = K_{2s}\left[\frac{r}{R}\sin\theta\;\varepsilon_{s(2)}\right]^{n_{2s}} \qquad \text{eqn 5.9b}$$

$$\text{3rd quadrant } \sigma_{s.y(3)} = K_{3s}\left[\frac{r}{R}\sin\theta\;\varepsilon_{-s(3)}\right]^{n_{3s}} \qquad \text{eqn 5.9c}$$

$$\text{4th quadrant } \sigma_{s.y(4)} = K_{4s}\left[\frac{r}{R}\sin\theta\;\varepsilon_{-s(4)}\right]^{n_{4s}} \qquad \text{eqn 5.9d}$$

At steady state, the hysteresis loop is closed, and $\varepsilon'_{-(s-1)} = \varepsilon'_{-s}$ in fig.5.4b.

If it is assumed that the stress $\sigma_{s.y}$ at any of the four quadrants equals the dynamic yield stress σ_e at $r = r^*$ say, r^* is not a constant, but varies with the angle θ.

$$\therefore \quad \sigma_{s.y}(r^*) = \sigma_e \qquad \text{eqn 5.10}$$

Substituting equation 5.10 into equations 5.9 gives the values or r^* at $\sigma_{s.y} = \sigma_e$ for various θ.

In 1st quadrant,

$$\therefore \quad \sigma_e = K_{1s}\left(\frac{r^*_{(1)}}{R}\sin\theta\;\varepsilon_{s(1)}\right)^{n_{1s}} \qquad \text{eqn 5.11a}$$

$$\text{and} \quad r^*_{(1)} = \frac{R}{\sin\theta\;\varepsilon_{s(1)}}\left[\frac{\sigma_e}{K_{1s}}\right]^{\frac{1}{n_{1s}}} \qquad \text{eqn 5.12a}$$

Similarly,

in 2nd quadrant,

$$r^*_{(2)} = \frac{R}{\sin\theta\;\varepsilon_{s(2)}}\left[\frac{\sigma_e}{K_{2s}}\right]^{\frac{1}{n_{2s}}} \qquad \text{eqn 5.12b}$$

in 3rd quadrant,

$$r^*_{(3)} = \frac{R}{\sin\theta\;\varepsilon_{-s(3)}}\left[\frac{\sigma_e}{K_{3s}}\right]^{\frac{1}{n_{3s}}} \qquad \text{eqn 5.12c}$$

in 4th quadrant,

$$r^*_{(4)} = \frac{R}{\sin\theta\ \varepsilon_{-s(4)}}\left[\frac{\sigma_e}{K_{4s}}\right]^{\frac{1}{n_{4s}}} \qquad \text{eqn 5.12d}$$

A line may be drawn through r* to establish the contour of the stress distribution $\sigma_{s.y} = \sigma_e$ around the specimen's cross-section. A hypothetical curve for a rotating bending specimen is illustrated in fig.5.5. The maximum depth of the plastic zone $h = R - r^*$ occurs at point B or D in fig.5.5, that is at $\theta = 90^o$ or $\sin\theta = 1$.

$\therefore$ equation 5.12a reduced to

$$r^*_{(1)} = \frac{R}{\varepsilon_{s(1)}}\left[\frac{\sigma_e}{K_{1s}}\right]^{\frac{1}{n_{1s}}} \qquad \text{eqn 5.13a}$$

Denoting the total bending moment of the member with plastic layers as shown in fig.5.5 by M_T, which is the sum of the bending moment over the plastic zone plus the sum of bending moment over the elastic zone

i.e. $M_T = M_{(plastic)} + M_{(elastic)}$

$$M_T = \int_{(plastic)} \sigma\, y\, da + \int_{(elastic)} \sigma\, y\, da \qquad \text{eqn 5.14}$$

The increase in the "load carrying capacity" is M_T/M_e, where M_e is the bending moment calculated from the elastic theory such that the maximum surface stress has just reached σ_e, i.e. plastic deformation of the surface layer is just on the verge of occurring, i.e. $M_e = \frac{\sigma_e I}{R}$

To evaluate M_T is, however, a very difficult task, as the hysteresis loop (consequently K_{1s} and n_{1s}) changes with stress cycles during the strain softening-hardening period, and the integrations have to be performed over the whole cross-section area. Also, there is an added complication due to residual stresses within fibres which have been deformed when they were

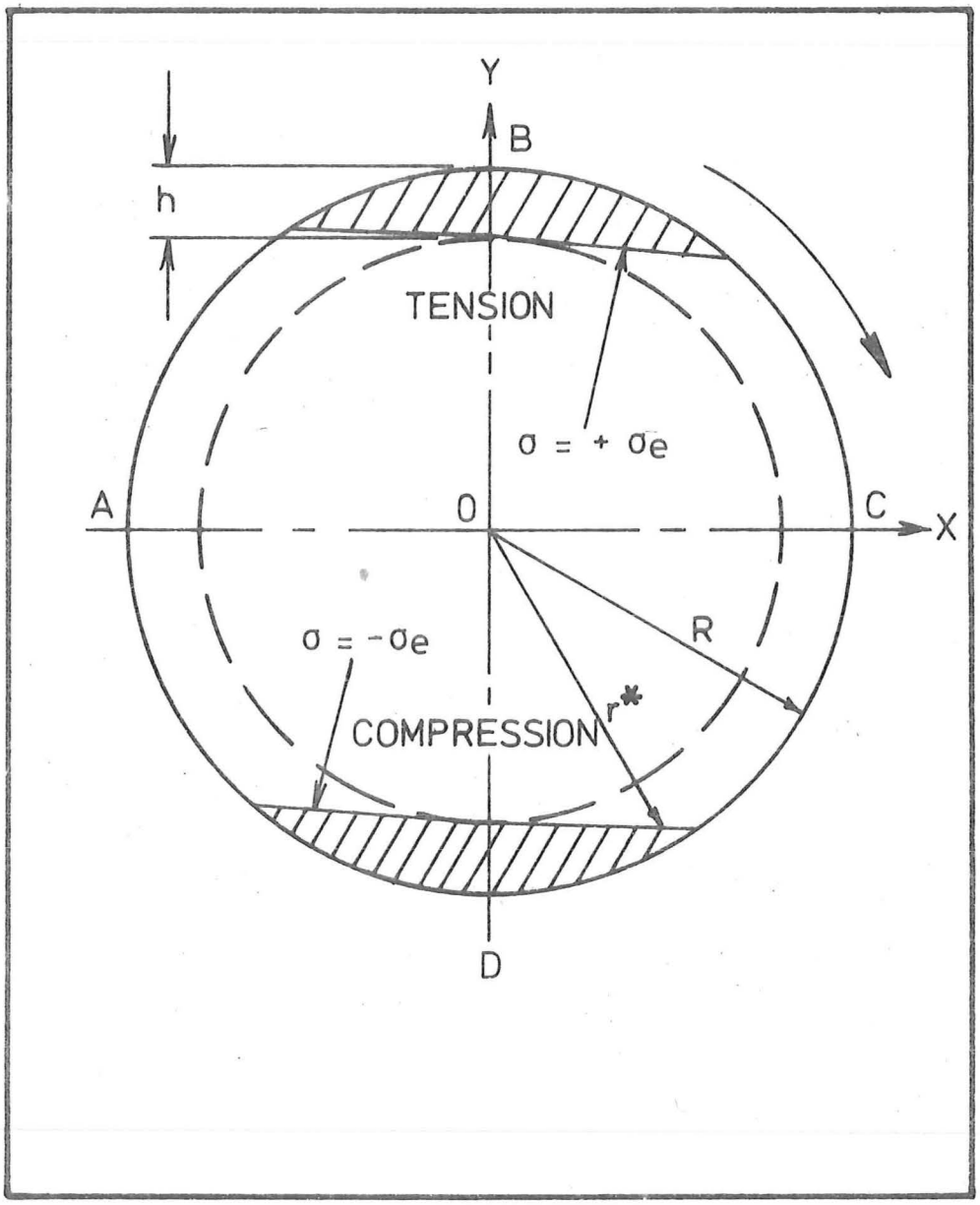

Fig. 5·5. HYPOTHETICAL STRESS CONTOUR WHERE $\sigma = \sigma_e$.

at maximum tension or compression, but due to rotation of the specimen are now at stresses less than σ_e.

A simplified approach to the evaluation of the load carrying capacity after stress redistribution on a rotating bending member is therefore necessary. The simplest approximation would be the case of a reversed plane bending with a perfect elastic-plastic material.

Referring to fig.5.6, for a simple case of reversed bending under constant bending moment, and assuming that:-

(a) the material is perfect elastic-plastic with a dynamic yield stress σ_e, and the effect of residual stresses is negligible,

(b) the strain is directly proportional to the distance from the centre of the specimen.

Referring to fig.5.6a.

Before dynamic yielding, let the applied bending moment be M

i.e. $$M = \frac{\sigma_{app} \pi r_1^3}{4} = \frac{\sigma_{app} I}{r_1} \qquad \text{eqn 5.15}$$

where σ_{app} = maximum applied surface stress, calculated with elastic theory.

I = moment of inertia = $\frac{\pi r_1^4}{4}$ for circular bar.

r_1 = specimen's radius.

After repeated bending, let's assume that dynamic yielding occurred at stress cycle N. The stress and strain distributions are as shown in fig.5.6b, and a plastic zone of depth h is developed. The total bending moment after stress redistribution can now be divided into two parts:-

(i) plastic bending moment M_p within the plastic zone, and

(ii) elastic bending moment M_e within the elastic area.

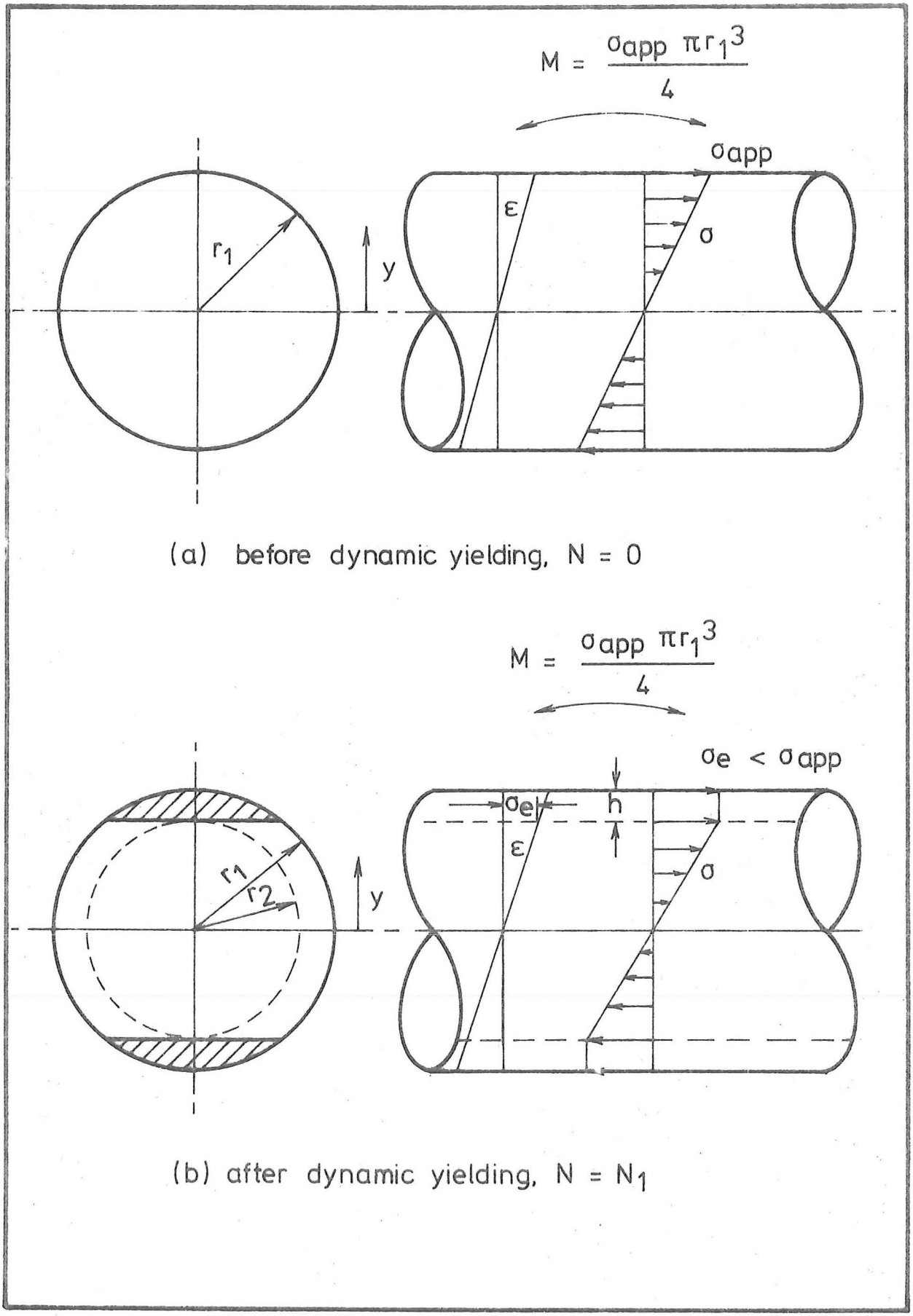

Fig. 5·6. STRESS AND STRAIN DISTRIBUTION ON A PERFECT ELASTIC PLASTIC MATERIAL

i.e. $M_T = M_p + M_e$

but $M_p = \int \sigma\, y\, da$

where a = area

$$\therefore \quad M_p = 4\int_{r_2}^{r_1} \sigma_e\, y \sqrt{(r_1^2 - y^2)}\, dy$$

$$= \frac{4\sigma_e}{3}\left(r_1^2 - r_2^2\right)^{3/2} \qquad \text{eqn 5.16}$$

The elastic bending moment is,

$$M_e = \int \sigma\, y\, da$$

$$= 4\int_0^{r_2} \frac{\sigma_e}{r_2}\, y.y \sqrt{(r_1^2 - y^2)}\, dy$$

$$M_e = 4\frac{\sigma_e}{r_2}\int_0^{r_2} y^2 \sqrt{(r_1^2 - y^2)}\, dy \qquad \text{eqn 5.17}$$

but for $\int y^2 \sqrt{(r_1^2 - y^2)}\, dy$

let $y = r_1 \sin\theta$

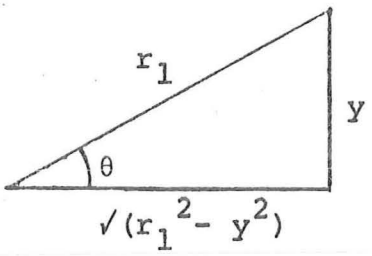

$$\therefore \quad dy = r_1 \cos\theta\, d\theta$$

and $r_1 \cos\theta = \sqrt{(r_1^2 - y^2)}$

$$\therefore \quad \int y^2 \sqrt{(r_1^2 - y^2)}\, dy$$

$$= \int r_1^2 \sin^2\theta . r_1 \cos\theta . r_1 \cos\theta\, d\theta$$

$$= \int r_1^2 \sin^2\theta . r_1^2 \cos^2\theta\, d\theta$$

$$= r_1^4 \left(\frac{\theta}{8} - \frac{1}{32}\sin 4\theta\right) + C \qquad \text{eqn 5.18}$$

Substitute eqn 5.18 into eqn 5.17

$$\therefore \quad M_e = \frac{4\sigma_e}{r_2}\int_0^{r_2} y^2 \sqrt{(r_1^2 - y^2)}\, dy$$

$$= 4\sigma_e \frac{r_1^4}{r_2}\left[\frac{\theta}{8} - \frac{1}{32}\sin 4\theta\right]_{\theta = 0}^{\theta = \sin^{-1}\frac{r_2}{r_1}} \qquad \text{eqn 5.19}$$

Therefore, total bending moment after dynamic yielding is

$$M_T = M_p + M_e$$

$$M_T = \frac{4\sigma_e}{3}(r_1^2 - r_2^2)^{3/2} + 4\sigma_e \frac{r_1^4}{r_2}\left(\frac{\theta}{8} - \frac{1}{32}\sin 4\theta\right)_{\theta = 0}^{\theta = \sin^{-1}\frac{r_2}{r_1}} \qquad \text{eqn 5.20}$$

but $M_T = M$, as the bending moment remains constant throughout the test,

i.e. equation 5.15 = equation 5.20

$$\text{or} \quad \frac{\sigma_{app}\pi r_1^3}{4} = \frac{4\sigma_e}{3}(r_1^2 - r_2^2)^{3/2} + \frac{4\sigma_e r_1^4}{r_2}\left[\frac{\theta}{8} - \frac{1}{32}\sin 4\theta\right]_{\theta = 0}^{\theta = \sin^{-1}\frac{r_2}{r_1}}$$

$$\therefore \quad \frac{\sigma_{app}}{\sigma_e} = \frac{16}{\pi r_1^3}\left[\frac{(r_1^2 - r_2^2)^{3/2}}{3} + \frac{1}{r_2}\left(r_1^4\left(\frac{\theta}{8} - \frac{1}{32}\sin 4\theta\right)\right)_{\theta = 0}^{\theta = \sin^{-1}\frac{r_2}{r_1}}\right] \qquad \text{eqn 5.21}$$

But $h = r_1 - r_2$

therefore, the relationship between σ_{app}/σ_e and $r = h/r_1$ may be derived, where r_1 is the specimen's radius. This is shown in fig.5.7.

For real materials, the stress-strain relationship is not as shown in fig.5.1g, but is usually of the form as shown in fig.5.8a, where the plastic flow curve may be described by the equation $\sigma = K\varepsilon^n$, and not represented by a horizontal straight line. For simplicity of calculations, the material characteristics after plastic yielding is assumed to be approximated by a straight line of slope $\alpha E^{(100)}$ (see fig.5.8b), where E is the modulus of elasticity and α is a constant whose

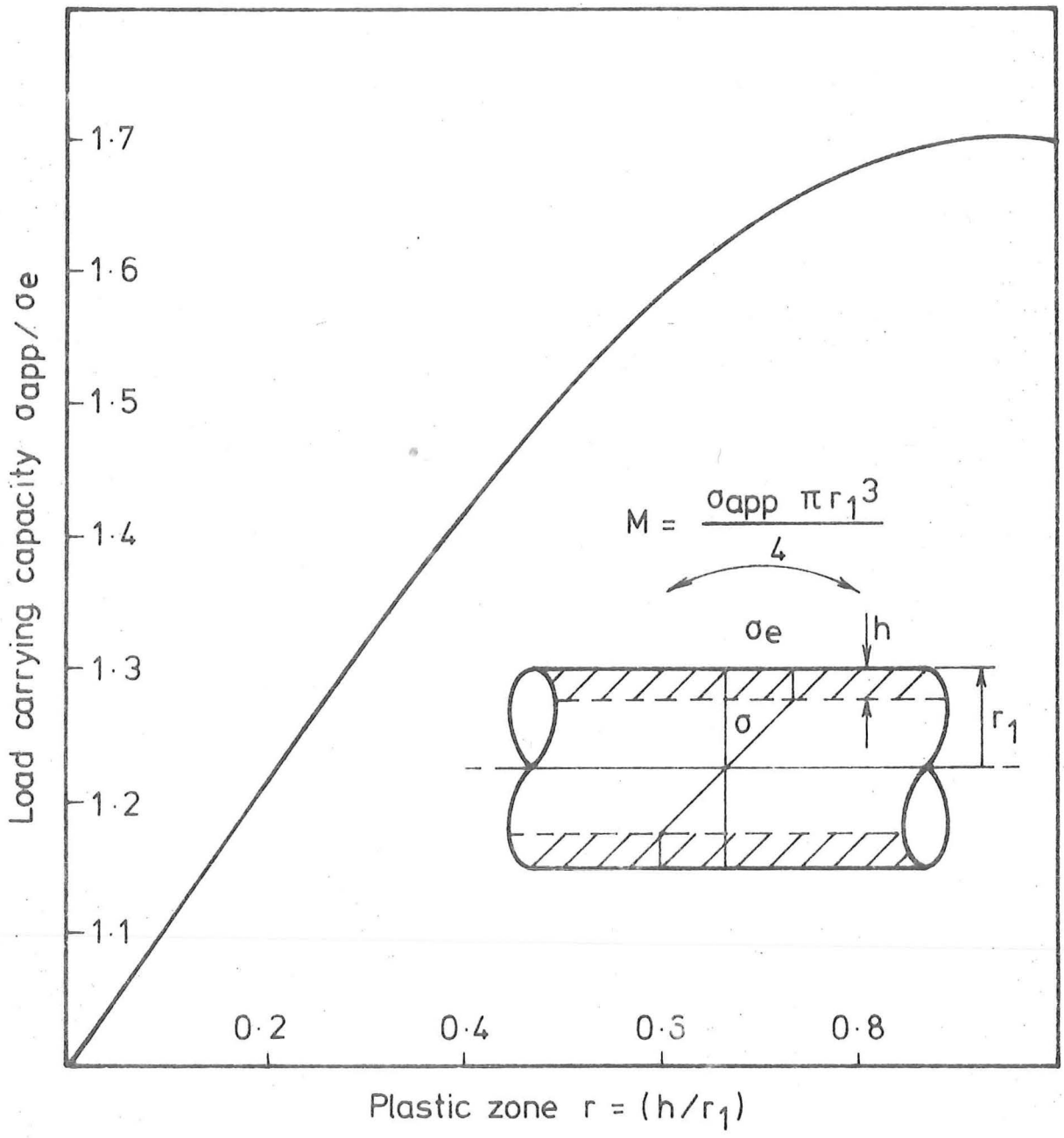

Fig. 5·7 RELATIONSHIP BETWEEN σ_{app}/σ_e AND THE DEPTH OF PLASTIC ZONE r FOR A PERFECT ELASTIC PLASTIC MATERIAL.

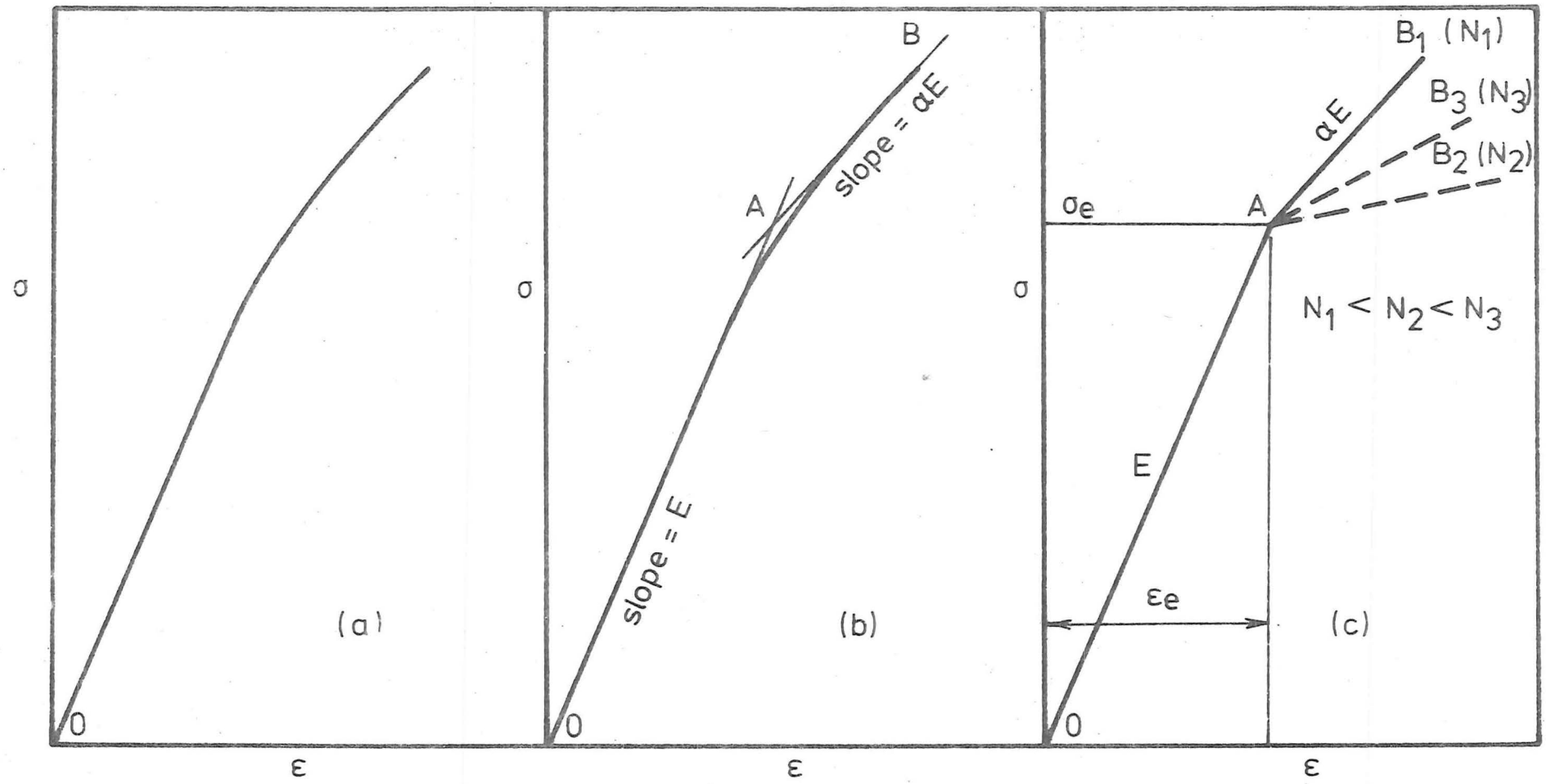

Fig. 5·8. APPROXIMATE STRESS STRAIN CURVE FOR SMALL STRAINS

value lies between 1 and zero. This straight line will be referred to as "plastic leg" as compared to "elastic leg" for the elastic portion of the stress-strain curve.

During cyclic stressing, the slope of the elastic leg remains constant, i.e. at E, however, the slope of the plastic leg varies with the number of stress cycles. For a strain softening material, the slope decreases with increasing stress cycles, while for the case of a strain hardening material, the slope increases. For materials such as low carbon steels which strain soften up to a certain number of cycles, and then followed by strain hardening, the slope of the plastic leg decreases during the strain softening period and then increases during the strain hardening period, this is illustrated in fig.5.8c. Blatherwick and Lazan[100] suggested that α may be expressed as

$$\alpha(N) = 1 - e^{-\lambda(N+N_o)} \qquad \text{eqn 5.22}$$

for a strain hardening material, and

$$\alpha(N) = 1 - \gamma N^q e^{-\lambda N} \qquad \text{eqn 5.23}$$

for a strain softening material, where γ, q, λ and N_o are suitable parameters chosen so as to approximate the behaviour of the material and give the desired initial conditions.

Referring to fig.5.9, for a similar specimen with material characteristic which may be approximated by fig.5.8c, the stress between OA is

$$\sigma = \varepsilon E \qquad \text{eqn 5.24}$$

and the stress for the plastic leg AB is

$$\sigma = \sigma_e + \alpha E(\varepsilon - \varepsilon_e)$$

$$= \sigma_e + \alpha\varepsilon \frac{\sigma_e}{\varepsilon_e} - \alpha\varepsilon_e \frac{\sigma_e}{\varepsilon_e}$$

$$= \sigma_e + \alpha \frac{\sigma_e y}{r_2} - \alpha\sigma_e$$

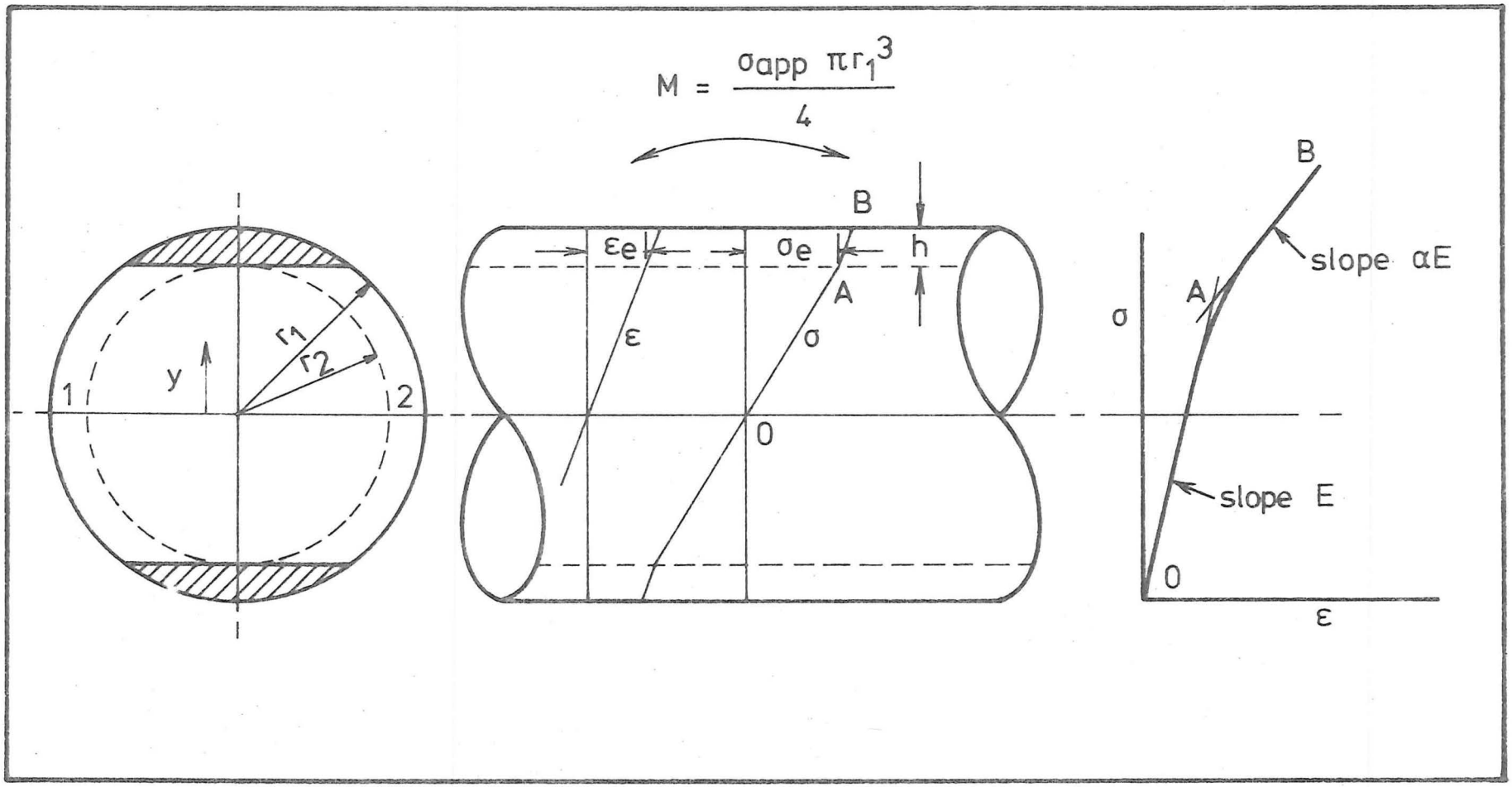

Fig. 5·9 STRESS AND STRAIN DISTRIBUTION FOR MATERIALS WHERE THE PLASTIC FLOW CURVE IS APPROXIMATED BY αE.

$$\therefore \quad \sigma = \sigma_e \left(1 - \alpha + \frac{\alpha y}{r_2}\right) \qquad \text{eqn 5.25}$$

where y is the distance from the centre of the specimen.

Again the total bending moment before dynamic yielding is

$$M = \frac{\sigma_{app} \pi r_1^3}{4} \qquad \text{eqn 5.15}$$

and total bending moment after dynamic yielding is

$$M_T = M_p + M_e$$

but $M_e = \int \sigma \, y \, da$

$$= 4\int_0^{r_2} \frac{\sigma_e}{r_2} y.y \surd(r_1^2 - y^2)dy$$

$$= 4\sigma_e \frac{r_1}{r_2}\left[\frac{\theta}{8} - \frac{1}{32}\sin 4\theta\right]_{\theta = 0}^{\theta = \sin^{-1}\frac{r_2}{r_1}} \qquad \text{eqn 5.19}$$

$$M_p = \int \sigma \, y \, da$$

$$= 2\int_{r_2}^{r_1} \sigma_e \left(1 - \alpha + \frac{\alpha y}{r_2}\right) y \, da$$

$$= 4\int_{r_2}^{r_1} \sigma_e \left(1 - \alpha + \frac{\alpha y}{r_2}\right) y \surd(r_1^2 - y^2)dy$$

$$= 4\int_{r_2}^{r_1} \sigma_e (1 - \alpha) y \surd(r_1^2 - y^2)dy + 4\int_{r_2}^{r_1} \frac{\sigma_e \alpha}{r_2} y^2 \surd(r_1^2 - y^2)dy$$

but $\int y^2 \surd(r_1^2 - y^2)dy = r_1^4\left(\frac{\theta}{8} - \frac{1}{32}\sin 4\theta\right) + C \qquad \text{eqn 5.18}$

$$\therefore \quad M_p = -\frac{4\sigma_e}{3}(1 - \alpha)\left[(r_1^2 - y^2)^{3/2}\right]_{r_2}^{r_1}$$

$$+ \frac{4\alpha\sigma_e r_1^4}{r_2}\left[\frac{\theta}{8} - \frac{1}{32}\sin 4\theta\right]_{y = r_2}^{y = r_1}$$

$$\text{or} \quad M_p = \frac{4\alpha\sigma_e r_1^4}{r_2}\left[\frac{\theta}{8} - \frac{1}{32}\sin 4\theta\right]_{\sin\theta = \frac{r_2}{r_1}}^{\sin\theta = 1}$$

$$+ \frac{4\sigma_e}{3}(1 - \alpha)(r_1^2 - r_2^2)^{3/2}$$

$$\therefore \quad M_T = M_p + M_e$$

$$= \frac{4\alpha\sigma_e r_1^4}{r_2}\left[\frac{\theta}{8} - \frac{1}{32}\sin 4\theta\right]_{\sin\theta = \frac{r_2}{r_1}}^{\sin\theta = 1}$$

$$+ \frac{4\sigma_e}{3}(1-\alpha)(r_1^2 - r_2^2)^{3/2} +$$

$$4\sigma_e \frac{r_1^4}{r_2}\left[\frac{\theta}{8} - \frac{1}{32}\sin\theta\right]_{\theta = 0}^{\theta = \sin^{-1}\frac{r_2}{r_1}} \qquad \text{eqn 5.26}$$

but the bending moment remains constant

i.e. $M = M_T$

or equation 5.15 = equation 5.26

$$\text{i.e. } \frac{\sigma_{app}}{\sigma_e} = \frac{16}{\pi r_1^3}\left[\frac{r_1^4}{r_2}\left(\frac{\theta}{8} - \frac{1}{32}\sin 4\theta\right)_{\theta = 0}^{\theta = \sin^{-1}\frac{r_2}{r_1}}\right.$$

$$+ \alpha\frac{r_1^4}{r_2}\left(\frac{\theta}{8} - \frac{1}{32}\sin 4\theta\right)_{\sin\theta = \frac{r_2}{r_1}}^{\sin\theta = 1}$$

$$\left. + \frac{(1-\alpha)}{3}(r_1^2 - r_2^2)^{3/2}\right] \qquad \text{eqn 5.27}$$

For the case of a perfect elastic-plastic material, $\alpha = 0$, therefore equation 5.27 reduces to equation 5.21.

The relationship between σ_{app}/σ_e and $r = h/r_1$ can again be derived and the relationship is illustrated in fig.5.10 for $\alpha = 0$, 0.2, 0.5 and 1. It can be seen from fig.5.10 that for small values of r ($\simeq$0.2) or σ_{app}/σ_e ($\simeq$1.2), the error associated in assuming α is rather small. For example, at $r = 0.2$, the deviation in σ_{app}/σ_e for α between 1 and 0 is $\simeq(1.25-1.21) \simeq 0.04$. The error, however, increases very rapidly as r or σ_{app}/σ_e increases. It would thus appear that, for normal rotating bending testings, (the average rotating bending fatigue limit to direct stress fatigue limit ratio

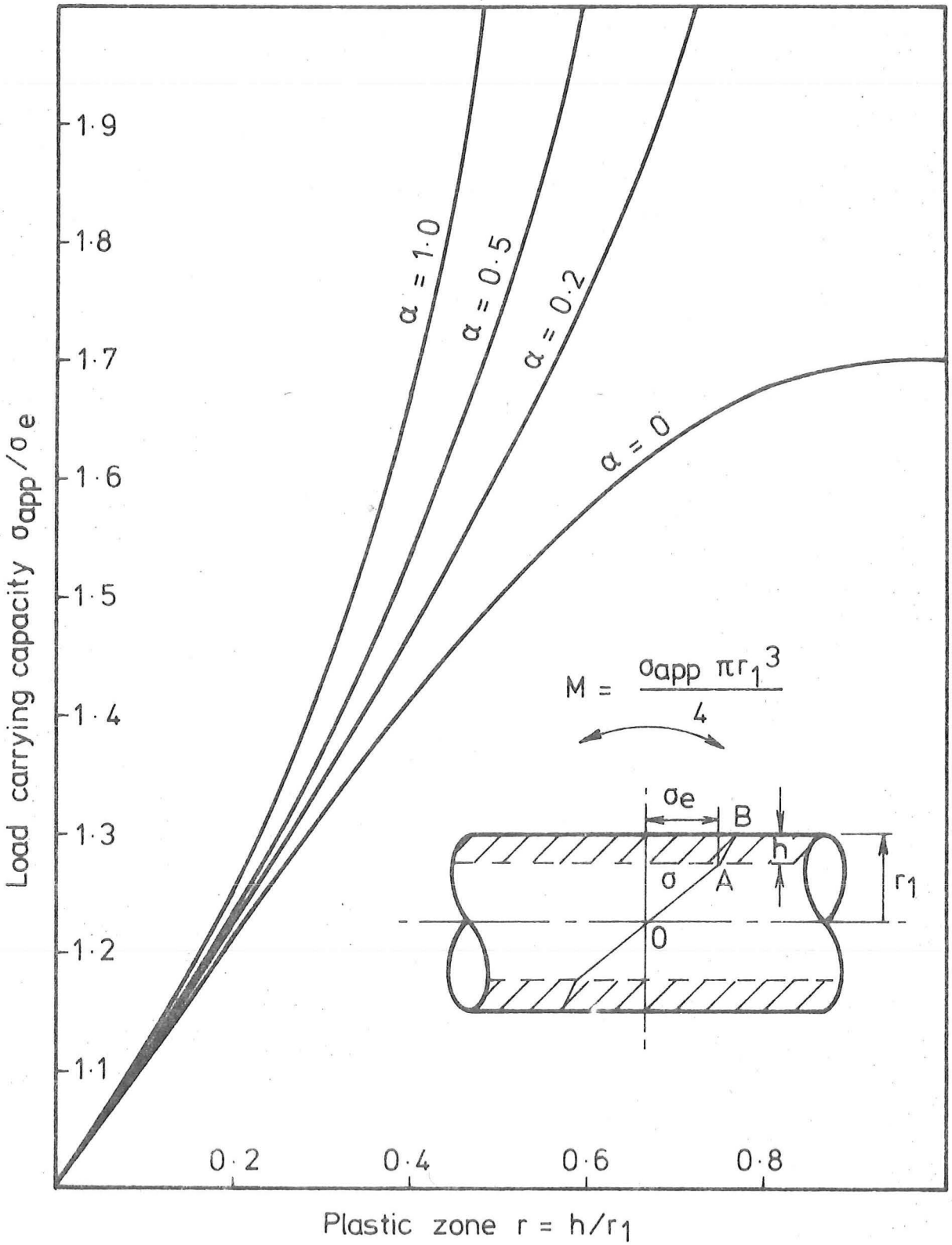

Fig. 5·10. RELATIONSHIP BETWEEN σ_{app}/σ_e AND PLASTIC ZONE r FOR A MODIFIED MATERIAL (see fig. 5·8b)

reported is about 1.18) the plastic zone developed would be small, hence the error associated in assuming α would not be large.

The above analysis is strictly speaking only applicable for a case of simple plane bending, nevertheless, it shows the importance of a small layer of inelastic strain on the load carrying capacity of a rotating bending member. If the contribution of residual stresses to the load carrying capacity in a rotating bending member is negligible, the above analysis (equation 5.27) may be used to approximate the case of a rotating bending member, and the effect of a layer of small inelastic strain on the load carrying capacity (hence, the rotating bending fatigue limit) of a rotating bending member may be evaluated.

CHAPTER 6.

THE REDUCTION OF ACTIVE NITROGEN IN STEELS BY THE PRECIPITATION OF ALUMINIUM NITRIDE AND THE CONTROL OF GRAIN SIZE.

6.1 KINETICS OF AlN PRECIPITATION:

As the fatigue limits of low carbon steels can be affected by the process of dynamic strain ageing, it is necessary to establish the level of "active" nitrogen in the experimental steels before attempting to assess the variation in strength brought about by other factors.

Aluminium is often added to steels to render them non-ageing. This process involves the reduction of "active" nitrogen to form stable aluminium nitride AlN. The reaction of Al + N to form AlN is, however, reversible, i.e. the dissociation of AlN to Al + N is possible.

Consider the reaction,

$$AlN \rightleftarrows Al + N \qquad \text{eqn 6.1}$$

by the Law of Mass Action, which states that the rate of a reaction at a given temperature is proportional to the product of the active masses of the reacting substances[101]. Therefore, the rate of forward reaction is

$$V_f \propto [AlN]$$

or $$V_f = K_f[AlN] \qquad \text{eqn 6.2a}$$

Similarly, the rate of reverse reaction is

$$V_r = K_r [Al][N] \qquad \text{eqn 6.2b}$$

where:-

V_f = rate of forward reaction

V_r = rate of reverse reactio·

K_f and K_r = proportionality constants

When dynamic equilibrium is achieved, the rate of forward reaction is equal to the rate of reverse reaction,

i.e. $V_f = V_r$

or $K_f[AlN] = K_r[Al][N]$

or $\frac{K_f}{K_r} = \frac{[Al][N]}{[AlN]} = K_c$ eqn 6.3

but the concentration of the compound AlN is a constant at a given temperature.

$\therefore \quad [Al][N] = K_c[AlN]$

$= K_s$ eqn 6.4

where K_s is known as the Solubility Product, and is equal to $K_c[AlN]$.

According to Arrhenuis equation, the effect of temperature on the rate of a reaction is:-

$V = \theta e^{-\frac{Q}{RT}}$ eqn 6.5a

or $\ln V = \ln \theta - \frac{Q}{RT}$

or $\log V = \log \theta - \frac{Q}{2.303RT}$ eqn 6.5b

where V = specific reaction rate

θ = integration constant

Q = activation energy

R = gas constant

T = absolute temperature.

From equations 6.2b and 6.4

$K_s \propto V$

Substituting in equation 6.5b a graph of K_s versus the reciprocal of temperature should give a straight line. This relationship was first proved by Darken for aluminium nitride dissolving in austenite to form a solid solution of aluminium and nitrogen. The solubility product was taken as the product of the weight percentages of aluminium and nitrogen in solution in austenite

in equilibrium with aluminium nitride, these being considered equivalent to the activities:-

i.e. $K_s = [\text{wt \% N}][\text{wt \% Al}]$ eqn 6.6

or $K_s = [C_N - C_C][C_{Al} - \frac{27}{14} C_C]$ eqn 6.7

where:-

C_N = wt % acid soluble nitrogen

C_C = wt % N combined as AlN

C_{Al} = wt % acid soluble aluminium

$(\frac{27}{14} C_C)$ = wt % Al combined as AlN

K_s = solubility product at that temperature

The value of C_N, C_{Al} and the nitrogen combined as AlN can be determined by chemical analysis.

For low carbon steel, the relationship between log K_s and temperature in the form of equation 6.5b is[102]:-

$$\log K_s = - \frac{6180}{T} + 0.725 \qquad \text{eqn 6.8}$$

where K_s is as given in equation 6.6 and T = absolute temperature in ^{o}K.

The formation of AlN precipitates has been studied in some detail[102,103,104,105]. Erasmus[102,103,104] investigated in some detail the effects of both isothermal "down-quenching" (quench to some intermediate temperature from a higher temperature and holding at this temperature to allow isothermal precipitation) and isothermal "up-quenching" (rapid heating from room temperature to the isothermal precipitation temperature, having previously quenched the specimen to room temperature from temperatures above the AlN solution temperature). All the above studies[102,103,104,105] have shown that the precipitation of AlN during "down-quenching" and continuous cooling conditions to be extremely sluggish, i.e. AlN will not necessarily be formed in steels containing aluminium and that its formation is largely dependent

on the solubility product K_s, the heat treatment temperature, the time at the temperature and the final cooling rate.

A graph of nitrogen as aluminium nitride in austenite of a low carbon steel with 0.006% N_{sol} and 0.027% Al_{sol} (i.e. typical of the experimental steels), according to equation 6.8 is shown in fig. 6.1.

6.2 FACTORS AFFECTING THE GRAIN SIZE OF STEELS:

A review of published work on austenite grain size of steels indicates that it can be affected by various factors; for example heating rate, prior microstructure, austenitizing time and austenitizing temperature.

The effect of heating rate is generally small, it is of the order of one grain size number (ASTM scale) for very large differences in the rate of heating. The effect due to prior microstructure is also small[106], the difference in grain size is again of the order of one ASTM number for wide variation in microstructure.

The work of Miller[107] indicates that austenite grain size increases with increasing austenitizing time at constant temperature in the austenite region. For constant austenitizing time, austenite grain size also increases with austenitizing temperature. However, the influence of austenitizing time and temperature can differ considerably for steels "killed" (deoxidized) with aluminium or aluminium plus silicon. For silicon killed steels, the grains grow with increasing austenitizing time or temperature, but for steels killed with aluminium or aluminium plus silicon, the pattern of growth is more complex, with grain size increasing always with time, but not always with temperature. The pattern of growth is as follows:-

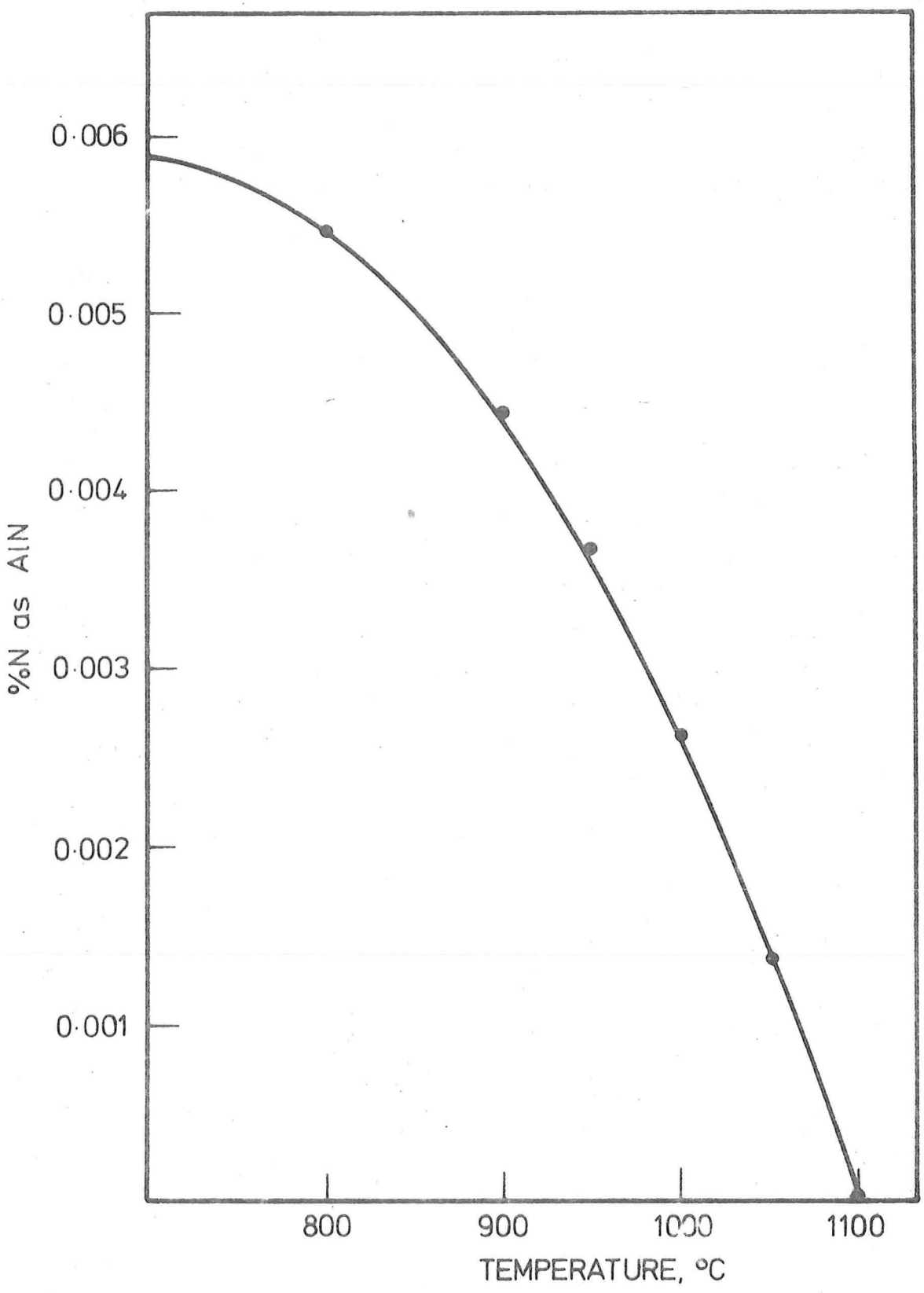

Fig. 6·1 EQUILIBRIUM N_{AlN} CONTENT IN AUSTENITE OF A LOW CARBON STEEL WITH N_{sol} = C 006%, Al_{sol} = 0·027%

(a) At low austenitizing temperature:- growth proceeds very slowly.

(b) At somewhat higher temperatures 925°C - 980°C:- few grains grow very rapidly to large grains, but after longer austenitizing, only very large grains remain.

(c) Around the temperature of 1040°C:- more grains grow, but this appears to be associated with a lessening of the average rate of growth, resulting in grain size actually smaller than that austenitizing at 925°C - 980°C.

(d) At 1150°C and 1260°C:- grain growth is rapid, and very large grains are obtained as compared to those at lower temperatures for the same austenitizing time.

6.3 THE CONTROL OF ACTIVE NITROGEN AND GRAIN SIZE IN THE EXPERIMENTAL STEELS:

In order to investigate fully the differences in the mechanism operating under direct stress and rotating bending fatigue in low carbon steels, specimens with varying grain sizes and two levels of "active" nitrogen were chosen. The methods of heat treatment to achieve these conditions are shown in table 6.1 and are briefly summarized as follows:-

(a) Coarse grain - "low active" nitrogen (B) specimens:- High temperatures ($\geq$ 1100°C) were used to produce large austenite grain size, very slow cooling rate (controlled cooling from 950°C to 650°C in 49 hours) ensured high precipitation of nitrogen as aluminium nitride. Extreme slow cooling rate also enables large precipitates of aluminium nitride to be formed, and these larger precipitates of aluminium nitride are less effective in hindering the grain growth process as compared tc the finer precipitates.

(b) Fine grain - "low active" nitrogen specimens:-

TABLE 6.1

METHODS OF HEAT TREATMENT FOR EXPERIMENTAL STEELS.

Specimen Identification.	Annealing Temperature ^{o}C	Soaking Time HR	Method of Cooling.
A 1	1350	3	Furnace cooled from 1350^{o}C
A 2	1200	2½	Furnace cooled from 1200^{o}C
A 3	1100	2	Furnace cooled from 1100^{o}C
A 4	1100	2	Air cooled.
A 5	900	1	Air cooled.
B 1	1350	3	Control cooled from 950^{o}C to 650^{o}C in 49 hours, then furnace cooled.
B 2	1100	2	Control cooled from 950^{o}C to 650^{o}C in 49 hours, then furnace cooled.
B 3	900 & 880	2 + 1 + 1	Initially normalized at 900^{o}C for 2 hours, air cooled to below 650^{o}C, then normalized again at 900^{o}C for 1 hour and air cooled to below 650^{o}C and heat treated again at 880^{o}C for 1 hour and air cooled.

Low austenitizing temperature (900°C) was used to obtain the fine grain structure required. As is shown in fig.6.1, at equilibrium condition, heat treatments at around 900°C should result in the combination of most of the nitrogen as aluminium nitride. To ensure a closer approach to the equilibrium condition, multiple heat treatment was employed for these specimens.

(c) Coarse grain - "high active" nitrogen (A) specimens:-
High austenitizing temperatures ($\geq$ 1100°C) were again used to obtain the coarse structures. Faster cooling rate was used so that as little aluminium nitride as possible is precipitated.

(d) Fine grain - "high active" nitrogen specimens:-
For these specimens, difficulty arises because fine grain size requires low austenitizing temperatures, but low austenitizing temperatures (under equilibrium conditions) will result in the precipitation of aluminium nitride. It was, however, found that when the soaking time was short and the cooling rate rapid, the precipitation of AlN was slow. As a result, these specimens were heat treated at 900°C for one hour and cooled in air.

Eight sets (sixteen specimens to a set) of specimens were produced for direct stress fatigue testings, five of these were of "high active" nitrogen steels, designated A1, A2, A3, A4 and A5 respectively, and three of these were of "low active" nitrogen steels, designated B1, B2 and B3 respectively. A similar eight sets of sixteen specimens were also produced for rotating bending fatigue testings together with two tensile specimens for each set of experimental steels for tensile testings.

The resultant analysis and chemical composition for the eight sets of experimental steels are tabulated in table 7.1.

CHAPTER 7.

EXPERIMENTAL PROCEDURES AND RESULTS.

7.1 TENSILE TESTS:

Standard 15 mm diameter tensile specimens with 90 mm gauge length made to B.S.18 were prepared from the eight sets of experimental steels (i.e. A1 - A5 and B1 - B3) and a special high nitrogen low carbon steel (C). Testings were carried out on a 250 KN Instron Universal Testing machine at a strain rate of about 2×10^{-4}/sec. The true stress-true strain data was calculated from measurements of specimen diameter and instantaneous force by using equation 4.3, and true stress-true strain relationship as given by equation 4.6 was assumed. Log true stress-log true strain curves (equation 4.7) from the experimental data are shown in figs.7.2-7.10. The equivalent friction stress σ_o as formulated by Erasmus[12] i.e.

$$\sigma_o = K\left(\frac{nK}{E}\right)^{\frac{n}{1-n}} \qquad \text{eqn 4.16}$$

was also determined for all experimental steels, and these tensile properties are tabulated in table 7.2 together with the fatigue properties.

7.2 DETERMINATION OF FATIGUE LIMITS:

As different heat treatments were used to produce the experimental steels, it was possible that the initial free dislocation densities in these experimental steels were different, and as Erasmus[12] has suggested that the presence of a "knee" on the fatigue S - N curves (i.e. the fatigue limit) in low carbon steels is mainly due to the initial low density of free dislocations in these materials. It is

TABLE 7.1

CHEMICAL COMPOSITION AND NITROGEN ANALYSIS OF THE EXPERIMENTAL STEELS (WT %).

Steel	C	Si	S	P	Mn	Al_{sol}	N_{sol}	N_{insol}	N_{AlN}	N_{active}
A 1	0.16	0.12	0.037	0.015	0.64	0.027	0.0050	0.0020	0.0011	0.0039
A 2	"	"	"	"	"	"	0.0056	0.0009	0.0011	0.0045
A 3	"	"	"	"	"	"	0.0066	0.0010	0.0027	0.0039
A 4	"	"	"	"	"	"	0.0052	0.0009	0.0016	0.0036
A 5	"	"	"	"	"	"	0.0065	0.0011	0.0030	0.0035
B 1	"	"	"	"	"	"	0.0049	0.0013	0.0036	0.0013
B 2	"	"	"	"	"	"	0.0052	0.0010	0.0037	0.0015
B 3	"	"	"	"	"	"	0.0060	0.0012	0.0049	0.0011
C	0.06	0.05	0.043	0.042	0.21	0.005	0.0121	0.002	-	0.0121

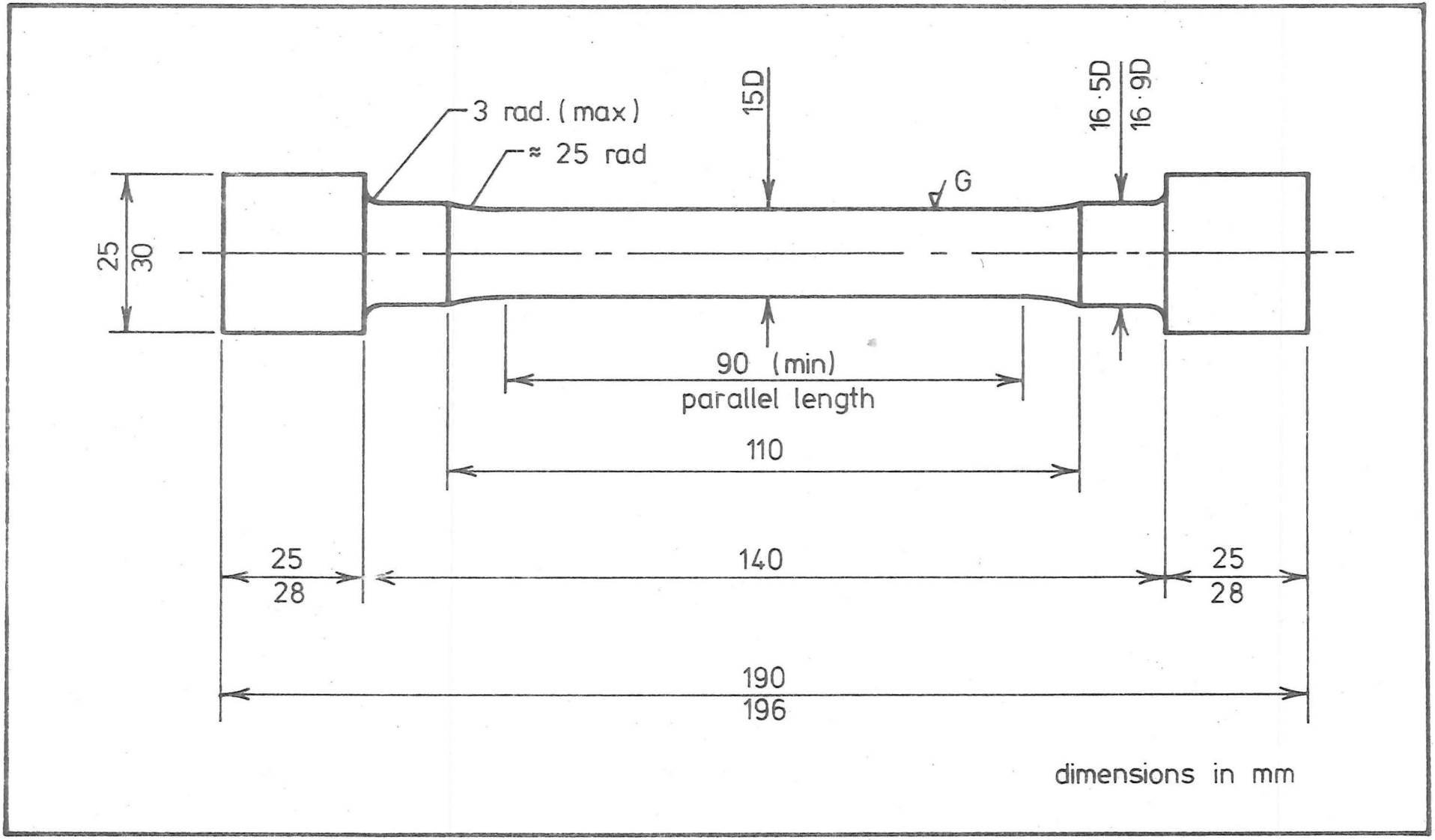

Fig. 7·1. TENSILE SPECIMEN

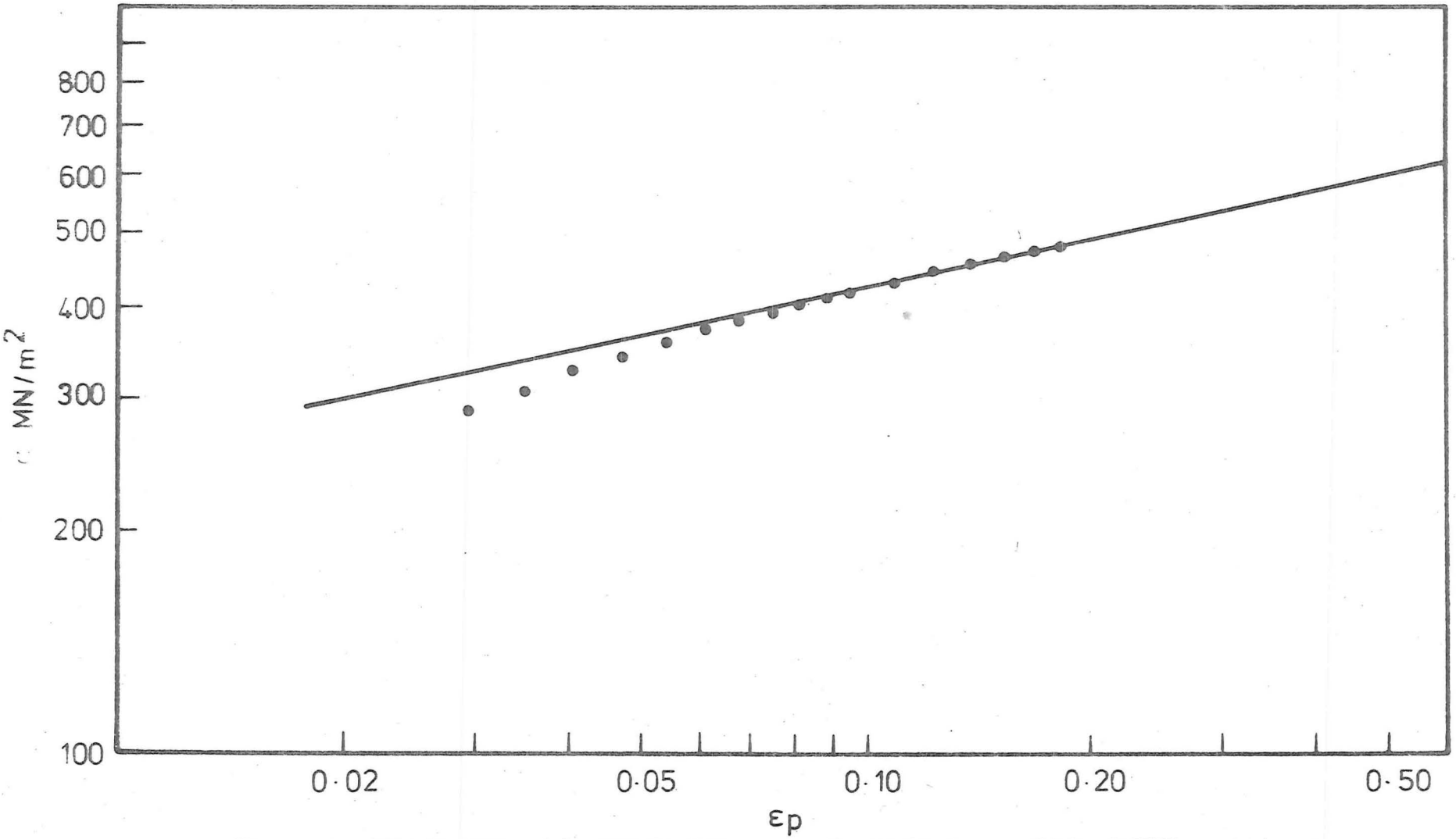

Fig. 7·2. TRUE STRESS-TRUE STRAIN RELATIONSHIP FOR STEEL A1.

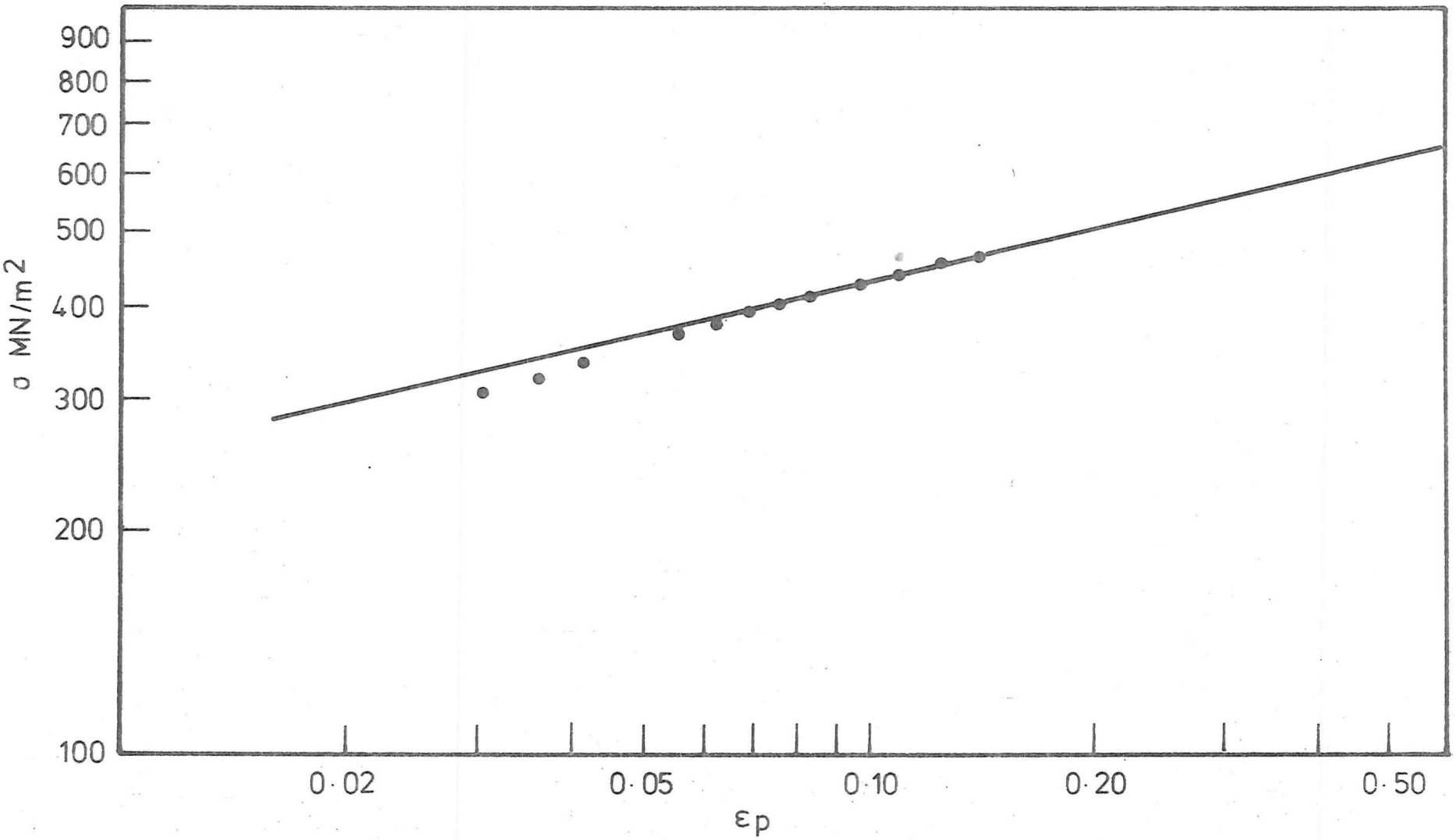

Fig. 7·3. TRUE STRESS–TRUE STRAIN RELATIONSHIP FOR STEEL A2.

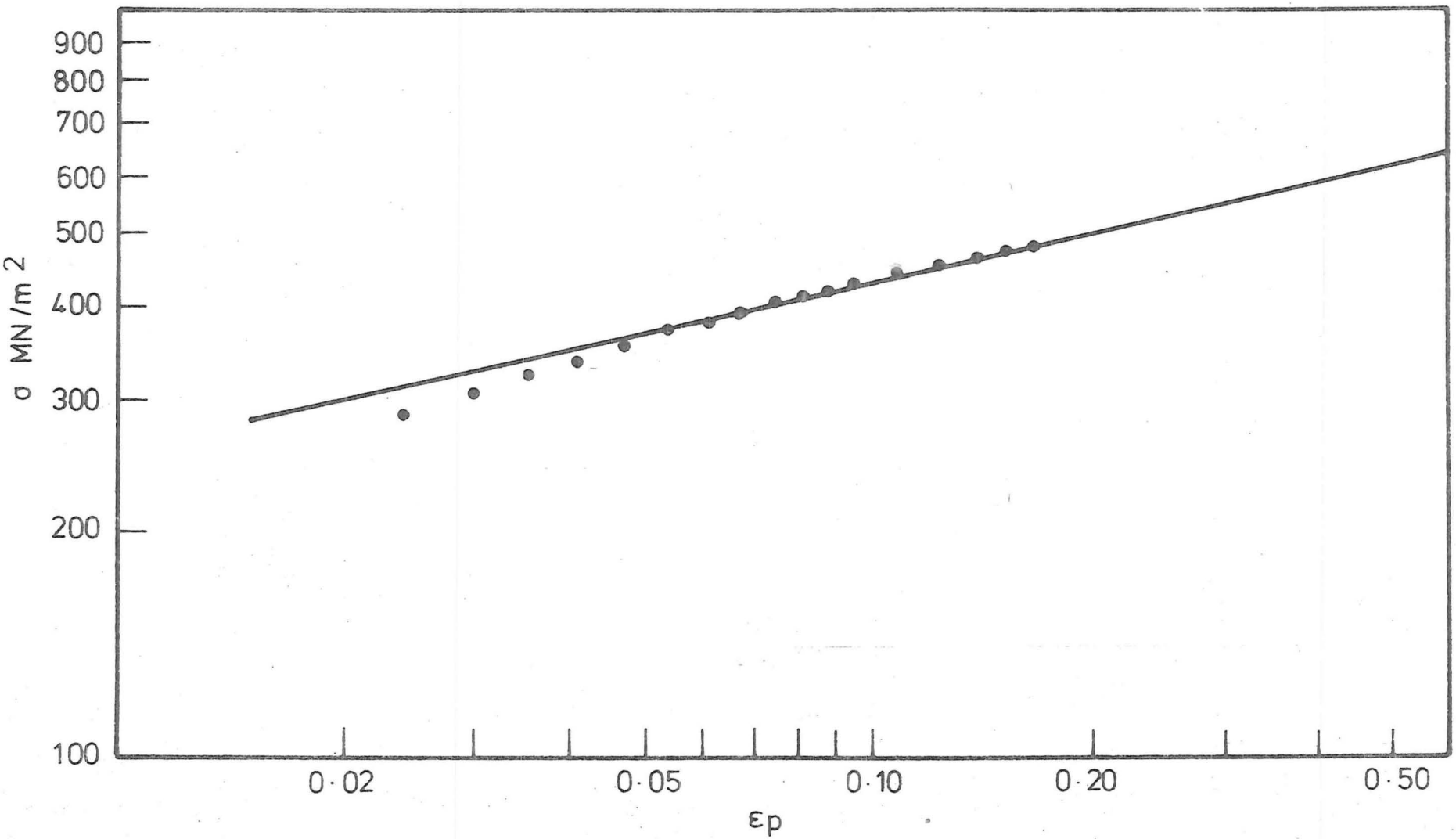

Fig. 7·4 TRUE STRESS-TRUE STRAIN RELATIONSHIP FOR STEEL A3.

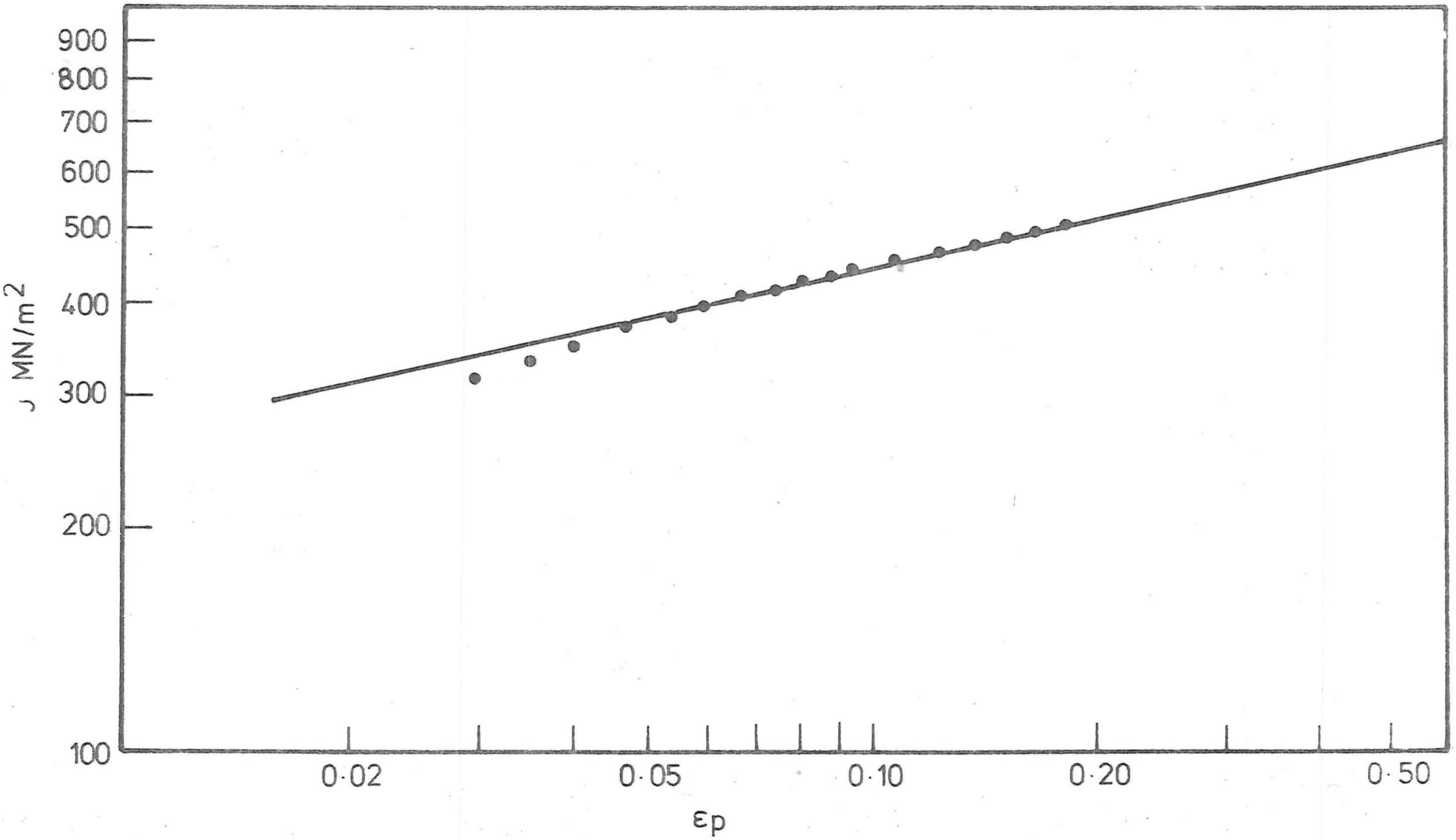

Fig. 7·5. TRUE STRESS-TRUE STRAIN RELATIONSHIP FOR STEEL A4.

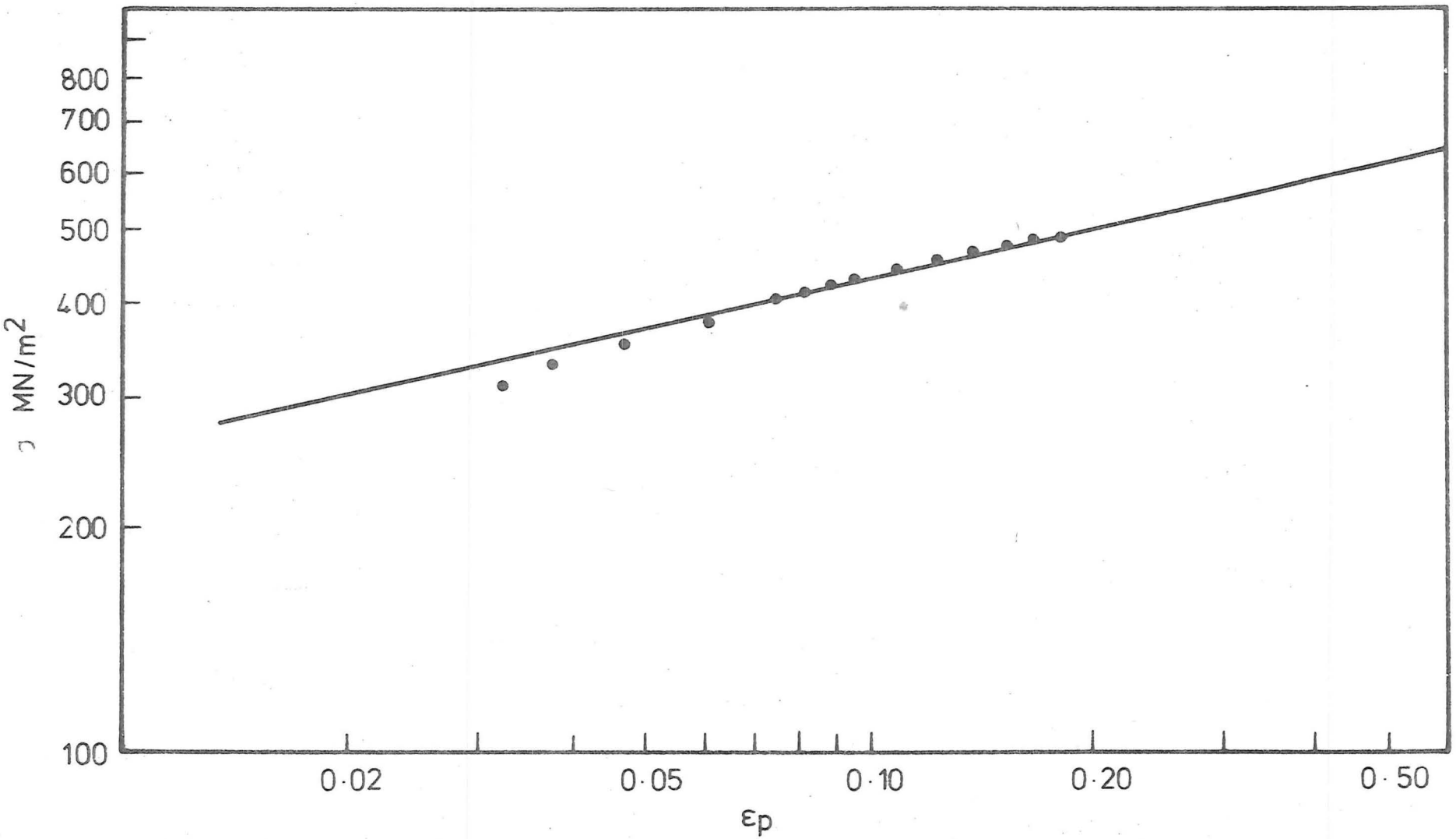

Fig. 7·6. TRUE STRESS-TRUE STRAIN RELATIONSHIP FOR STEEL A5

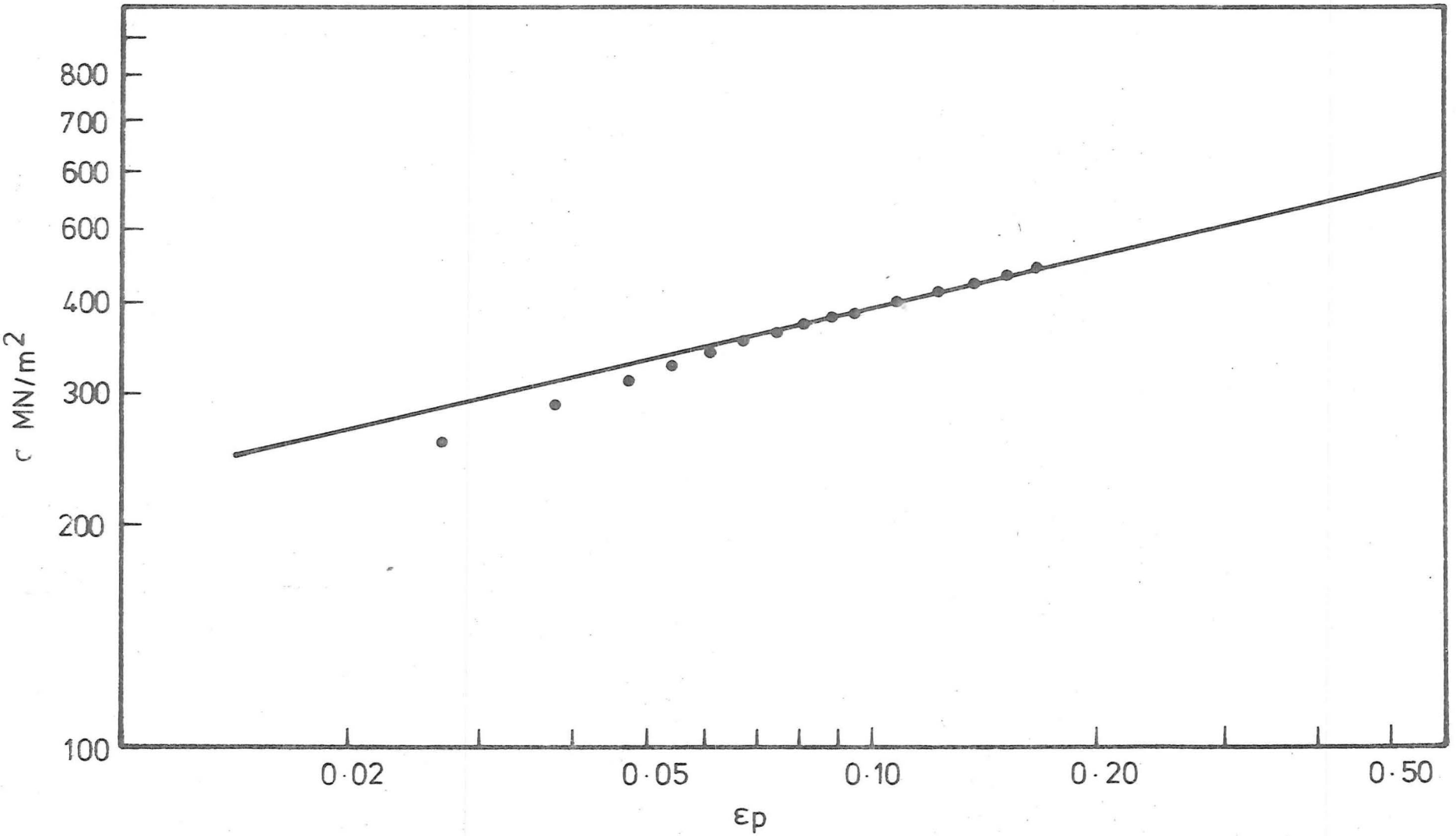

Fig. 7·7. TRUE STRESS-TRUE STRAIN RELATIONSHIP FOR STEEL B1

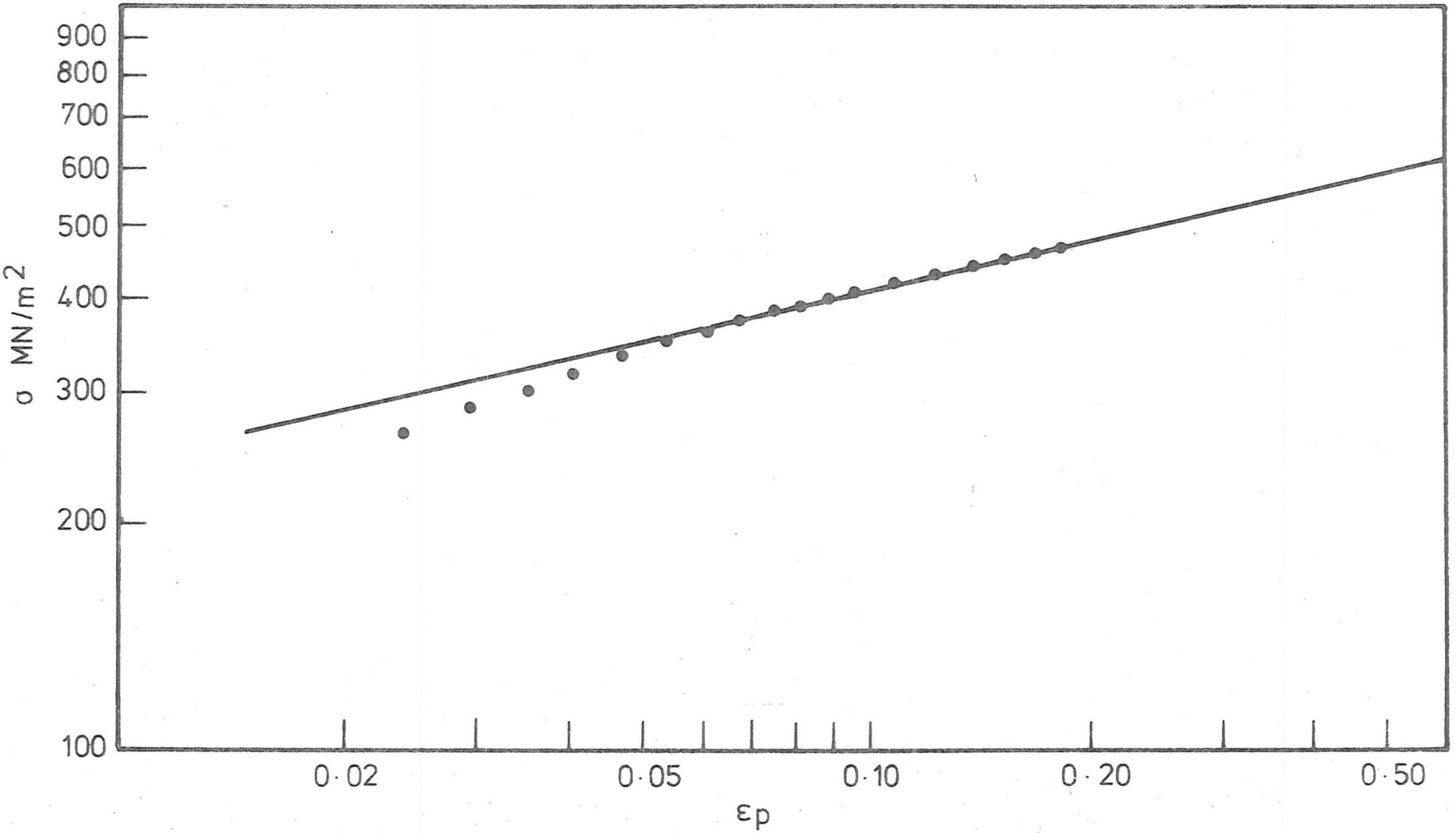

Fig. 7·8. TRUE STRESS-TRUE STRAIN RELATIONSHIP FOR STEEL B2

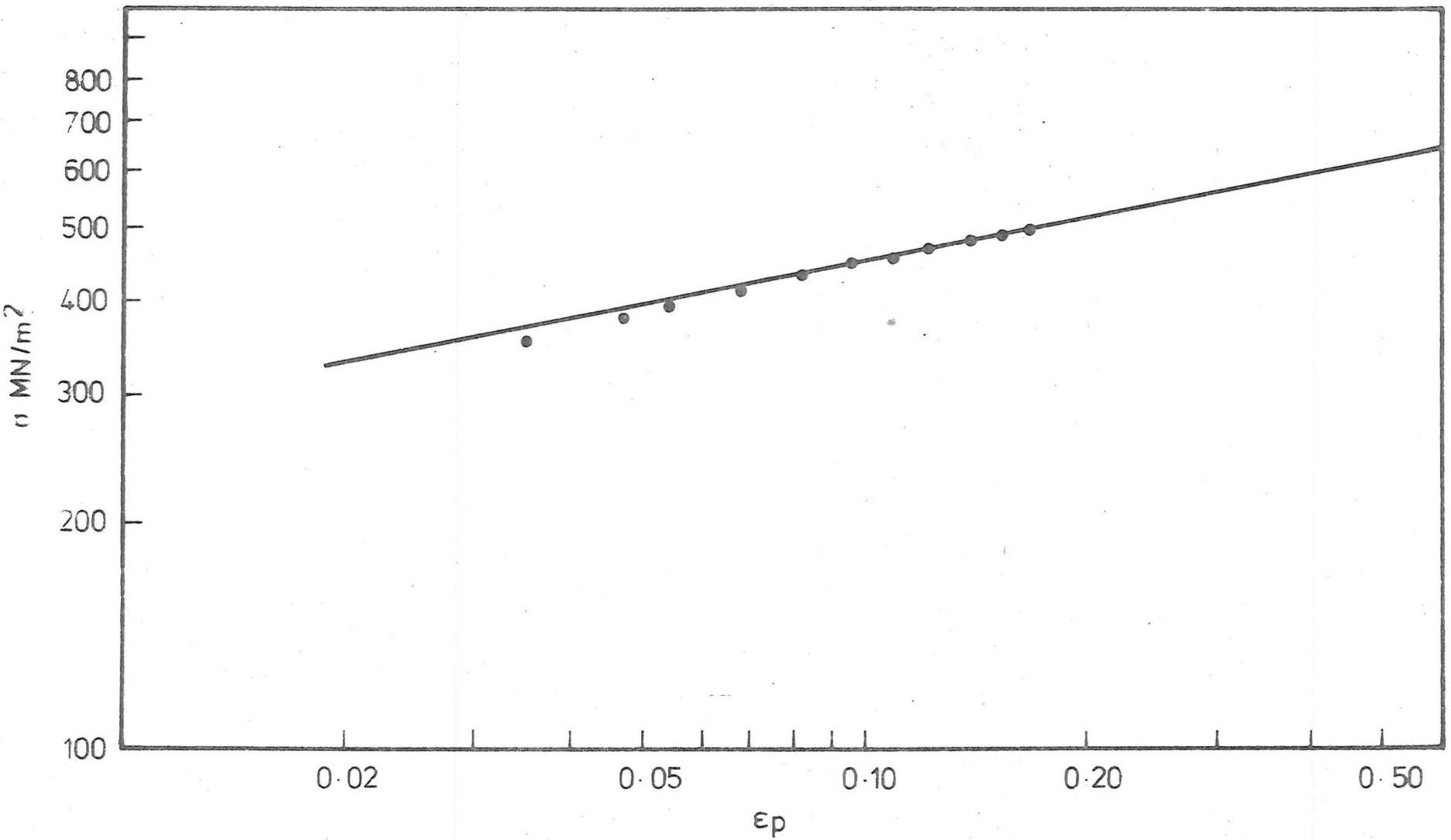

Fig. 7·9. TRUE STRESS – TRUE STRAIN RELATIONSHIP FOR STEEL B3

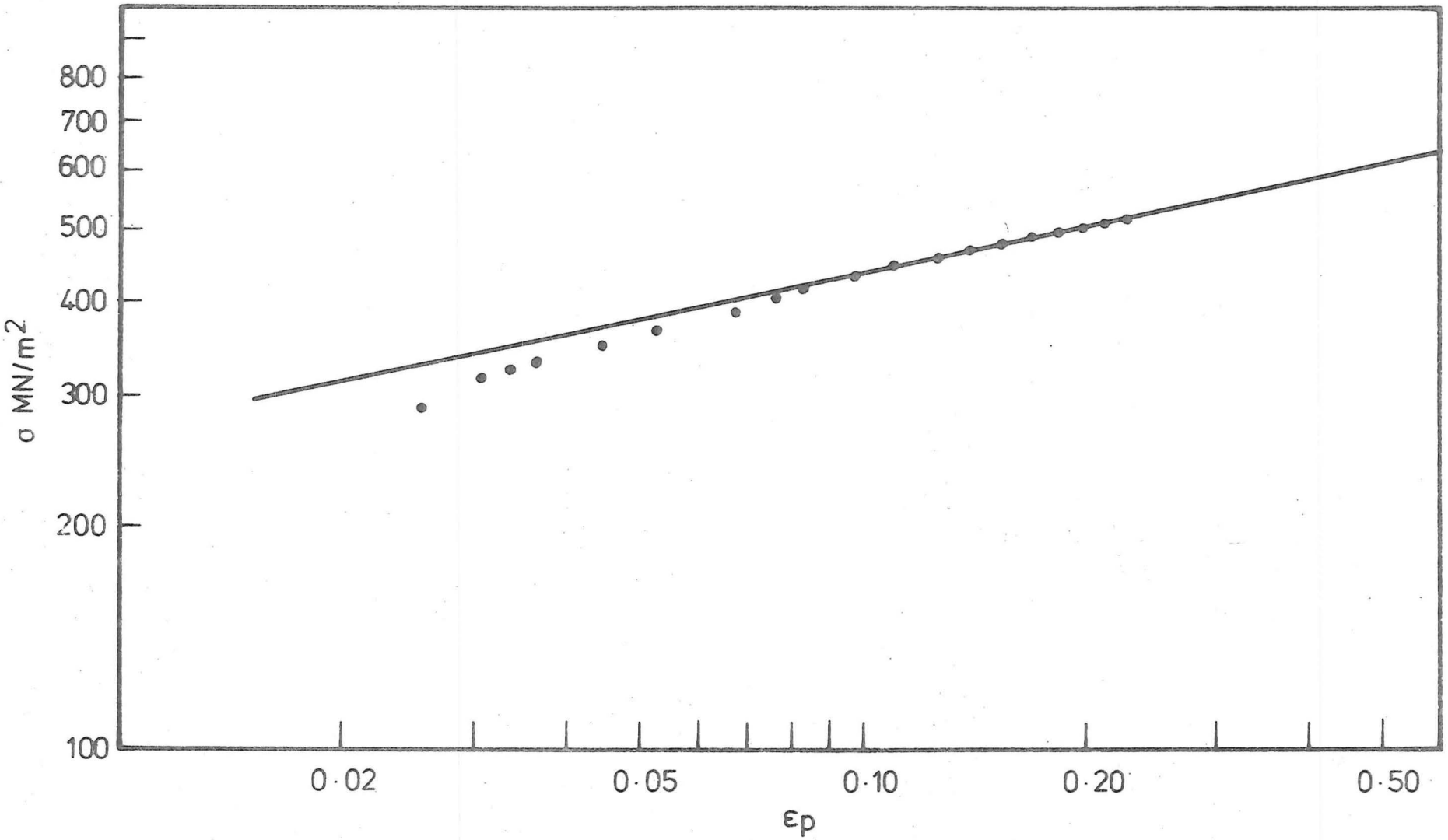

Fig. 7·10. TRUE STRESS–TRUE STRAIN RELATIONSHIP FOR STEEL C (SPECIAL HIGH NITROGEN LOW CARBON STEEL)

TABLE 7.2

Steel	Grain Size $d^{-\frac{1}{2}}$	Lower Yield Stress σ_y	K	n	Fatigue Limit		$\frac{\sigma_{RB}}{\sigma_{DS}}$	σ_o	Saturation Strain ε_p^*	$\frac{\sigma_{DS}}{\sigma_o}$
					σ_{DS}	σ_{RB}				
	$mm^{-\frac{1}{2}}$	MN/M^2	MN/M^2		MN/M^2	MN/M^2		MN/M^2		
A 1	4.72	187	690	0.2210	176	222	1.26	90	0.0021	1.96
A 2	5.07	192	730	0.2267	178	225	1.26	91	0.0020	1.96
A 3	5.60	195	730	0.2199	177	228	1.29	98	0.0016	1.81
A 4	6.77	218	730	0.2171	179	232	1.30	101	0.0015	1.77
A 5	8.09	255	720	0.2050	184	237	1.29	103	0.0013	1.79
B 1	3.72	155	670	0.2242	164	214	1.30	84	0.0019	1.95
B 2	4.65	175	700	0.2260	165	214	1.30	87	0.0017	1.90
B 3	9.14	271	730	0.2015	183	243	1.33	118	0.0010	1.55
C	8.85	280	710	0.2048	235	295	1.26	-	-	-

Note:- σ_{DS} ≡ direct stress fatigue limit

σ_{RB} ≡ rotating bending fatigue limit

$$\sigma_o = K \left(\frac{nK}{E}\right)^{\frac{n}{1-n}}$$

therefore important to ensure that the initial free dislocation densities of the fatigue specimens are fairly similar. This is especially so in the monitoring of the temperature change during fatigue cycling, as different levels of free dislocations will result in different temperature rises, see chapter 8. Consequently, all the fatigue specimens (from both the direct stress and rotating bending) were given a heat treatment at 110°C for 1 hour to eliminate most of the initial free dislocations.

(a) Direct stress fatigue testings:-

Direct stress fatigue testings were carried out in Amsler Vibrophore at a frequency of about 200 cycles/sec. The specimen used is as shown in fig.7.11. Full details of the testing machines used and the methods of specimen preparation are given in Appendix "A". Sixteen specimens were prepared for each set of steel for the determination of the direct stress fatigue limits and the method of fatigue limit determination used was that of the Staircase method (B.S.3518 part 5), the full details of which are given in Appendix "B".

Special care was taken to ensure that the alignment of the direct stress machine was of reasonable order. A special specimen was made on to which four strain gauges were attached at 90° to each other. This specimen was used to check the alignment of the direct stress machine from time to time. The alignment of the machine was found to be better than 35 micro strain throughout the tests. The direction of the crack initiation on the specimen surface relative to the direct stress machine was also recorded, and it was observed that the frequency of crack initiation was randomly distributed, which further confirmed the good alignment of the direct stress machine. The direct stress fatigue limits

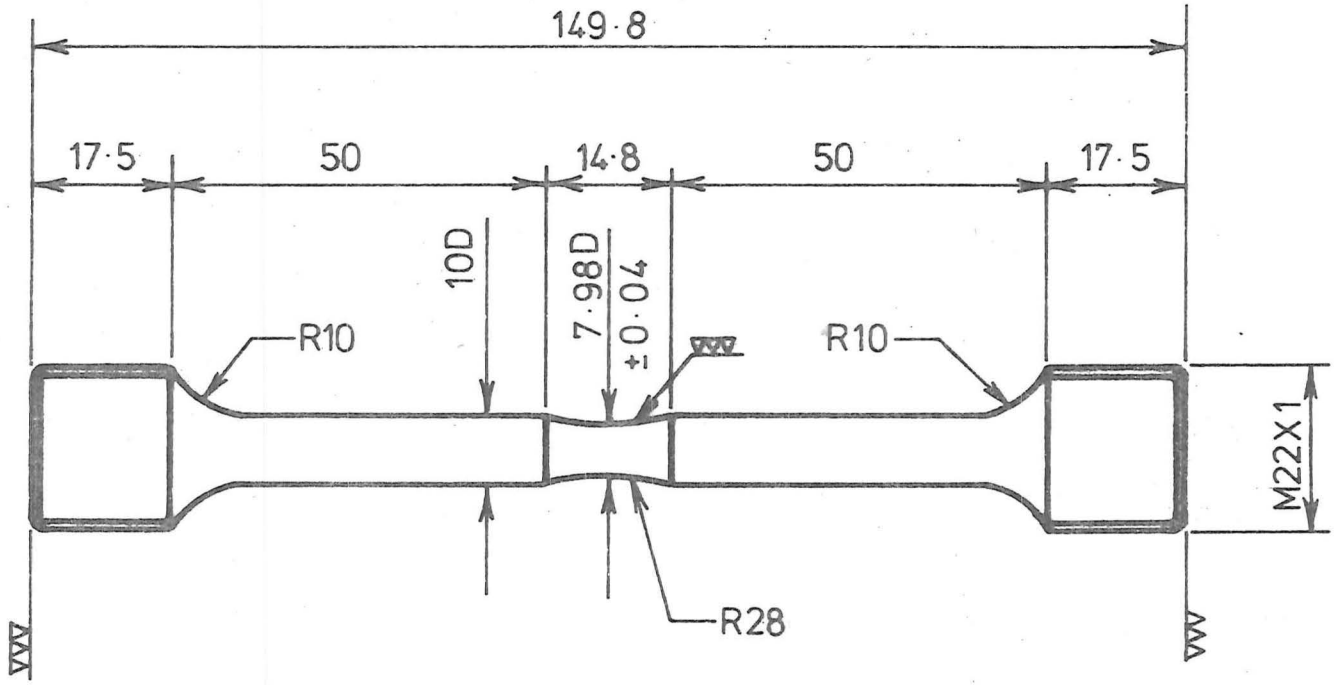

Fig. 7·11. DIRECT STRESS SPECIMEN FOR AMSLER VIBROPHORE

as determined with the Staircase method are tabulated in table 7.2.

(b) Rotating bending fatigue testings:-

Rotating bending fatigue testings were carried out in four Avery dual-ended fatigue machines at a speed of 50 cycles/sec. The specimen used is as shown in fig.7.12. Full details of the machines used and the techniques of specimen preparation are given in Appendix "A". Sixteen specimens were again prepared for each set of steel and the rotating bending fatigue limits were also determined by the Staircase method, see Appendix "B". Special care was also taken to ensure that all four rotating bending fatigue machines were used equally for all eight sets of experimental steels. The rotating bending fatigue limits as determined with the Staircase method are tabulated in table 7.2.

The relationship between fatigue limits (both direct stress and rotating bending) and the grain size for the eight sets of experimental steels are shown in fig.7.13 together with the lower yield stress σ_y and equivalent friction stress σ_o.

7.3 NITROGEN ANALYSIS AND GRAIN SIZE MEASUREMENT:

(a) Nitrogen analysis:-

The method of nitrogen analysis used is that put out by the United Steel Companies Ltd.[108].

The method includes the determination of the amount of nitrogen as insoluble nitrides and soluble nitrides. Since the soluble part consists mainly of AlN and free nitrogen, it may therefore be assumed that:-

$$\%\ N_{\substack{\text{as free} \\ \text{interstitials}}} = \%\ N_{\substack{\text{as soluble} \\ \text{nitrides}}} - \%\ AlN$$

The full details of this nitrogen analysis are given in Appendix "C".

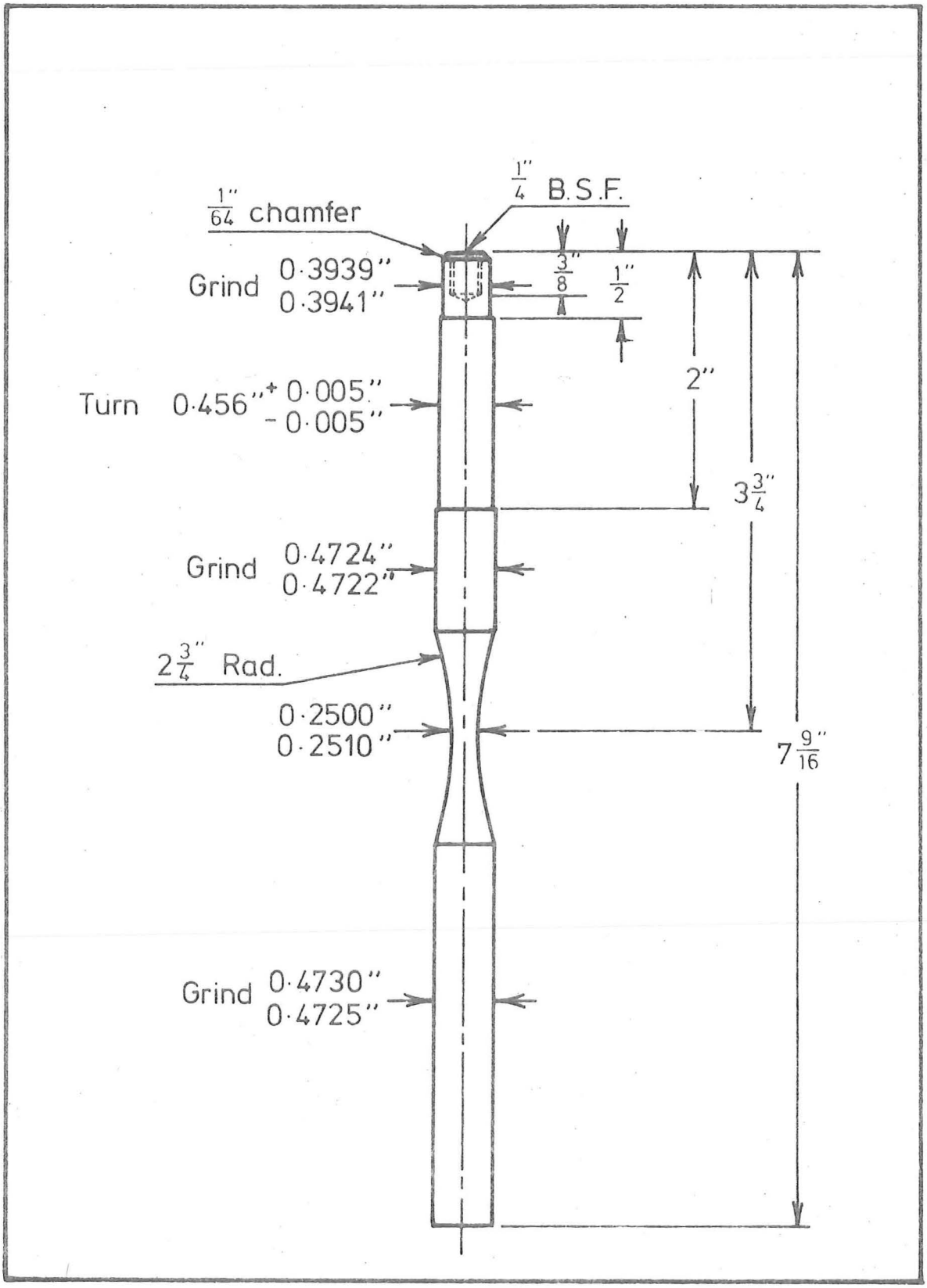

Fig. 7·12. ROTATING BENDING FATIGUE SPECIMEN

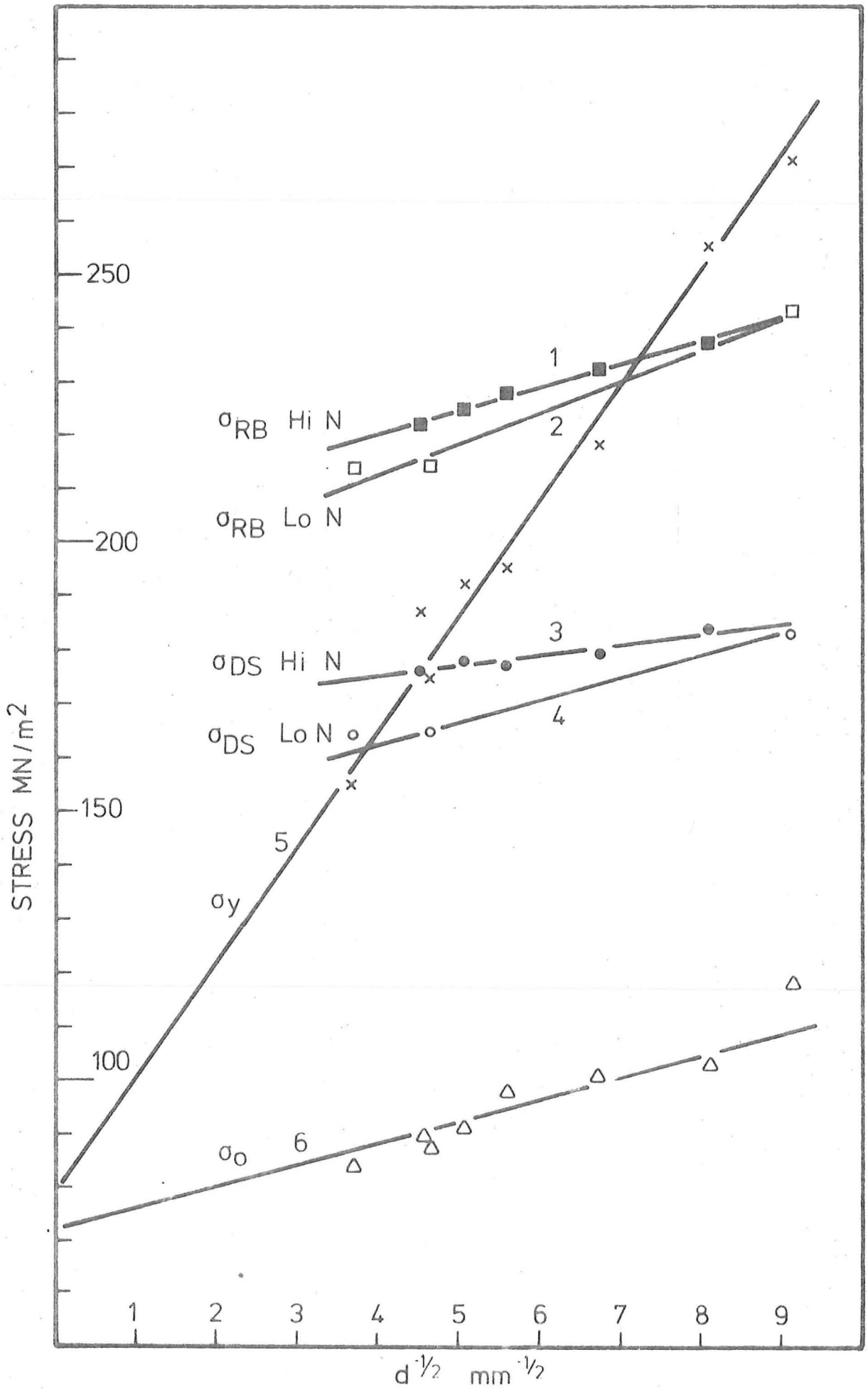

Fig. 7·13. EFFECT OF GRAIN SIZE ON THE FATIGUE AND TENSILE PROPERTIES.

(b) Grain Size Measurement:-

Microspecimens were prepared from the fatigued specimens away from the specimen gauge length. Polishing was carried on to diamond paste finish and etching was done with 2% nitric acid in alcohol. Three specimens from each set of experimental steels (one from direct stress specimen, one from rotating bending specimen and one from tensile specimen) were chosen at random, and the average value of the grain size determined.

The Linear Intercept method was used for grain counts on the micrographs of the specimens, which is illustrated in fig.7.14. In this method, parallel straight lines of fixed total length L were drawn on the micrographs. The total number of intercepts N_i made by these lines with the grain boundaries were counted and the average grain diameter may be calculated as follows:-

$$d = \frac{L}{N_i} \qquad \text{eqn 7.1}$$

At least 300 intersections are necessary for an accurate determination of grain size by this method. The grain sizes as determined by the above method are tabulated in table 7.2.

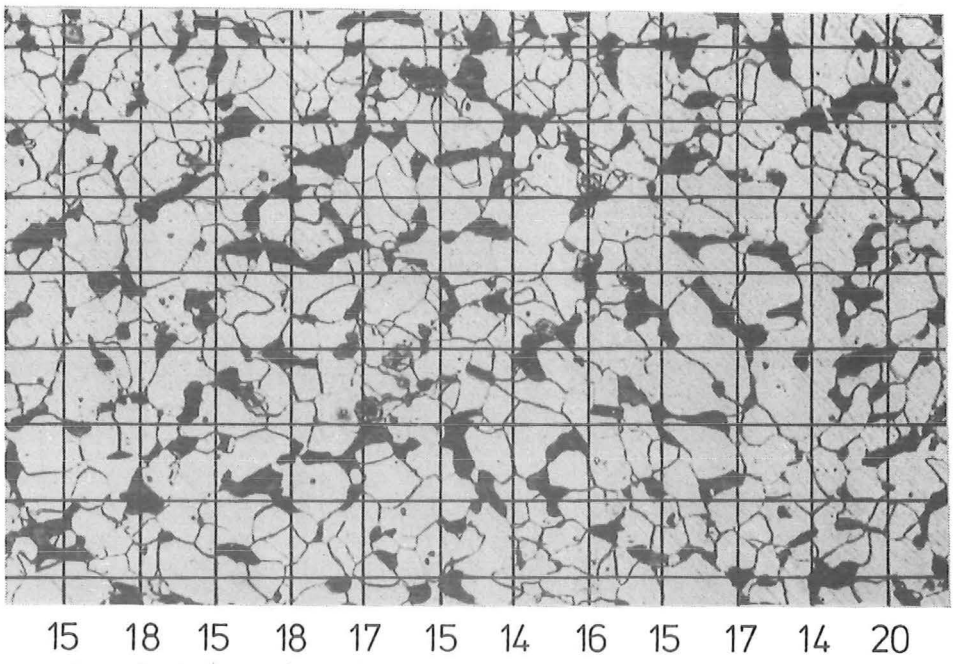

Fig. 7·14. ILLUSTRATION OF THE GRAIN COUNTING TECHNIQUE USED.

CHAPTER 8.

MONITORING FATIGUE DAMAGE, PROCEDURE AND RESULTS.

8.1 THE FRACTURE SURFACE:

Broken specimens from the fatigue tests analysed in Section 7.2 were examined and typical fatigue fracture surfaces from direct stress and rotating bending testings are shown in figs.8.1 and 8.2 respectively. For specimens broken under direct stress, crack initiation occurred at a point on the free surface and propagated in a "fan-like" manner from this point across the specimen. The crack-front remained straight and approximately at right angles to the line joining the centre of the specimen and the point of crack initiation. Polycrystalline grain size affected the appearance of the fracture surface with coarse grained specimens having a coarser "texture" on the fracture surface, see fig.8.1. No sign of twisting or rubbing was observed on the fracture surfaces of the direct stress specimens, indicating that secondary forces were absent and that the alignment of the direct stress fatigue machine was satisfactory. The position of crack initiation on the direct stress fatigue specimen's surface relative to the fatigue machine was also recorded, and it was found to be randomly distributed, which further confirmed the alignment of the direct stress fatigue machine.

Fatigue fracture surfaces from rotating bending specimens differed considerably from those fractured under direct stress. An indistinct "crescent" shaped region with the shape of a "quarter-moon" (see figs.8.2a and 8.2b) was observed opposite

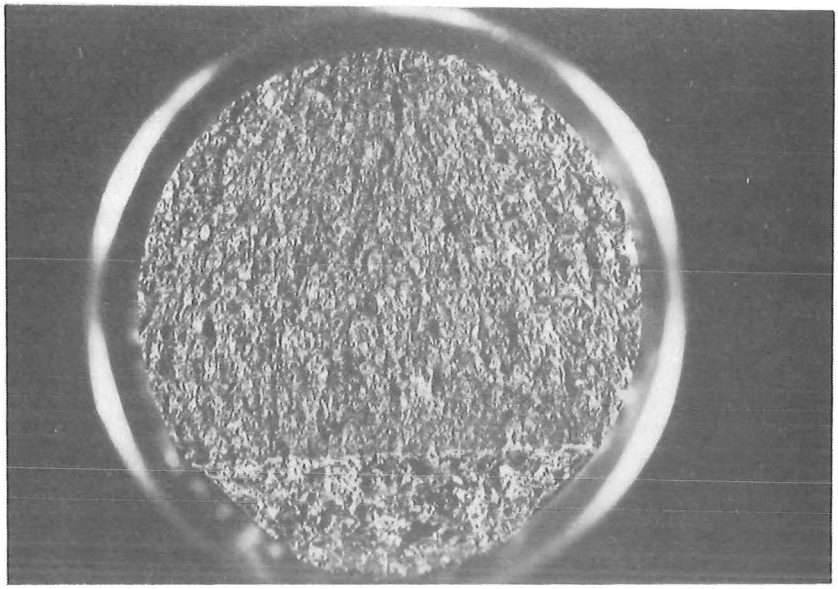

8×

(a) Coarse grained specimen (A1)
$d^{-1/2} = 4 \cdot 72 mm^{-1/2}$

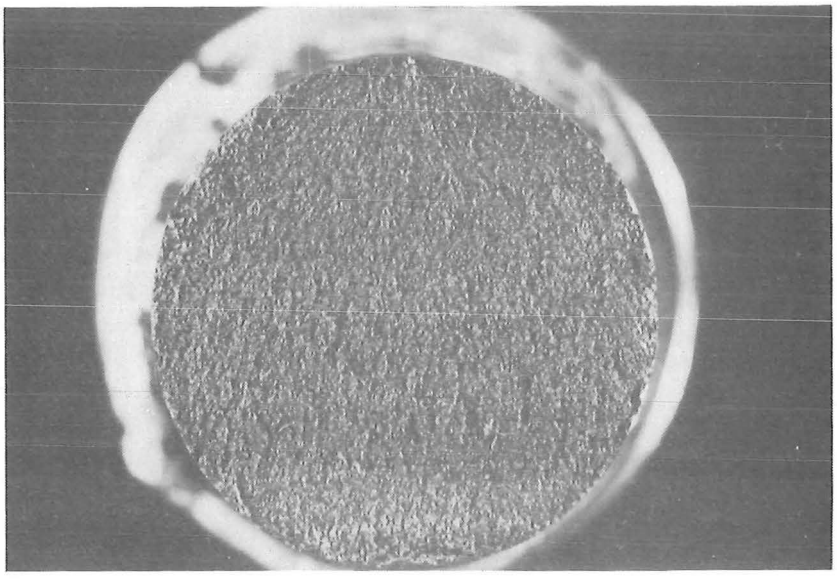

8×

(b) Fine grained specimen (A5)
$d^{-1/2} = 8 \cdot 09 mm^{-1/2}$

Fig. 8·1 DIRECT STRESS FATIGUE FRACTURE SURFACES.

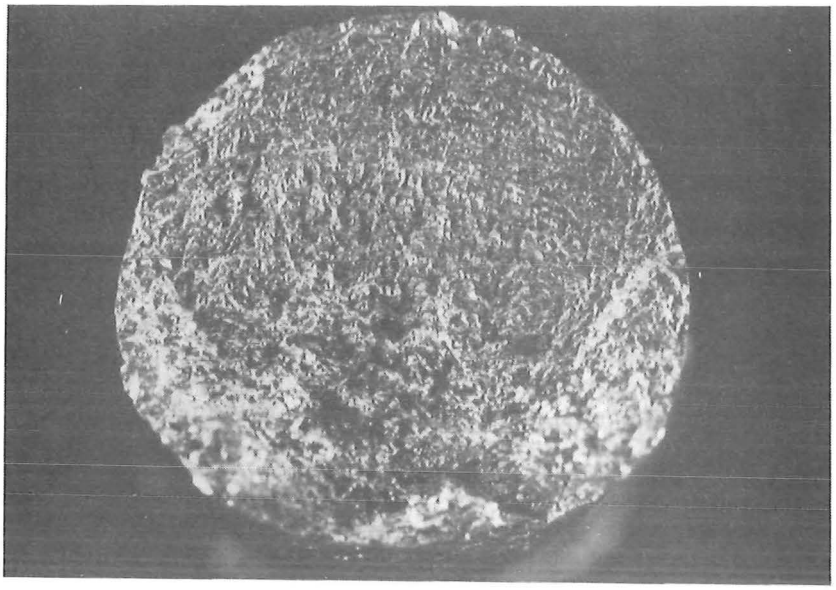

11×

(a) Coarse grained specimen (B1)
$d^{-1/2} = 3 \cdot 72 mm^{-1/2}$

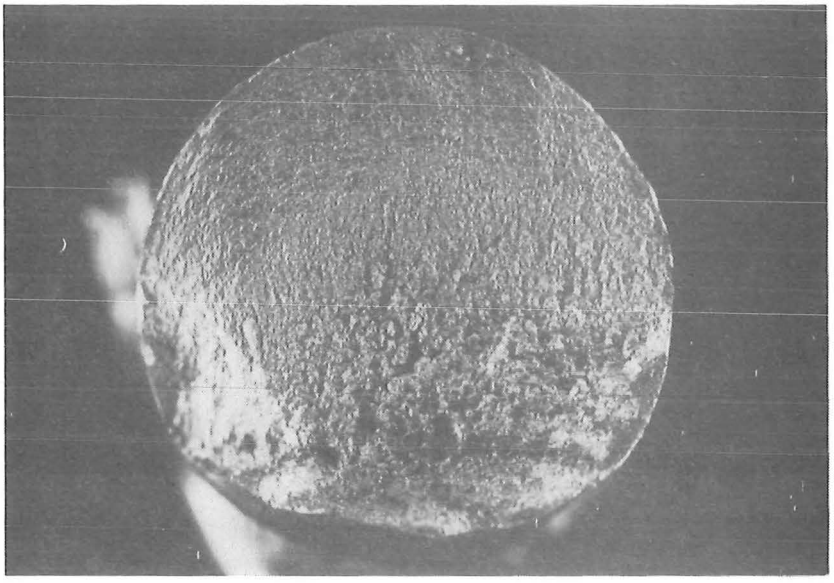

11×

(b) Fine grained specimen (B3)
$d^{-1/2} = 9 \cdot 14 mm^{-1/2}$

Fig. 8·2 ROTATING BENDING FATIGUE FRACTURE SURFACES.

the area of final separation. This "crescent" shaped region was relatively flat and a considerable amount of rubbing had taken place. This was probably due to rubbing between mating surfaces by the driving torque associated with rotating bending loading. The "crescent" shaped region was followed by an area similar in appearance to the fracture surface of a direct stress specimen. The area of final spearation had the normal ductile fracture associated with tensile separation. Like the direct stress specimens, coarse grained specimens had a coarser "texture" on the fracture surface.

8.2 TEMPERATURE MONITORING ON DIRECT STRESS FATIGUE SPECIMENS:

Temperature change during direct stress fatigue testings was monitored for three sets of specimens:- A1, B1 and B3, using a differential thermocouple comprising two Philips PR 6462 B/60 thermocouples with Ni-Ni Cr elements and a special aluminium heat conducting carrier, one thermocouple being attached to the specimen gauge length with P.V.A. tape and the opposite thermocouple to the fatigue machine.

Since specimen temperature rise has been shown to be proportional to the hysteresis loop width produced during fatigue cycling[15,109], the results shown in fig.8.3, 8.4 and 8.5 can be interpreted in terms of strain associated with the fatigue cycle, where the stress is maintained at a constant level. The following interpretations can therefore be made:-

(a) For specimens tested at stresses just below their respective direct stress fatigue limits, that is, the run-out specimens, the temperature rise (or the strain) curves may be divided into two parts. The first part comprising stress cycles up to about 2 to 3 x 10^7 cycles. The temperature

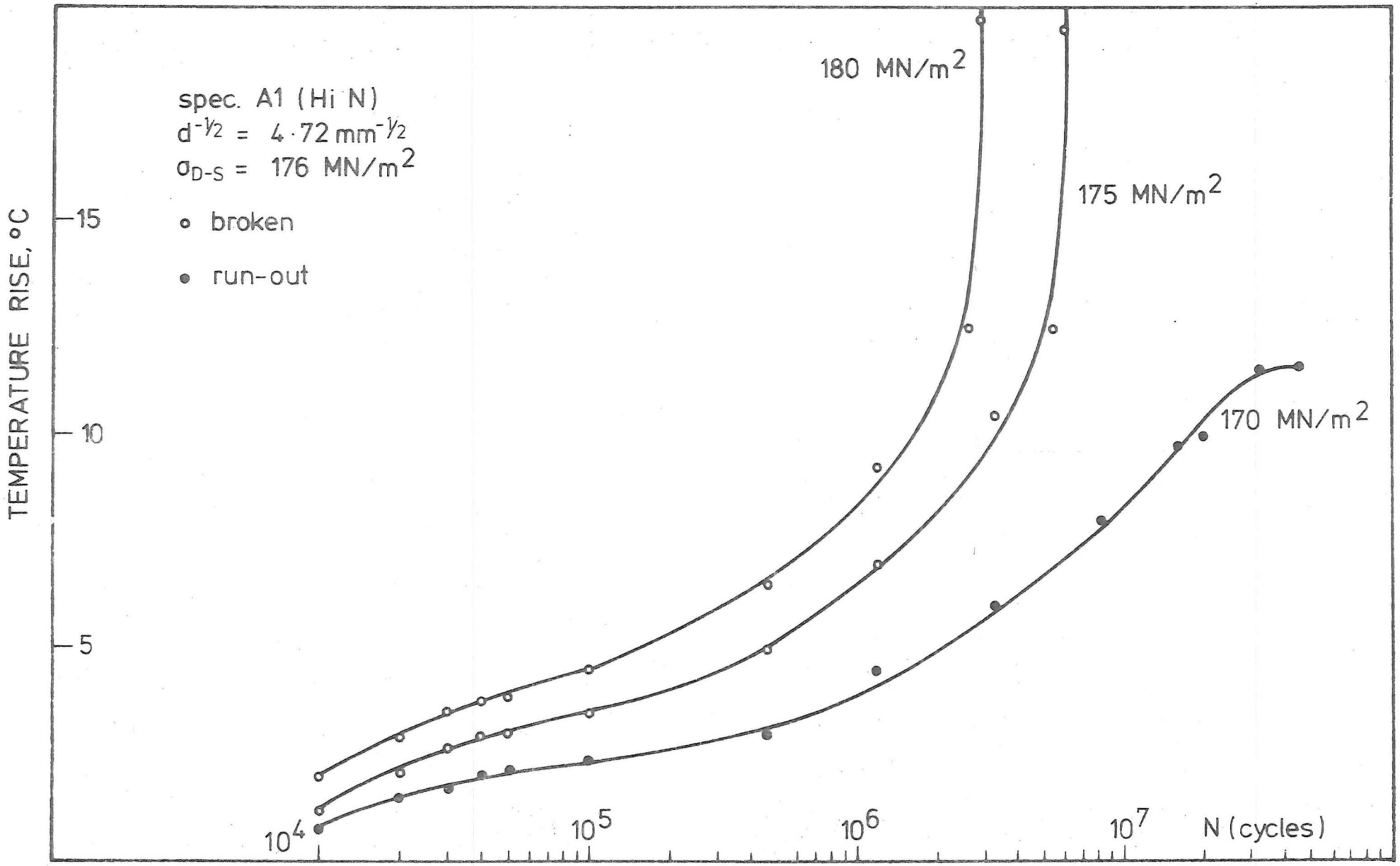

Fig. 8·3. TEMPERATURE RISE vs STRESS CYCLES

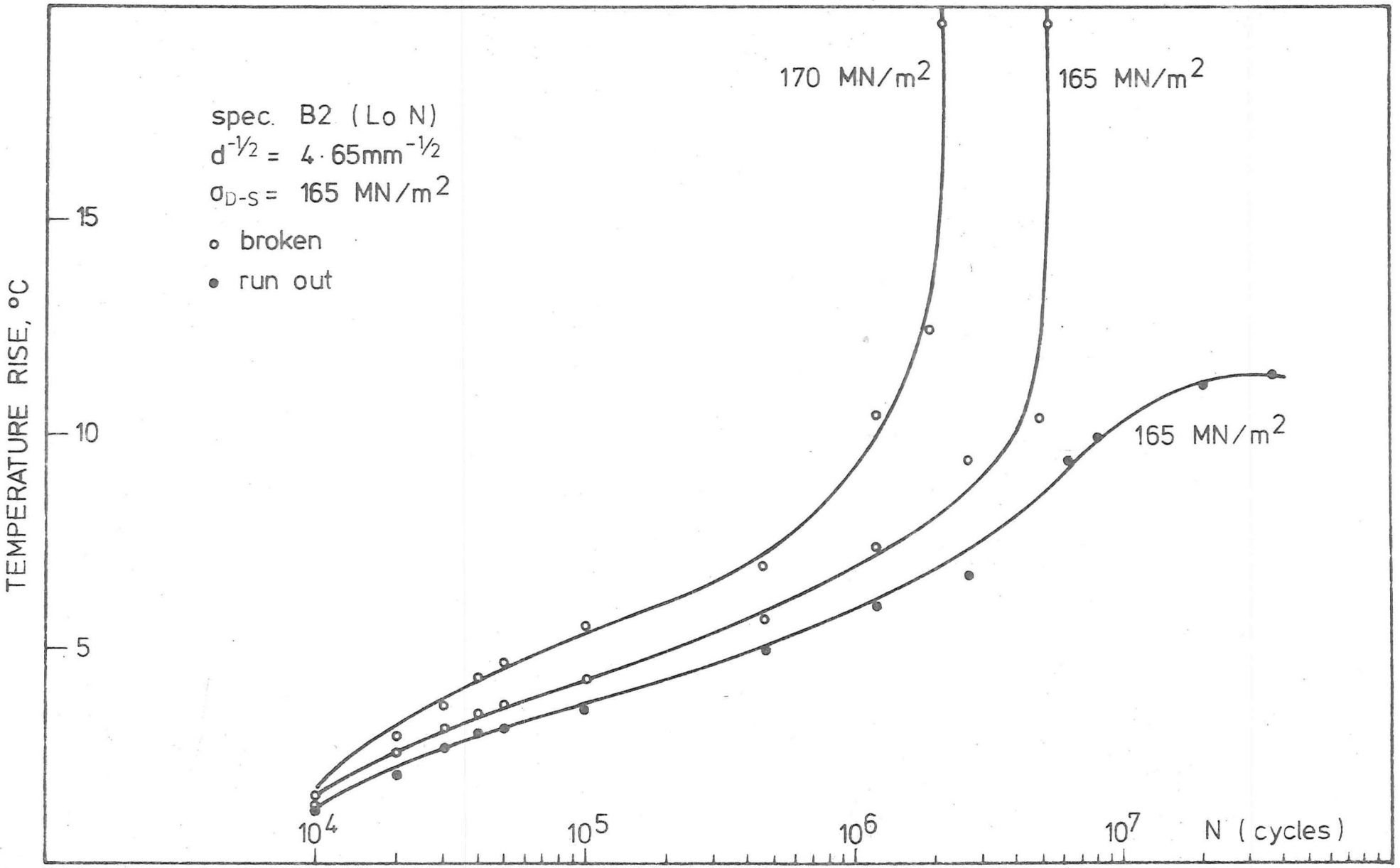

Fig. 8·4. TEMPERATURE RISE vs STRESS CYCLES

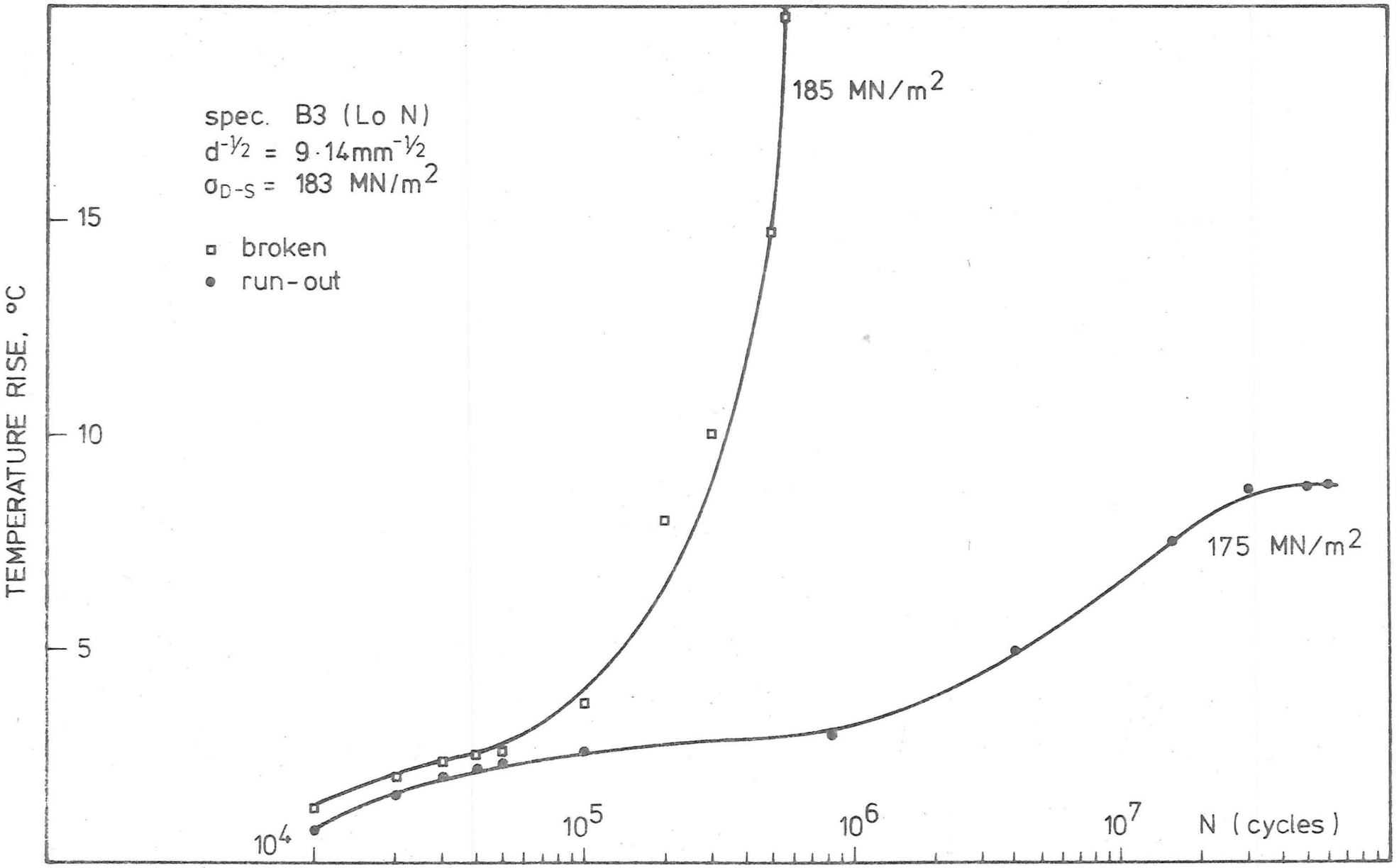

Fig. 8·5. TEMPERATURE RISE vs STRESS CYCLES

increased gradually in this part of the curve, however, too much emphasis should not be placed on the observation at the early stages (lives of up to 2×10^4 cycles) as there was a time lag in the monitoring of temperature change.

The gradual increase in temperature during this stage of fatigue cycling may be interpreted as a gradual widening of the hysteresis loop width or the gradual increase in the density of free or mobile dislocations, and probably corresponds to the cyclic hardening process as reported by Klesnil et al[19].

After about 2 to 3×10^7 cycles, the temperature remained fairly constant (for lives of up to 5×10^7 cycles), indicating that a steady state had been reached, and the production of free dislocations was counteracted by the gradual increase in the resistance to dislocation movement due to increasing numbers of defects (vacancies and their conglomerations, dislocation loops). This stage probably corresponds to the beginning of the hardening process reported by Klesnil et al[19]. Although the steady state was observed after 2 to 3×10^7 cycles as compared to lives of less than 2×10^4 cycles reported by Klesnil et al, the stresses used in this investigation were below the direct stress fatigue limits of the materials, whereas the stresses employed by Klesnil et al were well above the direct stress fatigue limits of their materials. As has been discussed in section 4.3, cyclic plastic strain is a function of stress cycle, and if dynamic yielding does occur at stresses equal to or below the direct stress fatigue limit in low carbon steels, it is reasonable to assume that cyclic stressing at stresses just above the dynamic yield stress of the material would require a much longer life for the onset of plastic deformation and strain hardening as compared to cyclic

stresses of well above the direct stress fatigue limit.

(b) For specimens tested above the direct stress fatigue limits, there was no corresponding steady state in the temperature curves as was observed for tests below the direct stress fatigue limits. The temperature increased gradually with stress cycle until the final stage in life, where the temperature increased very rapidly to failure. This observation is consistent with that reported by Oates and Wilson[15]. The continuous temperature rise to failure at stresses above the direct stress fatigue limit does not indicate the absence of the strain hardening process. The deepening of active slip bands, crack initiations and their propagations at these stress levels will contribute a much greater temperature increase, and thus obscure the hardening process as monitored with temperature change.

(c) The effect of active nitrogen on the temperature rise (or hysteresis loop width) can be seen in fig.8.6. A high level of active nitrogen lowers the temperature rise (or decreases the hysteresis loop width) at the corresponding stress level. Fig.8.6 shows the temperature increase for both high and low nitrogen steels of similar grain size ($d^{-\frac{1}{2}}$ of 4.72 $mm^{-\frac{1}{2}}$ and 4.65 $mm^{-\frac{1}{2}}$ respectively). It can be seen that the temperature increase due to cyclic loading at 165 MN/M^2 from the low nitrogen steel (steel B2, $d^{-\frac{1}{2}}$ = 4.65 $mm^{-\frac{1}{2}}$) was higher than that due to cyclic loading at 170 MN/M^2 from the high nitrogen steel (steel A1, $d^{-\frac{1}{2}}$ = 4.72 $mm^{-\frac{1}{2}}$). This trend of lower temperature rise for high nitrogen steel at corresponding stress level was observed at all stress levels.

The difference in the temperature rise between steels A1 and B2 could be due to the difference in the initial free

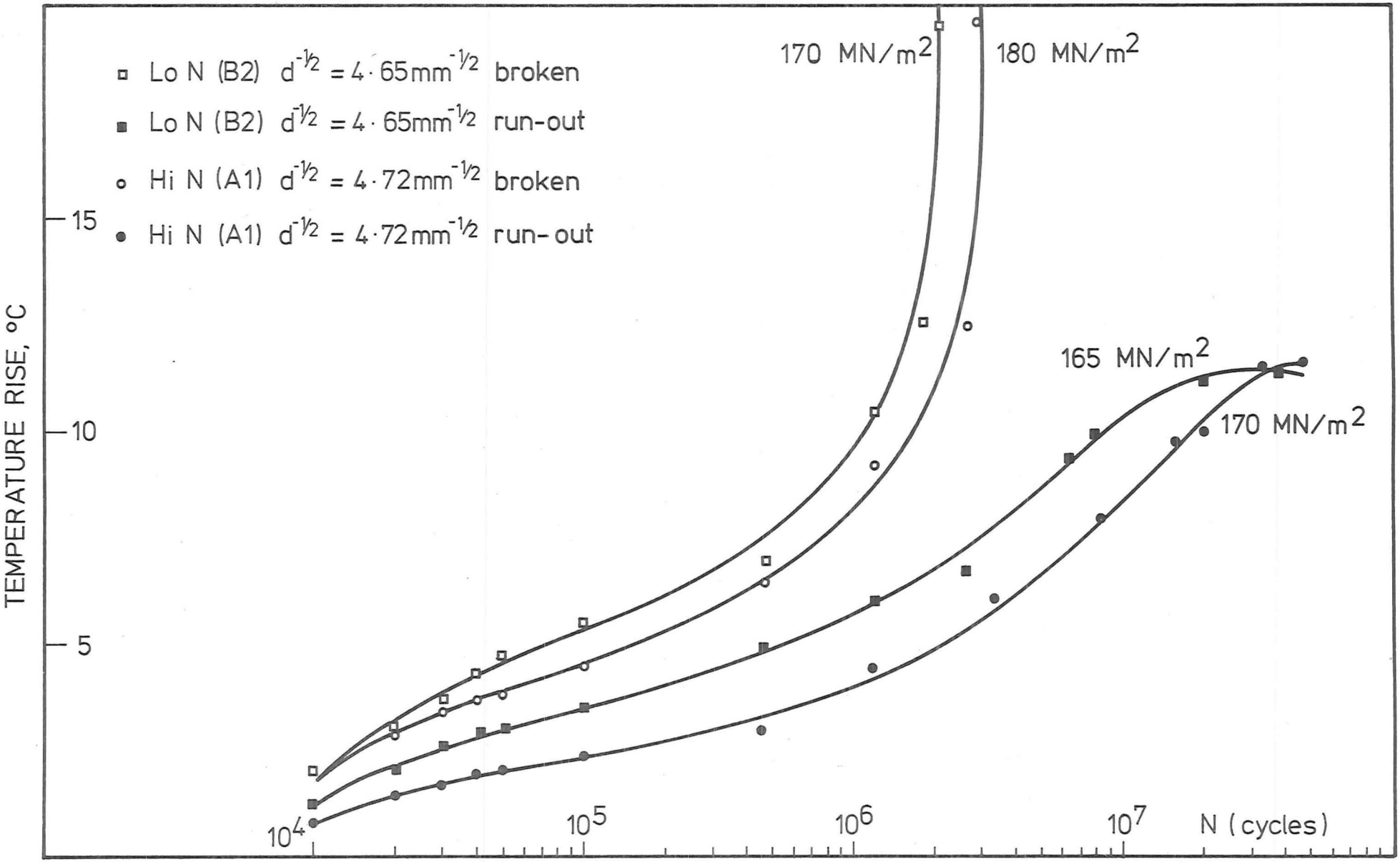

Fig. 8·6. EFFECT OF ACTIVE NITROGEN ON TEMPERATURE RISE.

dislocation density and/or the rate of strain hardening. However, the experimental steels were given a heat treatment at 110°C for one hour prior to fatigue testings, which should eliminate most of the initial free dislocations in the experimental steels. Also, the tabulated results in table 7.2 show that the K and n values for these two steels are fairly similar (K = 690 MN/M^2, n = 0.2210 for steel A1, and K = 700 MN/M^2, n = 0.2260 for steel B2), hence, the strain hardening rate for these two steels should be fairly similar. It is therefore reasonable to suggest that the lower temperature rise in the high nitrogen steel (A1) as compared to that in the low nitrogen steel (B2) was most likely due to the relocking of free dislocations by the active nitrogen, resulting in a lower free dislocation density.

(d) Reducing the grain size also has the effect of lowering the temperature rise. This is illustrated in fig.8.7, which compares the temperature rise of two sets of low nitrogen steels, with grain size of $d^{-\frac{1}{2}}$ = 4.65 $mm^{-\frac{1}{2}}$ and 9.14 $mm^{-\frac{1}{2}}$ respectively. The smaller temperature increase for the fine grained specimen suggests a smaller plastic strain, which is to a certain extent in agreement with the finding of Oates and Wilson[15], who reported little plastic deformation for their fine grained steel ($d^{-\frac{1}{2}}$ = 7.07 $mm^{-\frac{1}{2}}$) at stresses below the direct stress fatigue limit, but widespread plasticity for their coarse grained steel ($d^{-\frac{1}{2}}$ = 3.08 $mm^{-\frac{1}{2}}$) at stresses just below the direct stress fatigue limit.

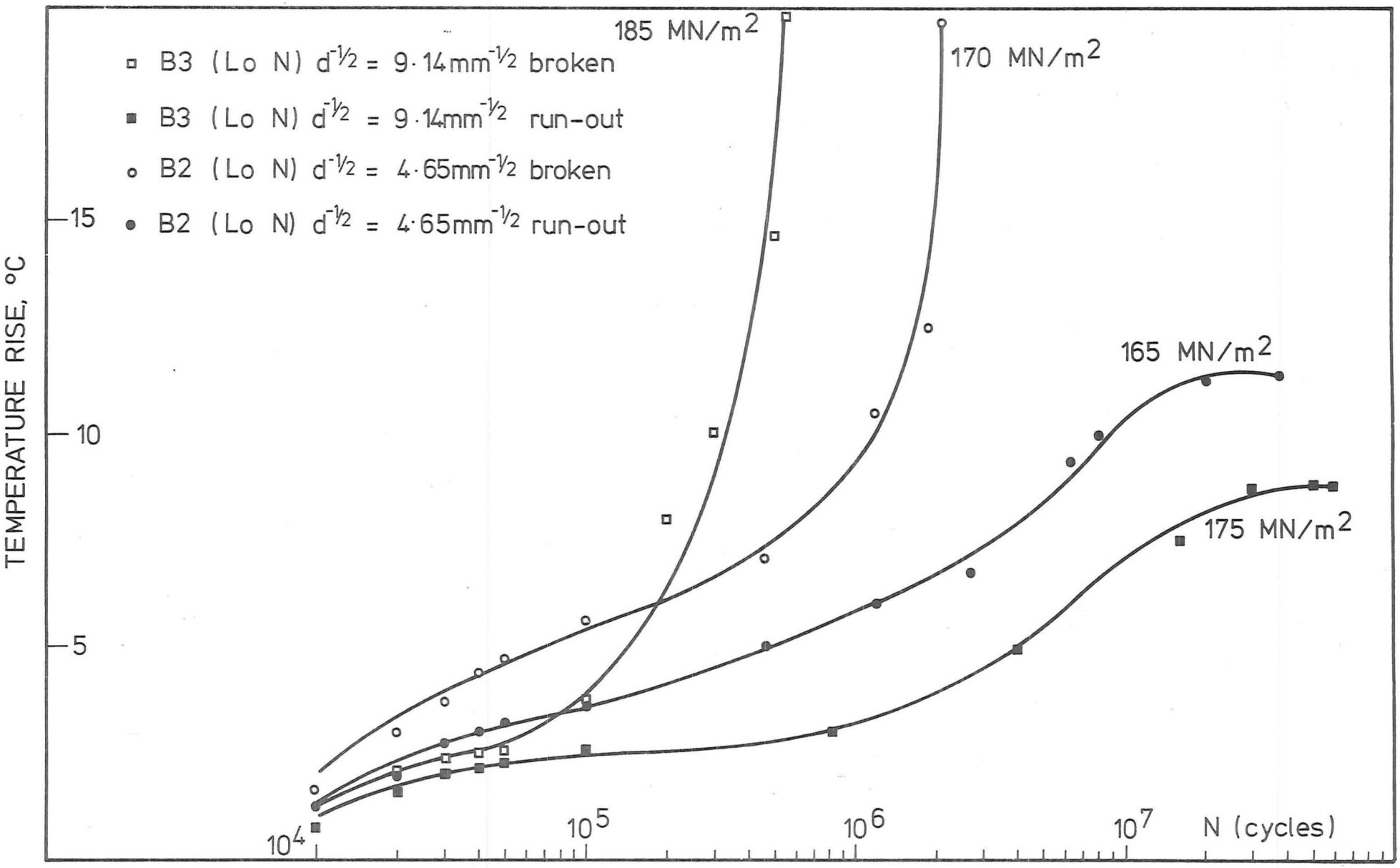

Fig. 8·7. EFFECT OF GRAIN SIZE ON TEMPERATURE RISE.

8.3 PLASTIC DEFORMATION REVEALED BY ETCHING WITH FRY's REAGENT:

Special high nitrogen-low carbon steel (steel C) was used to reveal the plastic strain accumulated during cyclic stressing. The chemical composition in wt % being:-

C	Si	S	P	Mn	Al_{sol}	N_{sol}
0.06	0.05	0.043	0.042	0.21	0.005	0.012

After cyclic stressing, specimens were aged at 250°C for 30 minutes and etched with Fry's reagent made up as follows:-

$CuCl_2$	HCl	H_2O
45 gms	180 ml	100 ml

The suitability of this special steel in revealing plastic deformation can be seen in figs.8.8a and 8.8b. Fig.8.8a shows the plastic zones on a Charpy specimen deformed under three-point bending, and fig.8.8b illustrates the deformation on a rotating bending specimen accidentally overloaded during testing.

One major disadvantage with the use of this technique is that this is a macro etching process, and plastic zone has to be of reasonable size before it can be detected. This technique however, gives a very positive indication of the onset of plastic deformation, and enables the progress of plastic deformation to be observed qualitatively, and to a certain extent, quantitative measurement can also be made.

Direct stress fatigue specimens similar to those used in Section 7.2 were used to reveal the plastic deformation accumulated during direct stress fatigue cycling. The direct stress fatigue limit for this high nitrogen low carbon steel (steel C) was found to be about 235 MN/M^2, and the static lower yield stress was 280 MN/M^2. Specimens were tested at 210, 220

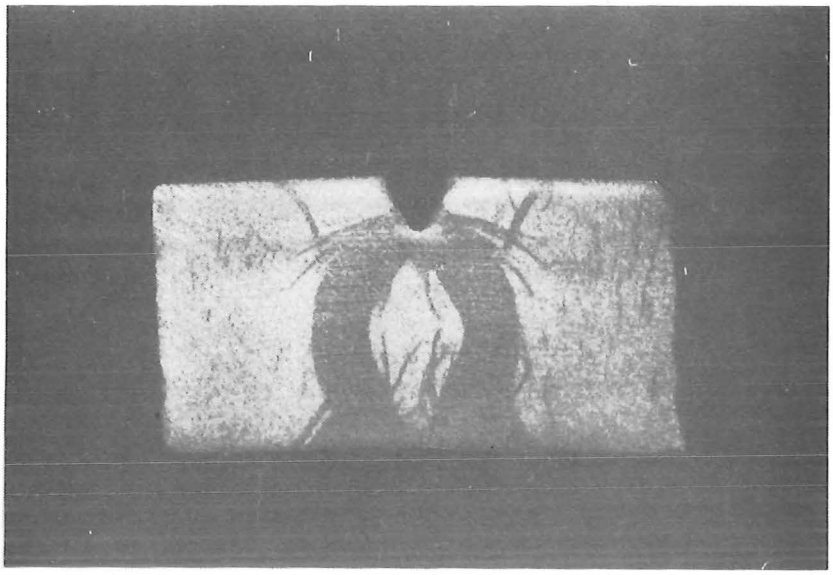

(a) Plastic deformation zones on a Charpy specimen (three point bending).

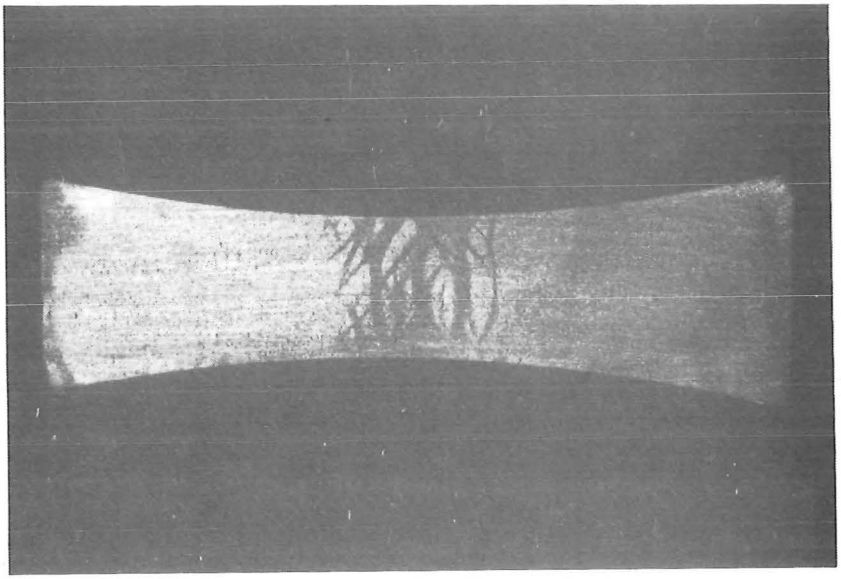

(b) Plastic deformation zones on a rotating bending specimen (accidentally overloaded).

Fig. 8·8. PLASTIC DEFORMATION REVEALED WITH FRY'S REAGENT.

and 230 MN/M^2 for up to 5×10^7 cycles, see fig.8.9. No plastic zone was revealed for the specimen tested at 210 MN/M^2 for lives of up to 5×10^7 cycles, this indicates the absence of plastic deformation or dynamic yielding at this stress level. This is further confirmed by the temperature change monitoring in fig. 8.10, which indicates negligible increase in temperature when the specimen was cycled at this stress level.

When the specimen was tested at 220 MN/M^2, significant amounts of plastic deformation can be seen, and the plastic zone spread across the whole cross section of the specimen. There was also a corresponding increase in the temperature at this stress level. As the applied stress of 220 MN/M^2 was below the direct stress fatigue limit of the material (235 MN/M^2), it can thus be deduced that the dynamic yield stress of this high nitrogen low carbon steel is less than the direct stress fatigue limit, and cyclic stressing at the direct stress fatigue limit should result in the modification or elimination of the sharp yield drop and the Luders strain if sufficient stress cycles are allowed.

The temperature change was also monitored for this steel at two stress levels: 210 and 220 MN/M^2, the results are shown in fig.8.10. Cyclic stressing at 210 MN/M^2 had little effect on the temperature change, indicating little dislocation movement or plastic deformation at stresses below 210 MN/M^2. Loading at 220 MN/M^2 resulted in significant temperature increases and the temperature curve was similar to those obtained in section 8.2 but, after about 10^7 cycles, the temperature started to decrease. This was probably due to the high level of active nitrogen in this special steel. During the process of dynamic yielding, dislocation multiplication may

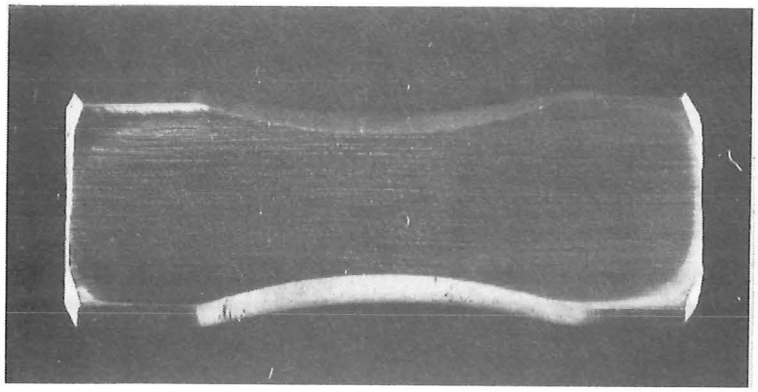

σ_{DS} = 235 MN/m^2
σ = 210 MN/m^2
N = 5 × 10^7

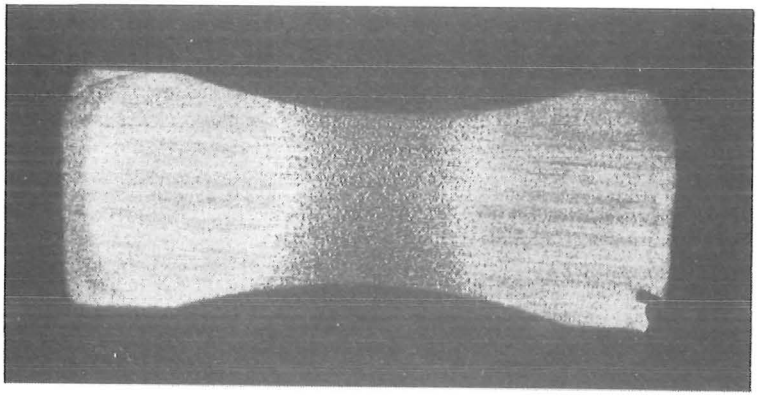

σ = 220 MN/m^2
N = 5 × 10^7

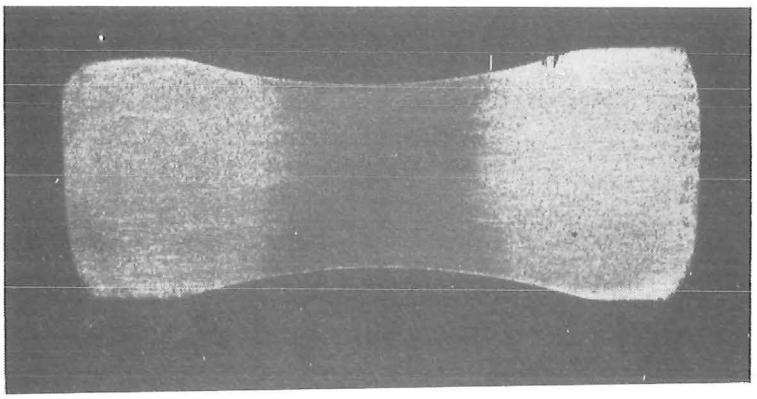

σ = 230 MN/m^2
N = 5 × 10^7

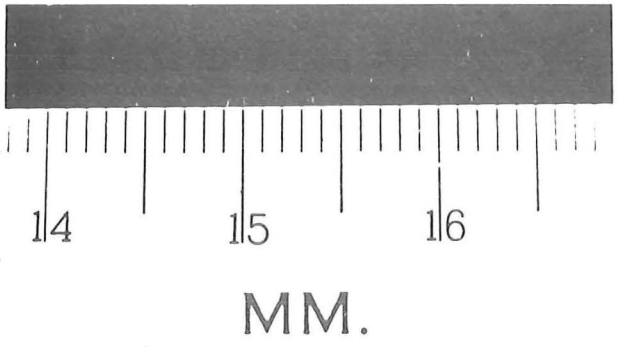

Fig. 8·9 PLASTIC DEFORMATION REVEALED WITH FRY'S REAGENT (REVERSED DIRECT STRESS SPECIMENS.)

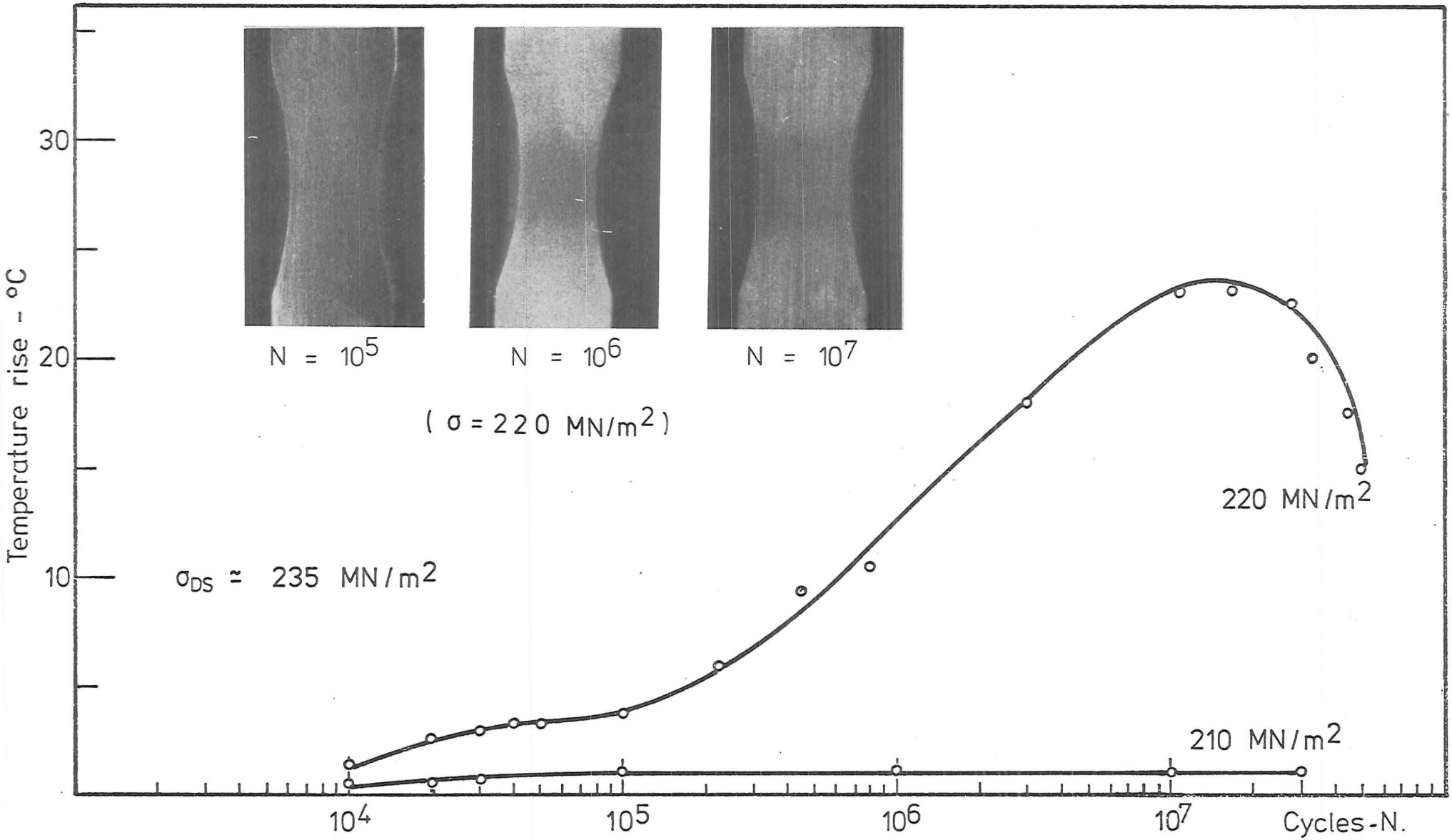

Fig. 8·10 TEMPERATURE RISE vs STRESS CYCLES (SPECIAL HIGH NITROGEN LOW CARBON STEEL - C)

outpace the relocking of free dislocations by active nitrogen and result in a higher density of mobile dislocations, which means a wider hysteresis loop width or higher increase in temperature. But after the process of strain softening, the continual relocking of free dislocations by the active nitrogen will result in strain aged hardening, or a decreasing hysteresis loop width, thus a decrease in temperature.

Three specimens were also tested at 220 MN/M^2 and stopped at 10^5, 10^6 and 10^7 cycles respectively. The amount of plastic deformation accumulated under these stress cycles is shown in fig.8.10. No plastic deformation zone was detected at 10^5 cycles. At 10^7 cycles, which corresponded to the maximum temperature rise, the plastic zone was also of maximum size. Although no quantitative correlations between the plastic zone size and temperature rise were made, it is reasonable to suggest from the above experimental results that the temperature monitoring may be used to detect the onset of plastic deformation during cyclic stressing, that is the onset of dynamic yielding.

This special high nitrogen low carbon steel was also used to reveal the plastic deformation accumulated during rotating bending testing. Rotating bending specimens similar to those used in section 7.2 were again used and the rotating bending fatigue limit for this steel was found to be approximately 295 MN/M^2. Plastic deformation accumulated during cyclic stressing at various stress levels is shown in fig.8.11. The specimens were sectioned above the centre of the specimen so that the plastic zone was magnified. Referring to fig.8.12, if the specimen is sectioned at a distance l above the centre of the specimen, then the actual plastic zone size at the diameter of the specimen can be calculated as follows:-

$$r_2 = \sqrt{(d^2 + l^2)}$$

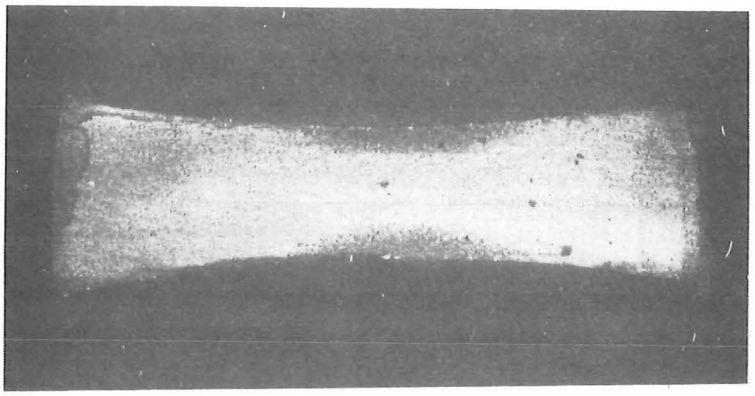

σ_{RB} = 295 MN/m^2
σ_{app} = 280 MN/m^2
N = 3 × 10^7

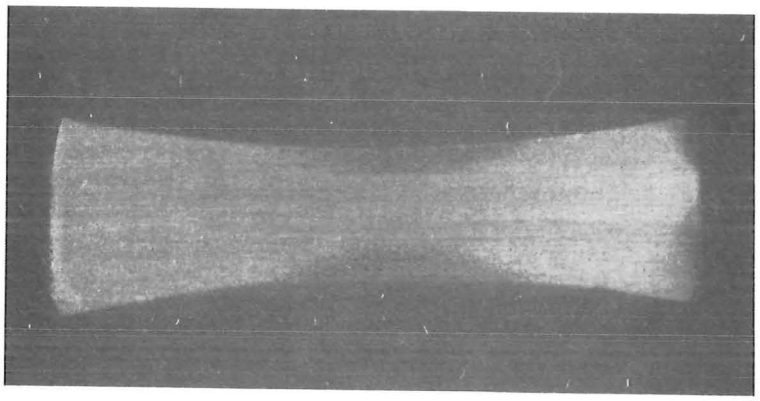

σ_{app} = 290 MN/m^2
N = 3 × 10^7

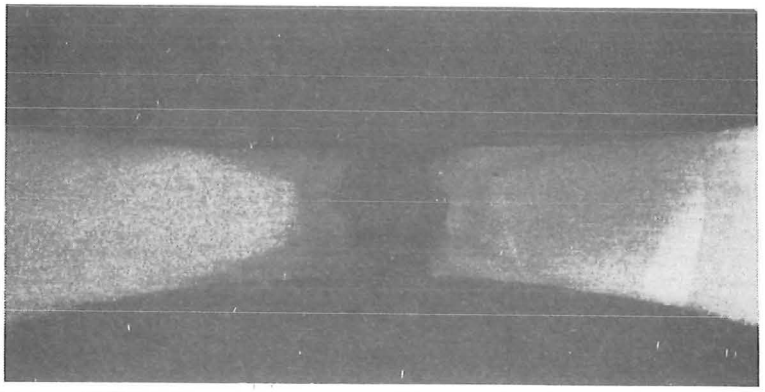

σ_{app} = 295 MN/m^2
N = 5·1 × 10^6

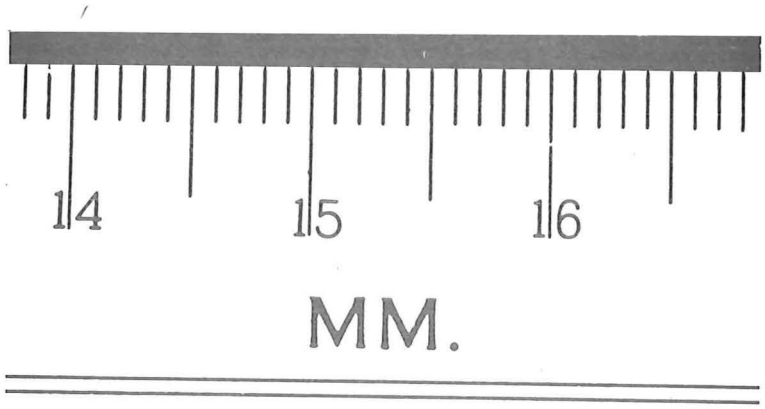

Fig. 8·11. PLASTIC DEFORMATION REVEALED WITH FRY'S REAGENT (ROTATING BENDING SPECIMENS)

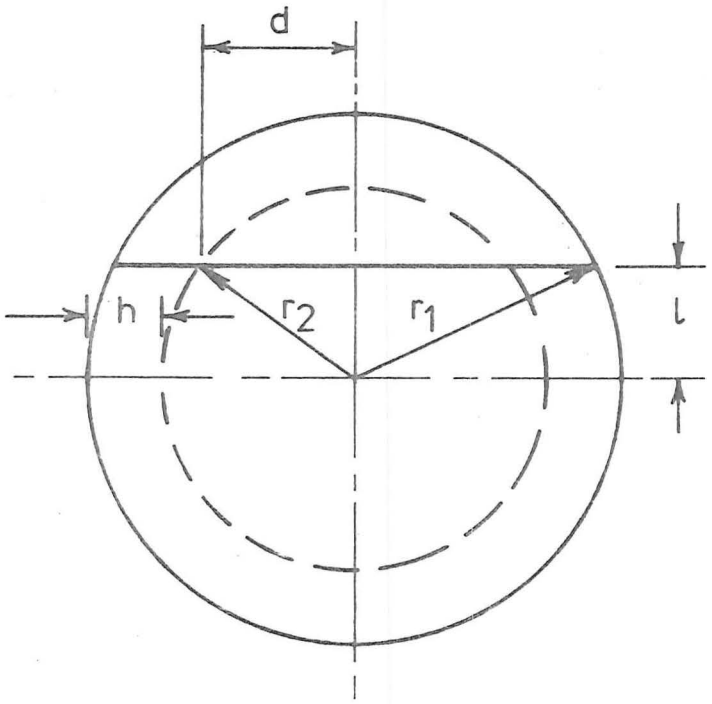

$$r_2 = \sqrt{(d^2 + l^2)}$$

$$\& \quad h = r_1 - r_2$$

$$\therefore \quad h = r_1 - \sqrt{(d^2 + l^2)}$$

Fig. 8·12. DETERMINATION OF PLASTIC LAYER AT SPECIMEN CENTRE.

and $h = r_1 - r_2$

$\therefore \quad h = r_1 - \sqrt{(d^2 + i^2)}$ eqn 8.1

where r_1 is the specimen radius.

As has been shown earlier, the dynamic yield stress of this special steel was about 220 MN/M^2, it can therefore be assumed that prolonged rotating bending cycling at a claculated applied stress σ_{app} (that is, calculated from the elastic theory, $M = \sigma I/n$) higher than 220 MN/M^2 should result in a plastically deformed layer on the specimen's surface. However, rotating bending testings with this high nitrogen low carbon steel showed that a calculated applied stress σ_{app} of above 270 MN/M^2 was required before the plastic layer could be detected and measured positively. At lower stress levels, staining of the surface layer by the reagent made it difficult to detect the darker etching plastic zone, particularly when the zone was thin.

The plastic zone $r_e = h_e/r_1$ and the stress ratio $R_e = \sigma_{app}/\sigma_{DS}$ are tabulated in table 8.1,

where h_e = absolute plastic zone size as revealed by etching,

r_1 = specimen radius,

σ_{app} = calculated applied stress from elastic theory,

i.e. $M = \sigma I/n$,

σ_{DS} = direct stress fatigue limit of the material.

Some error in the measurement of the plastic zone size h_e was possible since there was no sharp transition between elastic and plastic zones, the transition zone generally consisted of isolated patches of deformed grains. This transition zone was included in the measurement of h_e, and this could have resulted in a higher value of r_e.

TABLE 8.1

σ_{app}	N	$R_e = \sigma_{app}/\sigma_{DS}$	$r_e = h_e/r_1$
MN/M^2	$\times 10^6$		
305	3.8	1.30	0.240
295	5.1	1.26	0.210
290	>30	1.23	0.205
280	>30	1.19	0.190
270	>30	1.15	0.160

$\sigma_{DS} \simeq 235\ MN/M^2$

r_1 = specimen radius ($\simeq$3.2 mm)

h_e = depth of plastic deformation zone determined by etching

8.4 MICROHARDNESS SURVEY ON RUN-OUT SPECIMENS:

Run-out specimens from the eight sets of experimental steels and the special high nitrogen low carbon steels were aged at 250°C for 30 minutes, the specimens were then sectioned and microhardness tests carried out with a Vickers pneumatic micro-hardness testing machine. A load of 50 grams was found to give the optimum results.

For the direct stress specimens, testings were carried out along the specimen axis, and the results from the direct stress specimens are shown in figs.8.13, 8.14, 8.15, 8.16 and 8.17. For all eight sets of experimental steels and the high nitrogen low carbon steel, microhardness surveys revealed a zone of plastic deformation at stresses close to but below their respective direct stress fatigue limits. The size of the plastic zone obtained from the microhardness survey on the high nitrogen low carbon steel compared very well with that revealed by etching with Fry's reagent.

Microhardness results from the run-out rotating bending specimens are shown in figs.8.18, 8.19, 8.20, 8.21 and 8.22. Testings on rotating bending specimens were carried out across the specimen diameter and fig.8.23 illustrates a typical traverse. The specimens were sectioned at a distance 1 above the centre of the specimen, and as shown in fig.8.12, the appropriate distance of a point from the specimen surface at the specimen diameter was calculated using equation 8.1.

A curve fitting technique assuming a function of the form $y = ax^b$ was used to fit the experimental points obtained from the microhardness surveys. Very good correlations were obtained for all the experimental steels with the exception of steel B3. The discrepancy in steel B3 was probably due to the

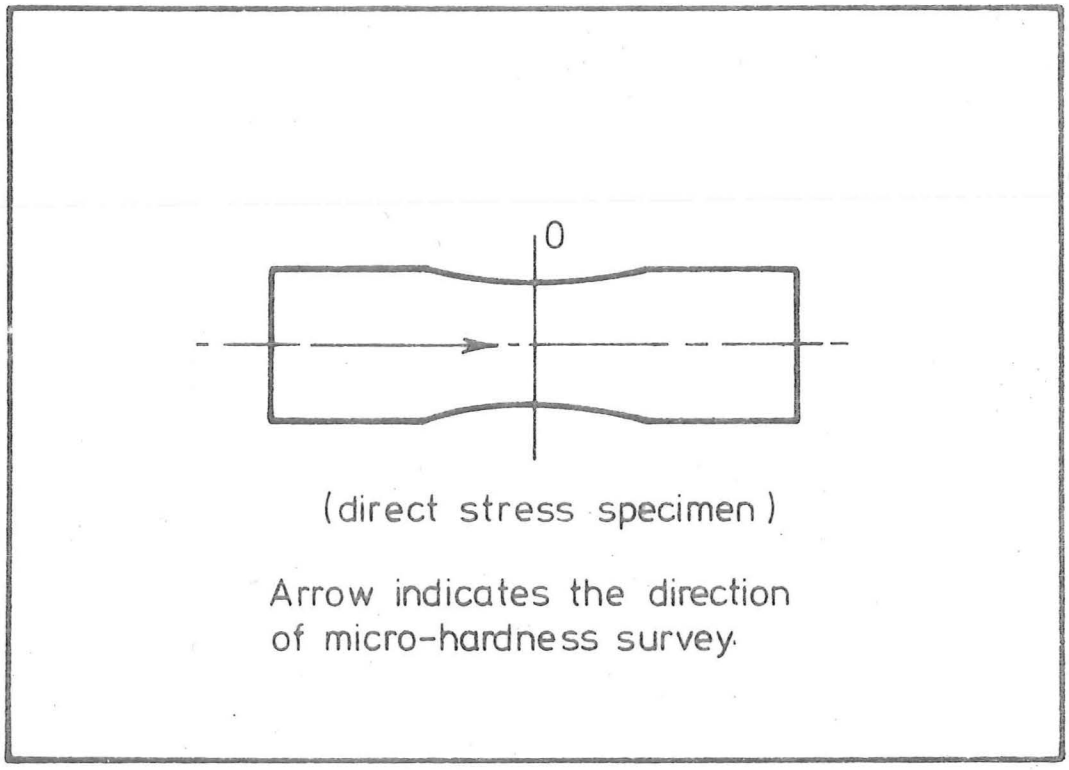

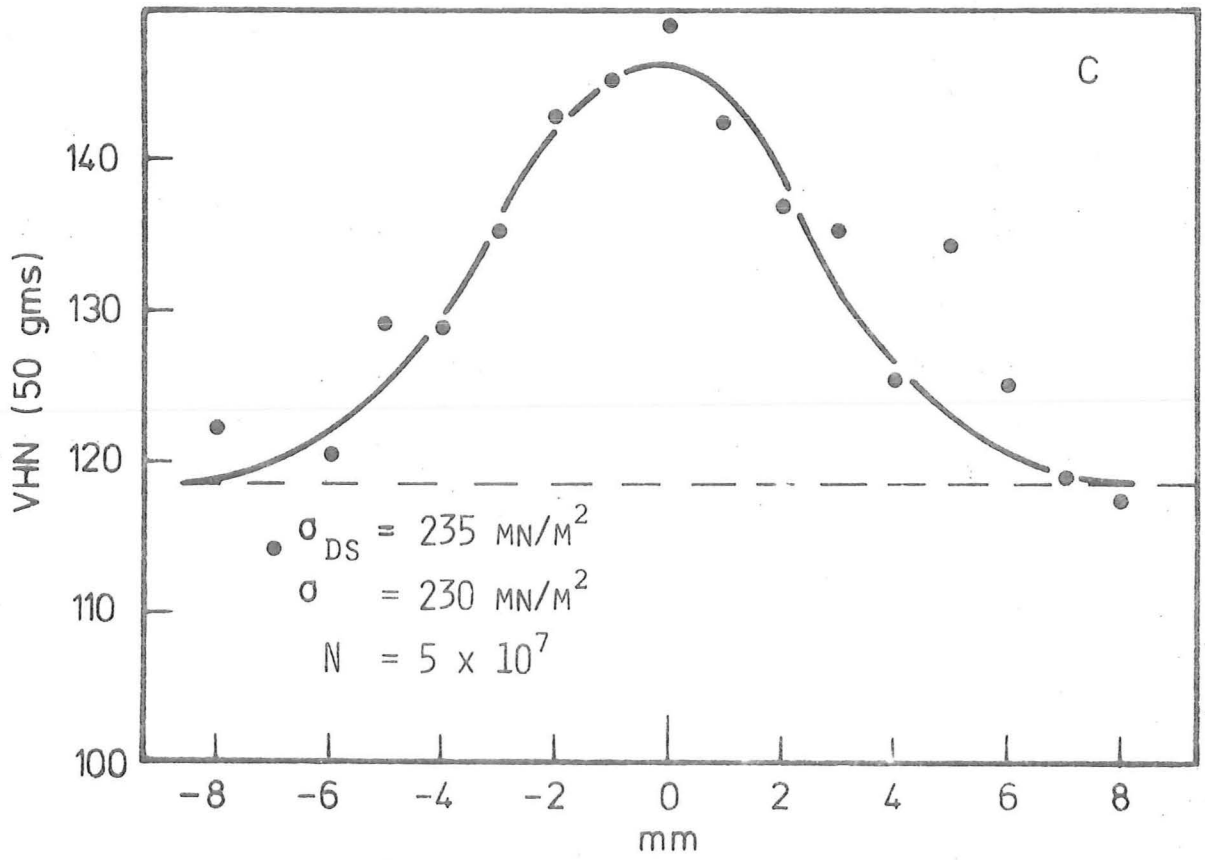

Fig. 8·13 MICROHARDNESS RESULT (DIRECT STRESS)

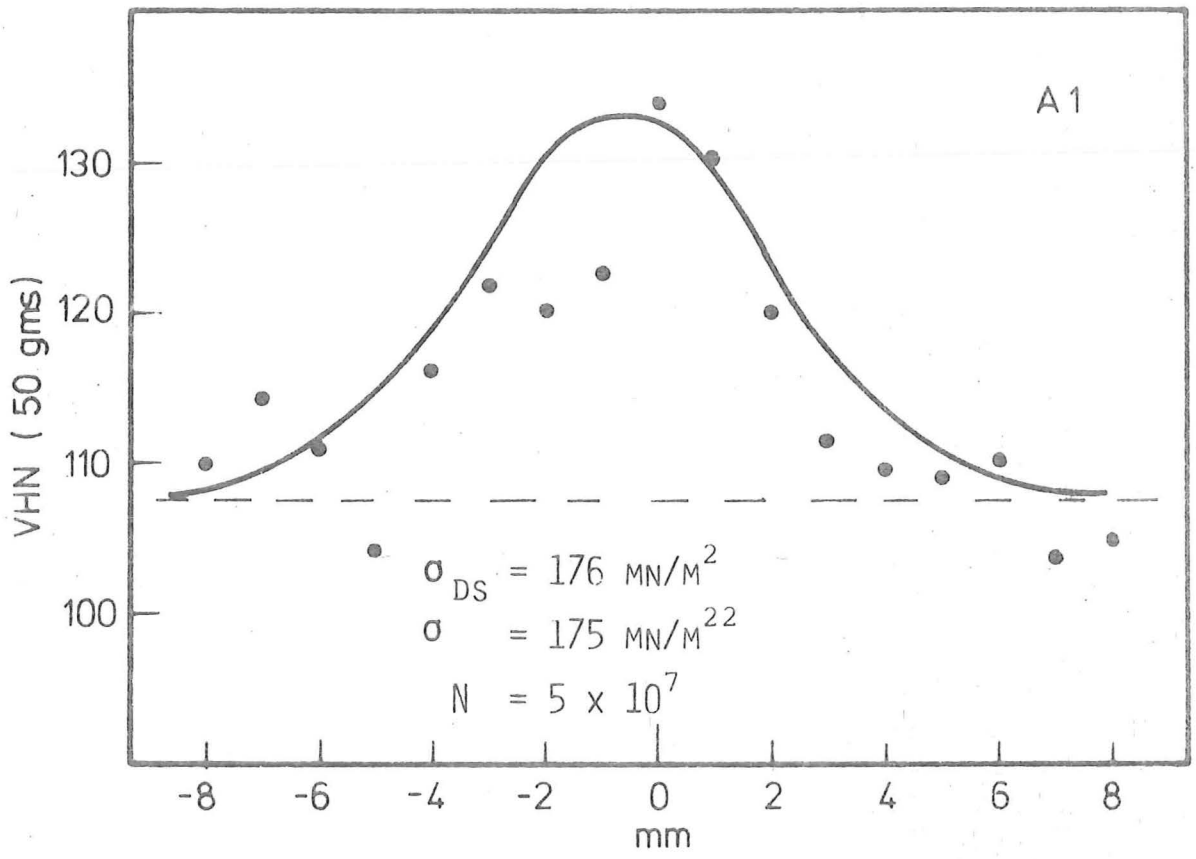

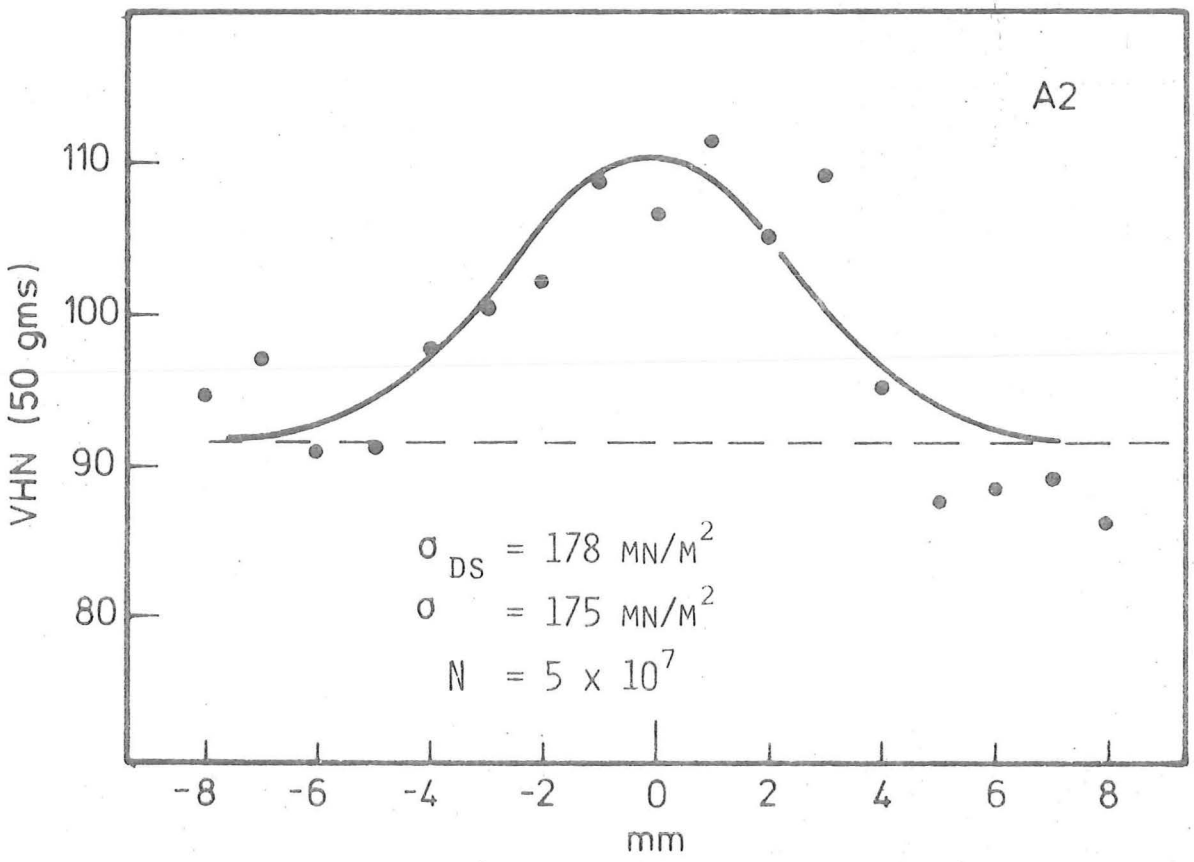

Fig. 8·14 MICROHARDNESS RESULTS (DIRECT STRESS)

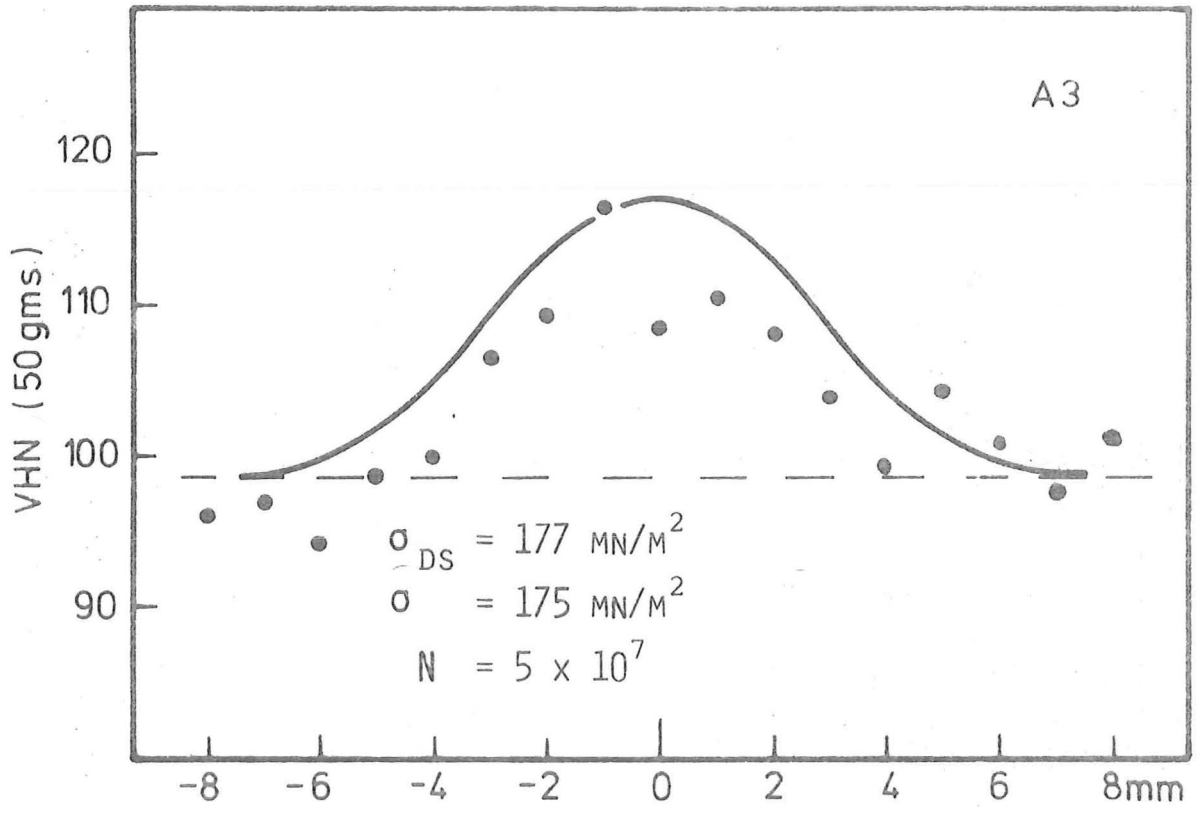

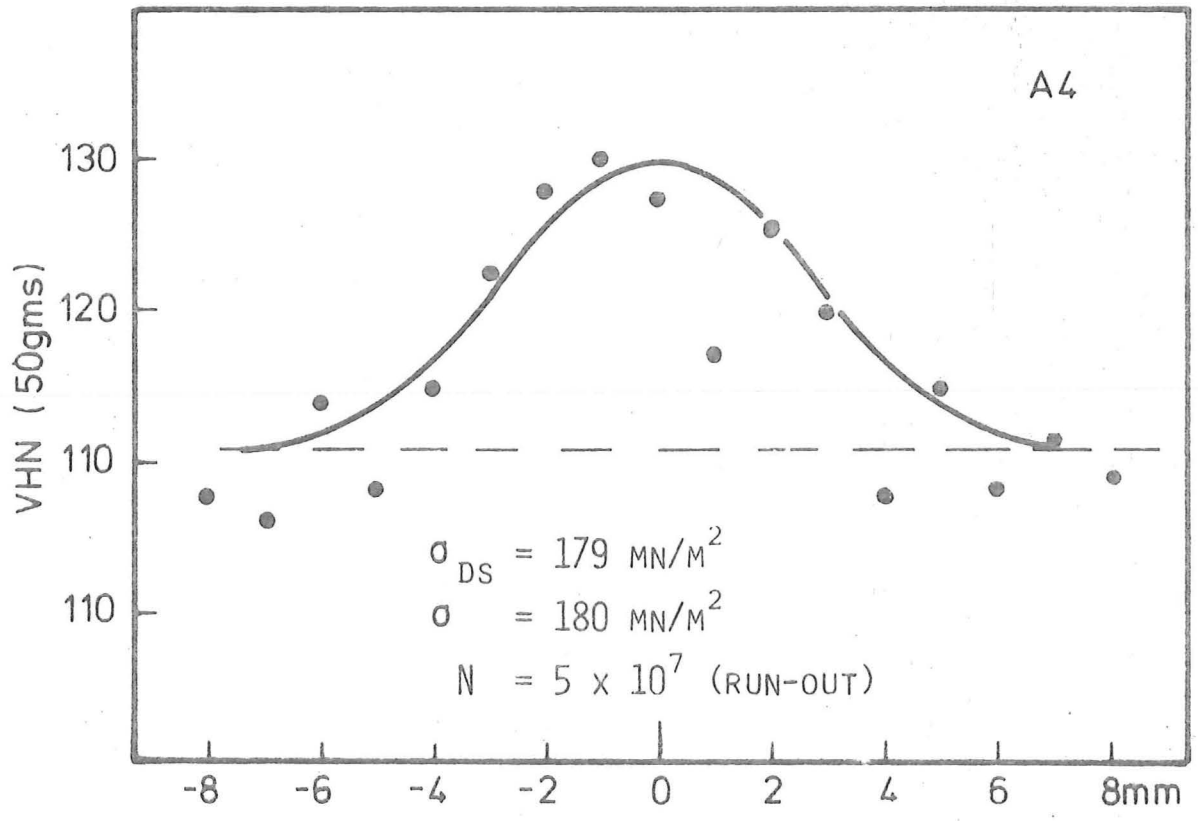

Fig. 8·15. MICROHARDNESS RESULTS (DIRECT STRESS)

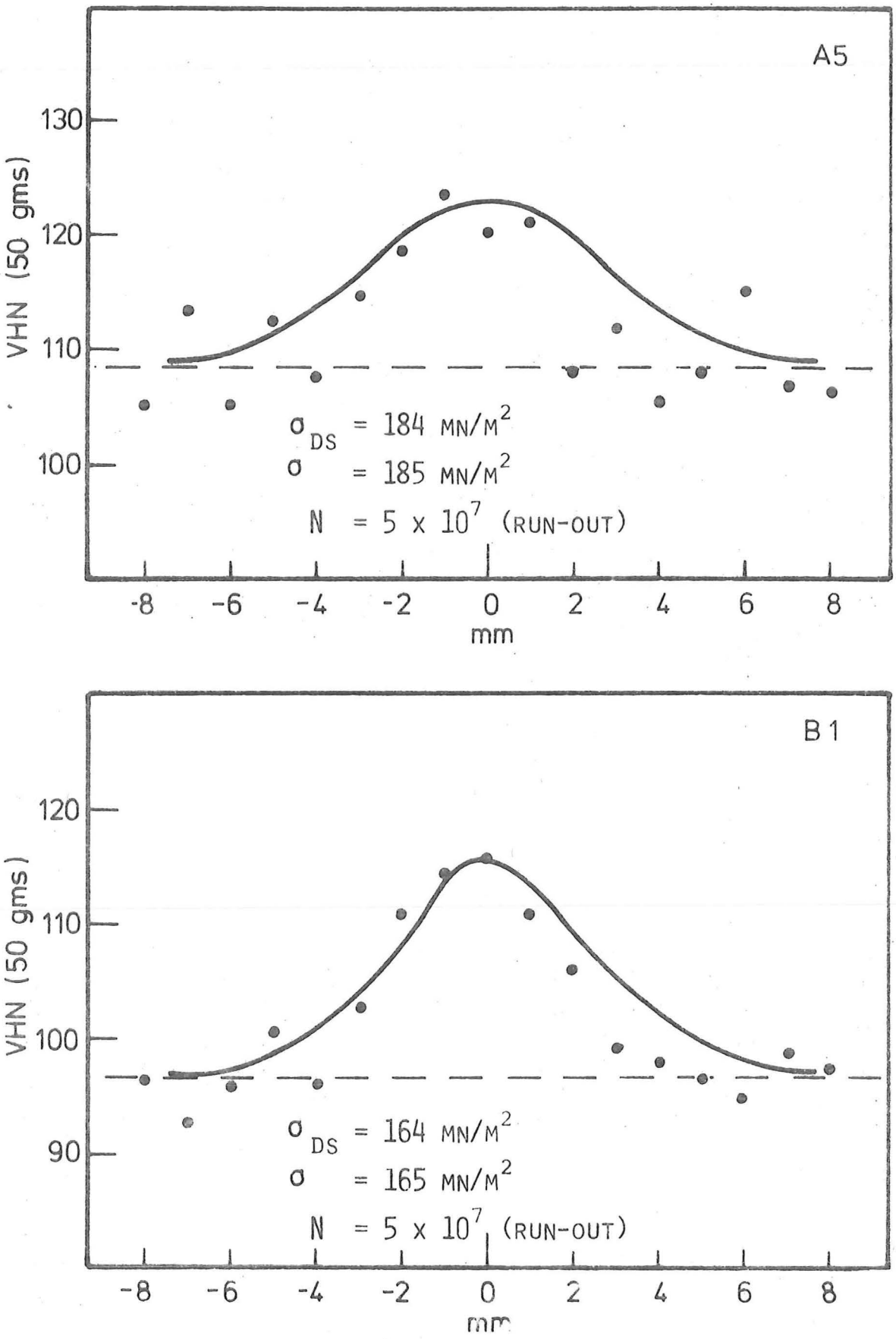

Fig. 8·16. MICROHARDNESS RESULTS (DIRECT STRESS)

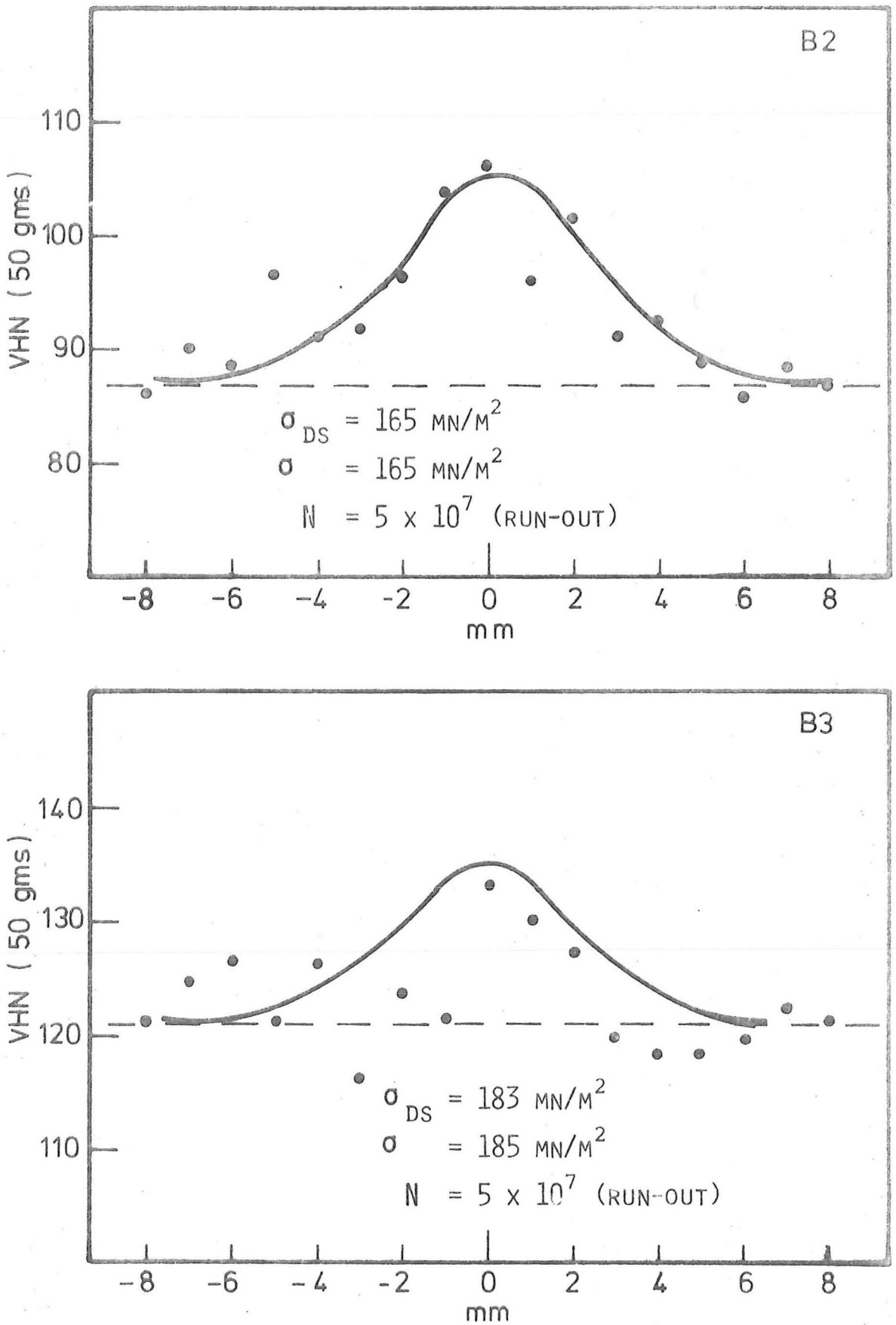

Fig. 8·17 MICROHARDNESS RESULTS (DIRECT STRESS)

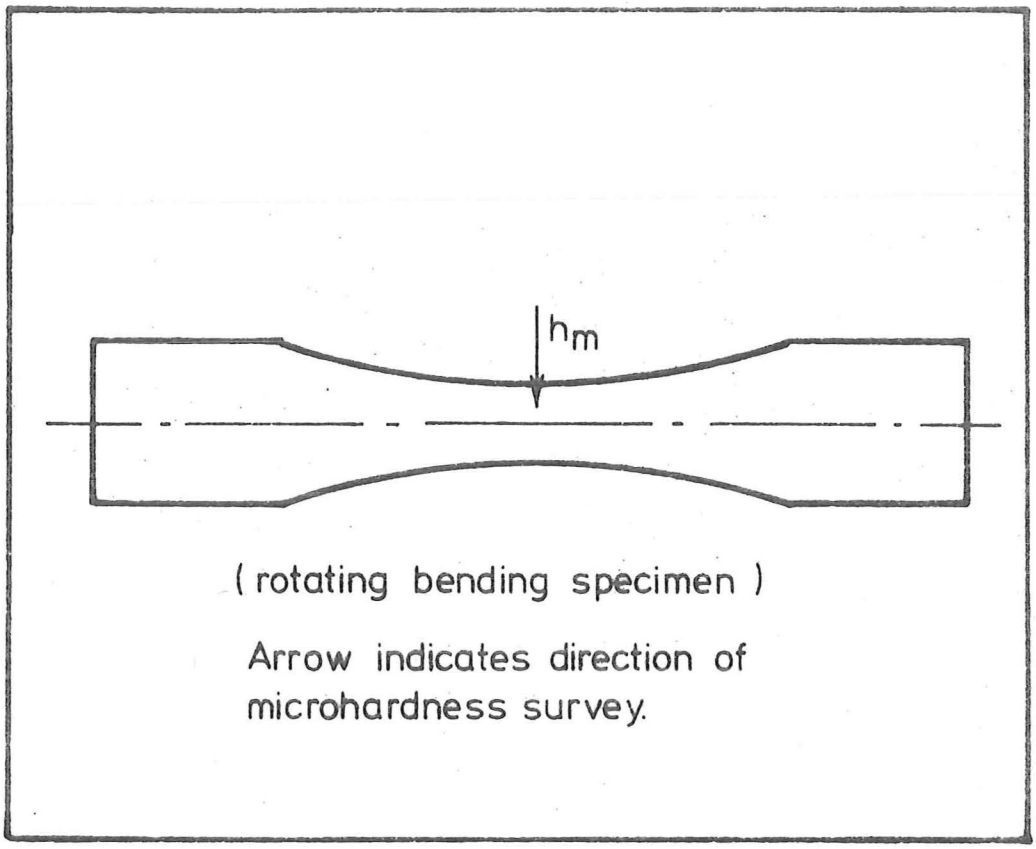

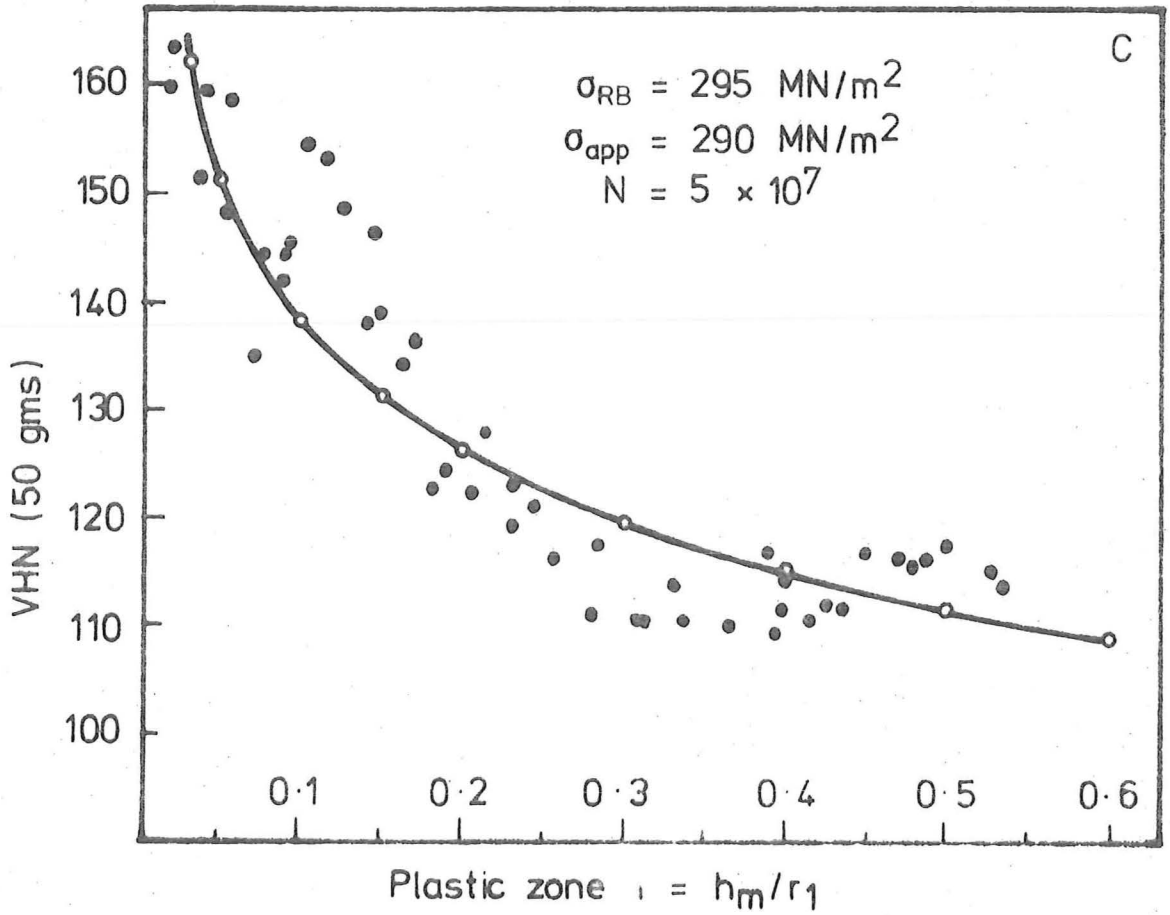

Fig. 8·18 MICROHARDNESS RESULT (ROTATING BENDING)

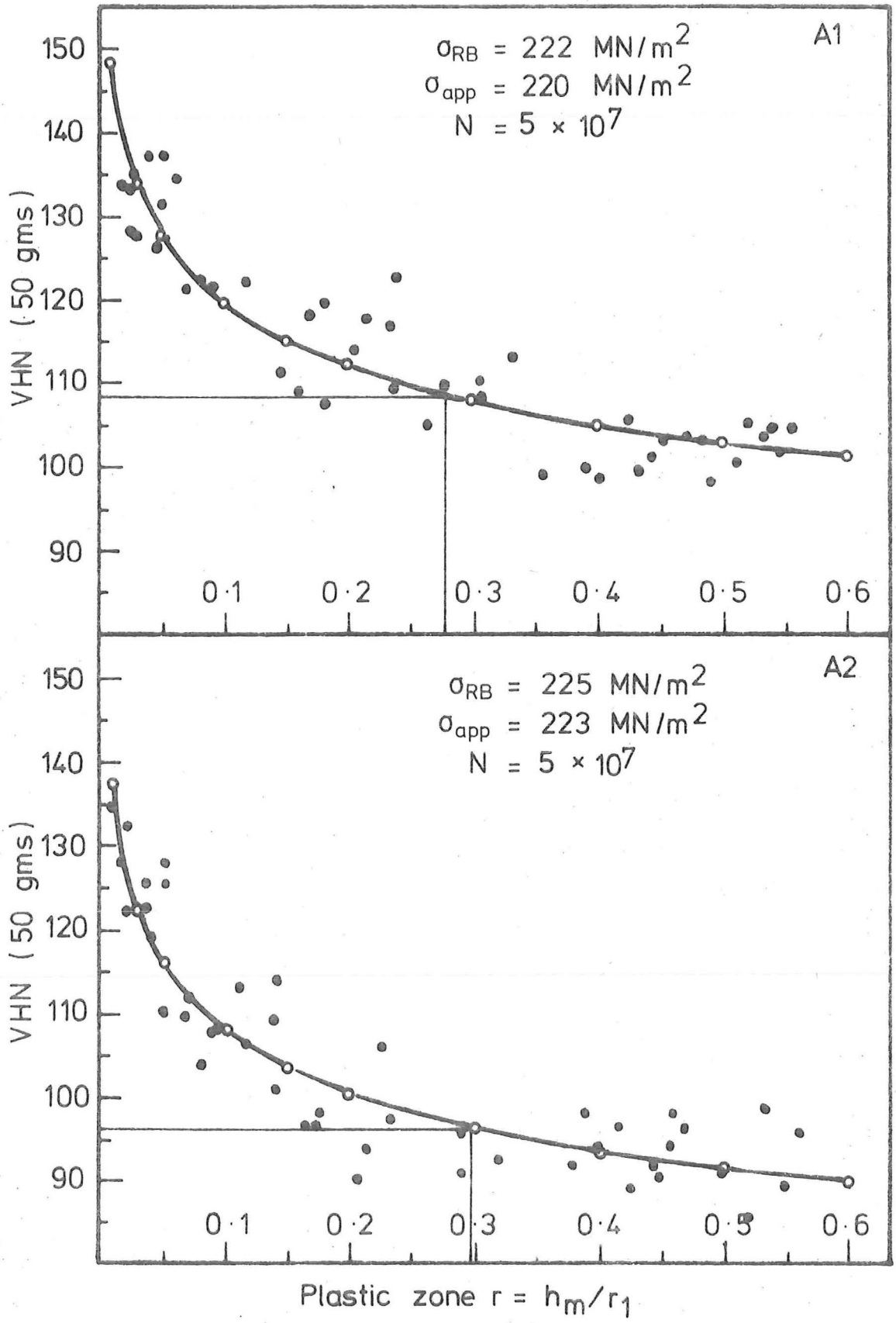

Fig. 8·19. MICROHARDNESS RESULTS (ROTATING BENDING).

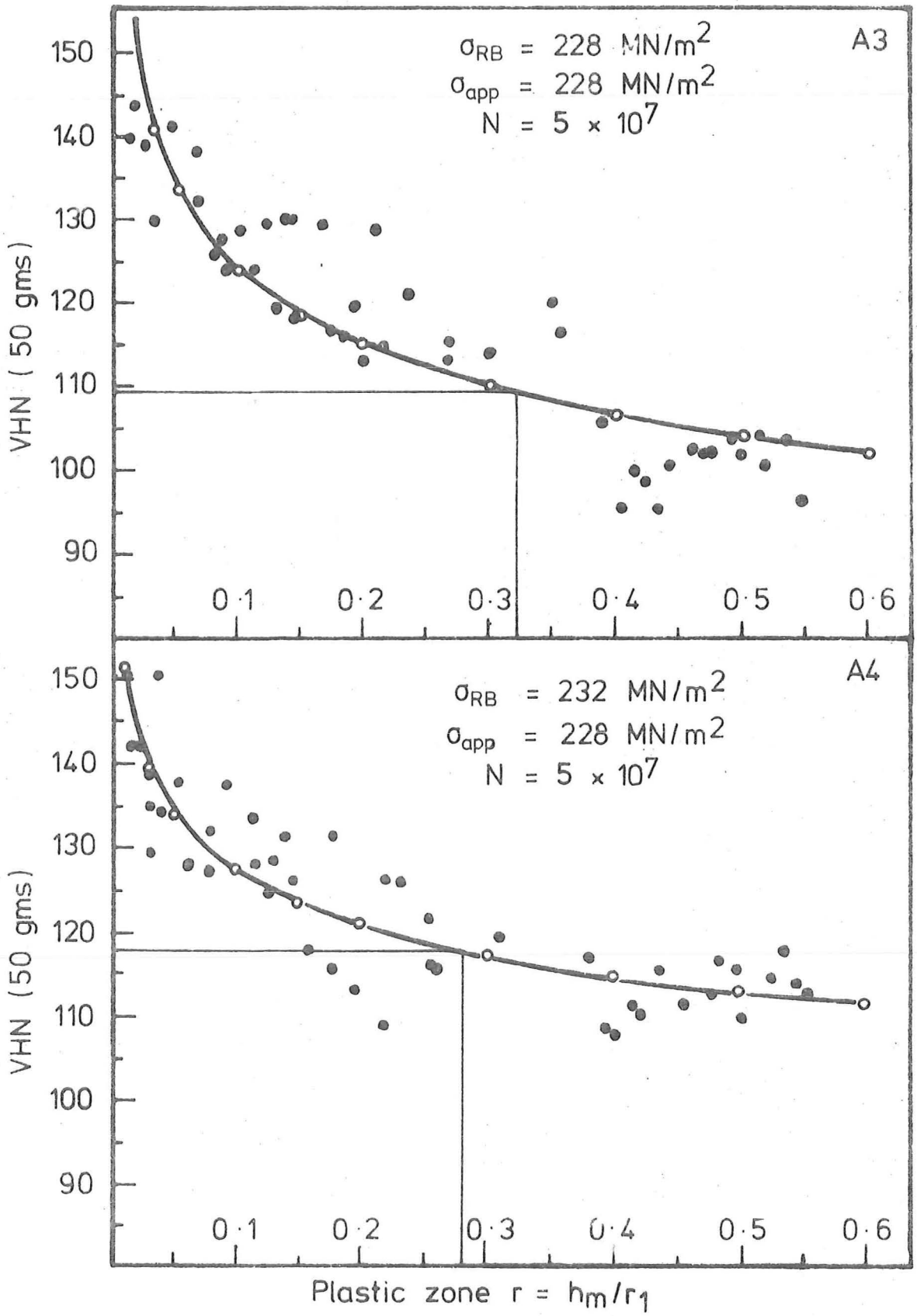

Fig. 8·20. MICROHARDNESS RESULTS (ROTATING BENDING)

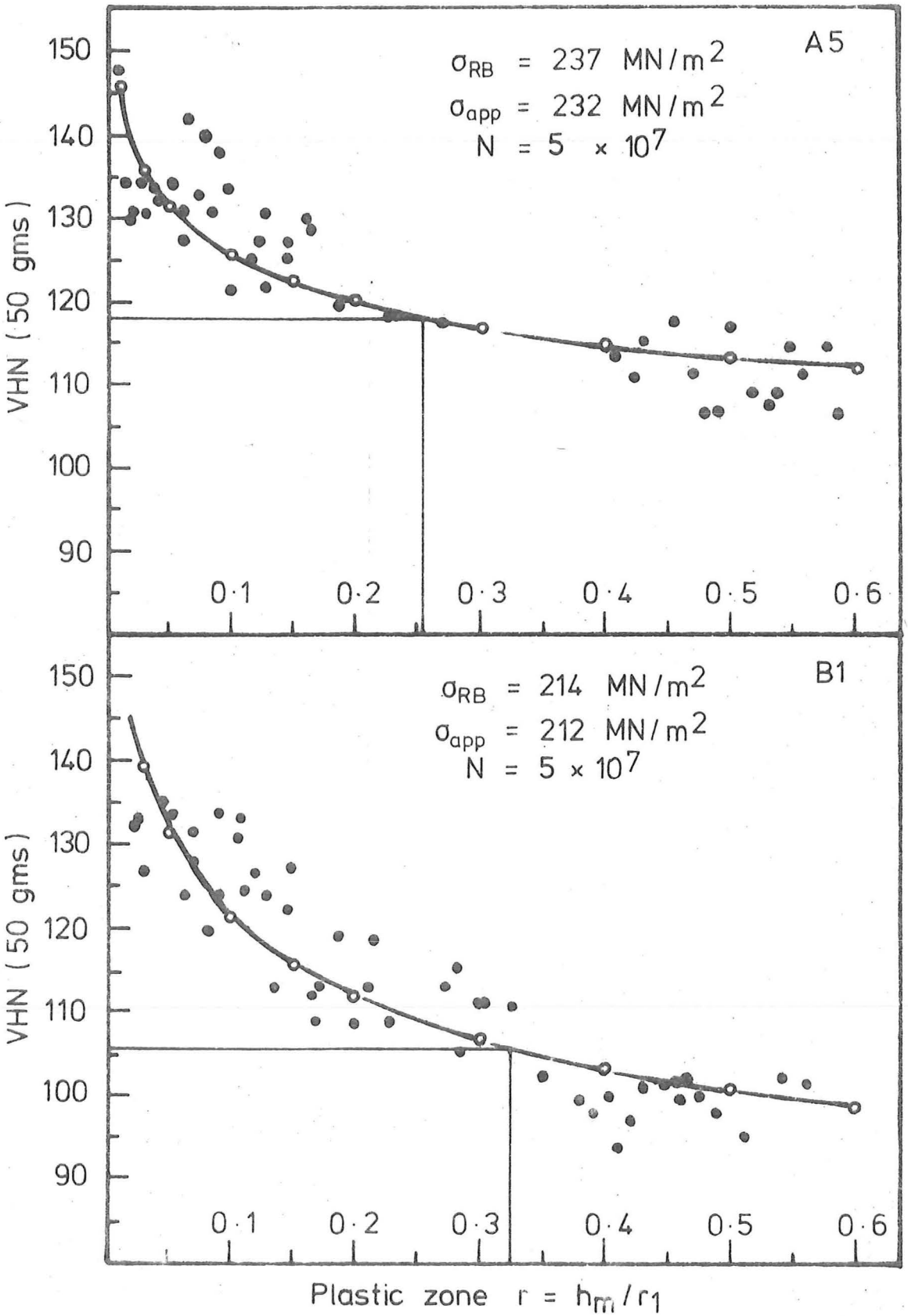

Fig. 8·21 MICROHARDNESS RESULTS (ROTATING BENDING)

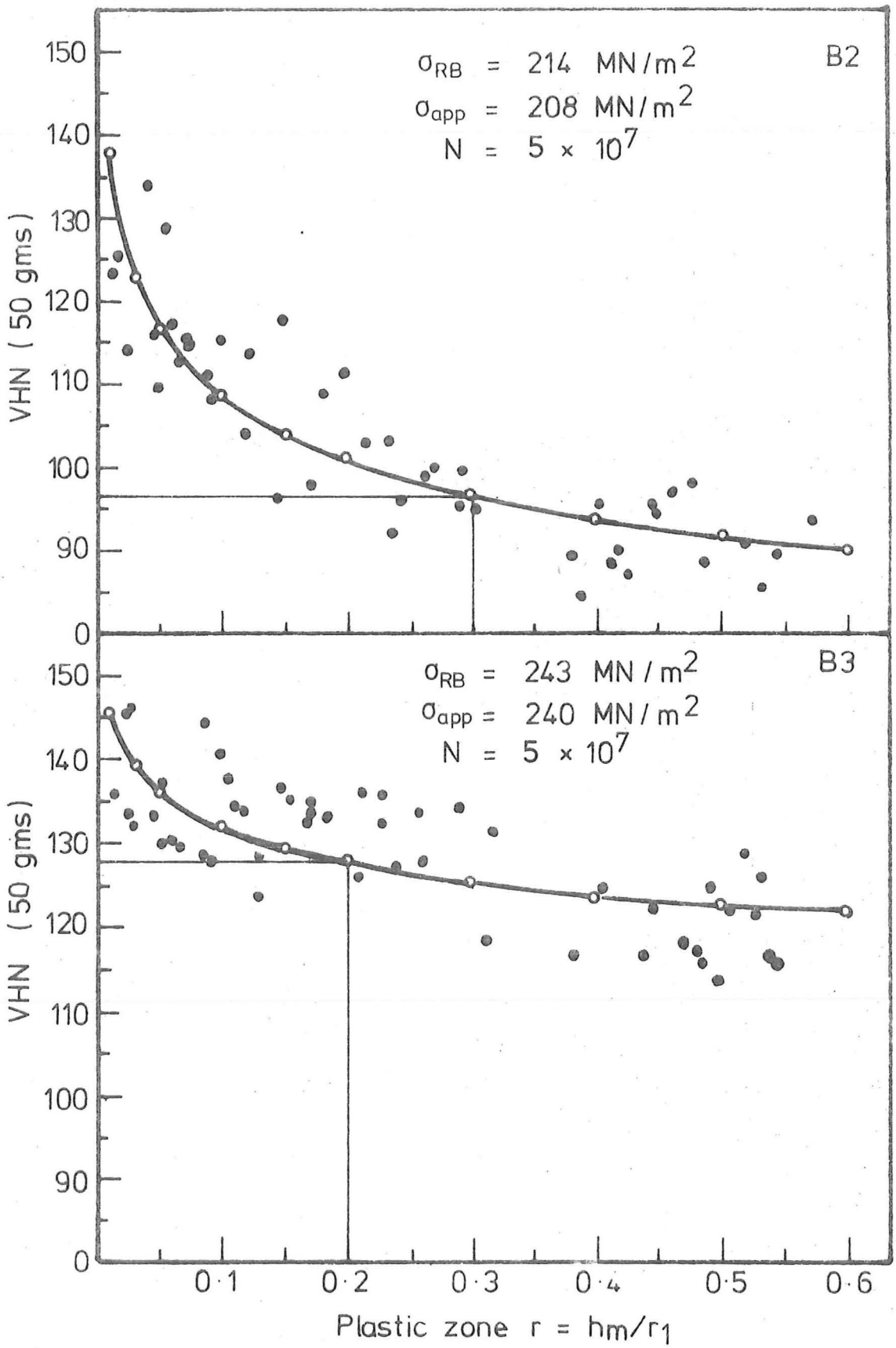

Fig. 8·22 MICROHARDNESS RESULTS (ROTATING — BENDING)

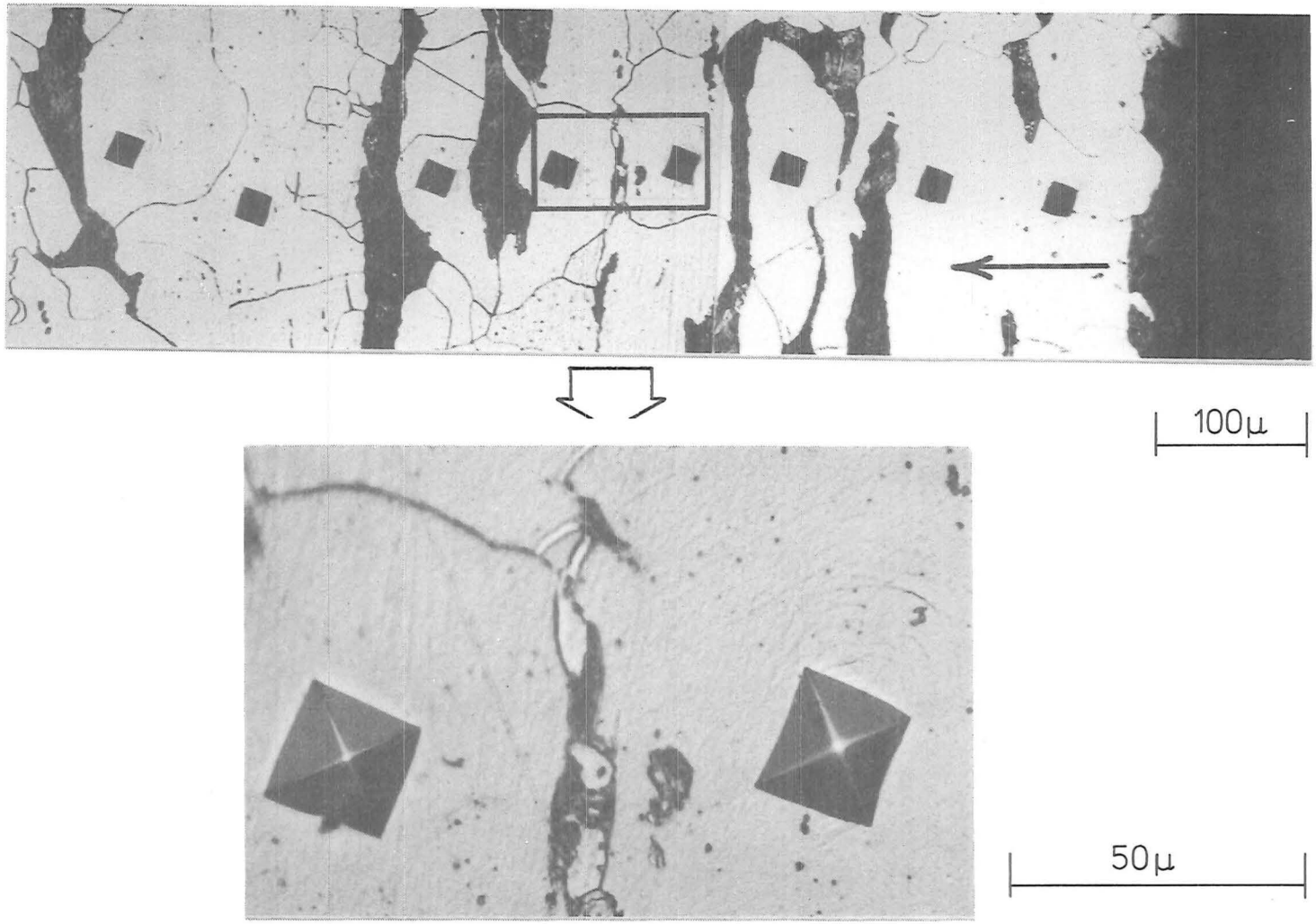

(⟶ direction of microhardness survey)

Fig. 8·23. TYPICAL MICROHARDNESS SURVEY ON ROTATING BENDING SPECIMENS.

very fine grain size of this steel, as it had a mean grain size of $d^{-\frac{1}{2}} = 9.14\ mm^{-\frac{1}{2}}$. The ferrite grains for this set of steel were generally smaller than the size of the microhardness indentations (with the applied load of 50 grams). It was therefore impossible to perform the microhardness survey within the ferrite grains. The effect of grain boundaries could have therefore affected the hardness values obtained for this set of specimens. However, despite the lower correlation coefficient for steel B3 (~0.6954), the correlation for this set of steel was still very good, with a significant level of less than 0.1%. The results of the curve fitting for all nine sets of steels are tabulated in table 8.2.

8.5 MICROSTRUCTURAL CHANGES:

It has been shown many times that cohesion defects appear on the surface of the specimen during cyclic loading, but little work has been done regarding the effect of grain size or types of loading on the microstructural changes on the specimen surfaces.

In this investigation, the effect of grain size on the surface metallographic features of both direct stress and rotating bending specimens were made using optical microscopy. Standard rotating bending and direct stress fatigue specimens were used, see figs.7.11 and 7.12, but polishing was continued for two additional steps using 7 micron and finally 1 micron diamond polishing paste. One set of the specimens (both direct stress and rotating bending) was etched in a solution of 2% nitric acid in alcohol prior to fatigue cycling, while the other set of specimens was fatigued without etching. The tests were interrupted at various intervals and the specimen surfaces

TABLE 8.2

Steel	Grain Size $d^{-\frac{1}{2}}$	Fatigue Limit		σ_{app}	N	$y = ax^b$				$R_m = \sigma_{RB}/\sigma_{DS}$	$r_m = h_m/r_1$
		σ_{RS}	σ_{DS}			a	b	r	s		
	$mm^{-\frac{1}{2}}$	MN/M^2	MN/M^2	MN/M^2	$\times 10^6$				%		5VHN
A 1	4.72	222	176	220	50	96.54	-.0935	.9199	<.1	1.26	.301
A 2	5.07	225	178	220	50	84.98	-.1044	.9187	<.1	1.27	.299
A 3	5.60	228	177	224	50	96.80	-.1085	.8830	<.1	1.29	.324
A 4	6.77	232	179	231	50	107.26	-.0748	.8847	<.1	1.30	.279
A 5	8.09	237	184	239	50	108.60	-.0443	.8680	<.1	1.28	.257
B 1	3.72	214	164	216	50	93.31	-.1148	.8947	<.1	1.32	.329
B 2	4.65	214	165	212	50	85.34	-.1045	.8776	<.1	1.30	.302
B 3	9.14	243	183	240	50	119.25	-.0438	.6954	<.1	1.33	.202
C	8.85	295	235	280	50	102.34	-.1315	.9213	<.1	-	-

r = correlation coefficient

s = significant level

Note:- Assuming $\sigma_{app} \simeq \sigma_{RB}$

$\sigma_{DS} \simeq \sigma_e$

examined under an optical microscope.

For direct stress specimens tested without etching, the fatigue limits were approximately equal to the fatigue limits of the direct stress specimens polished with 600 grade emery paper in section 7.2. Both coarse and fine grained specimens were tested at stresses above and below their respective direct stress fatigue limits. The observations generally confirmed the published results of Oates and Wilson[15]. Both coarse and fine grained specimens showed a wide spread of active slip bands at stresses above their respective direct stress fatigue limits, see fig.8.24 and 8.25. Grain boundaries appeared to be effective barriers in hindering the growth of active slip bands, and much shorter active slip bands were generally observed on the surfaces of the fine grained specimens. The density of active slip bands generally increased markedly during the final stage of the specimen's life, micro-cracks developed from these active slip bands and propagated to failure, see fig.8.26. The proportion of grains showing active slip bands generally increased with the number of stress cycles in a manner very similar to the curve for fatigue damage detected by temperature rise.

At stresses below the direct stress fatigue limit, the surfaces of both coarse and fine grained specimens were generally free of active slip bands, however, isolated patches of ill-defined slip bands were occasionally observed, see fig. 8.24. These observations contradict the observation of Oates and Wilson[15], who reported negligible slip markings on their fine grained steel but widespread active slip bands on their coarse grained steel at stresses just below the fatigue limit.

For direct stress specimens etched with 2% nitric acid in

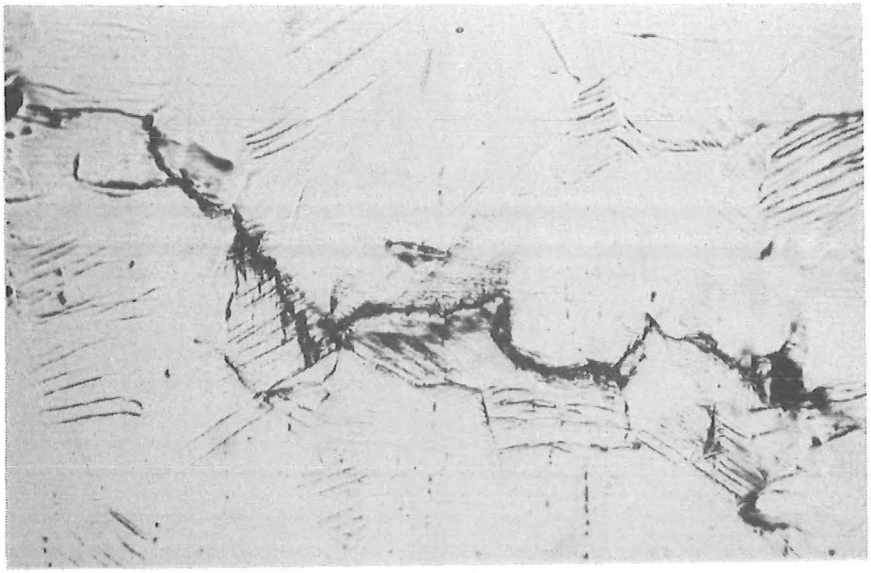

(a) Broken specimen — 100 μ

$d^{-1/2} = 4 \cdot 72 mm^{-1/2}$, $\sigma_{DS} = 176\ MN/m^2$

$\sigma = 180\ MN/m^2$, $N = 2 \cdot 75 \times 10^6$

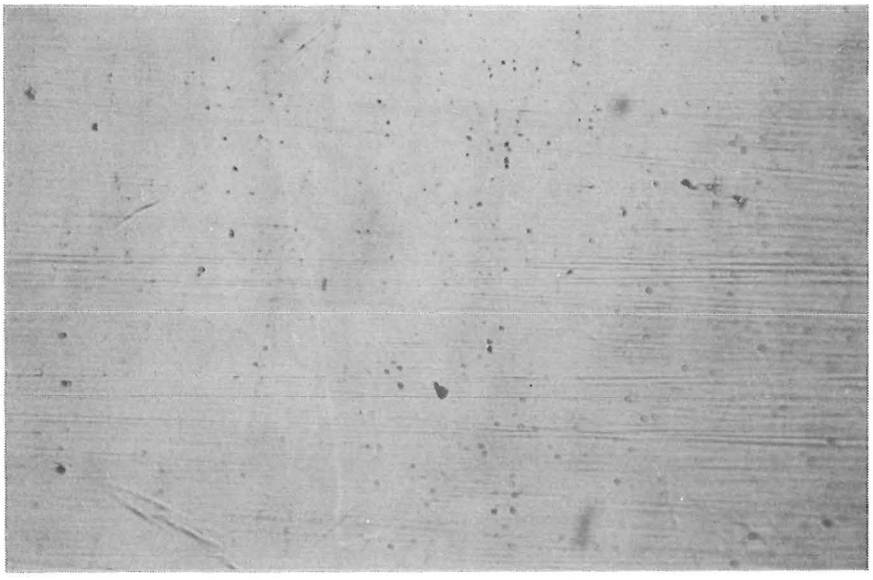

(b) Run-out specimen — 100 μ

$d^{-1/2} = 4 \cdot 72 mm^{-1/2}$ $\sigma_{DS} = 176\ MN/m^2$

$\sigma = 170\ MN/m^2$, $N = 5 \times 10^7$

Fig. 8·24. MICROSTRUCTURAL CHANGES ON COARSE GRAINED, DIRECT STRESS FATIGUED SPECIMENS.

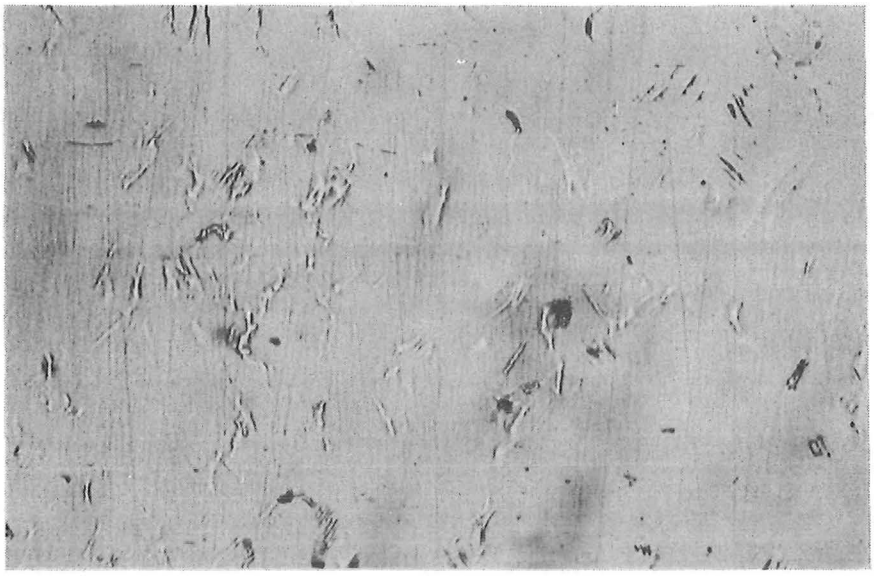

(a) Broken specimen — 100 μ

$d^{-1/2} = 8 \cdot 09 mm^{-1/2}$, $\sigma_{DS} = 184\ MN/m^2$

$\sigma = 190\ MN/m^2$, $N = 2 \times 10^6$

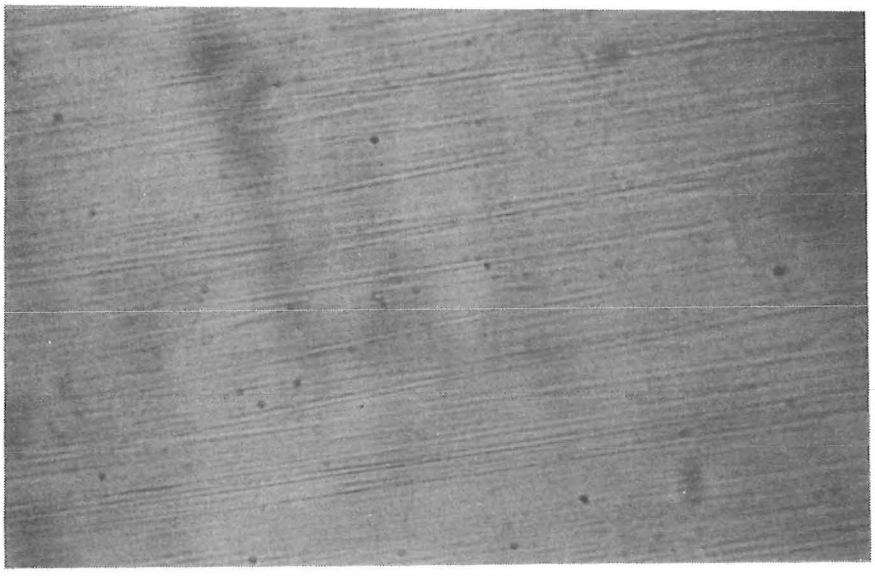

(b) Run-out specimen — 100 μ

$d^{-1/2} = 8 \cdot 09 mm^{-1/2}$, $\sigma_{DS} = 184\ MN/m^2$

$\sigma = 175\ MN/m^2$, $N = 5 \times 10^7$

Fig. 8·25. MICROSTRUCTURAL CHANGES ON FINE GRAINED, DIRECT STRESS FATIGUED SPECIMENS

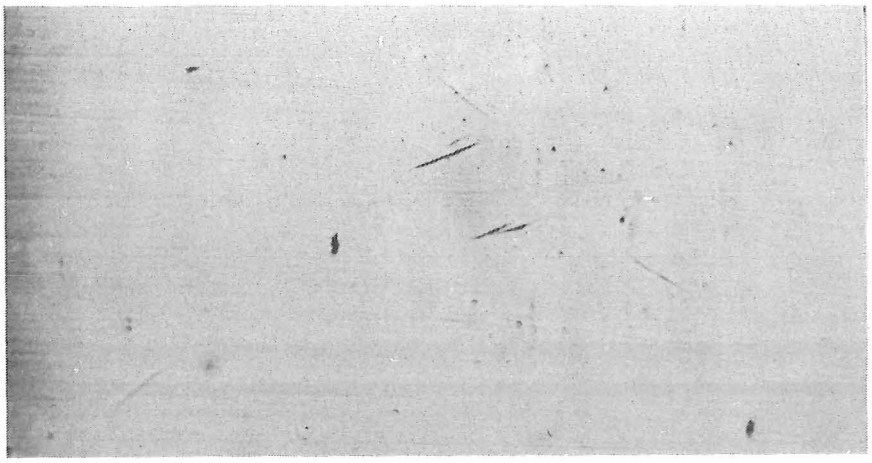

Spec:- A1
σ_{DS} = 176 MN/m^2
σ = 180 MN/m^2
N = 3·5 × 10^5

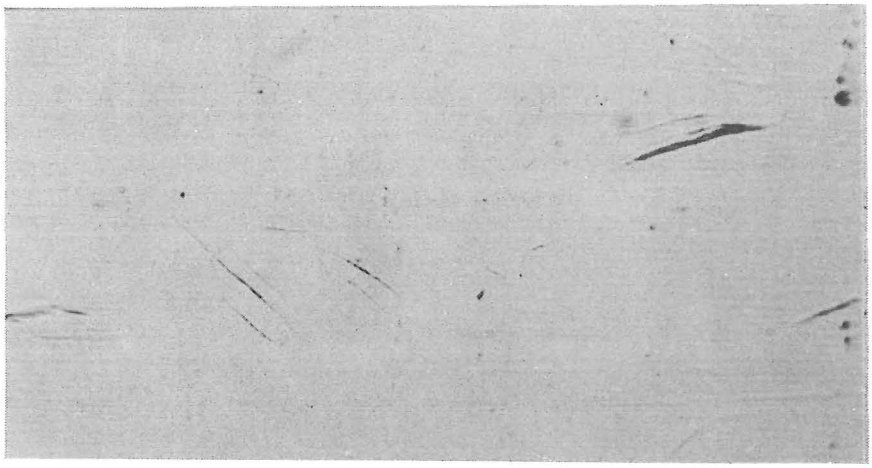

N = 8 × 10^5

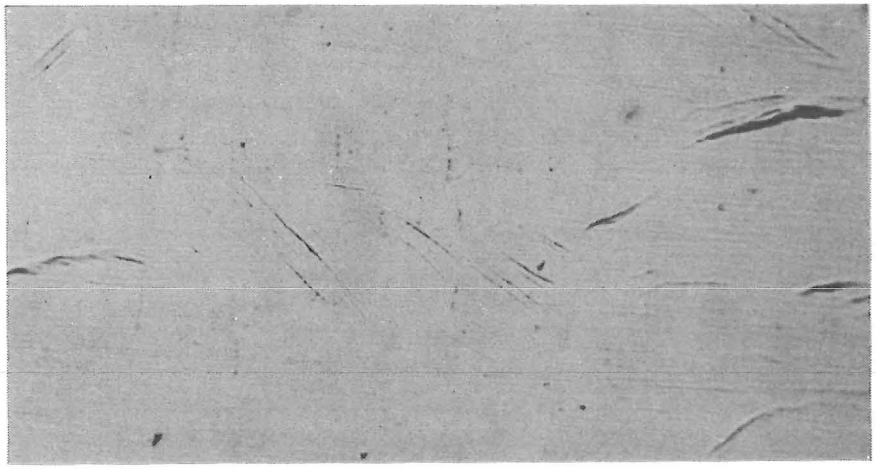

N = 2·5 × 10^6

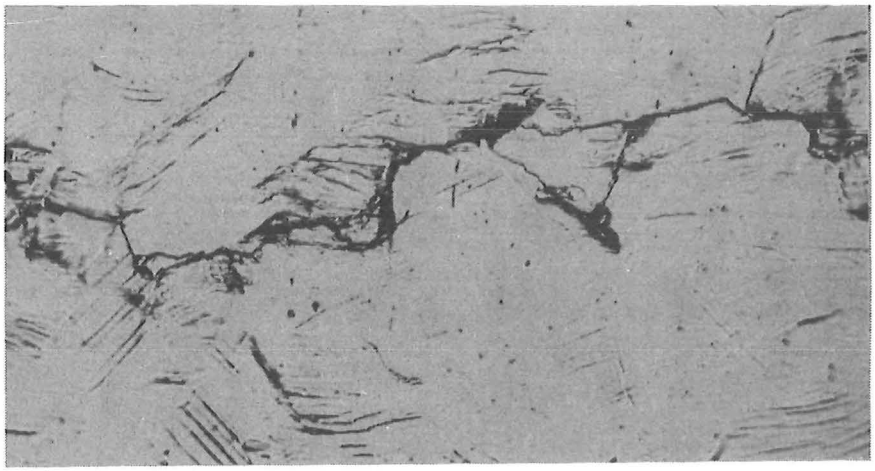

Propagating cracks developed
N = 2·75 × 10^6

Fig. 8·26. PROGRESSIVE FATIGUE DAMAGE ON DIRECT STRESS SPECIMEN

alcohol prior to fatigue loading, the fatigue limits were found to be about 5% lower than their respective as-polished fatigue limits. The surface metallographic features were similar to those observed on the as-polished specimens, that is, stresses above the direct stress fatigue limits resulted in widespread active slip bands in both coarse and fine grained specimens, and at stresses below the fatigue limit, specimen surfaces were generally free of active slip bands.

Under rotating bending loading, as-polished specimens tested at stresses between the direct stress fatigue limit σ_{DS} and rotating bending fatigue limit σ_{RB} were found to develop widespread active slip bands, these are shown in figs.8.27 and 8.28. These active slip bands were observed at lives as early as 10^6 cycles. However, the number of grains showing active slip bands decreased rapidly as the applied stress was lowered towards the direct stress fatigue limit, and at stresses below the direct stress fatigue limit, no active slip markings were observed on both coarse and fine grained rotating bending specimens.

A limited number of the run-out as-polished rotating bending specimens, tested at stresses just below the rotating bending fatigue limits, were etched with 2% nitric acid in alcohol to reveal the persistent slip bands. Large numbers of persistent slip bands were observed on both coarse and fine grained specimens, see fig.8.29. Most of the persistent slip bands were found to be confined within the grains, but quite a few did propagate across the grain boundaries.

Rotating bending specimens etched with 2% nitric acid in alcohol prior to fatigue loading showed similar results, except that the rotating bending fatigue limits were lowered by about 5% as compared to those of the as-polished specimens.

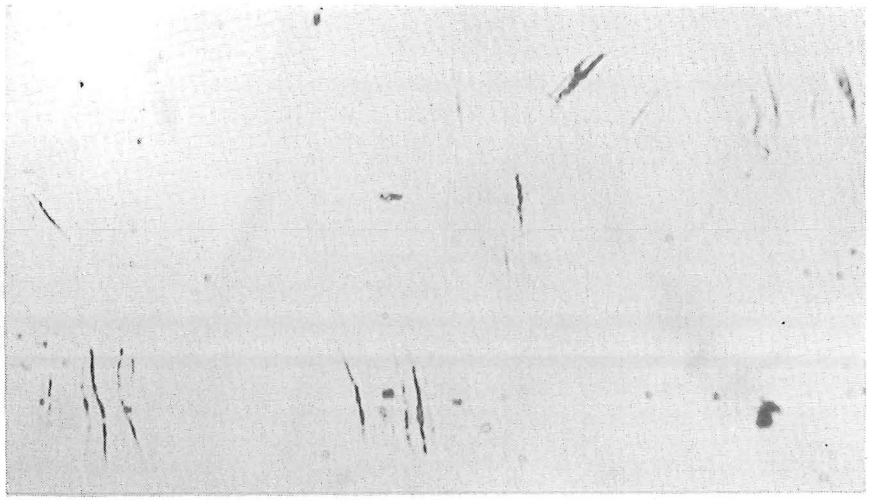

Spec:- B 1.
$d^{-1/2}$ = 3·72mm$^{-1/2}$
σ_{RB} = 214 MN/m^2
σ_{DS} = 164 MN/m^2
σ_{app} = 190 MN/m^2
N = 3 × 10^7
(run-out)

(a) As polished

100 μ

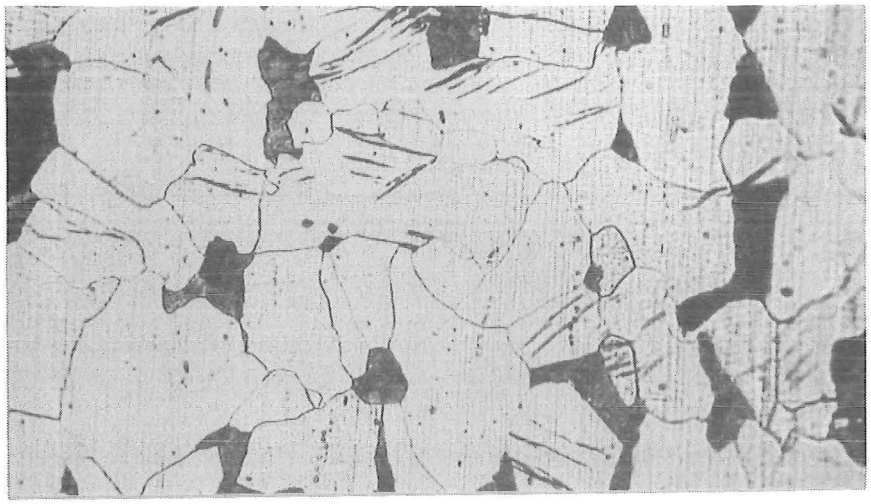

Spec:- A1.
$d^{-1/2}$ = 4·72mm$^{-1/2}$
σ_{RB} = 222 MN/m^2
σ_{DS} = 176 MN/m^2
σ_{app} = 212 MN/m^2
N = 3 × 10^7
(run-out)

(b) Etched before fatigue

100 μ

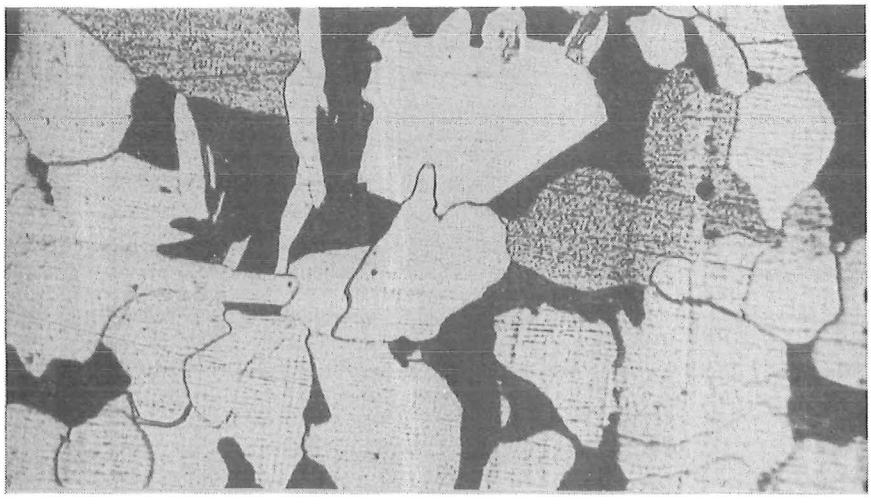

Spec:- A 1
$d^{-1/2}$ = 4·72mm$^{-1/2}$
σ_{RB} = 222 MN/m^2
σ_{DS} = 176 MN/m^2
σ_{app} = 160 MN/m^2
N = 3 × 10^7
(run-out)

(c) Etched before fatigue

100 μ

Fig. 8·27. MICROSTRUCTURAL CHANGES ON COARSE GRAINED, ROTATING BENDING FATIGUED SPECIMENS.

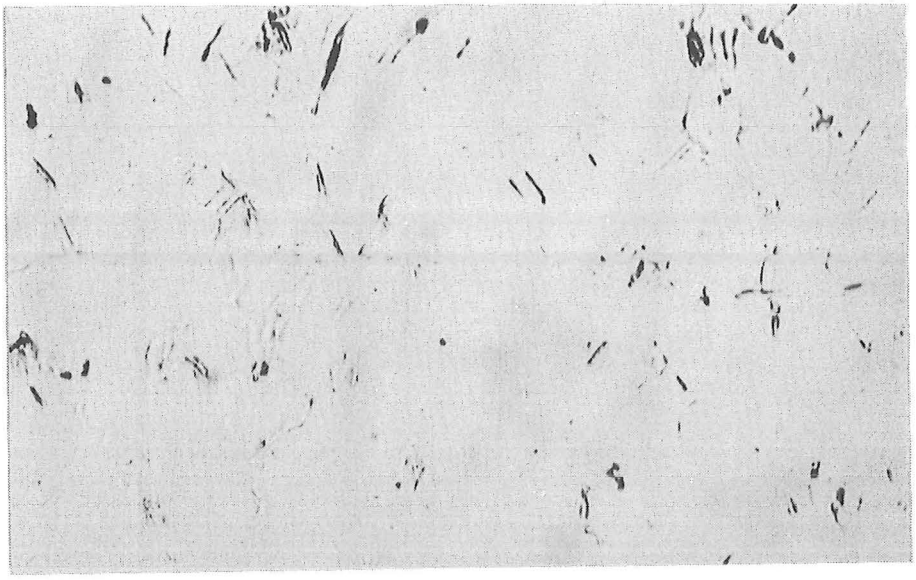

(a) Run-out specimen (3×10^7)
$d^{-1/2} = 9 \cdot 14 mm^{-1/2}$, $\sigma_{RB} = 243$ MN/m^2
$\sigma_{DS} = 183$ MN/m^2, $\sigma_{app} = 230$ MN/m^2

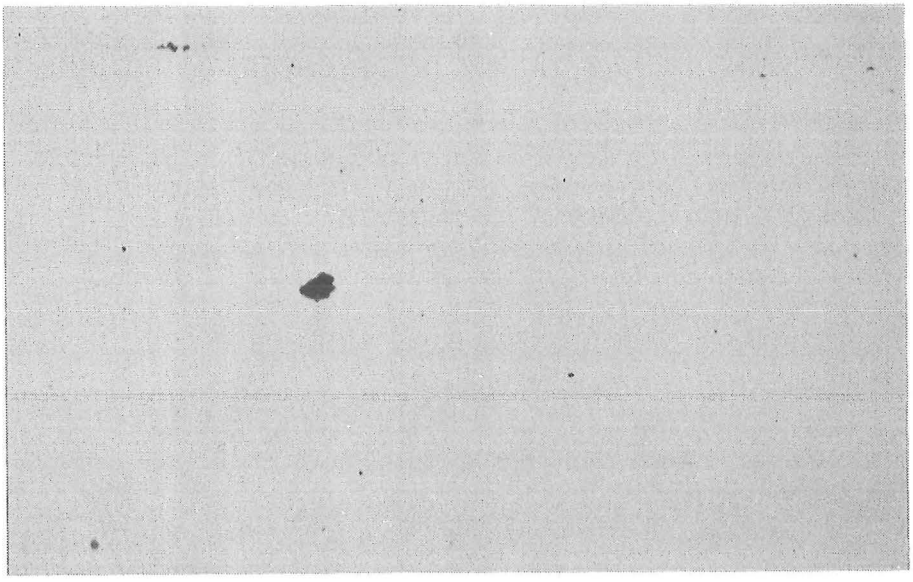

(b) Run-out specimen (3×10^7)
$d^{-1/2} = 9 \cdot 14 mm^{-1/2}$, $\sigma_{RB} = 243$ MN/m^2
$\sigma_{DS} = 183$ MN/m^2, $\sigma_{app} = 180$ MN/m^2

Fig. 8·28 MICROSTRUCTURAL CHANGES ON FINE GRAINED, ROTATING BENDING FATIGUED SPECIMENS.

(a) 100 μ

PERSISTENT SLIP BANDS ON
COARSE GRAINED SPECIMEN

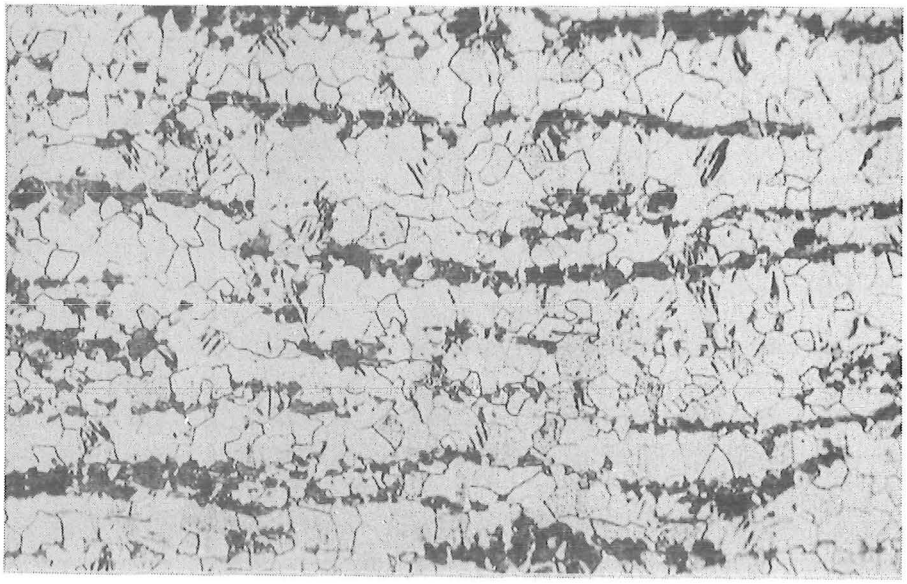

(b) 100 μ

PERSISTENT SLIP BANDS ON
FINE GRAINED SPECIMEN

Fig. 8·29 PERSISTENT SLIP BANDS
REVEALED AFTER ETCHING

The above observations show that, for both coarse and fine grained specimens, widespread fatigue damage in the form of active slip bands occurs on the specimen surfaces prior to fatigue failure in both direct stress and rotating bending loadings. But under direct stress loading, stresses which are sufficient to initiate widespread active slip bands are also sufficient to initiate micro-cracks and propagate these cracks to failure. Whereas under rotating bending loading, stresses just below rotating bending fatigue limit are sufficient to develop the wide spread of active slip bands, but are not sufficient to initiate micro-cracks and cause fatigue failures. Stresses above rotating bending fatigue limits are required to develop the active slip bands into cracks and propagate these cracks to failure.

8.6 EFFECT OF DIRECT STRESS CYCLING ON THE TENSILE PROPERTIES:

As discussed in section 4.3, when low carbon steels are subjected to cyclic stressing, the discontinuous yield point phenomenon can be modified and sometimes completely removed [19,90,91,92,93]. Most researchers[90,93] suggested that cyclic stresses above the direct stress fatigue limit of the material are necessary to accumulate sufficient plastic strain to modify the sharp yield drop and the Luders strain. But the etching results on the special high nitrogen low carbon steel and the microhardness tests in section 8.3 and 8.4 respectively suggested that plastic deformation can take place at stresses equal to or just below the direct stress fatigue limit of the material.

In order to examine this discrepancy further, a limited number of direct stress fatigue specimens from steels A1, A5, B1, B3 and C with a 30 mm parallel gauge length, see fig.8.30,

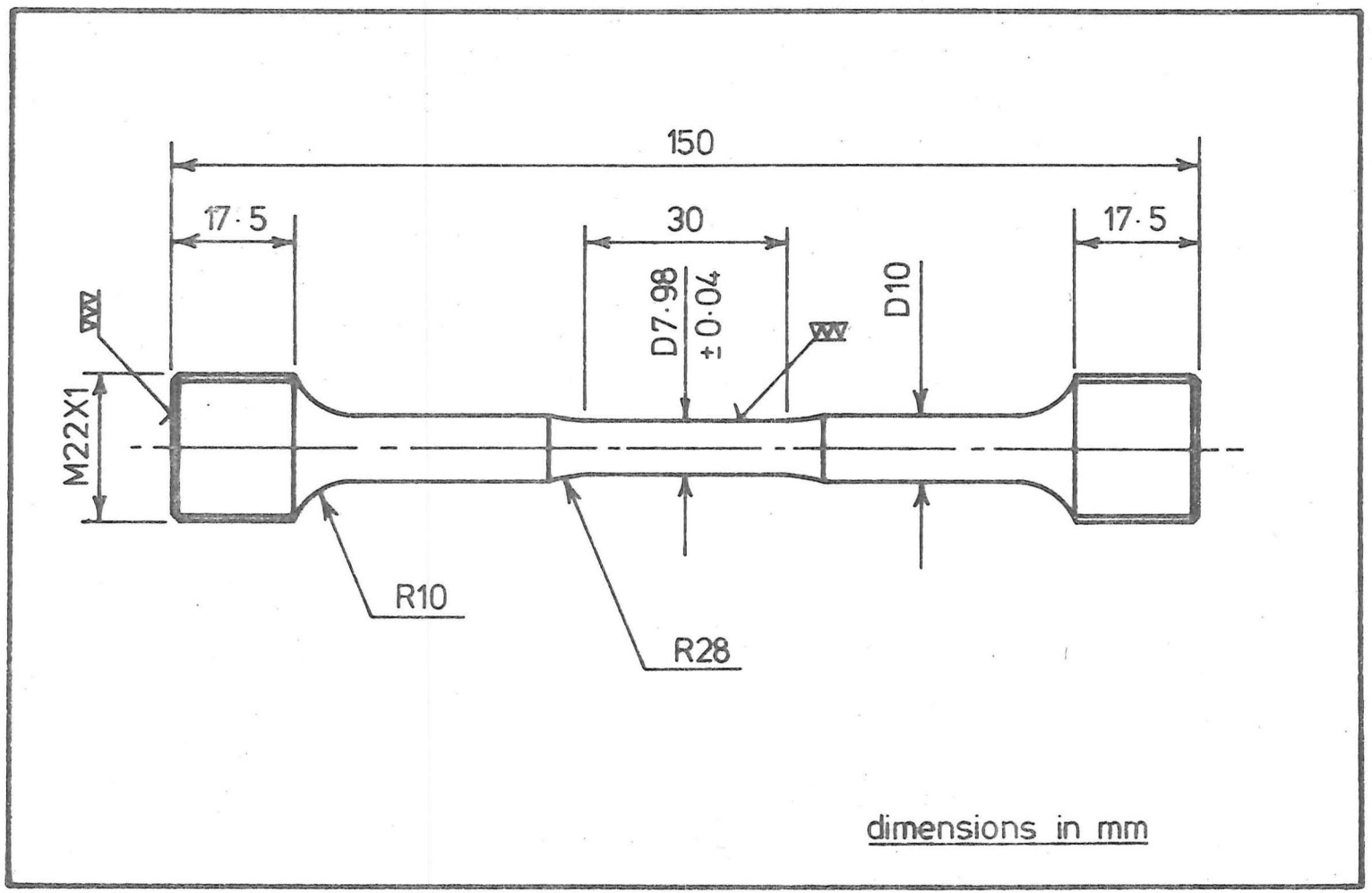

Fig. 8·30 DIRECT STRESS SPECIMEN FOR MONITORING YIELDING PHENOMENON AFTER FATIGUE CYCLING.

were used to examine the effect of fatigue cycling at stresses just below their respective direct stress fatigue limits on their static tensile flow curves. Specimens A1 and B1 were cycled to 1.5×10^7 cycles, but for specimens A5, B3 and C, the long gauge length resulted in very high damping and over-heating occurred before 10^7 cycles, these specimens were stopped at 2.3×10^5, 3.7×10^5 and 3.7×10^6 cycles respectively. After cyclic stressing, the specimens were transferred immediately to the Instron tensile machine, and the tensile flow curves of these specimens were recorded with a 25 mm gauge length extensometer. These tensile flow curves after direct stress cycling are shown in figs.8.31 and 8.32. Unfortunately, the flow curve for steel B3 was not recorded because of over-loading while aligning the specimen in the tensile machine. True stress-true strain data was also recorded by monitoring the reduction in the specimen's diameter. The results for steels A1, A5, B1, B3 and C are shown in figs.8.33, 8.34 and 8.35, together with the true stress-true strain data obtained before cyclic loading. The tensile properties of these specimens before and after cyclic stressing are also tabulated in table 8.3.

From figs.8.31 and 8.32, it can be seen that the sharp yield drops and the Luders strains were completely removed from these specimens after cyclic stressing at stresses just below their respective fatigue limits, and in steel A5, stress cycles as little as 2.3×10^5 cycles were sufficient to eliminate the discontinuous yield point phenomenon. In section 8.2, the temperature rise monitoring (fig.8.6) suggested that relocking of free dislocations during the course of cyclic stressing or dynamic strain ageing can occur in high nitrogen steels. However, the tensile flow curves in figs.8.31 and 8.32 show no

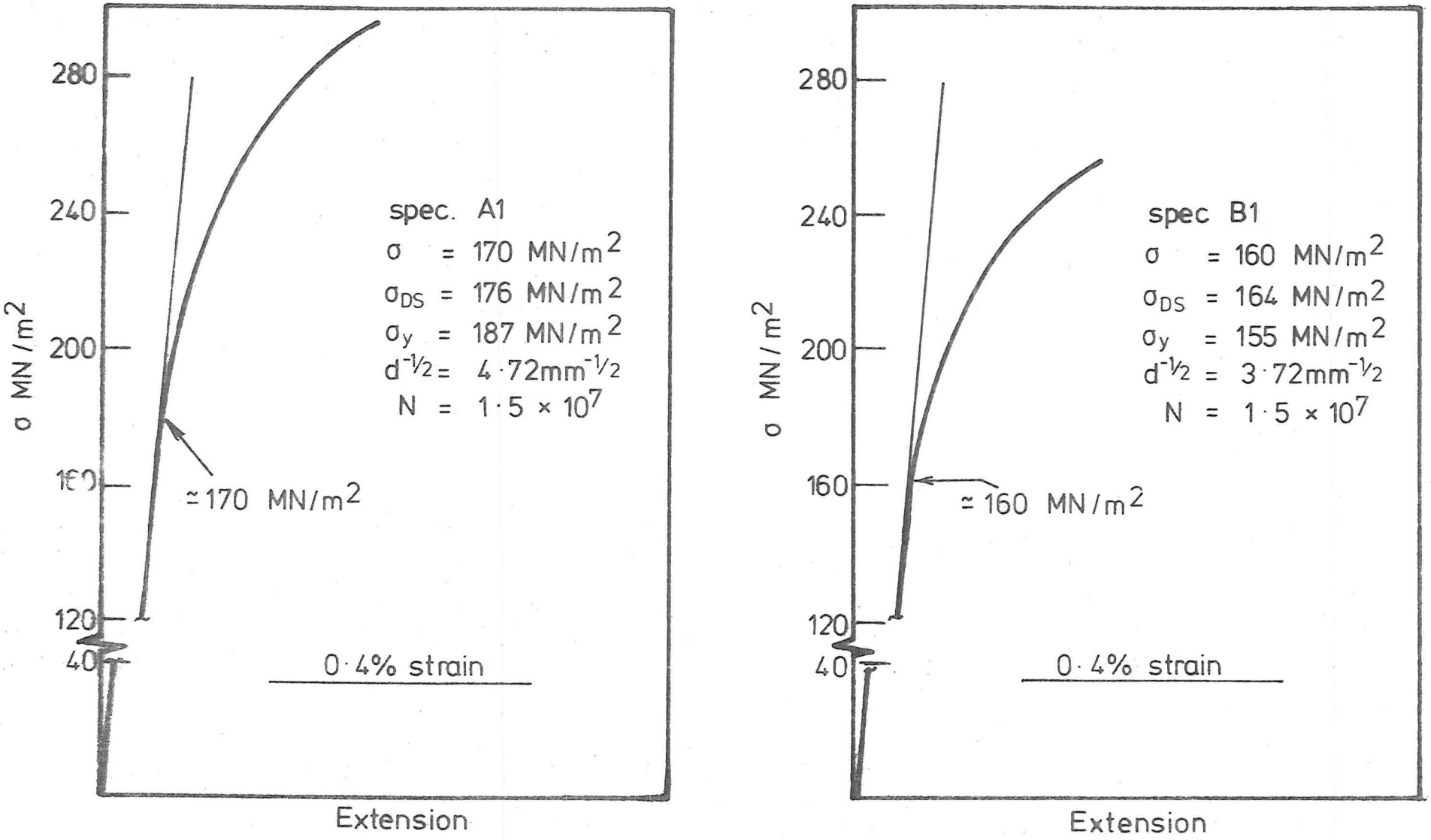

Fig. 8·31. EFFECT OF FATIGUE CYCLING ON THE TENSILE FLOW CURVE.

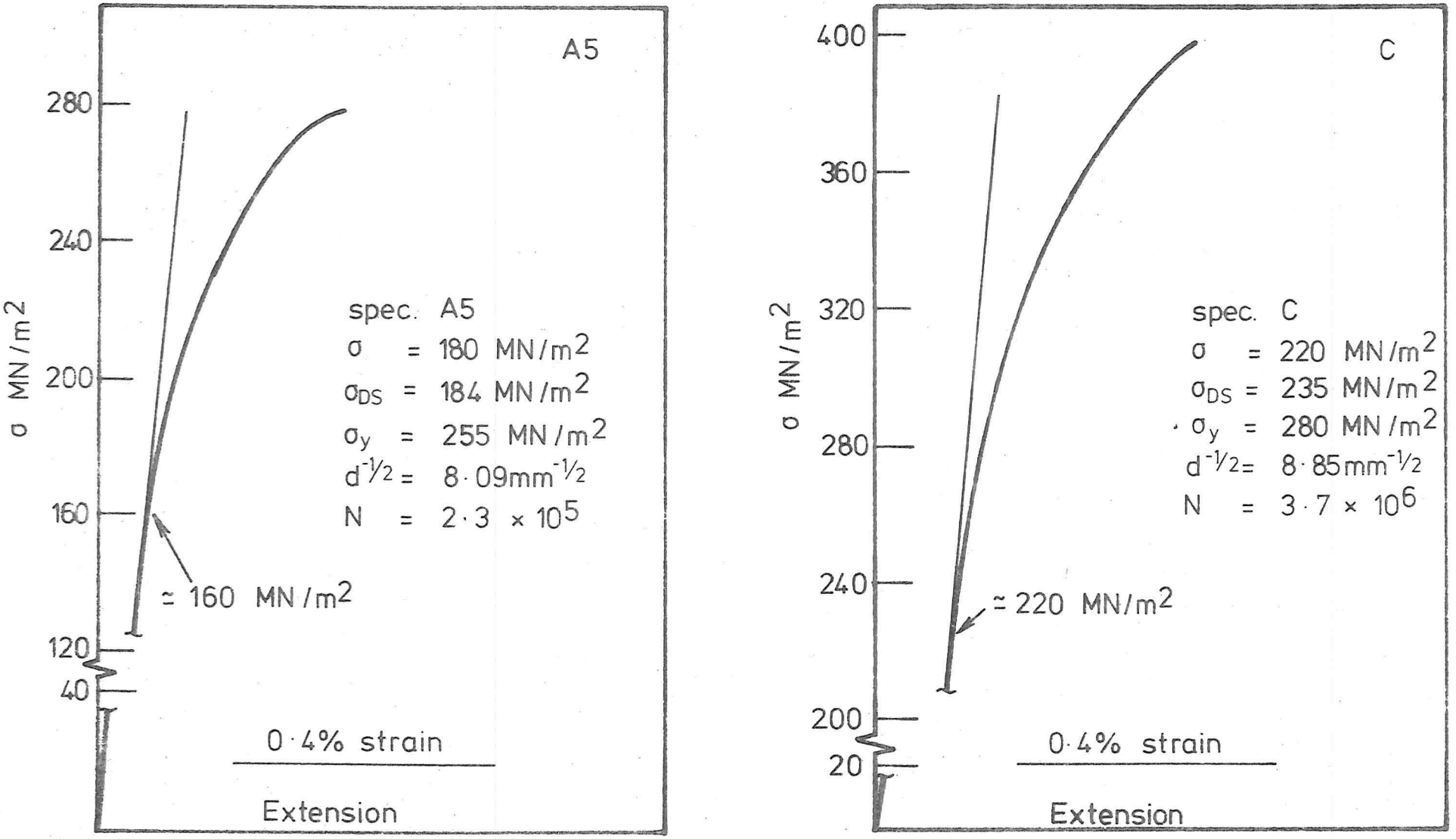

Fig. 8·32. EFFECT OF CYCLIC STRESSING ON THE TENSILE FLOW CURVE.

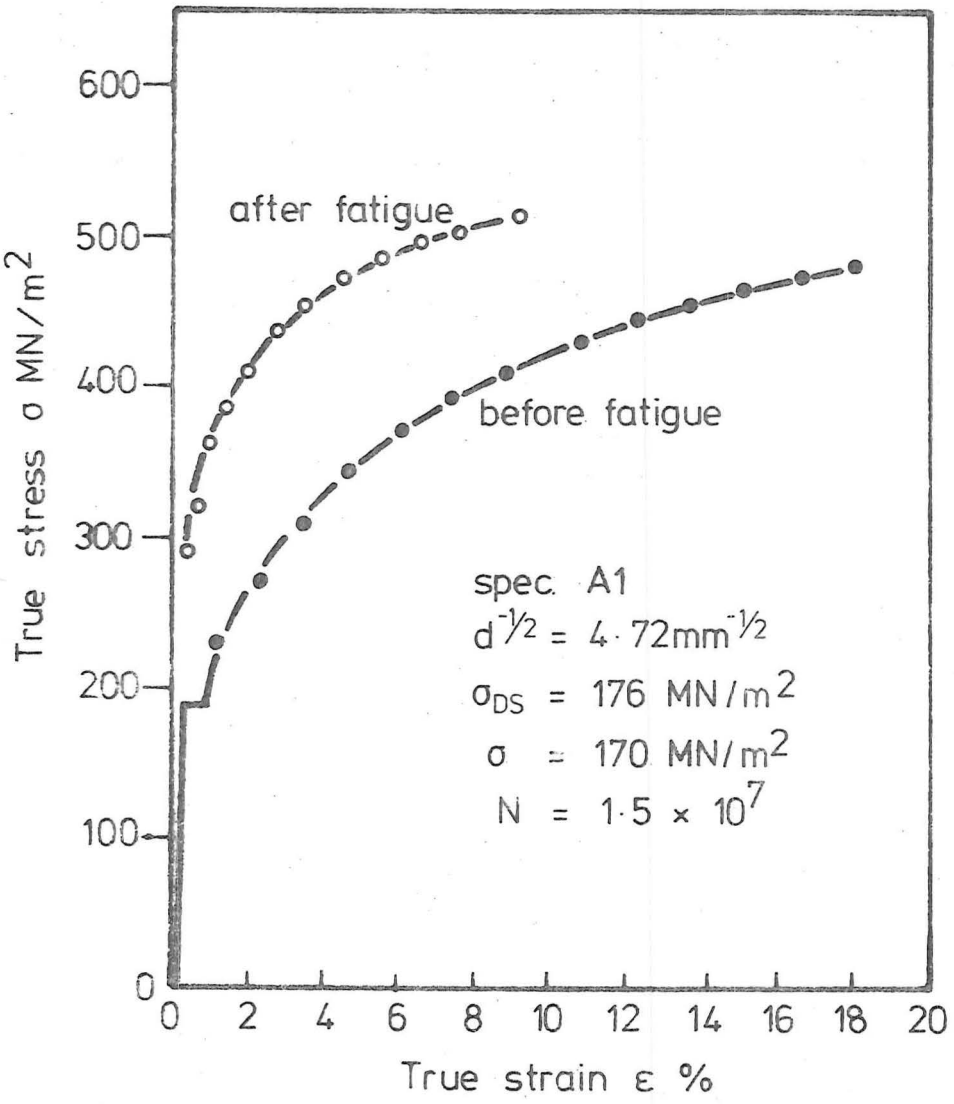

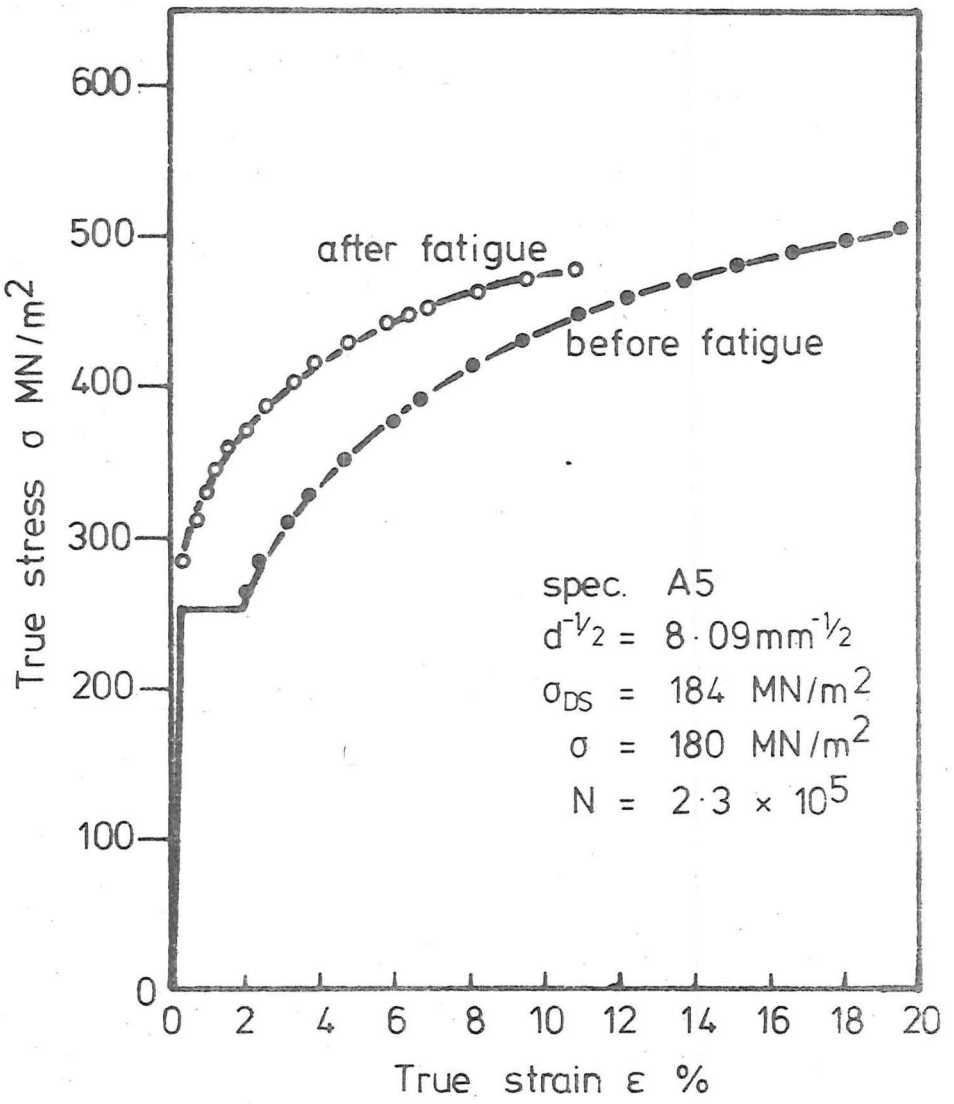

Fig. 8·33. EFFECT OF CYCLIC PRESTRESS ON THE TRUE STRESS – TRUE STRAIN RELATIONSHIP.

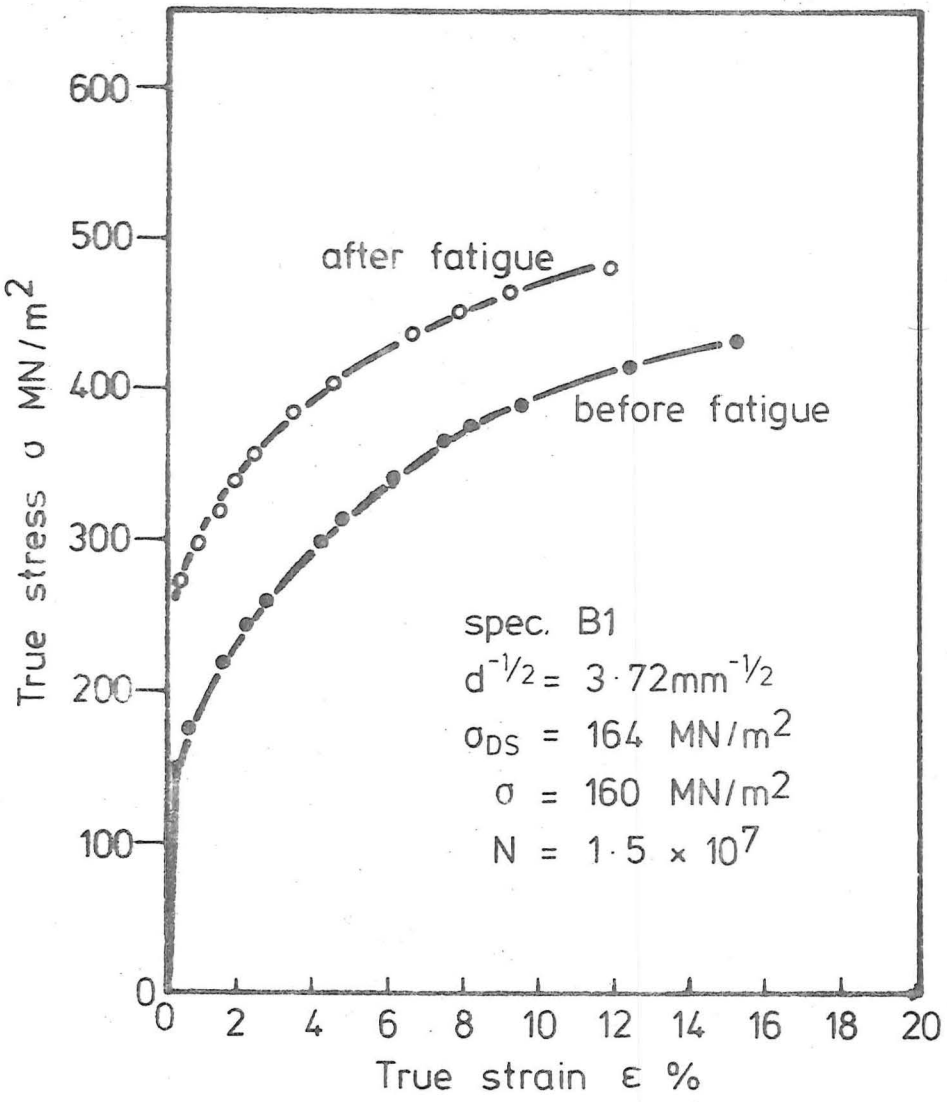

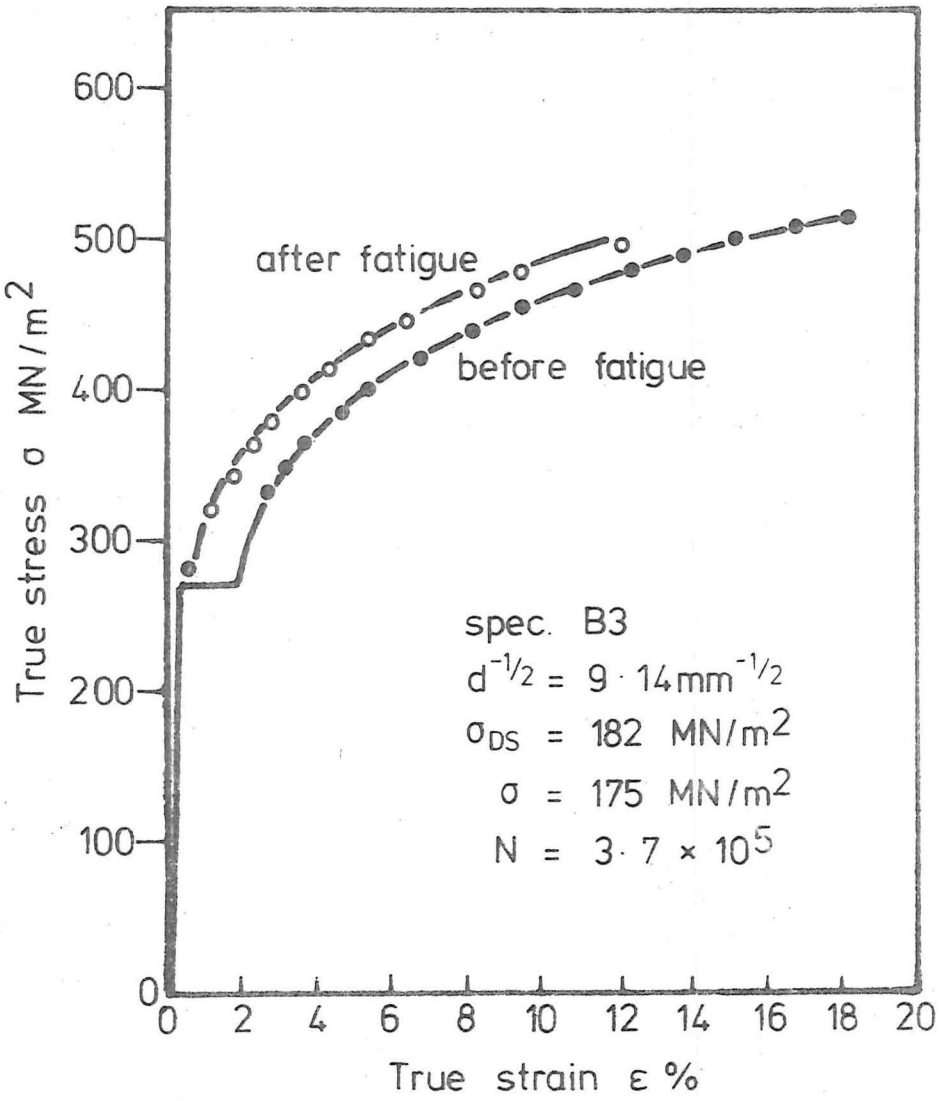

Fig. 8·34. EFFECT OF CYCLIC PRESTRESS ON THE TRUE STRESS-TRUE STRAIN RELATIONSHIP.

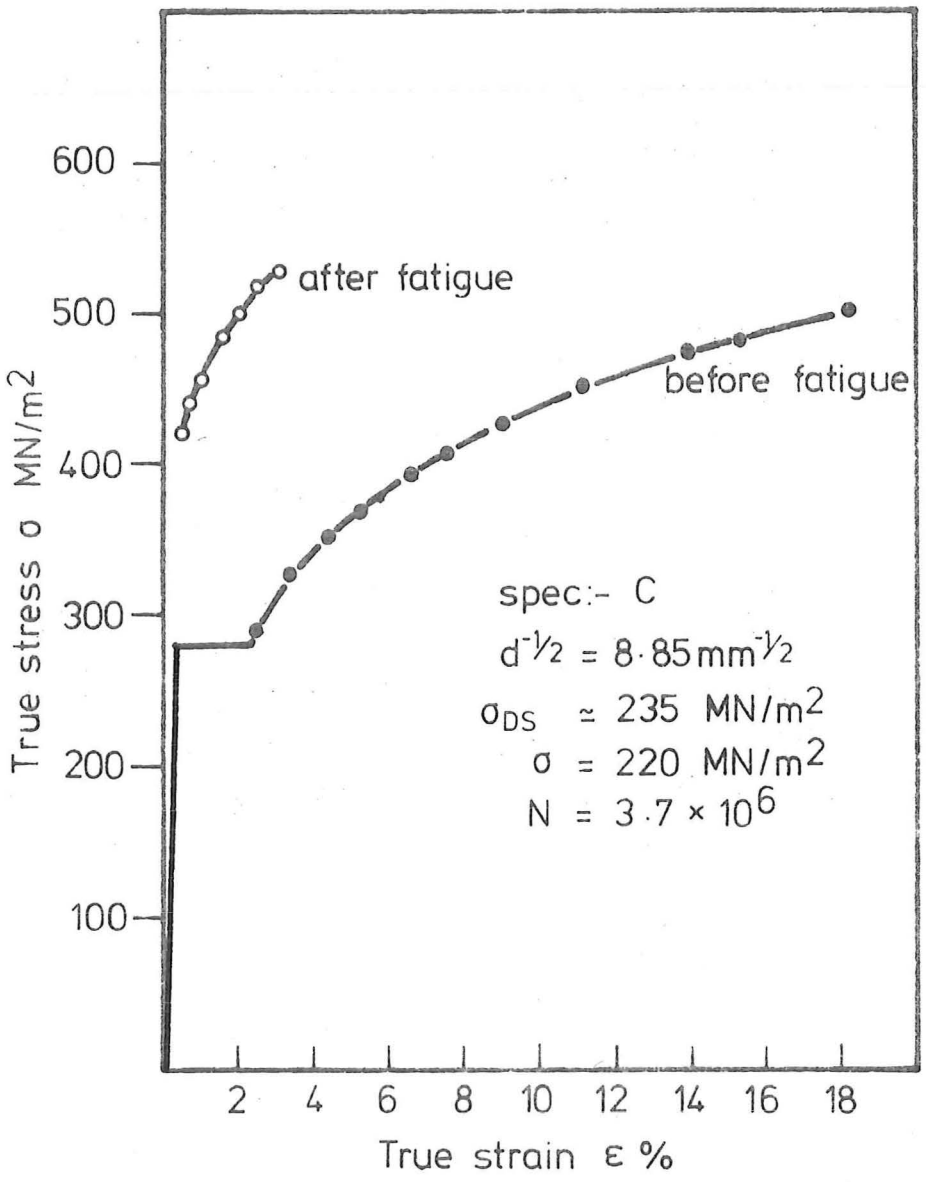

Fig. 8·35. EFFECT OF CYCLIC PRESTRESS ON THE TRUE STRESS-TRUE STRAIN RELATIONSHIP.

TABLE 8.3

Material	Lower Yield Stress σ_y	D-S Fatigue Limit σ_{DS}	Cyclic Stress σ	Stress Cycle N	Before Cycling		After Cycling		
					K	n	K*	n*	σ_y^*
	MN/M^2	MN/M^2	MN/M^2	$\times 10^6$	MN/M^2		MN/M^2		MN/M^2
A 1	187	176	170	15.00	690	0.2210	800	0.1752	~170
A 5	255	184	180	0.23	720	0.2050	730	0.1667	~160
B 1	155	164	160	15.00	670	0.2242	790	0.2212	~160
B 3	271	183	175	0.37	730	0.2015	780	0.2067	-
C	280	~235	220	3.70	710	0.2048	870	0.1412	~220

Note:- σ_y^* ≡ limit of proportionality

return of the sharp yield drop, which is the characteristic of stage I ageing, even in the high nitrogen low carbon steels. This can therefore be taken to suggest that relocking of the free dislocations by active nitrogen during the course of normal fatigue testing (about 1 day for 1.5×10^7 cycles) is not sufficient to result in complete Cottrell atmosphere formation or stage I ageing. This further confirms the finding of Erasmus[12], who reported that dynamic strain ageing had little, if not negligible, contribution towards the formation of the fatigue limits in low carbon steels.

As can be seen in table 8.3, except for specimen A5, the limit of proportionality after cyclic stressing was approximately equal to the applied cyclic stress. These results are in agreement with the finding of Luther and Williams[93]. The discrepancy in specimen A5 was probably due to insufficient stress cycles being applied, and the corresponding steady state at the applied stress had not been reached.

The log true stress-log true strain data for the above five specimens are also plotted in figs.8.36, 8.37, 8.38, 8.39 and 8.40. These results suggest that there was a certain amount of strain hardening after cyclic stressing, especially in the coarse grained steels (A1 and B1), as the log true stress-log true strain curves for all five specimens were shifted to a higher value after cyclic stressing. Unfortunately, the fine grained specimens for both high nitrogen (steel A5) and low nitrogen (steel B3) were not cycled beyond 10^7 cycles, and it is therefore not possible to conclude positively if coarse grained steels do in fact deform more readily than the fine grained steels, as the results of Oates and Wilson[15] seem to suggest.

Figs.8.36-8.40 also show that, for specimens which had been

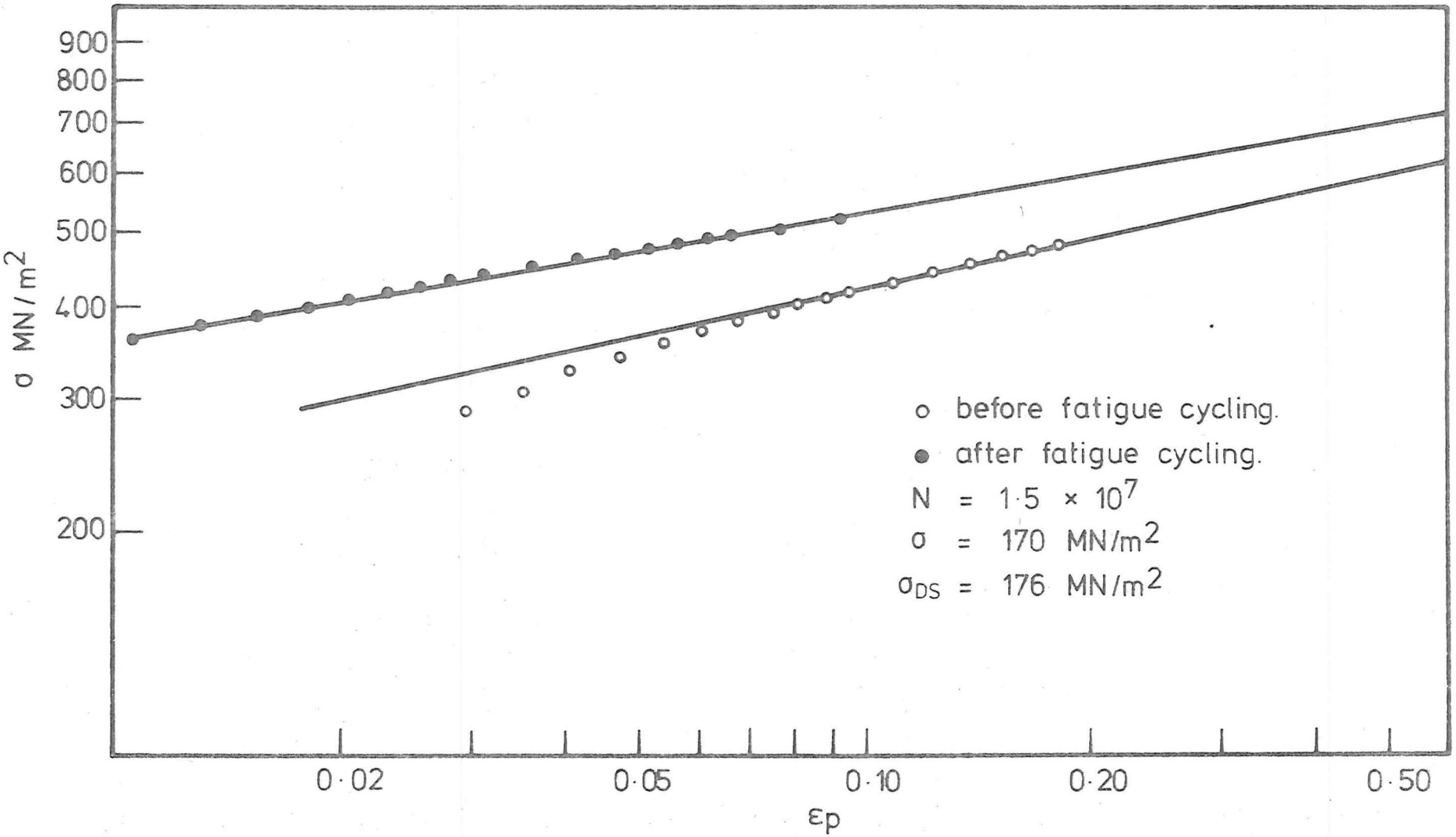

Fig. 8·36. TRUE STRESS-TRUE STRAIN RELATIONSHIP BEFORE AND AFTER FATIGUE CYCLING. (STEEL A1)

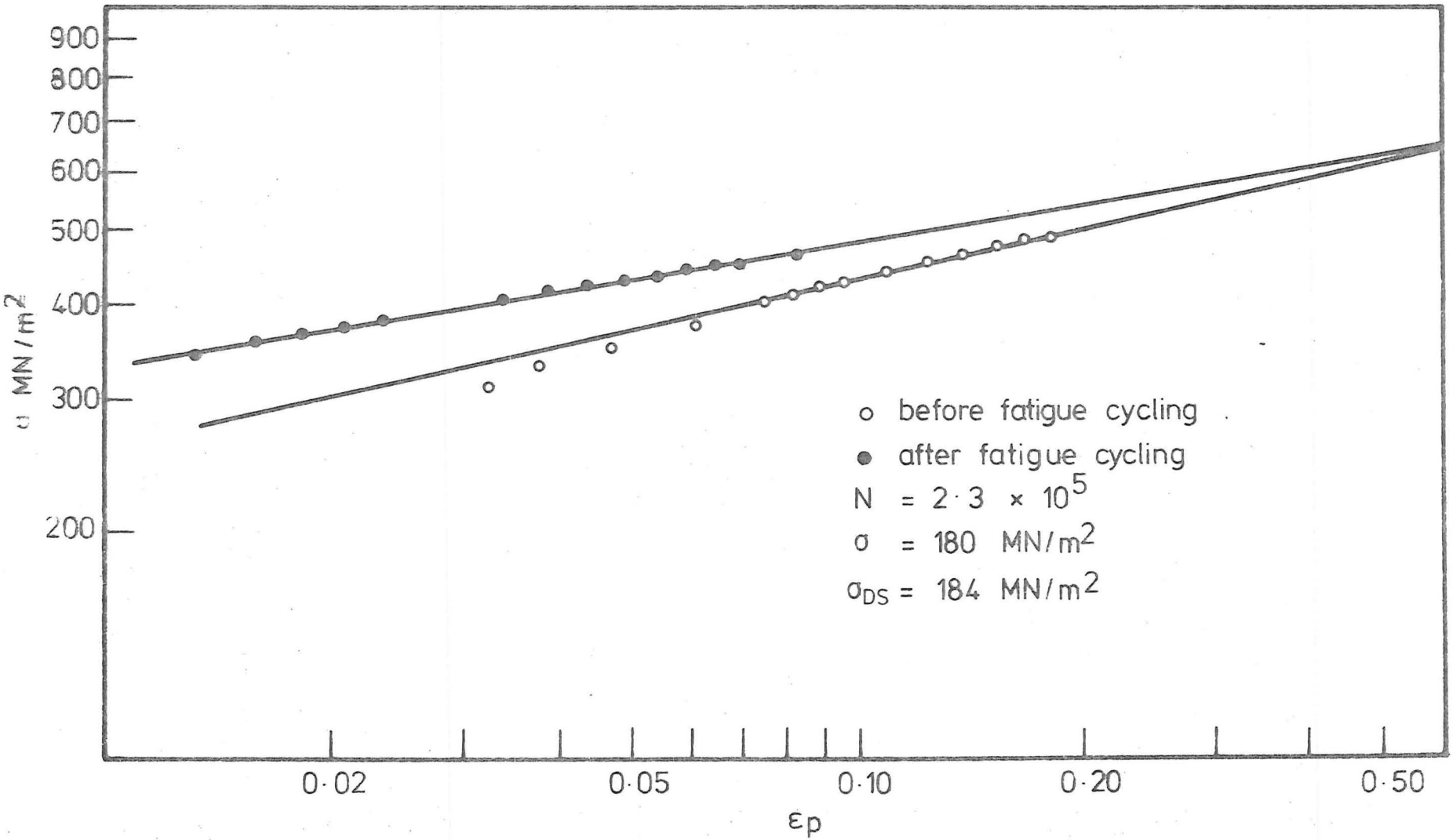

Fig. 8·37. TRUE STRESS - TRUE STRAIN RELATIONSHIP BEFORE AND AFTER FATIGUE CYCLING (STEEL A5)

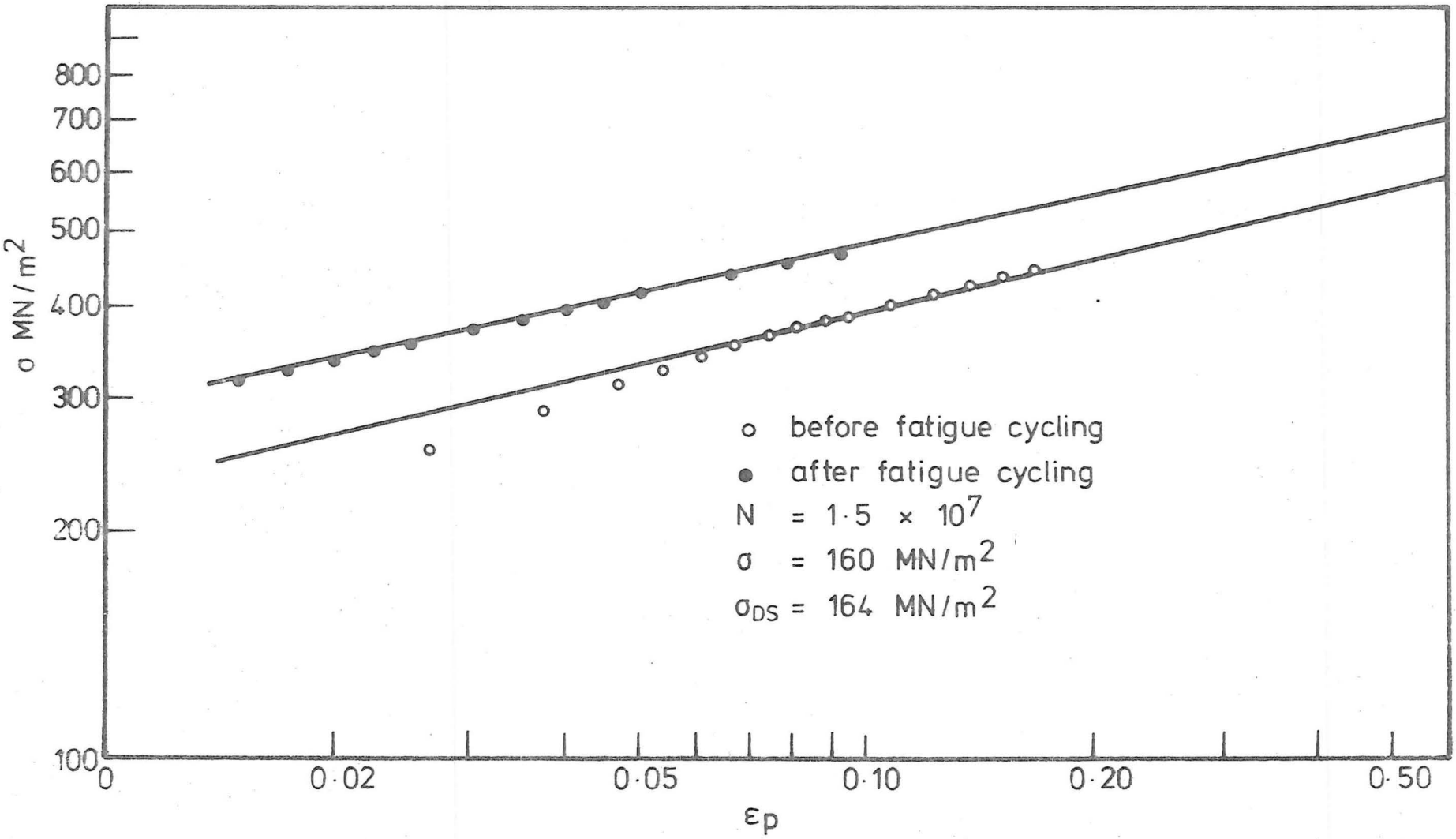

Fig. 8·38. TRUE STRESS–TRUE STRAIN RELATIONSHIP BEFORE AND AFTER FATIGUE CYCLING (STEEL B1)

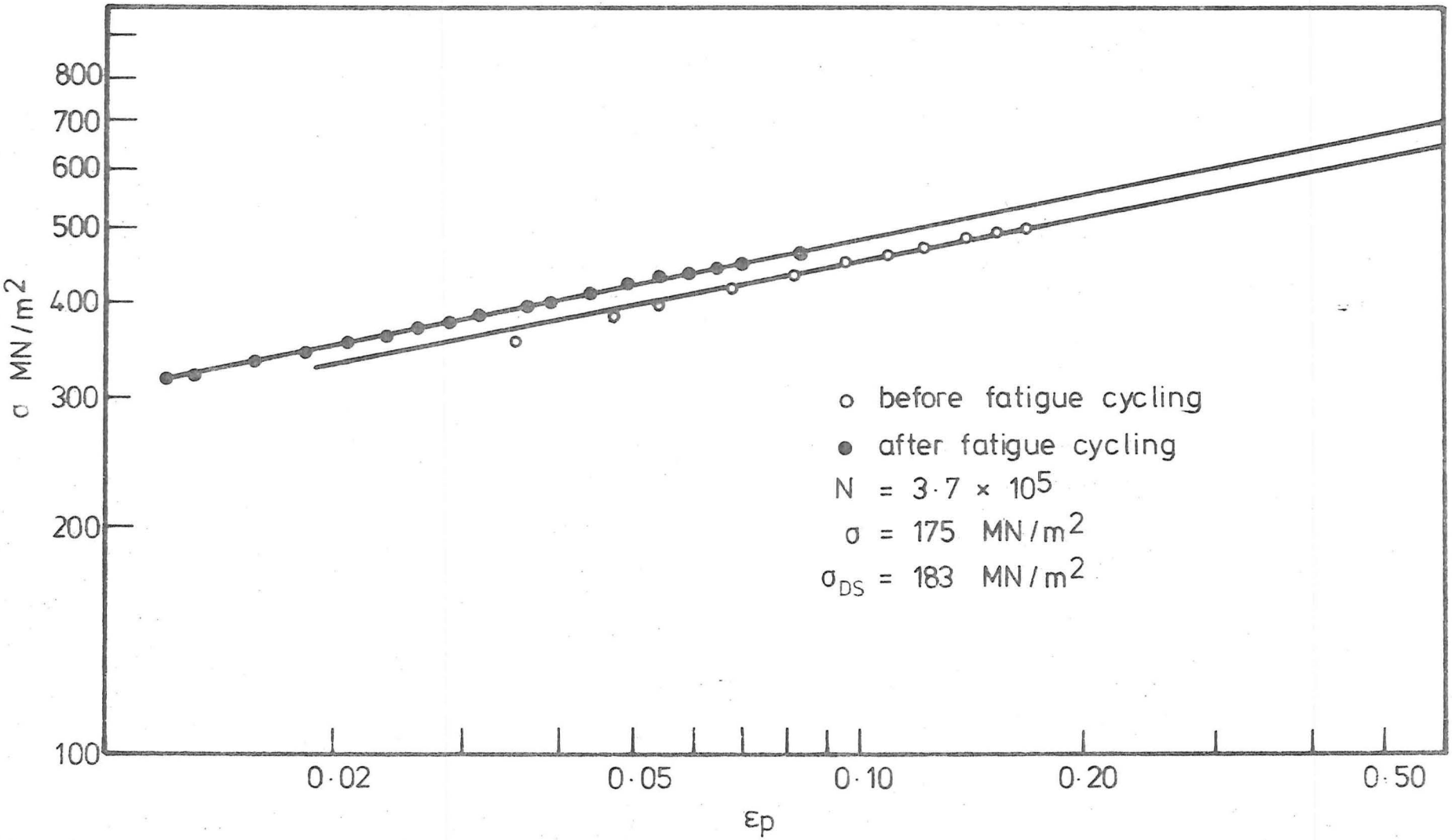

Fig. 8·39. TRUE STRESS-TRUE STRAIN RELATIONSHIP BEFORE AND AFTER FATIGUE CYCLING (STEEL B3)

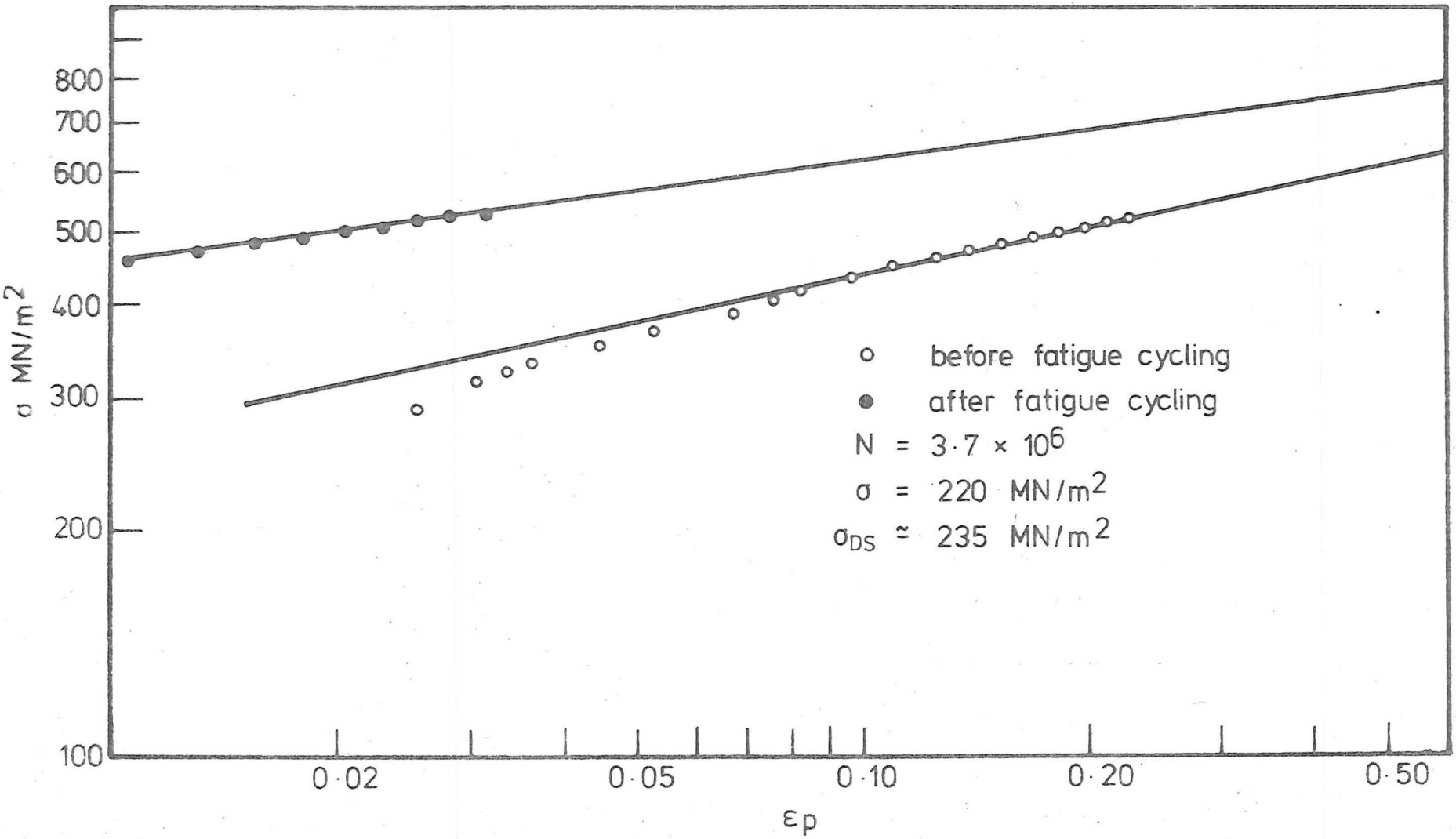

Fig. 8·40 TRUE STRESS-TRUE STRAIN RELATIONSHIP BEFORE AND AFTER FATIGUE CYCLING. (STEEL C)

cyclically prestressed, the log true stress-log true strain relationship remained linear down to very small strains. This is in contrast with the results obtained from specimens tested without cyclic prestress. These results suggest that there is a large transition strain region associated with the Luders strain during the normal tensile tests, and the K and n values (where $\sigma = K \varepsilon^n$) as obtained from the normal log true stress-log true strain plot have to be based on the true stress-true strain data after the transition region. Figs.8.36-8.40 also show that the strain hardening exponent n for steels containing low levels of active nitrogen (steels B1 and B3) was not affected by cyclic stressing to any significant extent, but for steels containing a high level of active nitrogen (steels A1, A5 and C) the n value was decreased after cyclic stressing.

8.7 FRACTOGRAPHIC STUDY OF FATIGUE FRACTURE SURFACES:

During the last decade, electron fractography has become one of the most powerful tools in the study of fatigue fracture mechanisms, especially with the introduction of scanning electron microscopes, which enable the fracture surfaces to be studied directly.

Fracture surfaces of both direct stress and rotating bending specimens tested at stresses equal to or just above their respective fatigue limits (that is, the case of high cycle fatigue) were examined using JEOL JSM-35 scanning electron microscope.

On the direct stress specimens, fatigue cracks initiated on the specimen surface and propagated in a "fan-like" manner across the specimen, see figs.8.1 and 8.41a. The crack front remained straight and approximately at right angles to the

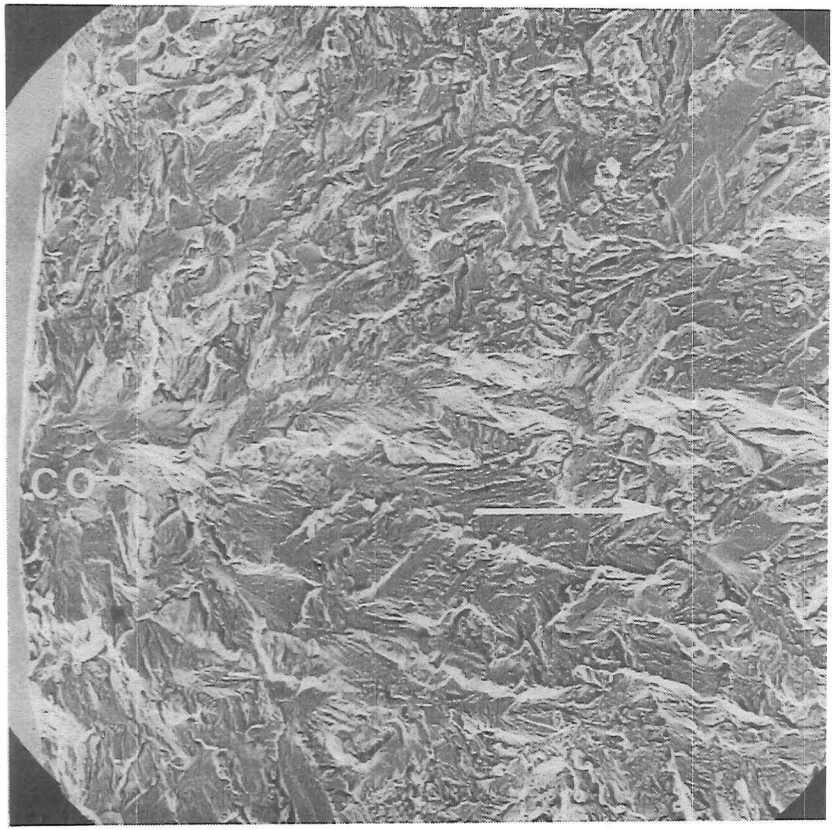

80×

(a) CO = crack origin(s)

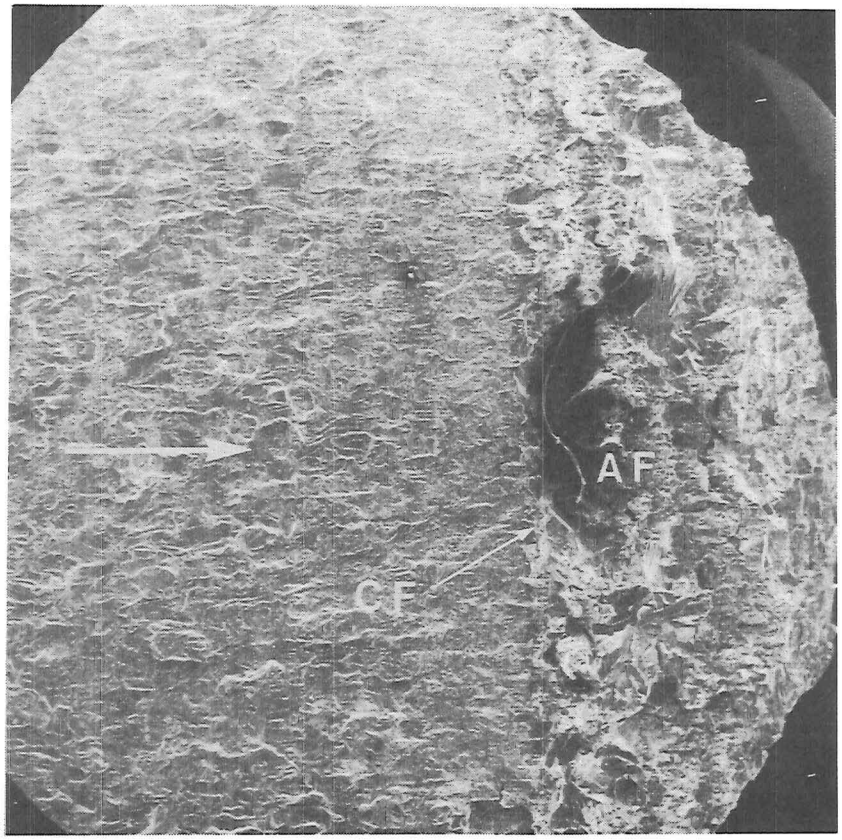

30 ×

(b) CF = crack front
AF = area of final separation

(⟶ general direction of crack propagation)

Fig. 8·41. DIRECT STRESS FATIGUE FRACTURE SURFACE.

line joining the centre of the specimen and the point of crack initiation, see fig.8.41b. The local direction of crack propagation may be deduced from the patterns of the striations formed, and fig.8.42 illustrates the typical patterns of striations on a direct stress fatigue fracture surface.

Unlike the striations formed under high stress (low cycle) fatigue loadings[53], well defined fatigue striations were generally observed on these fracture surfaces fatigued under high cycle loading, see fig.8.42. However, a fair amount of "quasi-striation" was also visible, especially at the early stages of crack propagation (i.e. the area near the crack origin(s)). Secondary "micro-cracks" or "fissures" were commonly observed within the striation regions, see fig.8.43a. Unlike the "macro" appearance in fig.8.1, the striation patterns were not affected by the polycrystalline grain size, and similar striation patterns appeared on both coarse and fine grained specimens.

Tire tracks as reported by Koterazawa et al[46] were not observed on the direct stress fatigue fracture surfaces, instead, random indentations due to hard particles were usually observed, see fig.8.43b. The absence of tire tracks on the direct stress fracture surfaces may be taken as an indication of the absence of secondary forces, or the alignment of the direct stress fatigue machine was good.

At the final stage of crack propagation, elements of cleavage or brittle type of fracture were observed on the direct stress fracture surfaces, see fig.8.44a. This was probably due to the high strain rate and high ratio of normal to shear stress at the crack front at the final stage of crack propagation.

For the case of rotating bending fatigue loading, the

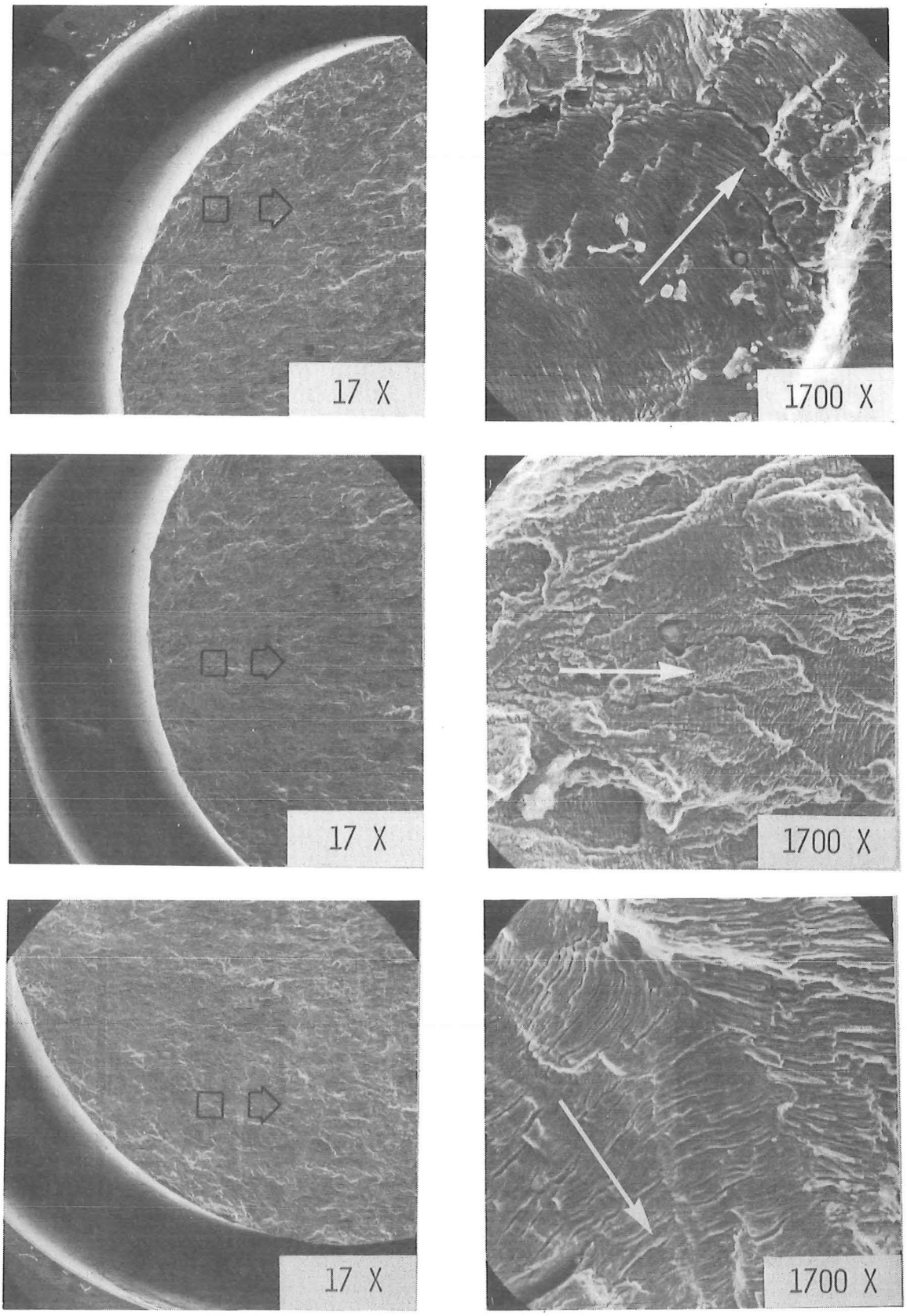

(⟶ direction of crack propagation)

Fig. 8·42. DIRECTION OF LOCAL CRACK PROPAGATION ON A DIRECT STRESS FATIGUE FRACTURE SURFACE.

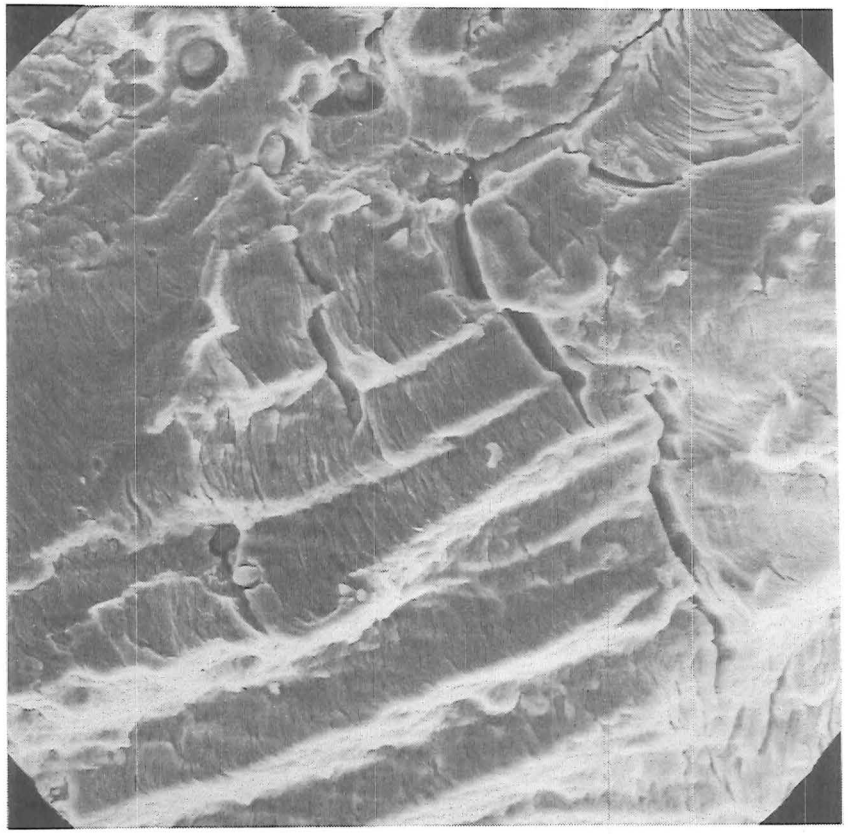

1400×

(a) Striations and 'fissures'

750×

(b) Random indentations

Fig. 8·43. STRIATIONS AND RANDOM INDENTATIONS ON THE DIRECT STRESS FATIGUE FRACTURE SURFACE.

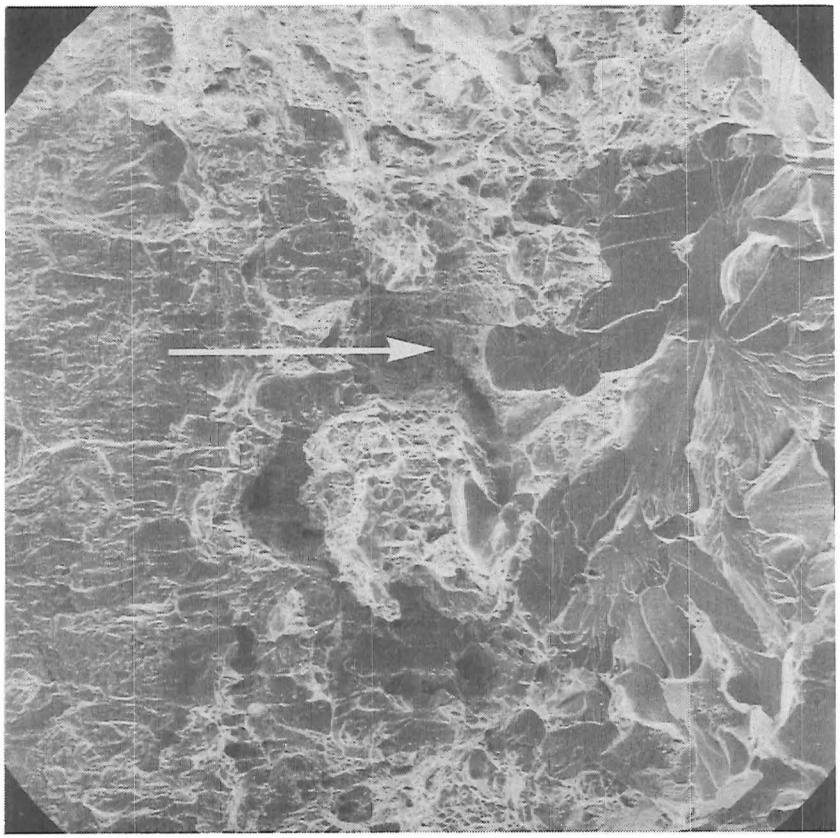

140×

(a) Cleavage fracture on direct stress fracture surface.
(⟶ direction of crack propagation)

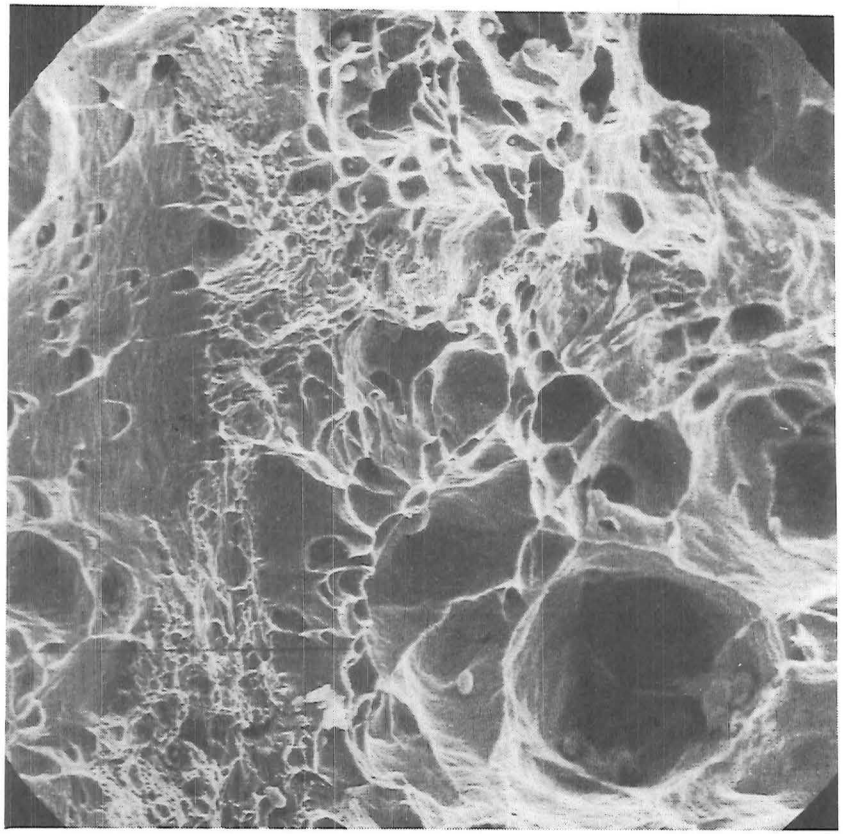

1400×

(b) Microvoid coalescence on rotating bending fracture surface.

Fig. 8·44. AREAS OF FINAL SEPARATION ON (a) DIRECT STRESS, (b) ROTATING BENDING FRACTURE SURFACES.

fracture surface had an inexpressive "crescent" shaped region. This region consisted mainly of rubbed marks indicating a considerable amount of rubbing and pressing between the mating surfaces during the course of fatigue cycling, see fig.8.45. Like the fracture surfaces of the direct stress specimens, fatigue cracks also appeared to initiate at a point on the free surface and propagated across the specimen in a "fan-like" manner. However, because of the amount of rubbing which had taken place between the mating surfaces, most of the evidence of crack propagation had been rubbed out within the "crescent" region.

After the "crescent" region, fatigue striations similar to those on the direct stress fracture surfaces were observed, and polycrystalline grain size did not appear to have any effect on the formation of striations. "Micro-cracks" or "fissures" similar to those on the direct stress fracture surfaces were common and were generally found within the striation regions, see fig.8.46a. However, in contrast to the direct stress fatigue fracture surfaces, secondary "macro-cracks" (observed at magnification of less than 20 times) were commonly observed, especially at and around the area of final separation, see fig.8.46b. These secondary "macro-cracks" could probably be attributed to the high shear force resulting from the rapid reduction of the load carrying area as fatigue cracks propagated through the specimen. There was no evidence of cleavage fracture as was observed on the direct stress fatigue fracture surfaces. Under rotating bending loading, the specimens were broken completely and the final separation was by microvoid coalescence, see fig.8.44b.

Tire tracks as reported by Koterazawa et al[46] were observed on the rotating bending fatigue fracture surfaces.

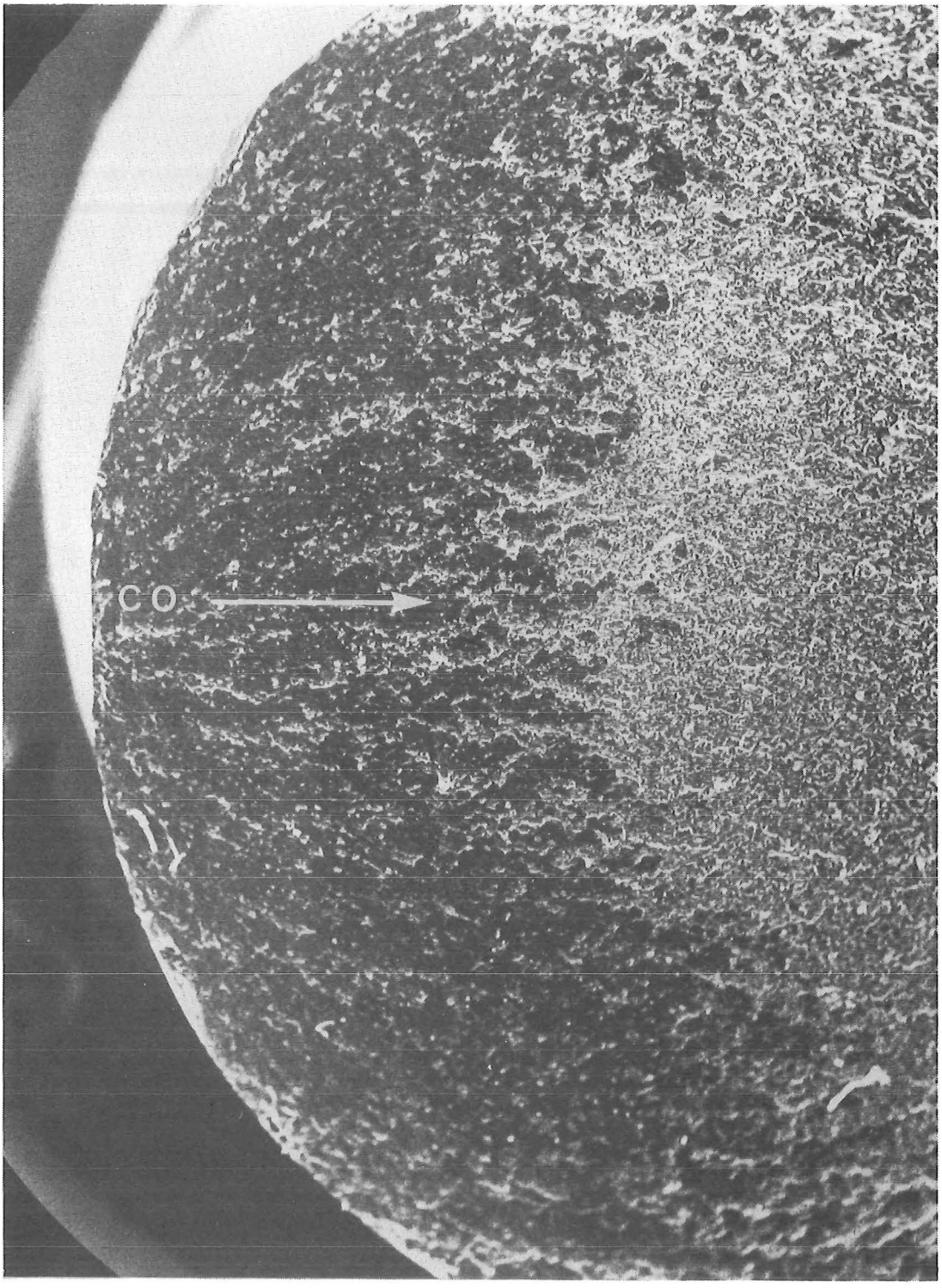

50×

CO = crack origin(s)
(⟶ direction of crack propagation.)

Fig. 8·45 'CRESCENT' SHAPED REGION ON ROTATING BENDING FRACTURE SURFACE.

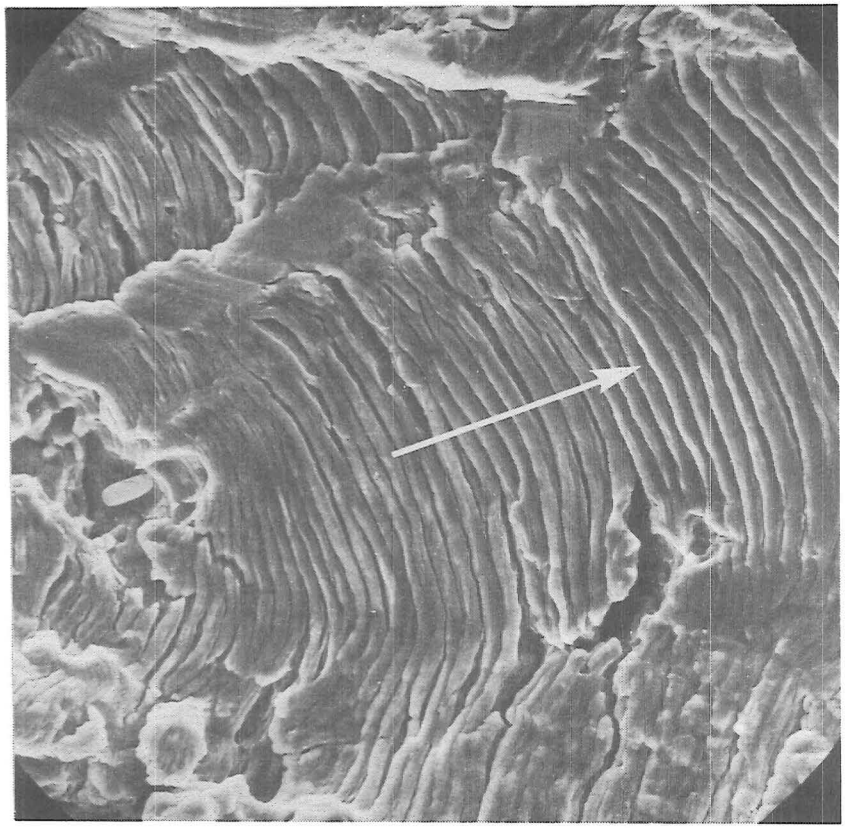

1400×

(a) Fatigue striations

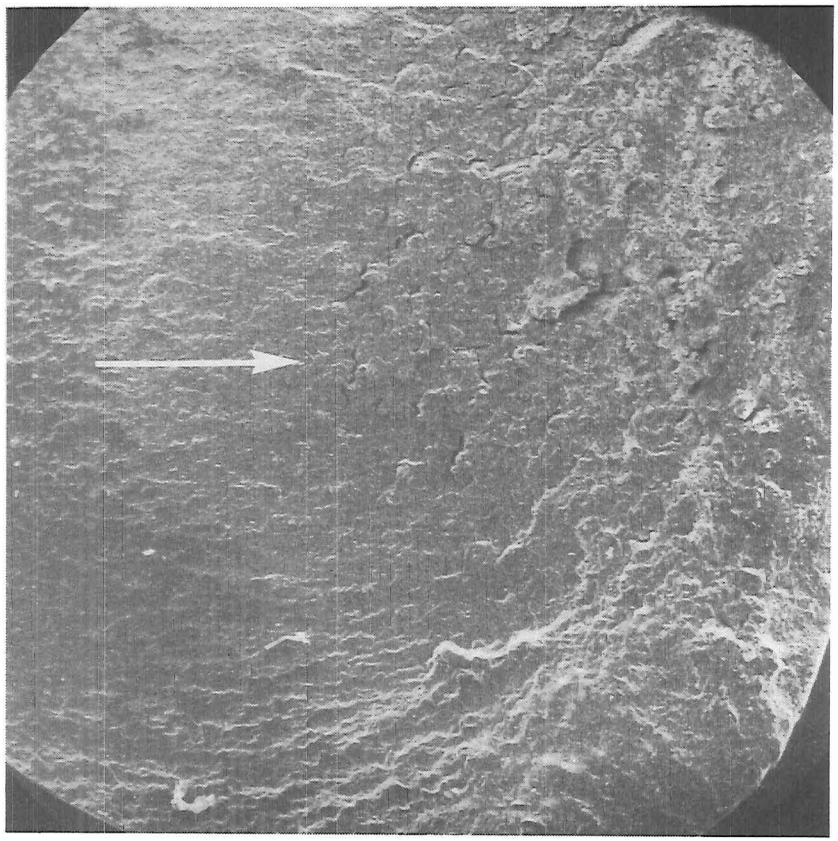

70×

(b) 'Macro-cracks' at the area of final separation.

(⟶ direction of crack propagation)

Fig. 8·46. STRIATIONS AND 'MACRO-CRACKS' ON ROTATING BENDING FRACTURE SURFACE

These tire tracks generally were confined to the "crescent" region and were usually observed close to the specimen surface. The spacing of these tire tracks appeared to increase in one direction along the circumference of the specimen, see fig.8.47.

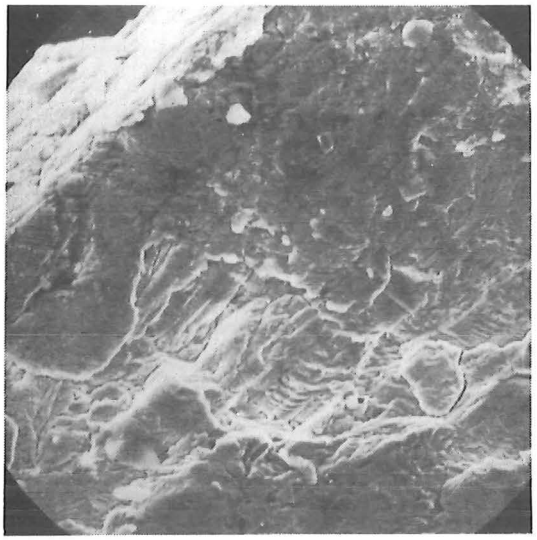

x 510

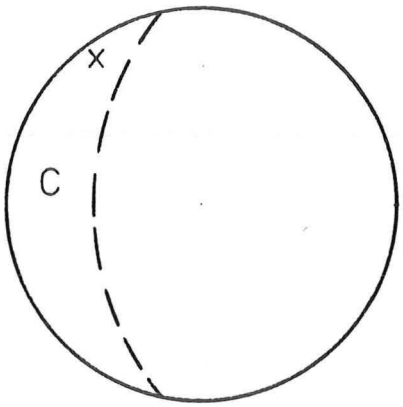

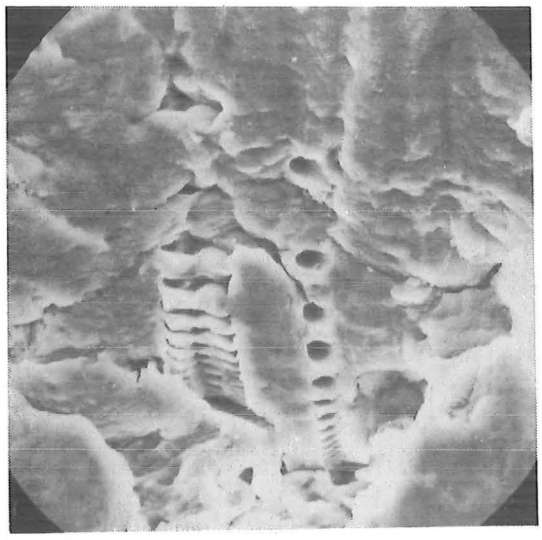

x 2600

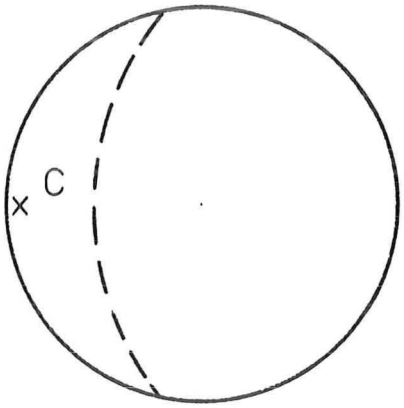

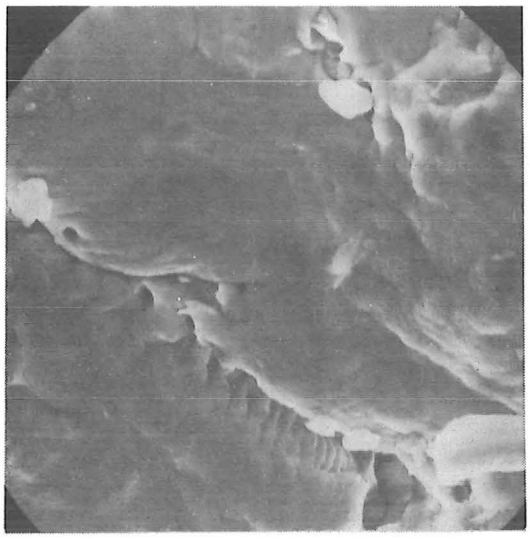

x2600

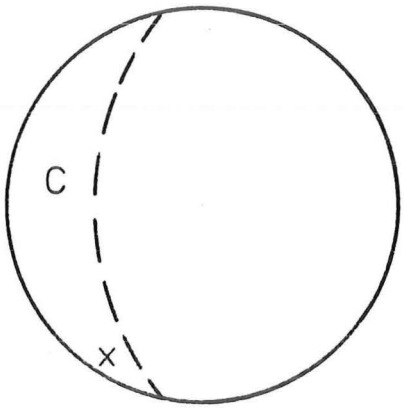

C = INEXPRESSIVE 'CRESCENT' SHAPED AREA
X = APPROXIMATE LOCATION OF TIRE TRACKS.

Fig. 8·47 TIRE TRACKS FORMED ON ROTATING BENDING FRACTURE SURFACE.

CHAPTER 9.

DISCUSSION.

9.1 THE DIRECT STRESS FATIGUE LIMIT AND THE DYNAMIC YIELD STRESS:

It has been shown[58] for annealed metals without discontinuous yield points that strain hardening occurs during fatigue cycling to some saturation value. The same metal in the cold worked state will progressively strain soften to the same saturation hardness value as found during cyclic hardening. This saturation hardness value is dependent on the cyclic stress amplitude.

Unlike these metals, low carbon steels may exhibit both effects. This is because of the low initial dislocation density due to interstitial locking. Cyclic stressing above the static lower yield point will result in massive dislocation multiplication during the first stress cycle, and as the dislocation density continues to increase on subsequent cycles, dislocation interaction results in strain hardening. That is, the hysteresis loop width increases to a maximum during the first stress cycle, and then decreases in an exponential manner with subsequent stress cycles[19].

When the applied cyclic stress is between the static lower yield point and the direct stress fatigue limit (assuming $\sigma_y > \sigma_{DS}$), the initial dislocation multiplication occurs more slowly and the effect of dislocation interaction or strain hardening is noticeable only after a large number of stress cycles. At these stress levels, the hysteresis loop width increases more slowly with stress cycles until a maximum width is obtained after a relatively large number of stress cycles

have been completed, after which the hysteresis loop width decreases with further cycling in an exponential manner[19]. Cyclic stressing between the static lower yield point and the direct stress fatigue limit has also been shown to be capable of removing the discontinuous yielding in low carbon steels [19,90,93].

Erasmus[12] has suggested that a fatigue saturation strain ε_p^* is necessary for the nucleation of fatigue cracks, and this saturation strain is related to the cyclic stress amplitude σ_a by the relationship:-

$$\sigma_a = K(\varepsilon_p^*)^n \qquad \text{eqn 9.1}$$

where K and n are constants determined from the normal tensile test. Based on the results of his fatigue data, Erasmus further suggested a saturation strain ε_p^* of ~0.002 in direct stress fatigue testings for his experimental steels.

The above theory implys that a finite plastic strain is accumulated at the direct stress fatigue limit σ_{DS}, provided that sufficient stress cycles are allowed, that is, without premature failure due to chemical activity. Further accepting the new definition for the anelastic limit σ_A, i.e. σ_A is the minimum stress for which tension-compression cyclic loading results in an open hysteresis loop or permanent strain, see section 4.3, the fatigue saturation strain ε_p^* at the direct stress fatigue limit which might be very small, will be larger than the plastic strain at the anelastic limit σ_A. The anelastic limit σ_A of a material is therefore less than the direct stress fatigue limit, that is, $\sigma_{DS} > \sigma_A$. This should be so at least for materials which have low equivalent friction stress σ_o, i.e. the "soft" materials where $\sigma_{DS} > \sigma_o$, see fig.4.5, section 4.2.

Abel and Muir[91,92] have also shown that cyclic prestressing just above the anelastic limit σ_A (as defined by the tension-compression method) can result in the complete removal of the sharp yield drop, provided that sufficient stress cycles are allowed. They also suggested that the gradual removal of the discontinuous yielding phenomenon with stress cycles at stresses well below the static yield stress can be better explained by the "Dynamic dislocation multiplication" theory of Johnston and Gilman[70], and Hahn[71]. If the effect of cyclic prestress is the production of mobile dislocations, then the mobile dislocation density should depend on the number of the stress cycles applied, provided that the stress amplitude is sufficient for the generation of mobile dislocations, i.e. above the anelastic limit σ_A of the material.

Since the direct stress fatigue limit σ_{DS} is above the anelastic limit σ_A, which is the minimum stress required to initiate an open hysteresis loop, cyclic stressing at σ_{DS} should theoretically result in the gradual removal of the discontinuous yield point phenomenon in low carbon steels, provided that sufficient numbers of stress cycles are allowed, so that the density of free dislocations necessary to satisfy the impose strain rate of tensile machine can be achieved. The results from tensile tests (figs.8.31 and 8.32) show that the discontinuous yielding phenomenon of these experimental steels was completely eliminated by cyclic stressing at stresses just below their respective direct stress fatigue limits. The removal of the discontinuous yielding phenomenon at stresses below the direct stress fatigue limit is contradictory to the finding of Stephen[90], Luther and Williams[93]. This discrepancy is most likely due to insufficient stress cycles being applied by the above researchers on their steels. Only

1×10^6 cycles by Stephen[90] and, although stress cycles of more than 2×10^7 cycles were applied by Luther and Williams[93], these stress cycles were apparently not sufficient to produce sufficient mobile dislocations for the elimination of the discontinuous yielding phenomenon in their steel. However, their results showed that the sharp yield drop was removed after cyclic prestressed at 230 MN/M^2 (σ_{DS} = 238 MN/M^2, at cyclic frequency of 100 Hz) for 2×10^7 cycles, although the Luders strain was retained and, as has been mentioned earlier, if the effect of cyclic stressing is the production of mobile dislocations, further cyclic stressing at this stress level should produce sufficient mobile dislocations to ensure that the Luder strain is completely eliminated. Also the applied cyclic stress amplitude was a bit low (230 MN/M^2 as compared to the direct stress fatigue limit of 238 MN/M^2), and it is likely that a slightly higher stress, but still below the direct stress fatigue limit, would remove the discontinuous yielding at a much lower number of stress cycles.

Evidence of dynamic yielding at stresses just below the direct stress fatigue limits can also be seen from the results of etching with Fry's reagent the special high nitrogen low carbon steel (steel C). These are shown in fig.8.9, which suggest a dynamic yield stress of about 220 MN/M^2 for this steel. This is well below the direct stress fatigue limit of about 235 MN/M^2. It is possible that a high level of active nitrogen in this steel may have resulted in a higher degree of dynamic strain ageing and thus a higher fatigue limit. However, the result from tensile tests after fatigue stressing for 3.7×10^6 cycles, see fig.8.32, indicates that dynamic strain ageing during fatigue cycling is not sufficient to result in complete formation of Cottrell atmosphere or stage I ageing

in this steel, as the characteristic sharp yield drop was not returned, at least for lives up to 3.7×10^6 cycles. Also, this steel has a reasonably fine grain size, $d^{-\frac{1}{2}} \simeq 8.85\ mm^{-\frac{1}{2}}$, and fig.7.13 suggests that, for fine grained steels, the effect of dynamic strain ageing on the fatigue limit is negligible. Microhardness results as shown in figs.8.13-8.17 again reveal that plastic deformation occurs at stresses close to but below the direct stress fatigue limit in these experimental steels.

Further deduction may also be made from the temperature rise measurements as obtained in figs.8.3, 8.4 and 8.5. Limited testings with special high nitrogen low carbon steel, see fig. 8.10, suggest that plastic deformation during cyclic loading is reflected in the temperature rise monitoring, and high increase in temperature during cycling indicates the onset of dynamic yielding. The use of temperature rise monitoring has the advantage that it is non-destructive, and fatigue damage can be monitored on the same specimen continuously. As temperature rise has been shown to be proportional to the hysteresis loop width produced during fatigue cycling[15,109], temperature rise monitoring during direct stress fatigue cycling can probably be used to establish a more accurate value of the anelastic limit σ_A of a material, as higher numbers of stress cycles can be applied in a direct stress fatigue machine. Also, as fatigue failures can occur at stress cycles as large as 10^7 cycles or more (especially for materials without a fatigue limit), stress cycles greater than 10^7 cycles should be used to establish the anelastic limit of the material.

The results from the tensile tests after fatigue cycling below σ_{DS}, etching of the special steel with Fry's reagent, microhardness surveys on the runout specimens and temperature

rise monitoring during fatigue cycling all indicate that the dynamic yield stresses of these experimental steels are somewhat lower than their respective direct stress fatigue limits. This is further confirmed by the results plotted in fig.7.13. This figure shows that the direct stress fatigue limits of these experimental steels are very much higher than their respective σ_o, which may be regarded as a limiting stress below which general plastic deformation cannot occur. The above finding is also in agreement with the results of a parallel research programme[110], which suggest a dynamic yield stress of between 3 to 6% lower than the direct stress fatigue limit for these experimental steels.

Accepting the hypothesis of Erasmus[12] that a fatigue saturation strain ε_p^* is necessary for the nucleation of fatigue cracks, and that saturation strain can be expressed by the equation

$$\sigma_a = K(\varepsilon_p^*)^n \qquad \text{eqn 9.1}$$

and if it is further assumed that sufficient stress cycles were allowed in the direct stress fatigue testings in section 7.2, such that the necessary fatigue saturation strains ε_p^* were achieved for all experimental steels, that is $\sigma_{DS} = \sigma_a$, by substituting appropriate values of K and n as determined in section 7.1 into equation 9.1, the fatigue saturation strain ε_p^* for each set of specimens can be calculated. These results are tabulated in table 7.2, and plotted in fig.9.1. The results from this limited range of data suggest that the fatigue saturation strain ε_p^* is not a constant, but varies with polycrystalline grain size, with decreasing ε_p^* for decreasing grain size or increasing material strength. This is reflected in the ratio of σ_{DS}/σ_o as tabulated in table 7.2, which shows a

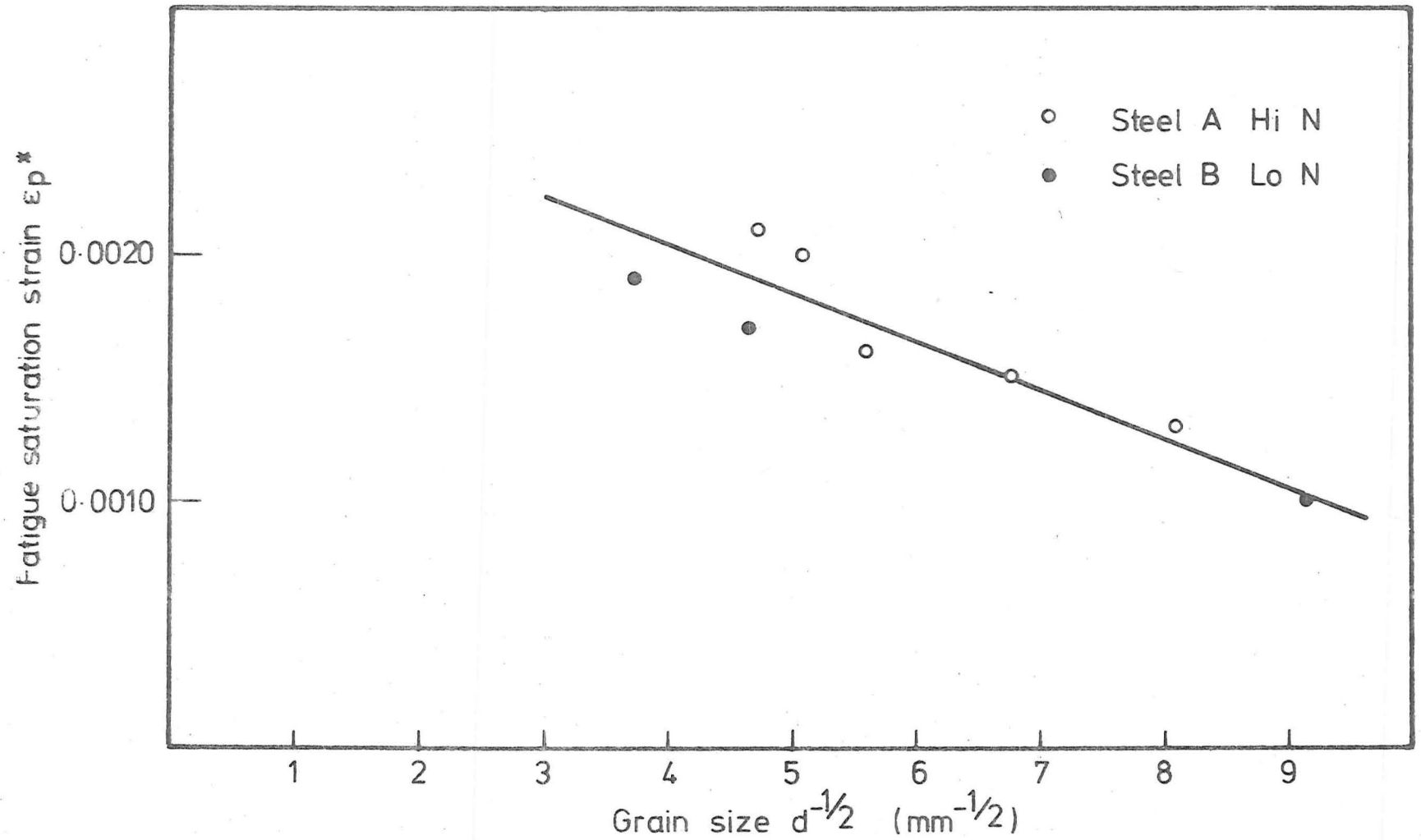

Fig. 9·1 EFFECT OF GRAIN SIZE ON THE FATIGUE SATURATION STRAIN ε_p^* (eqn. 9·1)

decreasing ratio of σ_{DS}/σ_o as the material strength increases, and is further confirmed by the temperature curve of fig.8.7, which shows that finer grained specimens generally have a lower temperature increase, which may be interpreted as a narrower hysteresis loop width or smaller plastic strain.

The relationships between the equivalent friction stress σ_o and the direct stress fatigue limit from the data of Erasmus[12] and Holloman et al[89] as shown in fig.4.5, section 4.2, is replotted in fig.9.2 together with the data from this investigation. Fig.9.2 shows that, for lower strength materials, stresses well above σ_o are required to initiate fatigue failure, that is, significant amounts of plastic deformation take place before fatigue failure (ε_p^* large). For higher strength materials, σ_{DS} approaches the equivalent friction stress σ_o, and very little plastic deformation is required prior to fatigue failure, (ε_p^* small). For extreme hard materials, it appears that premature failures due to crack nucleation at stress rises such as machining or polishing marks occur before the saturation strain ε_p^* of the material is reached, consequently, the direct stress fatigue limit σ_{DS} tends to a value lower than σ_o.

From the above results, it can be concluded that coarser grained or softer materials will deform more easily under cyclic stressing than the finer grained or harder materials. Consequently, under rotating bending loading conditions, this would mean that the maximum stressed outer fibre of a softer material will deform more easily and develop a much thicker depth of plastic zone, and as has been shown in section 5.2, this would result in a higher increase in the load carrying capacity for the softer materials under rotating bending loading. This would thus account for the variation in the

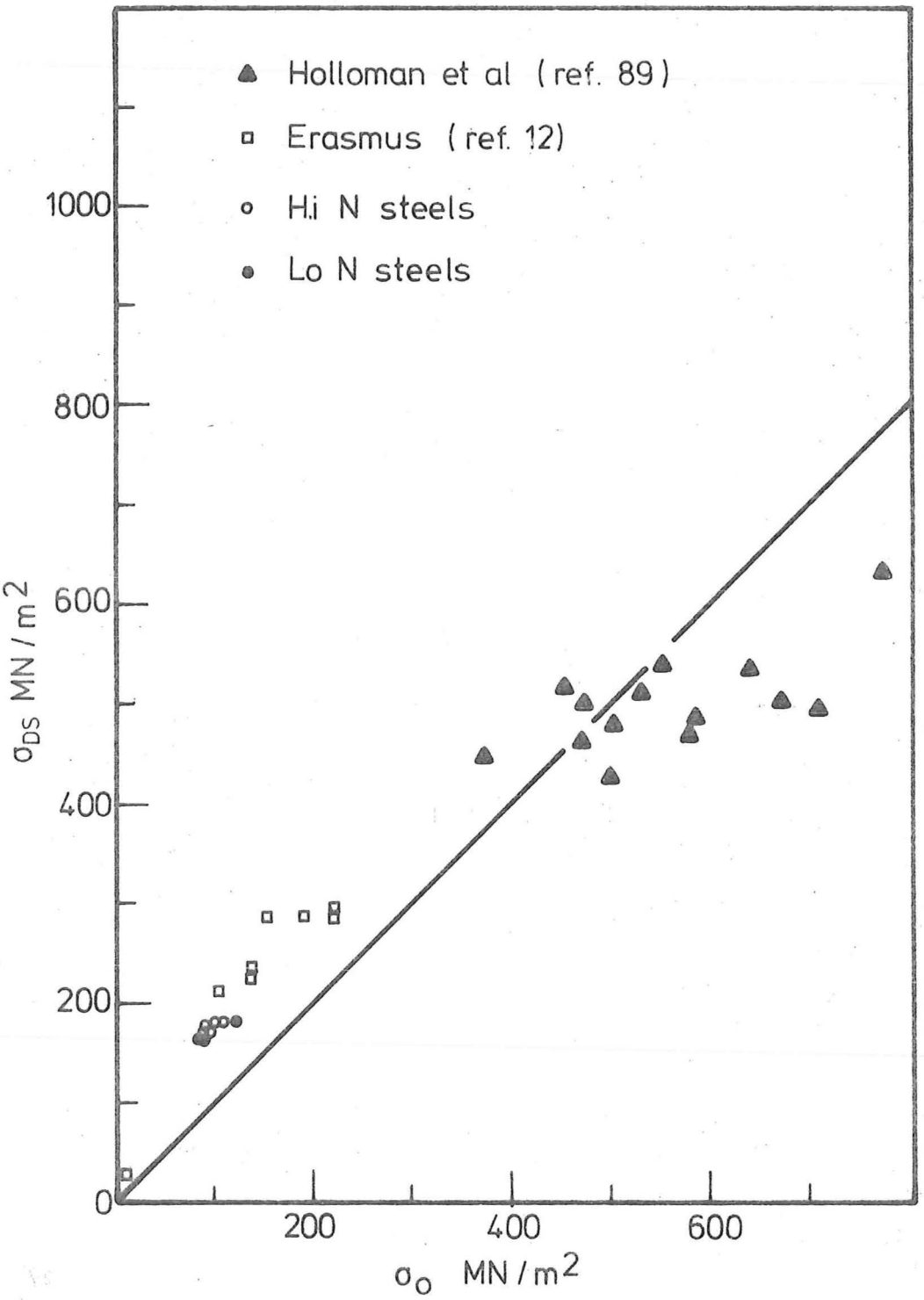

Fig. 9·2. RELATIONSHIP BETWEEN σ_{DS} AND σ_o

ratio

$$\frac{\text{rotating bending fatigue limit}}{\text{direct stress fatigue limit}}$$

with material strength, if we accept the stress redistribution theory in rotating bending fatigue loadings.

Microstructural changes on the direct stress specimen surfaces as monitored in section 8.5 show that, irrespective of the grain size, stresses above the direct stress fatigue limit are necessary to nucleate widespread active slip bands. Stresses below σ_{DS} generally only resulted in a few isolated patches of ill-defined slip markings. These observations give further support to the hypothesis of Erasmus[12] that a fatigue saturation strain ε_p^* is necessary before fatigue cracks can develop. It appears that cyclic stresses below σ_{DS} are not sufficient to accumulate the necessary saturation strain ε_p^* required to nucleate the wide spread of active slip bands, which are necessary for the formation of fatigue cracks under normal fatigue testings. Whereas stresses above σ_{DS} will accumulate sufficient strain for the nucleation of widespread active slip bands, which in turn develop into fatigue cracks after sufficient numbers of stress cycles have been applied.

9.2 THE EFFECT OF ACTIVE NITROGEN AND GRAIN SIZE ON THE FATIGUE LIMIT:

The effect of dynamic strain ageing and polycrystalline grain size on the fatigue properties of the experimental steels can be seen in fig.7.13. The relationship between fatigue limit and grain size was found to be in agreement with the published results, that is, it can be expressed by the relationship

$$\sigma_L = \sigma_1 + C_2 d^{-\frac{1}{2}} \qquad \text{eqn 3.15}$$

This relationship is applicable for both "high" and "low" nitrogen steels under both direct stress and rotating bending testings.

Evidence of relocking of free dislocations by active nitrogen during the course of fatigue cycling can be seen by comparing lines 1 and 2 for rotating bending and 3 and 4 for direct stress loadings. Under both loading conditions, higher levels of active nitrogen resulted in higher fatigue limit, and coarser grained specimens appeared to be affected more than the finer grained specimens. For example

$$\sigma_{RB(1)} - \sigma_{RB(2)} \simeq 8 \text{ MN/M}^2 \text{ for } d^{-\frac{1}{2}} = 4 \text{ mm}^{-\frac{1}{2}}$$

$$\sigma_{RB(1)} - \sigma_{RB(2)} \simeq 2 \text{ MN/M}^2 \text{ for } d^{-\frac{1}{2}} = 8 \text{ mm}^{-\frac{1}{2}}$$

$$\sigma_{DS(3)} - \sigma_{DS(4)} \simeq 13 \text{ MN/M}^2 \text{ for } d^{-\frac{1}{2}} = 4 \text{ mm}^{-\frac{1}{2}}$$

$$\sigma_{DS(3)} - \sigma_{DS(4)} \simeq 4 \text{ MN/M}^2 \text{ for } d^{-\frac{1}{2}} = 8 \text{ mm}^{-\frac{1}{2}}$$

These results are to a certain extent in agreement with the finding of Oates and Wilson[15] who reported that dynamic strain ageing only occurred in their coarse grained steel.

The results of temperature rise monitoring in section 8.2, fig.8.6, again suggests the possibility of Cottrell atmosphere formation. It can be seen that, for specimens with similar grain size, specimens containing higher level of active nitrogen (steel A1) always have a lower temperature rise at any particular time when compared with specimens containing a low level of active nitrogen (steel B2). As temperature increase has been shown to correspond to the hysteresis loop width produced during fatigue cycling[15,109], and also the works of Erasmus[12] and Wilson et al[109] have shown that the process of dynamic strain ageing results in a gradual decrease in temperature rise, that is, narrowing of hysteresis loop width, the lower temperature increase in the high nitrogen steel A1 as

compared to that for the low nitrogen steel B2, may be interpreted as the gradual relocking of free dislocations during the process of fatigue stressing, and thus resulting in a lower density of free or mobile dislocations. It is likely that prior heat treatments to obtain different levels of active nitrogen and grain sizes may have resulted in different levels of initial free dislocation density. But prior to fatigue testings, all specimens were given a heat treatment at 110^{o}C for 1 hour, which should eliminate most of the initial free dislocations. However, a problem may arise in the low nitrogen steels (see section 3.2), since locking of dislocations below 150^{o}C is predominantly by nitrogen. As a result, heat treatment at 110^{o}C may not completely lock all the initial free dislocations in low nitrogen steels, especially those containing high initial free dislocation density. This problem was in fact encountered in steel B3, where rapid cooling during annealing to obtain fine grain size could have resulted in higher initial free dislocation density and heat treatment at 110^{o}C for 1 hour apparently was not sufficient to lock most of the initial free dislocations, as a result, the damping was very high, the temperature increased very rapidly and the direct stress fatigue machine was unable to maintain a constant load. This problem was finally overcome by heat treating the specimens at 150^{o}C for 2 hours. Heat treatment at 110^{o}C for 1 hour was, however, found to be sufficient for other low nitrogen steels (B1 and B2).

The above discussion suggests that dynamic strain ageing does take place in high nitrogen steels during fatigue cycling but that the extent of the dynamic strain ageing is insignificant. This can be seen from the limited numbers of tensile flow curves obtained after fatigue cycling at stresses

just below the direct stress fatigue limit, see fig.8.31 and 8.32 in section 8.6. The absence of the characteristic sharp yield drops, especially in the coarse grained, high nitrogen specimen, steel A1, which was most vulnerable to dynamic strain ageing[15], suggests that Cottrell atmosphere formation or stage I ageing is definitely not complete during normal fatigue testings, at least for lives up to 1.5×10^7 cycles. It is therefore unlikely that the formation of a fatigue limit in low carbon steels is the result of dynamic strain ageing, especially in the fine grained specimens, where the high level of active nitrogen has negligible effects on the fatigue limits of the steels.

The influence of active nitrogen on the fatigue limits of coarse grained steels may be explained by the following mechanism, accepting the hypothesis that a minimum saturation strain ε_p^* is required for fatigue failure, and assuming that this saturation strain ε_p^* for a particular material with a particular grain size is a constant, then for steels containing a high level of active nitrogen, relocking of free dislocations during fatigue cycling will result in a lower density of free dislocations, that is, a narrower hysteresis loop width as compared to that for steels containing a low level of active nitrogen. This is reflected in a lower temperature increase in fig.8.6. As the fatigue saturation strain ε_p^* for coarse grained steels is large, a higher stress is therefore necessary to generate sufficient free dislocation density to achieve the saturation strain necessary for the nucleation of fatigue damage in the form of active slip bands, intrusions and extrusions, etc. This postulation is supported by the temperature curves of fig.8.6. This figure shows that, although the temperature rise for the high nitrogen specimens was always less than that

of the low nitrogen steels (even with a higher stress amplitude), the final saturation temperatures attained by the run-out specimens of both high and low nitrogen steels of similar grain size ($d^{-\frac{1}{2}}$ of 4.72 and 4.65 $mm^{-\frac{1}{2}}$ respectively) were very similar. This may be interpreted to mean that the final hysteresis loop widths for both steels were the same or the saturation strains were similar. This is in contrast with the temperature curves of fig.8.7, which shows that, for steel of similar active nitrogen content, higher fatigue stress amplitude always results in higher saturation temperature. In fine grained steels, as the fatigue saturation strain ε_p^* required for the nucleation of fatigue cracks is small, weak dislocation relocking as is occurring during fatigue cycling may not significantly alter the stress required to produce the necessary saturation strain, perhaps a much larger number of stress cycles is required to produce the necessary saturation strain. If the above argument is correct, it may be inferred that dynamic strain ageing as is occurring during normal fatigue cycling, should not have a significant effect on the fatigue limits of high strength materials, as the fatigue saturation strain ε_p^*, as shown in fig.9.2 for high strength materials, is small.

Fig.7.13 also indicates that dynamic strain ageing does not affect the rotating bending fatigue limits as much as the direct stress fatigue limit, which implies that other factor(s) are involved in determining the fatigue limits of rotating bending specimens.

It also appears that most of the above observations could be explained by a higher strain hardening rate in the high nitrogen steels. That is, dislocation interaction occurs at a

faster rate than dislocation multiplication, resulting in a narrower hysteresis loop width. However, it is difficult to differentiate the role of strain hardening and relocking of dislocations (before the completion of atmosphere formation) by active nitrogen, and no positive conclusion can be made if the strain hardening rate does affect the fatigue strength (limit) of a material. The tensile results on fatigued specimens do, however, show conclusively that Cottrell atmosphere formation is not complete during normal fatigue testings.

9.3 THE EFFECT OF DYNAMIC YIELDING ON THE ROTATING BENDING FATIGUE LIMIT AND THE NOTCHED FATIGUE PROPERTIES:

As has been shown in section 9.1, the dynamic yield stress of low carbon steels is somewhat lower than the direct stress fatigue limit. Under rotating bending loading conditions, when the maximum calculated applied stress σ_{app} (calculated from the elastic theory $M = \frac{\sigma I}{n}$) is greater than the dynamic yield stress σ_e, but below the rotating bending fatigue limit σ_{RB}, dynamic yielding of the maximum stressed fibre where $\sigma \geqslant \sigma_{DS}$, after prolonged cycling will result in stress redistribution, and the effective surface stress will therefore be less than the calculated elastic stress σ_{app}. The formation of an inelastic layer will thus increase the load carrying capacity (hence, the fatigue strength) of the rotating bending member.

Referring to fig.9.3, for a case of plane bending, and assuming that the strain after plastic deformation is linearly proportional to the distance from the centre of the specimen, at cyclic stresses within the elastic range, that is, below the dynamic yield stress σ_e of the material, the stress and strain distributions are as shown by a and a' respectively in fig.9.3.

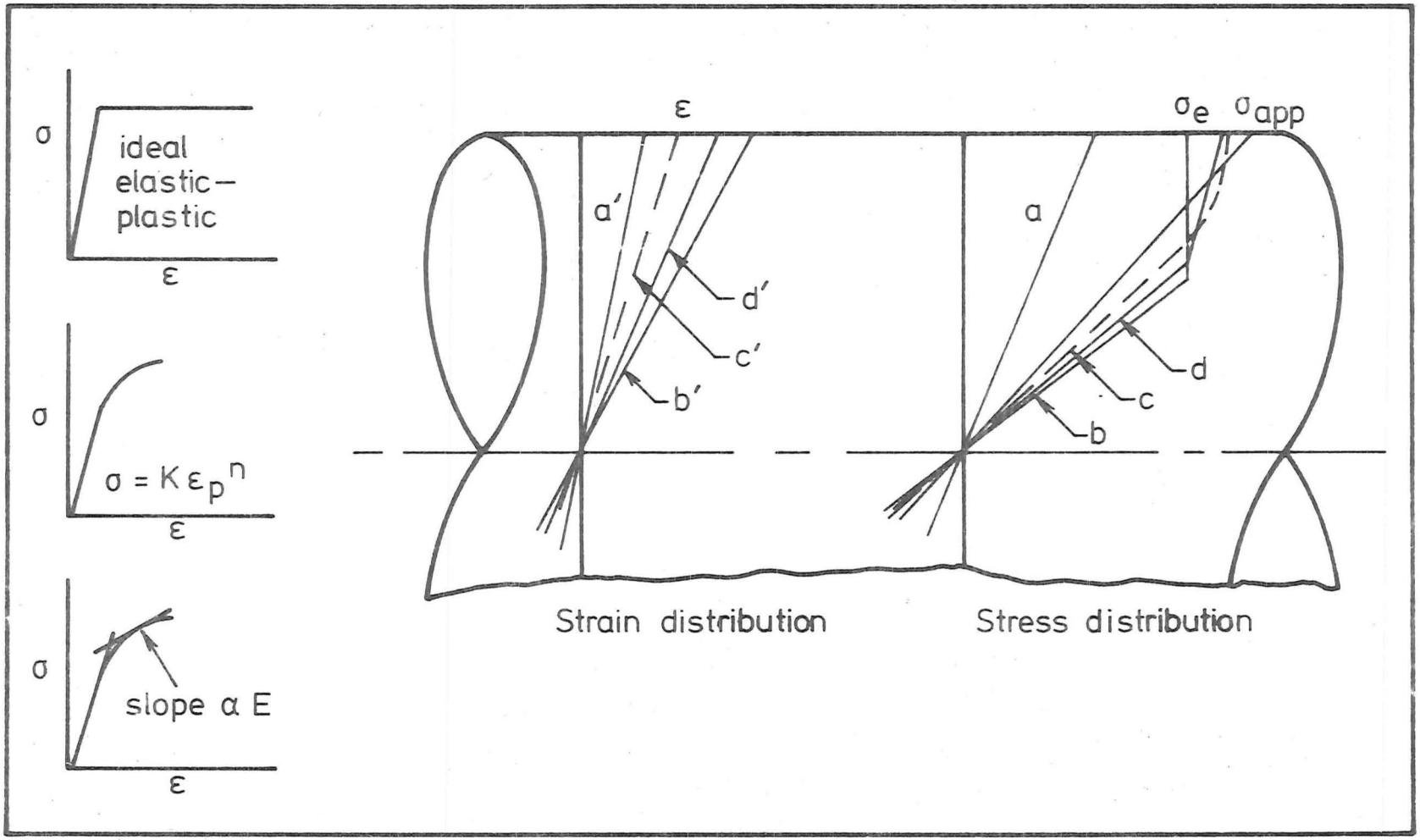

Fig. 9·3 EFFECT OF DYNAMIC YIELDING ON THE STRESS AND STRAIN DISTRIBUTIONS.

If the applied bending moment is increased such that the maximum calculated applied stress σ_{app} is greater than σ_e, dynamic yielding after prolonged cycling will result in stress redistribution. For a simple case of an ideal elastic-plastic material, the stress and strain distributions after dynamic yielding may be represented by lines b and b' respectively. For materials which strain harden according to the relationship $\sigma = K\varepsilon_p^n$, the stress and strain distributions are as shown by lines c and c' in fig.9.3, and when the flow curve of a material is simplified to a straight line with slope αE, see section 5.2, the stress and strain distributions may be represented by d and d' respectively. For an ideal elastic-plastic material under bending or rotating bending, where σ_{app} is greater than σ_e, the maximum surface stress will theoretically remain at σ_e after dynamic yielding, until the fully plastic situation has been reached. This however is not the case in real materials, since the materials will strain harden. Evidence of stress redistribution under rotating bending loading when the calculated applied stress σ_{app} is above σ_e may be seen from the results of etching the special high nitrogen low carbon steel (steel C) with Fry's reagent in fig.8.11, and the microhardness surveys in figs.8.18-8.22.

As the results from a parallel research programme have suggested that the dynamic yield stresses of these experimental steels were about 3 to 6% below the direct stress fatigue limits, it appears reasonable to approximate the dynamic yield stresses of these steels by their respective direct stress fatigue limits so that the increase in the "load carrying capacity" (taken as the ratio of σ_{app}/σ_{DS}, assuming $\sigma_{DS} = \sigma_e$) of the rotating bending specimens may be correlated with the depth of the

plastic layers developed, and comparison may therefore be made with the theoretical model for a simple case of plane bending. The tabulated results of load carrying capacity R_e ($=\sigma_{app}/\sigma_{DS}$, assuming $\sigma_{DS} = \sigma_e$) and depth of plastic layer r_e ($= h_e/r_1$) from the etching results in table 8.1 are plotted in fig.9.4 together with the theoretical curves as derived in section 5.2 for a simple case of plane bending

where h_e = plastic zone size revealed by etching

r_1 = specimen radius

The results as revealed by this etching technique agreed very well with the theoretical curve derived for the case of plane bending where $\alpha = 0$, that is, the case of an ideal elastic-plastic material, which suggests that the plastic zone was fully developed before cyclic strain hardening began, and it appears reasonable to approximate the plastic zone size of a rotating bending member by a simple case of plane bending in determining the load carrying capacity, provided that the contribution due to the difference in surface area and volume being subjected to $\sigma > \sigma_e$ is small. However, a possible source of error is in assuming $\sigma_{DS} = \sigma_e$ in the calculation of R_e ($= \sigma_{app}/\sigma_{DS}$), as σ_e is always slightly smaller than σ_{DS}, the use of σ_e instead of σ_{DS} would result in a slightly higher value of R_e, and shift the points in fig.9.4 away from the ideal elastic-plastic curve to one where α equals some finite value, but still small.

The relationship between plastic zone size and load carrying capacity may also be examined from the results of microhardness surveys in figs.8.18 - 8.22. Accepting that plastic deformation may be assumed to correspond to a particular increase in hardness, say 5 VHN above the original hardness of the material, the plastic deformation zone size may then be obtained from the microhardness survey. The results

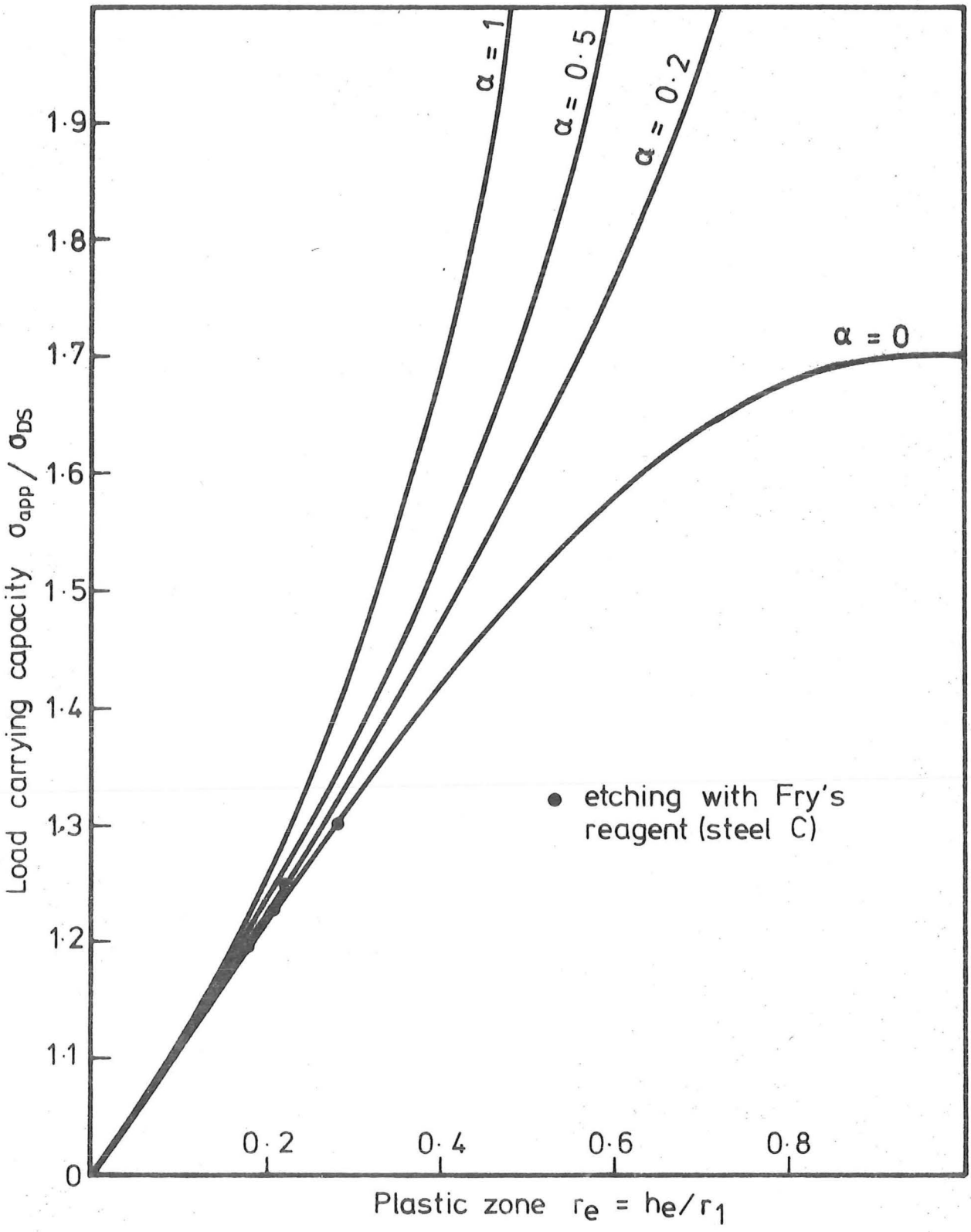

Fig. 9·4. CORRELATION BETWEEN EXPERIMENTAL RESULTS (ETCHING) AND THEORETICAL ANALYSIS FOR A CASE OF PLANE BENDING.

of R_m (= σ_{app}/σ_{DS}, again assuming $\sigma_{DS} = \sigma_e$) and r_m (= h_m/r_1) as tabulated in table 8.2 are plotted in fig.9.5 together with the theoretical curves derived for the case of plane bending and the results from the etching of the special steel. The results from the microhardness tests again agreed very well with the theoretical curves for the case of plane bending.

The results from the etching of the special steel and the microhardness tests as discussed above all showed that the relationship between the load carrying capacity (taken as the ratio of σ_{app}/σ_{DS}) and the depth of plastic deformation zone of a rotating bending member may be approximated by a simple case of plane bending as derived in section 5.2, equation 5.27. Strictly speaking, equation 5.27 is only applicable to a simple case of plane bending, nevertheless, the good agreement between this equation and the experimental results suggests the importance of a small layer of plastically deformed fibre in determining the load carrying capacity (hence, the fatigue strength) of a rotating bending member.

The results of microhardness surveys as shown in fig.8.18 - 8.22 also appear to suggest that a critical depth of plastic deformation zone is required for fatigue failure under rotating bending, and this critical plastic zone varies with material strength or grain size. This is further confirmed by the results of microstructure changes on the fatigue specimen surfaces as monitored in section 8.5. Under direct stress cycling, stresses above the direct stress fatigue limit are required to nucleate widespread active slip bands which in turn develop into fatigue cracks and propagate to failure, that is, the necessary fatigue saturation strain ε_p^* of the material has been reached. At stresses just below the direct stress fatigue limit, which are insufficient to accumulate the fatigue

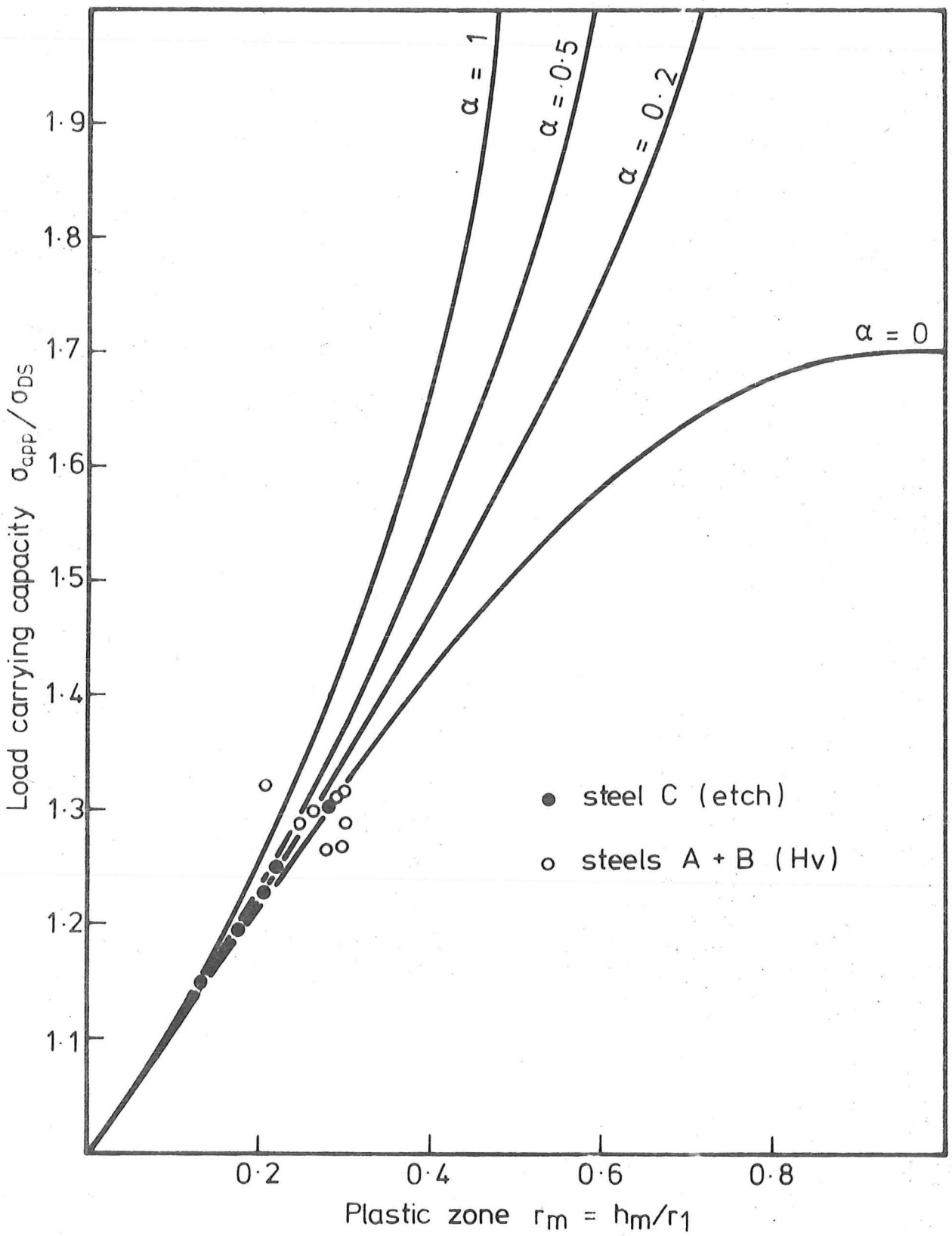

Fig. 9·5 CORRELATION BETWEEN EXPERIMENTAL RESULTS (ETCHING AND MICROHARDNESS) AND THEORETICAL ANALYSIS FOR A CASE OF PLANE BENDING.

saturation strain ε_p^*, widespread active slip bands cannot develop, and fatigue cracks cannot be nucleated, consequently, only isolated patches of ill-defined slip markings are formed and fatigue failure cannot occur. Under rotating bending loading, calculated applied stress σ_{app} between σ_{DS} and σ_{RB} is sufficient to accumulate the necessary fatigue saturation strain ε_p^* on the maximum stressed outer fibre, such that widespread active slip bands are developed. However, it appears that the depth of the plastic zone developed is insufficient for the development of these active slip bands into propagating fatigue cracks to cause fatigue failure, and calculated applied stresses σ_{app} above σ_{RB} are necessary to develop the necessary depth of plastic deformation zone for propagating cracks to develop.

If the above postulation is correct, that is, a critical depth of plastic deformation zone is required to initiate fatigue failure under rotating bending loading, and this critical depth of plastic deformation zone, denoted by r_c ($= h_c/r_1$, where h_c is the absolute plastic zone size at σ_{RB}) is achieved when the calculated applied stress σ_{app} equals the rotating bending fatigue limit σ_{RB}, the microhardness results as tabulated in table 8.2 may therefore be taken to represent the critical depth of plastic deformation sizes for these experimental steels, as these run-out specimens were fatigued at stresses just below their respective rotating bending fatigue limits. A graph of r_c versus the static lower yield stress σ_y can therefore be plotted, this is illustrated in fig. 9.6. The relationship between r_c and σ_y for this limited range of data may be expressed by the equation of the form:

$$r_c = r_o - K_o\sigma_y \qquad \text{eqn 9.2}$$

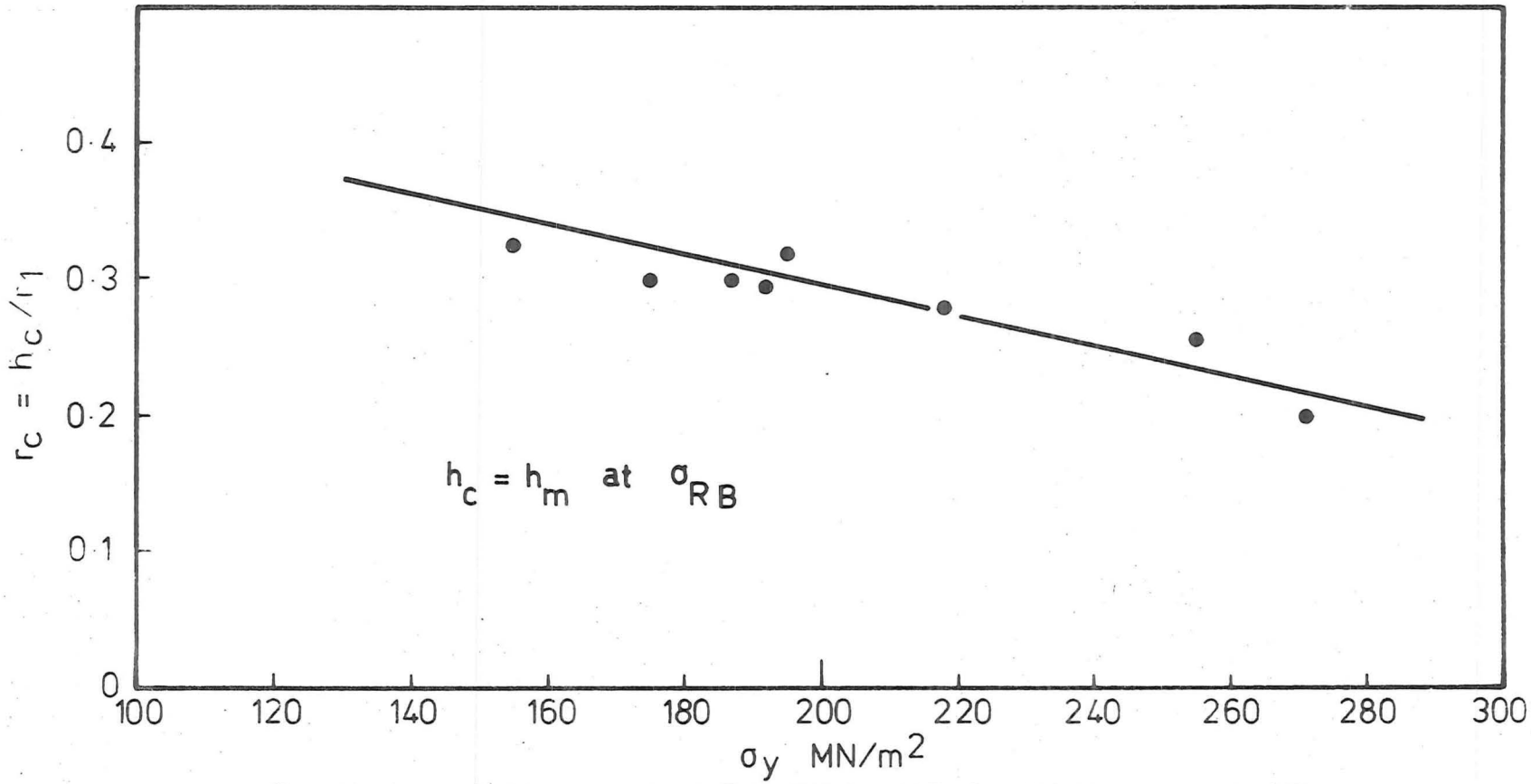

Fig. 9·6 RELATIONSHIP BETWEEN THE CRITICAL DEPTH OF PLASTIC DEFORMATION (r_c) AND THE STATIC LOWER YIELD STRESS (σ_y).

which suggests that there is a limiting value of σ_y, above which the plastic zone $r_c = 0$, that is $r_o = K_o\sigma_y$. At this limiting value, the rotating bending fatigue limit should theoretically approach the direct stress fatigue limit of the material, as no plastically deformed layer exists on the rotating bending member, and according to equation 5.27, there will be no increase in the load carrying capacity (hence, the fatigue strength) of the rotating bending member. This would thus imply that for materials with high strength, the ratio of

$$\frac{\text{rotating bending fatigue limit}}{\text{direct stress fatigue limit}}$$

decreases to unity, which is in accordance with the published results. The experimental results as tabulated in table 7.2 however, showed that the tendency is for the ratio σ_{RB}/σ_{DS} to remain constant (~1.3), or even increase slightly with increasing static strength. This discrepancy is apparently due to the very limited range of material strength (σ_y from ~155 MN/M^2 to ~271 MN/M^2) being examined, and the presence of active nitrogen in the experimental steels. As can be seen from table 7.1, the free nitrogen level of the "low nitrogen" steels (steels B1, B2 and B3) was rather high (~0.001 wt %) as compared to the level of <0.0001 wt % required for complete non-ageing[73,74], and as is shown in fig.7.13, the presence of active nitrogen increases the direct stress fatigue limits more than the rotating bending fatigue limits (especially the coarse grained specimens). It is therefore possible that, for steels containing negligible amounts of free nitrogen or materials which are non-ageing, a direct stress fatigue limit versus $d^{-\frac{1}{2}}$ (line 4' in fig.9.7) of a much steeper slope than line 4 may be obtained, whereas the slope of the rotating bending fatigue limit versus $d^{-\frac{1}{2}}$ (line 2' in fig.9.7) may not be very much different from that of line 2,

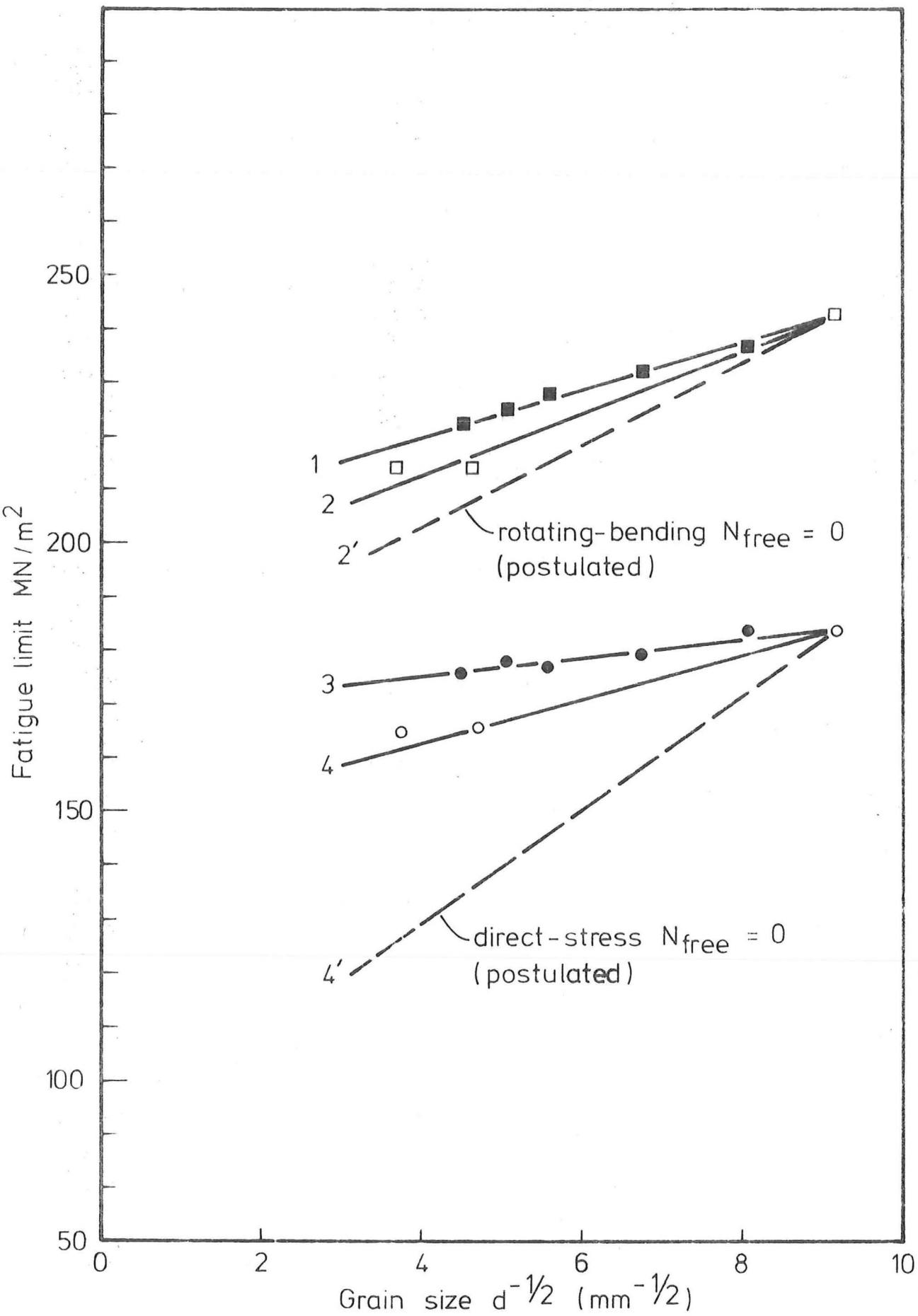

Fig. 9·7 SUGGESTED FATIGUE LIMIT vs GRAIN SIZE CURVES WHEN $N_{free} = 0$

and with a much wider range of material strength, the ratio of σ_{RB}/σ_{DS} would decrease with increasing material strength. Also it is possible that the discrepancy in the experimental results is due to the experimental difficulty in determining precisely the direct stress fatigue limits and rotating bending fatigue limits of the experimental steels.

The existence of a critical depth of plastically deformed zone under rotating bending loading can therefore explain the "size effect" generally observed in rotating bending or other types of fatigue loading where the applied stress is non-uniform. Referring to fig.9.8, which illustrates the relationship between specimen size and the depth of plastic zone under similar calculated applied stress σ_{app} ($\sigma_{app} > \sigma_{DS}$, and assuming $\sigma_{DS} = \sigma_e$), it can be seen that a specimen with twice the size will theoretically develop a plastic zone twice as deep, if sufficient numbers of stress cycles are allowed for the plastic zone to develop fully, that is, without premature failure. Therefore larger specimens will develop the same critical depth of plastic zone r_c with a lower calculated applied stress σ_{app} ($\sigma_{app} > \sigma_{DS}$). For very large specimens, the necessary calculated applied stress σ_{app} (hence, the rotating bending fatigue limit) required to develop the same critical depth of plastic zone would approach the direct stress fatigue limit of the material. Hence, the ratio of

$$\frac{\text{rotating bending fatigue limit}}{\text{direct stress fatigue limit}}$$

approaches unity as the size of the rotating bending specimen increases.

The existence of a dynamic yield stress below the direct stress fatigue limit, and the need to develop a minimum depth of plastically deformed zone under non-uniform fatigue stressing

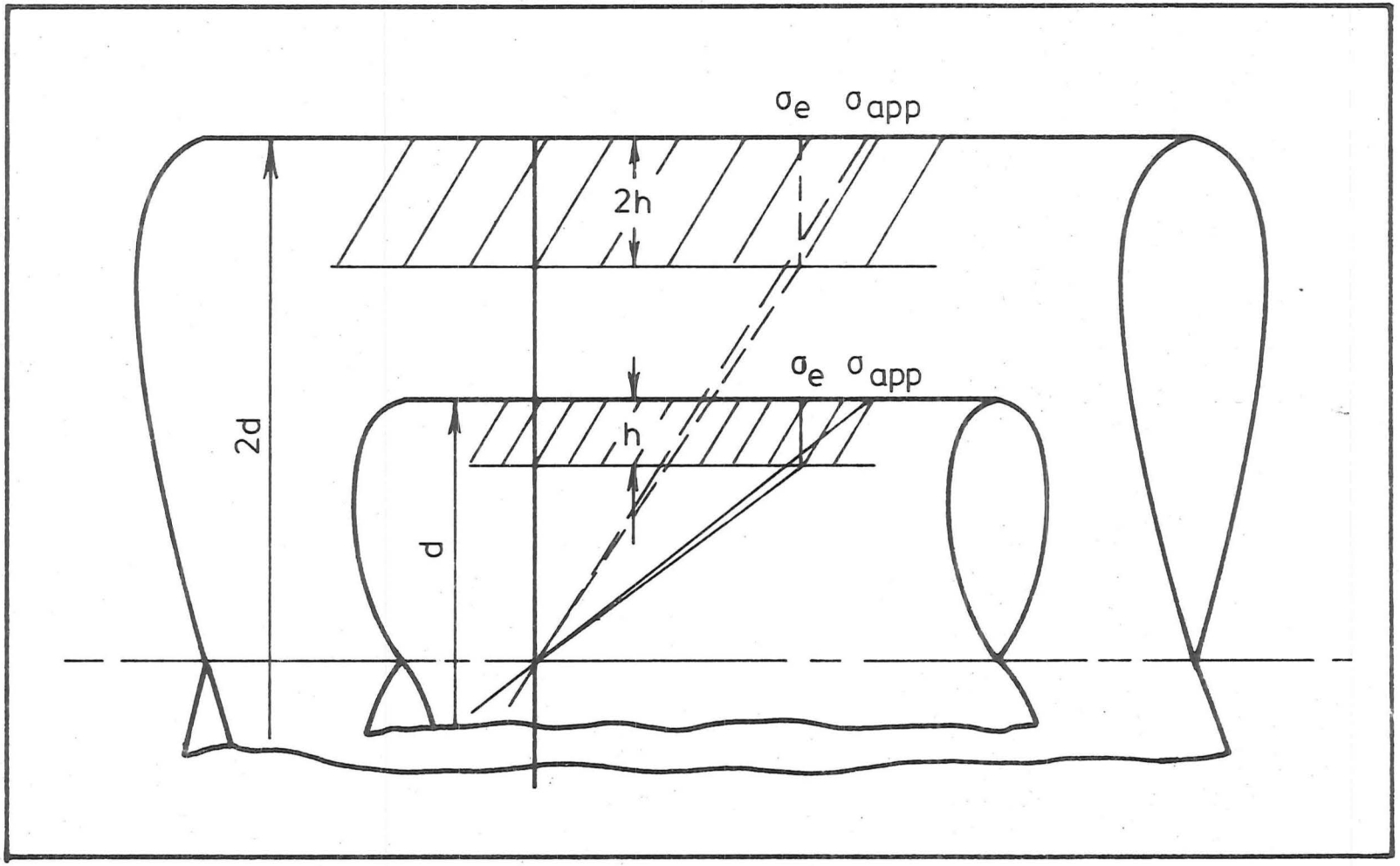

Fig. 9·8 EFFECT OF SPECIMEN SIZE ON THE DEPTH OF PLASTIC DEFORMATION ZONE.

could probably also account for the observed fatigue properties of notched specimens as discussed in section 2.2. Taking the case of a notched specimen under direct stress loading, see fig.9.9, if the nominal stress is σ_n, the maximum stress σ_{max} will occur at the notch root, and is equal to $K_t\sigma_n$, where K_t is the theoretical stress concentration factor. Under direct stress fatigue cycling, when $K_t\sigma_n$ is greater than the direct stress fatigue limit of the material σ_{DS}, dynamic yielding will occur at the notch root where $K_t\sigma_n \geq \sigma_{DS}$, after sufficient numbers of stress cycles have been applied and will result in stress redistribution with a plastically deformed zone h at the notch root. As the stress at the notch root is above the direct stress fatigue limit of the material, the fatigue saturation strain ε_p^* can be achieved, hence, active slip bands or even micro-cracks can develop at the notch root, but as the necessary depth of plastic deformation zone has not been reached, the micro-cracks if nucleated will remain non-propogating.

The effect of this critical depth of plastic zone on the notched fatigue properties may be qualitatively discussed by examining the variation in the load carrying capacity of a notched member under uniaxial loading. Again, the case of an ideal elastic plastic material, for a simple case of a plate with a circular hole of radius ρ under tension, as discussed in section 5.1, is re-examined. Referring to fig.9.10, let the plate be subjected to an axial load P_e, such that the maximum stress at the edge of the hole equals the yield stress σ_e. As the stress concentration factor for a hole is $K_t = 3$,

$$\therefore \quad \sigma_n = 1/3\ \sigma_e$$

where σ_n is the nominal stress at a section some distance away

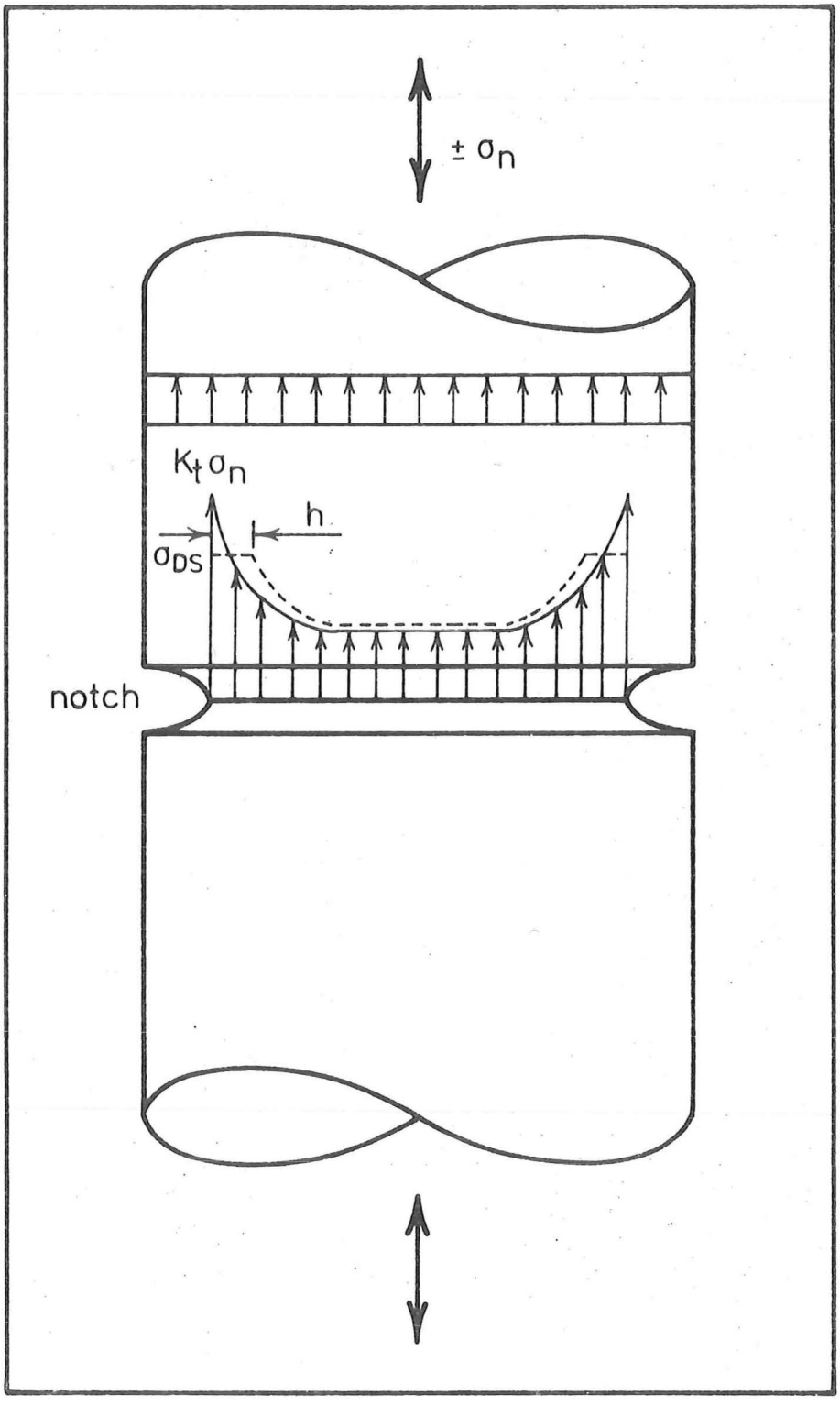

Fig. 9·9 STRESS REDISTRIBUTION ON A CIRCUMFERENTIALLY NOTCHED MEMBER.

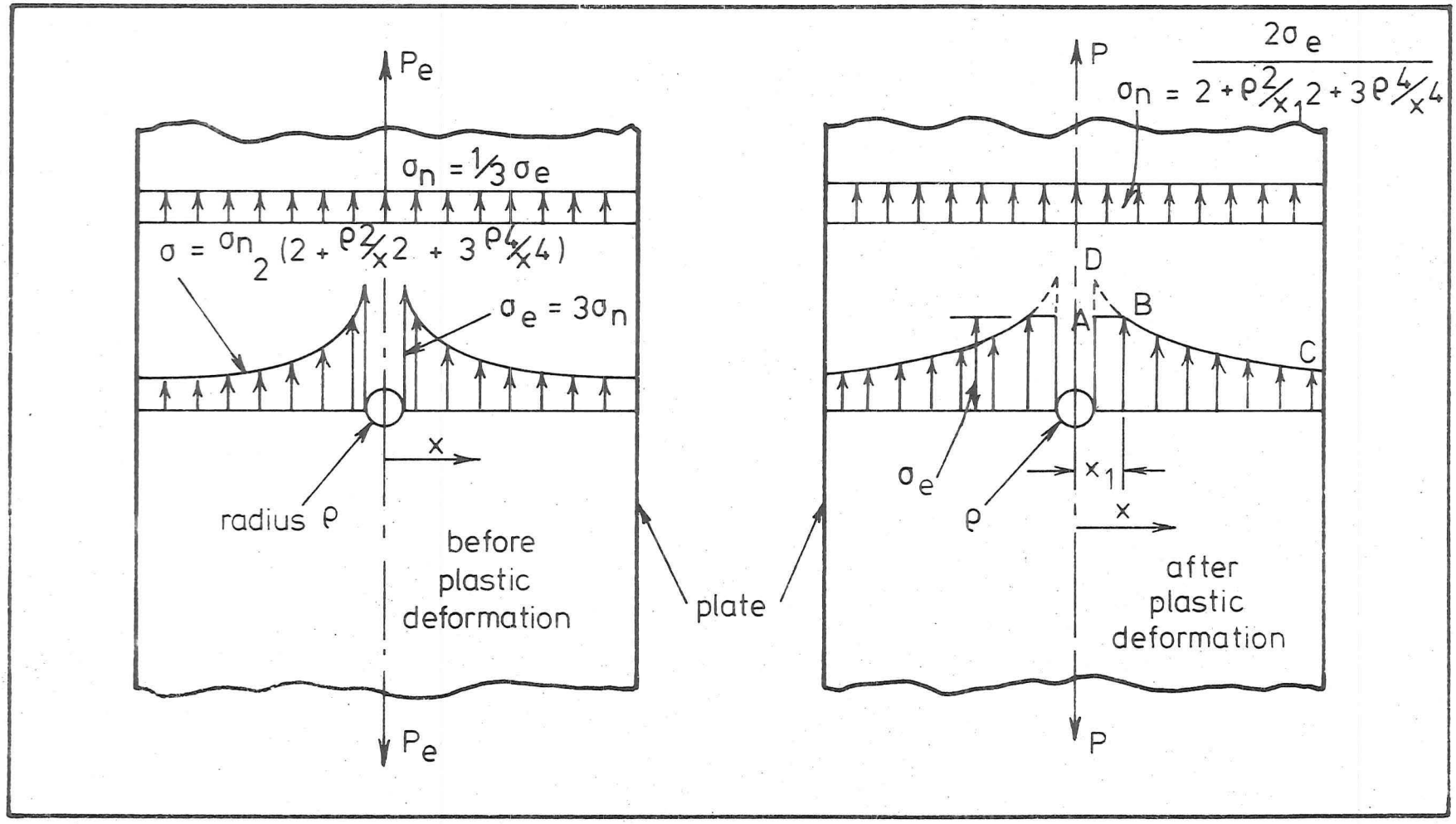

Fig. 9·10 STRESS DISTRIBUTION ON A PLATE CONTAINING A CIRCULAR HOLE BEFORE AND AFTER PLASTIC DEFORMATION

from the hole.

$\therefore \quad P_e = (1/3)\sigma_e \, a$ eqn 9.3

where a is the cross section area of the plate.

The stress distribution around the hole may be shown[98] to be

$$\sigma = (\sigma_n/2)(2 + \rho^2/x^2 + 3\rho^4/x^4) \qquad \text{eqn 9.4}$$

If the load on the plate is increased to $P > P_e$, but not enough to cause fully plastic yielding, the stress distribution will be as shown in fig.9.10 by A B C, with A B representing the uniform stress across the plastic zone.

The curve DBC may be approximated by the elastic stress distribution equation with only small error[98], provided

(a) the plate is very wide,

(b) the plastic zone x_1 is relatively small.

i.e. $\sigma = (\sigma_n/2)(2 + \rho^2/x^2 + 3\rho^4/x^4)$ eqn 9.4

This curve must pass through point B

i.e. $x = x_1$ and $\sigma = \sigma_e$

or $\sigma_n = 2\sigma_e/(2 + \rho^2/x_1^2 + 3\rho^4/x_1^4)$ eqn 9.5

That is, σ_n represents the nominal stress at some distance from the hole (erroneous) with the assumption that the stresses on the plastic region are represented by ordinates to the curve DB instead of AB, but the error is small, especially when x_1 is small.

Therefore, the load P corresponding to a plastic zone x_1 is

$$P = \sigma_n \, a$$

or $P = 2\sigma_e \, a/(2 + \rho^2/x_1^2 + 3\rho^4/x_1^4)$ eqn 9.6

but $P_e = (1/3)\sigma_e \, a$ eqn 9.3

$\therefore$ the load carrying capacity of the plate with a plastic zone x_1 is increased to P/P_e where

$$P/P_e = 6/(2 + \rho^2/x_1^2 + 3\rho^4/x_1^4) \qquad \text{eqn 9.7}$$

The variation in the load carrying capacity P/P_e as the depth of the plastic zone x_1 increases is shown in fig.9.11.

Now, let's assume that the dynamic yield stress of the material is σ_e, and the critical depth of plastic deformation zone required for fatigue failure (complete separation) is h_c. If it is further assumed that this critical plastic deformation zone size h_c is achieved at $P/P_e = 2$, when the hole is of radius $\rho = \rho_c$ say

i.e. x_1 in equation 9.7 equals $\rho_c + h_c$, and $P/P_e = 2$.

Therefore, from equation 9.7

$$2 = 6/(2 + \rho_c^2/x_1^2 + 3\rho_c^4/x_1^4)$$

or $$x_1^4 - \rho_c^2 x_1^2 - 3\rho_c^4 = 0$$

$$\therefore \quad x_1^2 = \frac{\rho_c^2 \pm \rho_c^2\sqrt{13}}{2}$$

$$= 2.3\ \rho_c^2$$

or $$x_1 = 1.52\ \rho_c$$

but $x_1 = \rho_c + h_c$ see fig.9.11

$$\therefore \quad h_c = 0.52\ \rho_c \qquad \text{eqn 9.8}$$

where ρ_c is the hole radius such that the critical depth of plastic zone h_c is achieved at $P/P_e = 2$.

Now, for a plate with a hole of radius $\rho = b\rho_c$, the load carrying capacity P/P_e, such that the same critical depth of plastic deformation h_c is achieved may be obtained by substituting $\rho = b\rho_c$ and $x_1 = b\rho_c + h_c$ in equation 9.7

i.e. $$P/P_e = 6/\left[\, 2 + (b\rho_c)^2/(b\rho_c + h_c)^2 + 3(b\rho_c)^4/(b\rho_c + h_c)^4 \,\right]$$

but $$h_c = 0.52\ \rho_c \qquad \text{eqn 9.8}$$

$$\therefore \quad P/P_e = 6/\left[\, 2 + b^2/(b + 0.52)^2 + 3b^4/(b + 0.52)^4 \,\right]$$

$$\text{eqn 9.9}$$

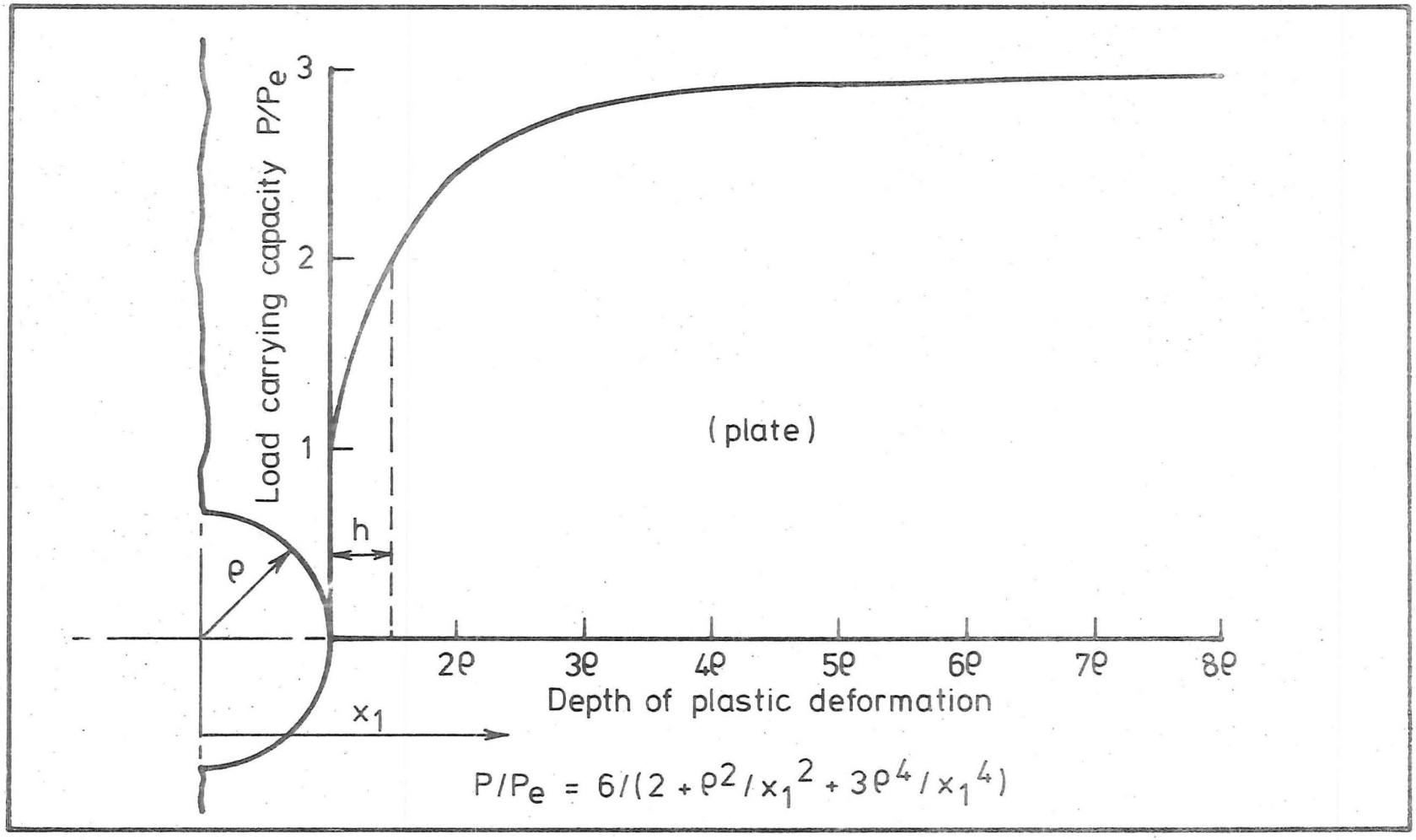

Fig. 9·11. EFFECT OF INELASTIC STRAIN ON THE LOAD CARRYING CAPACITY OF A PLATE CONTAINING A CIRCULAR HOLE

The load carrying capacity P/P_e of a plate containing a hole $\rho = b\rho_c$ may be calculated from equation 9.9.

The variation in P/P_e with $\rho = b\rho_c$ is illustrated in fig. 9.12.

For the case when the hole radius ρ ($= b\rho_c$) approaches zero, i.e. $b \to 0$, from equation 9.9

$P/P_e \to 3$ as $b \to 0$

but $P_e = (1/3)\sigma_e a$ eqn 9.3

$\therefore$ $P \to \sigma_e a$ when $b \to 0$

where a = cross section area of the plate

and assuming $\sigma_e = \sigma_{DS}$

then $P \to \sigma_{DS} a$

i.e. the case of a "plain" specimen without notch.

For the case where the hole radius is increasing, such that $\rho = b\rho_c$ is very large, but still small in comparison to the width of the plate, from equation 9.9 and fig.9.12

$P/P_e \to 1$ as b becomes very large

or $P \simeq P_e$

but $P_e = (1/3)\sigma_e a$ eqn 9.3

$\therefore$ $P \simeq (1/3)\sigma_e a$ where $K_t = 3$ or $K_f \to K_t$

where K_f is the fatigue strength reduction factor.

Therefore, for geometrically similar specimens, and assuming that the critical depth of plastic deformation zone h_c is only a function of material and does not vary with specimen size, this would explain the "size effect" generally observed in notched fatigue specimens.

The above discussion may also be extended to the most common notched specimens, that is, the case of a cylindrical specimen with a circumferential notch. Provided that the notch depth is at least equal to the notch root radius ρ, the stress distribution around the notch root may be expressed[111] by

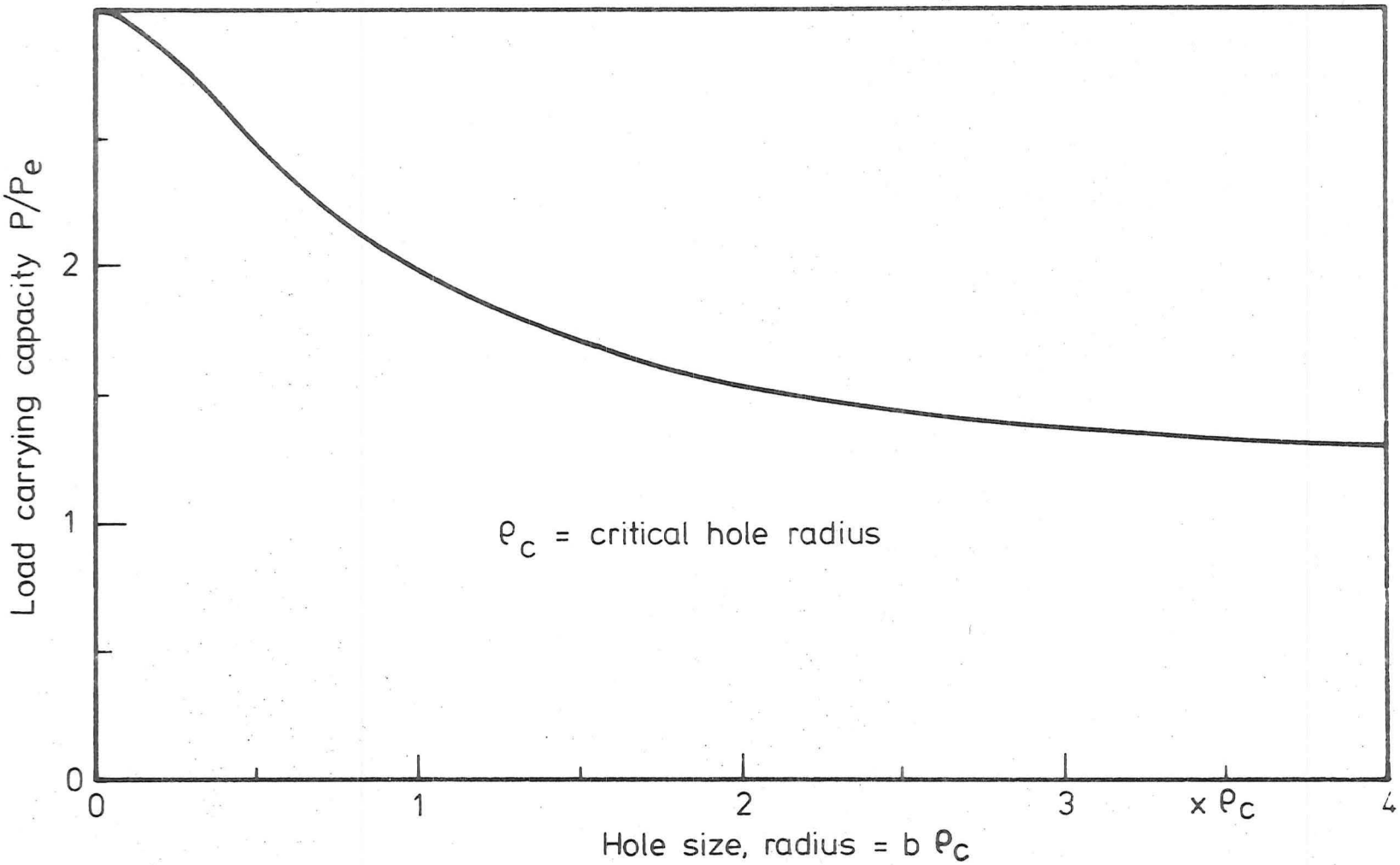

Fig. 9·12 RELATIONSHIP BETWEEN P/P_e AND HOLE SIZE ρ SUCH THAT THE CRITICAL DEPTH OF PLASTIC ZONE IS ACHIEVED

the following equation

$$\sigma = \frac{\sigma_{max}}{2\sqrt{(1 + \frac{2x}{\rho})}} \left[1 + \frac{1}{(1 + \frac{2x}{\rho})} \right] \qquad \text{eqn 9.10}$$

where σ_{max} is the stress at the root of the notch.

Referring to fig.9.13, and let the nominal stress applied at some distance away from the notch root be σ_n

$\therefore \quad \sigma_{max} = K_t \sigma_n$

Again, let the specimen be subjected to an axial load P_e such that the maximum stress at the notch root just reaches the yield stress σ_e of the material

i.e. $\sigma_{max} = \sigma_e = K_t \sigma_n$ eqn 9.11

or $P_e = \sigma_n a = \sigma_e a/K_t$ eqn 9.12

where a is the minimum cross section area of the specimen.

Again assuming that, for small plastic deformation zones, the stress distribution may be approximated by the elastic stress distribution, i.e. equation 9.10.

Referring to fig.9.13, at point B

$x = x_1$ and $\sigma = \sigma_e$

from equation 9.10

$$\sigma_e = \frac{\sigma_{max}}{2\sqrt{(1 + \frac{2x_1}{\rho})}} \left[1 + \frac{1}{1 + \frac{2x_1}{\rho}} \right] \qquad \text{eqn 9.13}$$

but $\sigma_{max} = K_t \sigma_n$ eqn 9.11

$$\therefore \quad \sigma_n = \frac{2\sigma_e}{K_t} \sqrt{(1 + \frac{2x_1}{\rho})} \Big/ \left(1 + \frac{1}{1 + \frac{2x_1}{\rho}} \right) \qquad \text{eqn 9.14}$$

also $P = \sigma_n a$

and $P_e = \sigma_e a/K_t$ eqn 9.12

$$\therefore \quad \frac{P}{P_e} = 2\sqrt{(1 + \frac{2x_1}{\rho})} \Big/ \left(1 + \frac{1}{1 + \frac{2x_1}{\rho}} \right) \qquad \text{eqn 9.15}$$

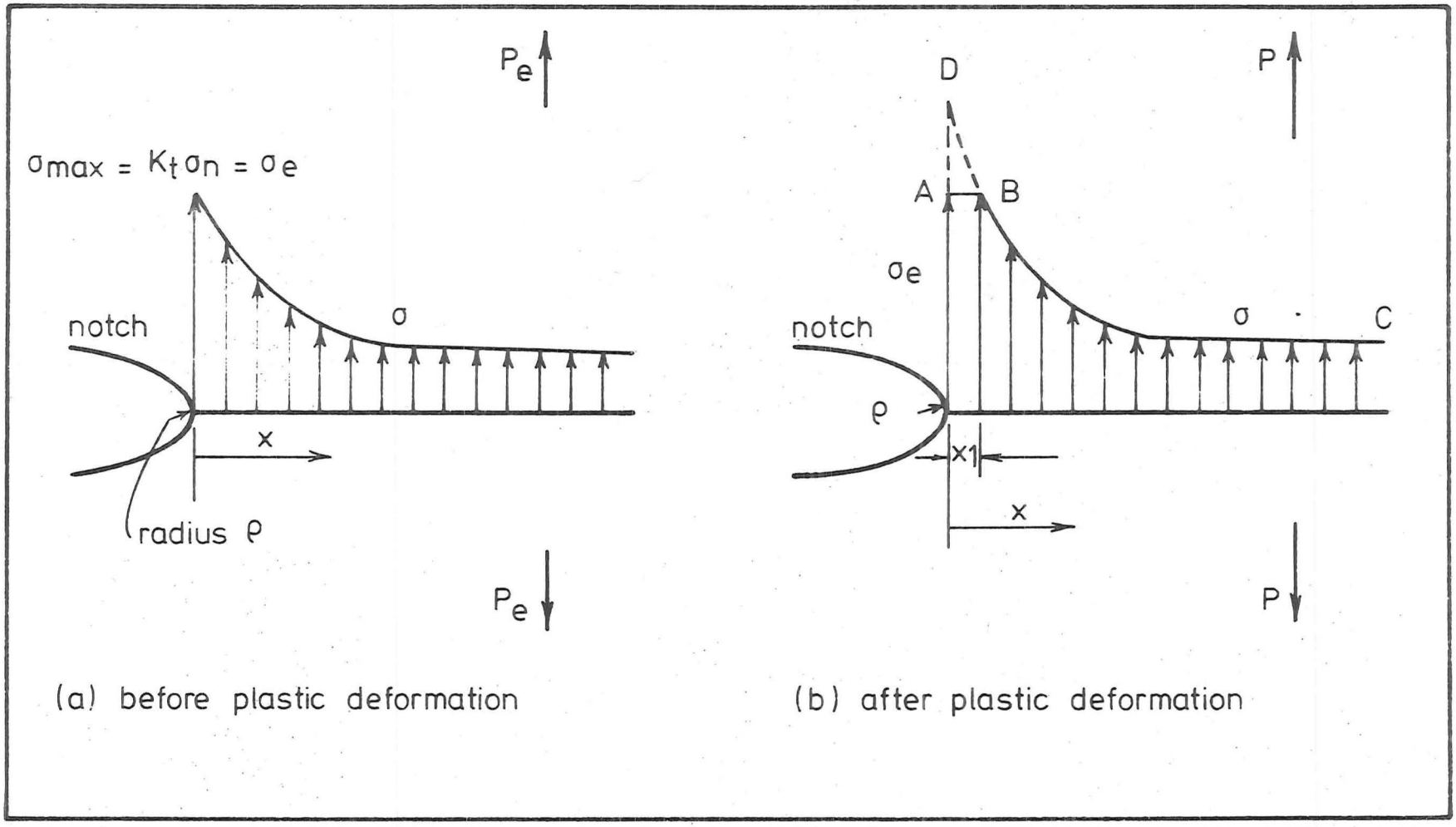

Fig. 9·13 STRESS DISTRIBUTION OF A CIRCUMFERENTIALLY NOTCHED MEMBER BEFORE AND AFTER STRESS REDISTRIBUTION.

where x_1 is the depth of plastic zone measured from the notch root.

The relationship between the load carrying capacity P/P_e and the depth of plastic zone x_1 is shown in fig.9.14.

Again assuming that a critical depth of plastic deformation zone h_c is needed before fatigue cracks can propagate to failure, and let's assume that this critical depth of plastic deformation zone $h_c = 0.5\rho$ at $\rho = \rho_c$ say

i.e. $h_c = o.5\rho_c$ eqn 9.16

From equation 9.15 and fig.9.14

at $h_c = 0.5\ \rho_c$

i.e. $x_1 = 0.5\ \rho_c$ and $\rho = \rho_c$

$P/P_e = 1.89$

Now, for a member with a notch root radius $\rho = b\rho_c$, the load carrying capacity P/P_e such that the same critical depth of plastic deformation h_c is achieved, may be obtained by substituting $\rho = b\rho_c$ and $x_1 = 0.5\ \rho_c$ in equation 9.15,

i.e. $P/P_e = 2\sqrt{(1 + \frac{1}{b})}/\left[1 + 1/(1 + \frac{1}{b})\right]$ eqn 9.17

The load carrying capacity P/P_e of a circumferentially notched member whose notch root radius $\rho = b\rho_c$ may then be obtained from equation 9.17.

The relationship between P/P_e and $\rho = b\rho_c$ from equation 9.17 is illustrated in fig.9.15.

From fig.9.15, P/P_e decreases as $\rho = b\rho_c$ increases.

Now let $P/P_e = A$

because $P_e = \sigma_e\ a/K_t$ eqn 9.12

$\therefore \quad P = A\ a\ \sigma_e/K_t$ eqn 9.18

but the fatigue strength reduction factor

$$K_f = \frac{\sigma_{DS}\ \text{(plain specimen)}}{\sigma_{DS}\ \text{(notched specimen)}}$$

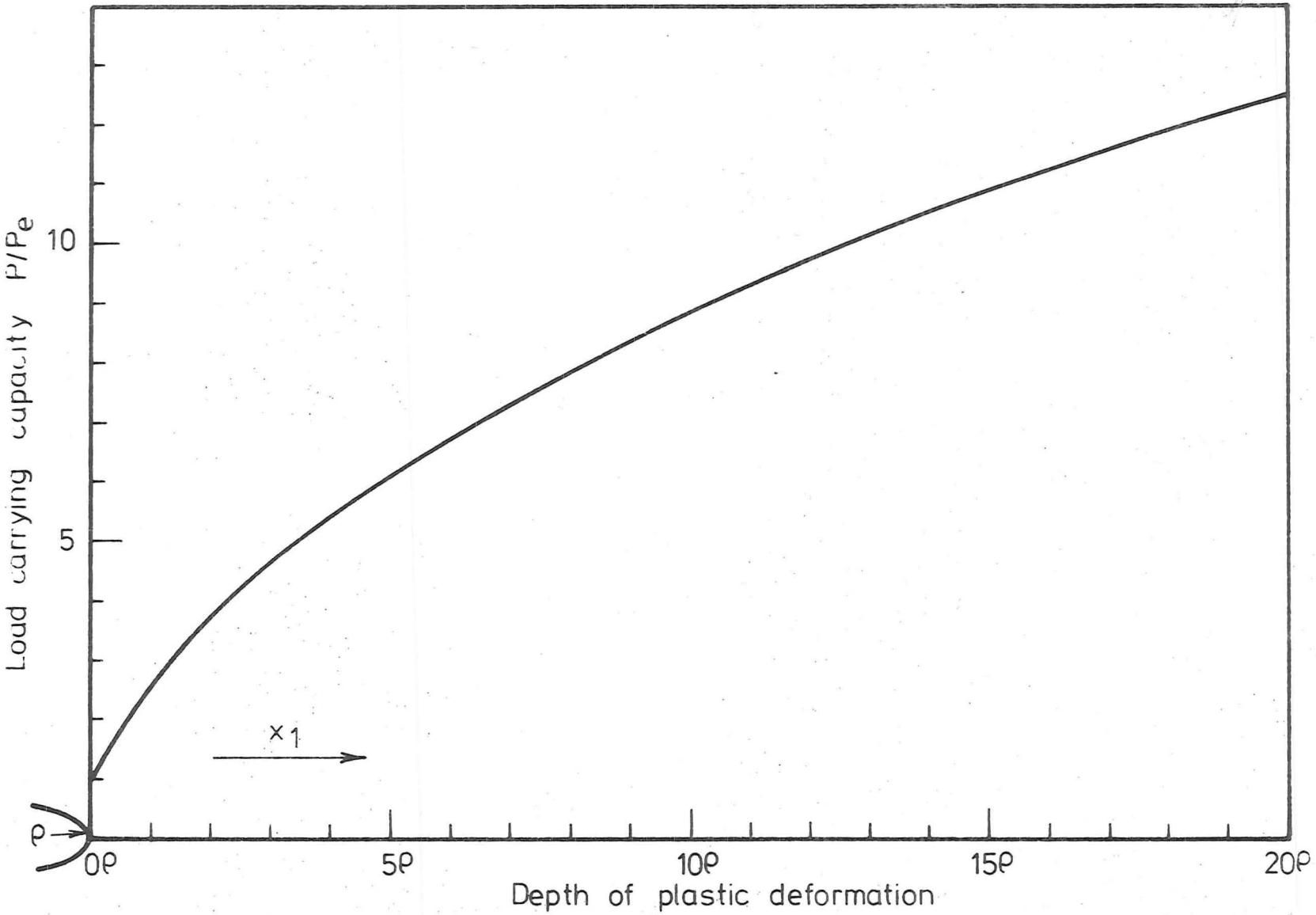

Fig. 9·14 EFFECT OF INELASTIC STRAIN ON THE LOAD CARRYING CAPACITY OF A CIRCUMFERENTIALLY NOTCHED MEMBER.

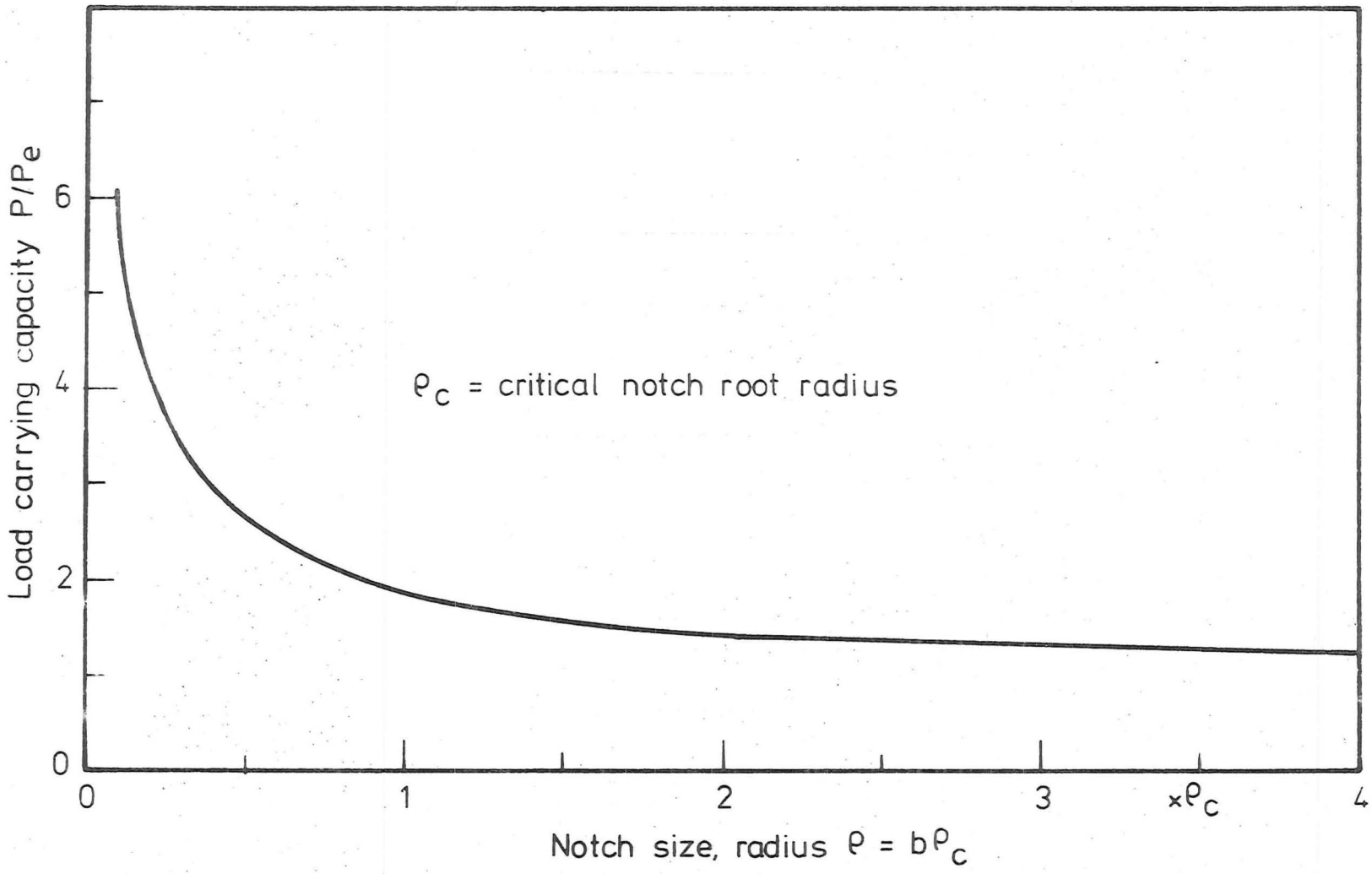

Fig. 9·15 RELATIONSHIP BETWEEN P/P_e AND NOTCH SIZE ρ SUCH THAT THE CRITICAL DEPTH OF PLASTIC ZONE IS ACHIEVED

and σ_{DS} (notched specimen) = P/a

$\therefore$ $K_f = [K_t \sigma_{DS}(\text{plain})]/(\sigma_e A)$

assuming that $\sigma_e = \sigma_{DS}$ (plain)

$\therefore$ $K_f = K_t/A$ eqn 9.19

Now, for the case of geometrically similar specimens, i.e. K_t remains constant, increasing specimen size will also increase the notch root radius ρ ($=b\rho_c$), therefore increases b.

Referring to fig.9.15, when the specimen size increases, i.e. $\rho = b\rho_c$ increases, $P/P_e = A$ decreases.

Therefore, $K_f = K_t/A$ increases with specimen size, or the notched fatigue strength decreases with increasing specimen size, (assuming that the critical depth of plastic deformation zone h_c does not vary with specimen size). This can again account for the "size effect" generally observed in notched fatigue specimens.

For the case of constant specimen size but varying notch root radius, from equation 9.19

i.e. $K_f = K_t/A$ eqn 9.19

and referring to fig.9.15,

as $\rho = b\rho_c$ increases, i.e. K_t decreases,

$P/P_e = A$ decreases

and $P/P_e \to 1$ for very large ρ ($= b\rho_c$), i.e. K_t very small

but $K_f = K_t/A$ eqn 9.19

$\therefore$ $K_f \to K_t$ for very large ρ ($= b\rho_c$)

or $K_f \to K_t$ when K_t is small.

If $\rho = b\rho_c$ decreases, K_t increases (constant specimen size) and from fig. 9.15

$A = P/P_e$ increases rapidly as $\rho = b\rho_c$ decreases,

i.e. $A \gg 1$

or K_f ($= K_t/A$) decreases rapidly

i.e. $K_f << K_t$ when $\rho = b\rho_c$ is very small,

or $K_f << K_t$ when K_t is large.

Under normal conditions $P/P_e = A$ is always greater than 1, see fig.9.15,

i.e. K_f $(= K_t/A)$ is always less than K_t.

Also, from the rotating bending results in fig.9.6, it appears that for high strength materials, the critical depth of plastically deformed zone r_c $(= h_c/r_1)$ required for fatigue cracks to propagate is small. That is, the increase in the load carrying capacity (hence, the fatigue limit) for a high strength material is less than that for a soft material, hence the fatigue strength reduction factor

$$K_f = \frac{\text{plain fatigue limit}}{\text{notched fatigue limit}}$$

approaches K_t as σ_y increases. This would thus account for the higher values of Notch Sensitivity Index q or more "notch sensitive" for the high strength materials.

The above illustrations suggest that most of the fatigue properties of the notched specimens may probably be explained by the need to develop a critical depth of plastic deformation zone when the stress distribution in the fatigue specimen is non-uniform, before fatigue cracks can propagate to failure. If this critical depth is not achieved, micro-cracks may form when the highly stressed area at the notch root has deformed after dynamic yielding, and the necessary fatigue saturation strain ε_p^* of the material has been reached at the notch root, but these micro-cracks will remain non-propagating until the necessary critical depth of plastic deformation zone has been developed.

The analysis as shown in section 5.2 is strictly speaking only applicable to the simple case of plane bending, this

analysis, nevertheless, shows the importance of a small layer of plastically deformed fibre in determining the load carrying capacity (hence, the fatigue limit) of a rotating bending member.

9.4 FRACTOGRAPHY:

The results of fractography study in section 8.7 show that well defined fatigue striations were formed on both the direct stress and the rotating bending fracture surfaces, and similar striation patterns were observed on both coarse and fine grained specimens. This may be taken to indicate that the crack propagation process (stage II) under both direct stress and rotating bending loading is not affected by the polycrystalline grain size, as the striation formation has been shown to be mainly associated with stage II crack propagation and has a one to one relationship with the stress cycles[45,46].

On the direct stress fatigue fracture surfaces, tire tracks were not observed, instead, random indentation marks due to loose particles were formed, indicating the absence of secondary forces or the alignment of the direct stress machine was of reasonable order. Tire tracks were, however, a common feature on the rotating bending fracture surfaces and were generally formed within the "crescent" shaped area where a considerable amount of rubbing and pressing had taken place.

Few mechanisms have been proposed for the formation of the tire tracks, Ansell et al[112] suggested that hydrogen contained in the material diffuses into the site of high hydrostatic tension ahead of the crack tip during the tensile half cycle, and precipitates out during the compression half cycle, resulting in the formation of rows of voids. Tokuda[113]

suggested that tire tracks may be the result of piling up of dislocation array against an obstacle. Beachem[114] proposed that tire tracks are formed when the local portions of the fracture surfaces rub against each other after a crack front has passed, and he further suggested three types of tire tracks formed by three different mechanisms. Koterazawa et al[46] on the other hand suggested that tire tracks are impressions made by protrusions or edges on the mating fracture surface each time repeated stress is applied, and different types of tire tracks are formed according to the size and shape of the protrusions, and the secondary forces on the mating surface.

Both the hypothesis of Ansell et al and Tokuda can be ruled out, because their models would suggest tire tracks of similar dimensions at the same position on the mating surface, which is not always the case. The observations from this investigation tend to support the hypothesis of Koterazawa et al, as tire tracks were not observed on the direct stress fracture surfaces, where the secondary forces on the fracture surface were absent, because of good alignment of the direct stress fatigue machine. On the rotating bending fracture surfaces, tire tracks were only observed within the "crescent" shaped region where rubbing and pressing have taken place. Also, as is shown in fig.8.47, tire tracks of different shapes may be found together.

Although tire tracks do not generally give any information regarding the rate or the mechanism of crack propagation, their presence on a fracture surface is a definite evidence that the fracture was by fatigue cycling. The direction and spacing of the tire tracks may also suggest the type and magnitude of the secondary forces applied. Therefore, tire tracks are a useful tool in the failure analysis, although they may not be as

valuable as striations in the study of fatigue mechanism.

CHAPTER 10.

CONCLUSIONS.

The complete absence of the sharp yield drops on the tensile flow curves of the fatigued specimens, indicates that the extent of dynamic strain ageing during normal fatigue testings is not sufficient to result in complete Cottrell atmosphere formation or Stage I ageing. It also appears that dynamic strain ageing (if any) affects the coarse grained steels more than the fine grained steels.

The results from the tensile tests on specimens fatigued at stresses just below the direct stress fatigue limit, the etching results of the special high nitrogen low carbon steel, the microhardness surveys on the run-out specimens and the temperature rise monitoring during direct stress testings show conclusively that the dynamic yield stress of low carbon steels is somewhat below the direct stress fatigue limit. The results of a parallel research programme[110] have suggested that the dynamic yield stress for low carbon steels is only about 3 to 6% below the direct stress fatigue limit.

Accepting the hypothesis of Erasmus[12] that a fatigue saturation strain ε_p^* is needed before fatigue damage in the form of active slip bands, intrusions and extrusions, etc., can develop, and that this fatigue saturation strain ε_p^* may be described by the equation

$$\sigma_a = K(\varepsilon_p^*)^n \qquad \text{eqn 9.1}$$

the fatigue saturation strain ε_p^* was shown to vary with polycrystalline grain size, with higher value of ε_p^* for lower static yield strength or larger polycrystalline grain size, suggesting

that softer materials will deform more easily during fatigue cycling.

Under direct stress cycling, when the cyclic stress amplitude is above the direct stress fatigue limit of the material, the fatigue saturation strain ε_p^* is accumulated after prolonged cycling, and widespread active slip bands are nucleated, which in turn develop into propagating fatigue cracks and result in fatigue failure. While cyclic stressing below the direct stress fatigue limit, the necessary fatigue saturation strain of the material cannot be achieved, and only isolated patches of ill-defined slip markings are formed on areas of high localized stress.

Under rotating bending loading, when the calculated applied stress σ_{app} (calculated from the elastic theory) is above the direct stress fatigue limit σ_{DS} of the material, dynamic yielding of the highly stressed outer fibre, where $\sigma \geqslant \sigma_{DS}$, results in stress redistribution. The formation of this plastically deformed layer after dynamic yielding results in an increase in the load carrying capacity (hence, the fatigue strength) of a rotating bending member. It also appears that a critical depth of plastic deformation zone is required for fatigue failure to occur under rotating bending loading, and the size of this critical plastic zone decreases with increasing static yield strength or decreasing grain size.

The higher fatigue strength generally obtained under rotating bending testing as compared to that under direct stress testing is due to the formation of this small layer of plastic zone after stress redistribution. The increase in strength appears to be determined by the depth of the plastic zone formed, and not the actual stress on the rotating bending specimen surface as suggested by Forrest and Tapsell[56,57]. The main

deficiency in the model of Forrest and Tapsell is that it could not account for the "size effect" generally observed under rotating bending testings and in the notched fatigue specimens.

According to the model of Forrest and Tapsell, similar microstructural changes are expected to develop on both the direct stress and rotating bending specimen surfaces when fatigued at equivalent stress levels, that is, microstructural changes on a run-out direct stress specimen should be similar to those on the surface of a run-out rotating bending specimen, as their model suggests similar surface stress on both the direct stress and rotating bending specimen surfaces at the corresponding fatigue limit. The microstructural changes as observed in this investigation, however, showed that under rotating bending loading, cyclic stresses (σ_{app}) between σ_{DS} and σ_{RB} (i.e. the run-out specimens) will result in widespread active slip bands, whereas under direct stress loading, cyclic stresses just below σ_{DS} (i.e. the run-out specimens) are not sufficient to cause the nucleation of widespread active slip bands. The microstructural changes from the rotating bending specimens showed that at stresses between σ_{DS} and σ_{RB}, i.e. $\sigma_{DS} < \sigma_{app} < \sigma_{RB}$, the fatigue saturation strain ε_p^* is accumulated on the specimen surface and widespread fatigue damage in the form of active slip bands are developed. However, as the critical depth of plastic deformation can only be achieved at stresses equal to or greater than the rotating bending fatigue limit σ_{RB}, stresses between σ_{DS} and σ_{RB} are not sufficient to develop the active slip bands into propagating cracks to cause failure, and stresses above the rotating bending fatigue limit are necessary to result in fatigue failure.

The higher value of fatigue saturation strain ε_p^* in softer materials may be taken to indicate that softer materials are

able to deform more easily and, under rotating bending loading, this will result in a thickened depth of plastic deformation zone which in turn results in a higher increase in the load carrying capacity of a softer material, which explains the increase in the ratio

$$\frac{\text{rotating bending fatigue limit}}{\text{direct stress fatigue limit}}$$

with decreasing material strength.

The "size effect" generally observed in the rotating bending, bending and notched fatigue specimens may be explained by the need to develop a critical depth of plastic deformation zone when the stress distribution is non-uniform, before propagating cracks can develop to cause failure. Under bending or rotating bending types of loading with similar applied stress σ_{app}, a specimen with twice the diameter will theoretically develop a plastic zone twice as deep, therefore, the applied stress σ_{app} needed to develop the required critical plastic zone in a larger specimen will be less than that of a smaller specimen, hence, the decrease in the fatigue strength (limit) with increasing specimen diameter.

The existence of a dynamic yield stress below the direct stress fatigue limit of the material, and the need to develop a minimum depth of plastic deformation zone before fatigue cracks can propagate under non-uniform stress distribution also account for most of the fatigue properties of the notched specimens, for example, the variation of K_f with K_t, the size effect and the formation of non-propagating cracks at the notch root at stresses between σ_{DS}/K_t and the notched fatigue limit.

The effect of stress redistribution under bending or rotating bending types of loading also casts doubt on the

results and deductions of some published works with understressing and coaxing, as all of the published results from understressing and coaxing were obtained from rotating bending types of testing, hence any increase in fatigue strength may simply be the result of a more gradual stress redistribution which enables a thicker plastic zone to develop under understressing or coaxing testings.

REFERENCES.

1. RANKINE, W.J.M., 1843, Proc. Instn. Civ. Engrs, Vol.2, P.105.

2. WOHLER, A.Z., 1871, Engineering, Vol.11, P.199.

3. MOORE, H.F. and KOMMERS, J.B., 1927, "The Fatigue of Metals", McGraw-Hill, New York.

4. LESSELLS, J.M., 1954, "Strength and Resistance of Metals", Wiley, London, P.172.

5. IRWIN, P.L., 1925, Proc. Am. Soc. Test. Mater., Vol.25, P.53.

6. IRWIN, P.L., 1926, Proc. Am. Soc. Test. Mater., vol.26, P.218.

7. MANN, J.Y., 1967, "Fatigue of Materials", Melbourne University Press, Victoria.

8. FRANCE, R.D., 1931, Proc. Am. Soc. Test. Mater., vol.31, P.176.

9. GOUGH, H.J. and SOPWITH, D.G., 1933, Engineering, vol.136, P.75.

10. LOW, A.C., 1955, J.R. Aeronaut. Soc., vol.59, P.629.

11. CINA, B., 1960, J.I. S.I., vol.194, P.324.

12. ERASMUS, L.A., 1972, Ph.D. Thesis, University of Cape Town, South Africa.

13. LEVY, J.C. and KANITKAR, S.L., 1961, J.I.S.I., vol.197, P.296.

14. SINCLAR, G.M., 1952, Proc. Am. Soc. Test. Mater., vol.52, P.743.

15. OATES, G. and WILSON, D.V., 1964, Acta. Met., vol.12, P.21.

16. LEVY, J.C., 1957, Metallurgia, vol.56, P.71.

17. LIPSITT, H.A. and HORNE, G.T., 1957, Proc. Am. Soc. Test. Mater., vol.57, P.587.

18. ABDEL-RAOUF, H., et al., 1973, "Fatigue at Elevated Temperatures", Am. Soc. Test. Mater., STP 520, P.300.

19. KLESNIL, M., et al., 1965, J.I.S.I., vol.203, P.47.

20. YEN, C.S., 1969, "Metal Fatigue", P.107, Wiley, New York.

21. WOOD, W.A., et al., 1963, Acta. Met., vol.11, P.643.

22. COFFIN, L.F., 1962, Apply Mat. Research, vol.1, P.129.

23. WOOD, W.A., et al., 1964, Trans A.I.M.E., vol.230, P.511.

24. THOMPSON, N. and WADSWORTH, N.J., 1958, Advances in Physics, vol.7, P.72.

25. LAIRD, C., 1967, "Fatigue crack Propagation", (Special Tech. Publ. No.415) Philadelphia, Pa., (A.S.T.M.), P.131.

26. GROSSKREUTZ, J.C., 1964, "Fatigue - an Interdisciplinary Approach", Syracuse University Press, New York, P.27.

27. PLUMBRIDGE, W.J. and RYDER, D.A., 1969, Metallurgical Reviews No.136, vol.14, P.119.

28. FORSYTH, P.J.E., 1951, J. Inst. Metals, vol.80, P.181.

29. WOOD, W.A. and DAVIES, R.B., 1953, Proc. Roy. Soc., A.220, P.255.

30. SEGALL, R.L. and PARTRIDGE, P.G., 1959, Phil. Mag., vol.4, P.912.

31. SNOWDEN, K.U., 1963, Acta. Met., vol.11, P.675.

32. SEGALL, R.L. and FINNEY, J.M., 1963, Acta. Met., vol.11, P.685.

33. KLESNIL, M. and LUKAS, P., 1965, J.I.S.I., vol.203, P.1043.

34. FELTNER, C.E. and LAIRD, C., 1967, Acta. Met., vol.15, P.1633.

35. HIRSCH, P.B., et al., 1959, Phil. Mag., vol.4, P.721.

36. CROSSKREUTZ, J.C. and WALDOWN, P., 1963, Acta. Met., vol.11, P.717.

37. FORSYTH, P.J.E., 1963, Acta. Met., vol.11, P.703.

38. LUKAS, P., et al., Phys. Stat. Sol., 1968, vol.27, P.545.

39. WILSON, D.V. and TROMANS, J.K., 1970, Acta. Met., vol.18, P.1197.

40. HAM, R.K., 1962, Phil. Mag., vol.7, P.1177.

41. WILSDORF, H.G.F. and SCHMITZ, J., 1962, J. Appl. Phys., vol.33, P.1750.

42. THOMPSON, N., WADSWORTH, N. and LOUAT, N., 1956, Phil. Mag., vol.1, P.113.

43. WOOD, W.A. and GATES, R.G., 1968, J. Inst. Metals, vol.96, P.242.

44. FORSYTH, P.J.F., STUBBINGTON, C.A. and CLARK, D., 1961, J. Inst. Metals, vol.90, P.238.

45. FORSYTH, P.J.E. and RYDER, D.A., 1961, Metallurgia, vol.63, P.117.

46. KOTERAZAWA, R. and SHIMO, D., 1971, Bull. J.S.M.E.,vol 14, No.68, P.127.

47. HERTZBERG, R.W., 1967, "Fatigue Crack Propagation", A.S.T.M., STP 415, Philadelphia Pa., P.205.

48. MEYN, D.A., 1968, Trans. Am. Soc. Metals, vol.61, No.1, P.42.

49. PELLOUX, R.M.N., 1969, Trans. Am. Soc. Metals, vol.62, P.281.

50. GROSSKREUTZ, J.C. and SHAW, G.G., "Fatigue Crack Propagation" A.S.T.M., STP 415, Philadelphia Pa., P.226.

51. KLESNIL, M. and LUKAS, P., 1969, International Conference on Fracture, Brighton, Chapman and Hall, P.725.

52. AWATANI, J., KATAGIRI, K. and SHIRAISHI, T., 1976, Met. Trans., vol.7A, P.807.

53. KOTERAZAWA, R., et al., 1973, Trans. A.S.M.E., vol.95, P.202.

54. HORGER, O.J. and NEIFERT, H.R., 1939, Proc. Am. Soc. Test. Mater., vol.39, P.723.

55. FROST, N.E. and DENTON, K., 1962, Metallurgia, vol.65, P.287.

56. FORREST, P.G. and TAPSELL, H.J., 1952, Engineering, vol.173, P.757.

57. FORREST, P.G. and TAPSELL, H.J., 1954, Proc. Instn. Mech. Engrs., vol.168, P.763.

58. TETELMAN, A.S. and McEVILY, A.J., 1967, "Fracture of Structural Materials", Wiley, New York.

59. HEYWOOD, R.B., 1962, "Design against Fatigue", Chapman and Hall, London.

60. NEUBER, H., "Theory of Notch Stresses", 1946, Edwards, J.W., Ann Arbor, Michigan.

61. MOORE, H.F. and MORKOVIN, P., 1944, Proc. Am. Soc. Test. Mater., vol.44, P.137.

62. FROST, N.E., MARSH, K.J. and POOK, L.P., 1974, "Metal Fatigue", Clarendon Press, Oxford.

63. KARRY, R.W. and DOLAN, T.J., 1953, Proc. Am. Soc. Test. Mater., vol.53, P.789.

64. PETERSON, R.D., 1966, "Stress Concentration Design Factors" John Wiley, New York.

65. FORREST, P.G., 1956, "International Conference on Fatigue", Inst. of Mech. Engrs., P.171.

66. FORREST, P.G., 1962, "Fatigue of Metals", Addison-Wesley, London, P.134.

67. ERASMUS, L.A., et al., 1968, "Advanced Ferrous Metallurgy", Seminar Notes, University of Canterbury, Christchurch, N.Z.

68. DALBY, W.E., 1913, Proc. Roy. Soc., vol.A88, P.281.

69. COTTRELL, A.H. and BILBY, B.A., 1949, Proc. Roy. Soc., vol.A62, P.49.

70. JOHNSTON, W.G. and GILMAN, J.J., 1959, J. Appl. Phys., vol.30, P.129.

71. HAHN, G.T., 1962, Acta. Met., vol.10, P.727.

72. HUNDY, B.B., 1954, J.I.S.I., vol.178, P.34.

73. BAIRD, J.D., 1963, "Strain-Ageing of Steel - A Critical Review", Iron and Steel, vol.36, P.186.

74. BAIRD, J.D., 1971, "The Effect of Strain-Ageing due to Interstitial Solutes on the Mechanical Properties of Metals", International Conf. on Mech. Behaviour of Material, Japan, Metallurgical Review, vol.16, P.1.

75. BISHOP, S.M., SPRETNAK, J.W. and FONTANA, M.G., 1953, Trans. Am. Soc. Metals, vol.45, P.993.

76. FERRO, A. and MONTALENTI, G., 1963, Phil. Mag., vol.8, P.105.

77. PUSKAR, A., 1976, Met. Trans., vol.7A, P.1529.

78. KETTUNEN, P.O., 1964, J.I.S.I., vol.202, P.209.

79. FORREST, P.G. and TATE, A.E.L., 1964-65, J. Inst. Metals, vol.93, P.438.

80. THOMPSON, A.W. and BACKOFEN, W.A., 1971, Acta. Met., vol.19, P.597.

81. GIBSON, R.C., HAYDEN, H.W. and BROPHY, J.H., 1968, Trans. Am. Soc. Metals, vol.61, P.85.

82. YAMADA, T., HATANAKA, K. and HIROSE, Y., 1973, Proc. of 16th Jap. Congr. on Matls. Resh., Kyoto, P.143.

83. YOSHIKAWA, A. and SUGENTO, T., 1965, Trans. Met. Soc., A.I.M.E., vol.233, P.1314.

84. CRACKNELL, A. and PETCH, N.J., 1955, Acta. Met., vol.3, P.186.

85. HESLOP, J. and PETCH, N.J., 1956, Phil. Mag., vol.1, P.866.

86. ROSENFIELD, A.R., 1962-63, J. Inst. Metals, vol.91, P.104.

87. PHILLIPS, R. and CHAPMAN, J.A., 1965, J.I.S.I., vol.203, P.511.

88. ERASMUS, L.A., 1969, Proc. Second Australasian Conf. on the Mechanics of Structures and Materials, University of Adelaide, Australia, P.16.1.

89. HOLLOMAN, J.H., et al., 1966, J. of Materials, vol.1, P.689.

90. STEPHENS, R.I., 1968, J. of Materials, vol.3, No.2, P.386.

91. ABEL, A. and MUIR, H., 1973, Acta. Met., vol.21, P.93.

92. ABEL, A. and MUIR, H., 1973, Acta. Met., vol.21, P.99.

93. LUTHER, R.G. and WILLIAMS, T.R.G., 1977, Metal Sci., vol.5, P.164.

94. SUITS, J.C. and CHALMERS, B., 1961, Acta. Met., vol.9, P.854.

95. BROWN, N. and EKVALL, R.A., 1962, Acta. Met., vol.10, P.1101.

96. BROWN, N. and KOSSOWSKY, R., 1966, Acta. Met., vol.14, P.131.

97. FORD, H., 1972, "Advanced Mechanics of Materials", Longman.

98. SEELY, F.B., et al., 1952, "Advanced Mechanics of Materials" Wiley, London.

99. MINAMISAWA, C., et al., 1972, Proc. of the 15th Jap. Congr. Matls. Resch., The Soc. of Matls. Sci., Kyoto, Japan, P.86.

100. BLATHERWICK, A.A. and LAZEN, B.J., 1956, Proc. Am. Soc. Test. Mater., vol.56, P.1012.

101. MACKOWIAK, J., 1965, "Physical Chemistry for Metallurgists", Allen and Unwin, London.

102. ERASMUS, L.A., 1964, J.I.S.I., vol.202, P.32.

103. ERASMUS, L.A., 1964, J.I.S.I., vol.202, P.1018.

104. ERASMUS, L.A., 1966, Iron and Steel, vol.40, P.477.

105. LESLIE, W.C., et al., 1954, Trans. Am Soc. Metals, vol.46, P.1470.

106. WHITELEY, J.H., 1943, J.I.S.I., vol.148, P.513.

107. MILLER, O.O., 1951, Trans. Am. Soc. Metals, vol.43, P.260.

108. -- 1962, "The Determination of Aluminium Nitride in Steel", The United Steel Companies Ltd., Swindon Laboratories, Rotherham.

109. WILSON, D.V. and MINTZ, B., 1965, Acta. Met., vol.13, P.947.

110. CHONG, C.J., Private Communication, University of Canterbury, Christchurch, N.Z.

111. NISITANI, H., 1968, Bull. J.S.M.E., vol.11, P.947.

112. ANSELL, G.S., et al., 1966, Trans. Am. Soc. Metals, vol.59, P.630.

113. TOKUDA, A., 1960, Trans. Jap. Inst. of Metals, vol.1, No.2, P.108.

114. BEACHEM, C.D., 1967, Trans. Am. Soc. Metals, vol.60, P.325.

115. LUTHER, R.G. and WILLIAMS, T.R.G., 1973, Metals and Materials, vol.7, P.357.

116. OUCHIDA, H., 1959, Proceedings of the 2nd Japan Congress on testing materials, Kyoto, P.14.

117. MASSONET, C., 1956, Proc. Am. Soc. Test. Mater., vol.56, P.954.

118. PHILLIPS, C.E. and HEYWOOD, R.B., 1951, Proc. Instn. Mech. Engrs., vol.165, P.113.

APPENDIX 'A'

FATIGUE MACHINES AND SPECIMEN PREPARATION.

(a) DIRECT STRESS FATIGUE MACHINE:

The direct stress fatigue machine used was a 100 KN Amsler High Frequency Vibrophore. The machine makes use of the resonance principle which permits the use of frequencies up to 300 cycles per sec. The manufacturer suggested that the machine can maintain stresses to within 1%, both as regards magnitude and time constancy.

The resonance principle employed in this machine also enables the determination of the damping characteristic of the material. A disadvantage with the resonance principle used in this machine is that, for materials with high damping such as low carbon steels, the machine may not be able to cope with the high energy lost, especially at stresses well above the fatigue limit. Consequently, the determination of the full fatigue S - N curve may not be possible. This problem was encountered in the early stages of the testing programme. It was found that for experimental steels machined to the specimen specification supplied by the manufacturer, the machine was unable to maintain a constant stress level at stresses around the fatigue limit. The specimen design was subsequently modified such that the volume of material subjected to deformation was reduced and the elastic portion of the specimen was increased, see fig.7.11.

The alignment of the machine was found to be very good. A special specimen with four strain gauges attached at 90^{o} to each other was used to monitor the alignment of the machine. The alignment was found to be better than 35 micro strain.

The method of specimen gripping is illustrated in fig.A1. A similar gripping method was also employed for tensile tests in the Instron tensile machine on the fatigued specimens, see fig.A2.

(b) DIRECT STRESS SPECIMEN PREPARATION:

The test specimen is shown in fig.7.11 and specimen preparation was carried out in accordance with B.S.3518 part 2. Final preparation after machining was by successive finer grades of emery paper, alternating between longitudinal and circumferential polishing, finishing with 600 grade paper polishing in a longitudinal direction. Longitudinal polishing was carried out in a Morrison polishing machine, and the circumferential polishing was done in a lathe with the emery paper held on a hard-wood former. A final polishing was carried out with a 600 grade polishing paper after the specimen diameter had been checked and just before the specimen was loaded in the fatigue machine. Prior to testing, the specimen surface was cleaned with carbon tetrachloride.

(c) ROTATING BENDING FATIGUE MACHINES:

The rotating bending machines used were 3000 r.p.m. Avery dual-ended fatigue machines. These machines originally had a simple cantilever single-point load application. They had been modified[12] to a two-point load cantilever system, see fig.A3. The modified two-point load cantilever system resulted in a constant bending moment over the specimen gauge length, and enabled better prediction of stress at the gauge length. The alignment of the specimen in the rotating bending machine was checked by detecting the vibration set up at critical speeds as the machine was slowed from running speed.

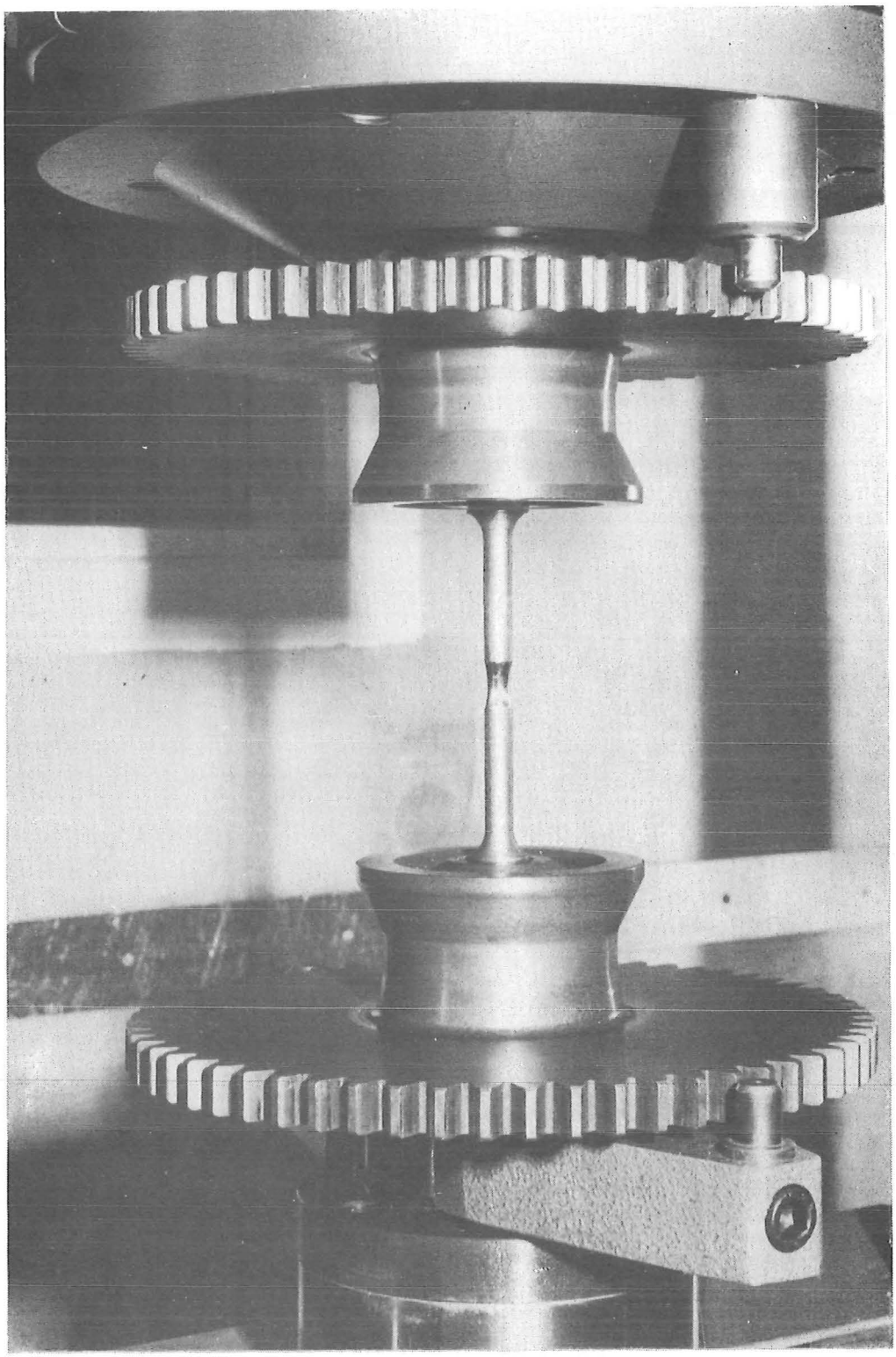

Fig. A1 DIRECT STRESS FATIGUE TEST IN AMSLER VIBROPHORE.

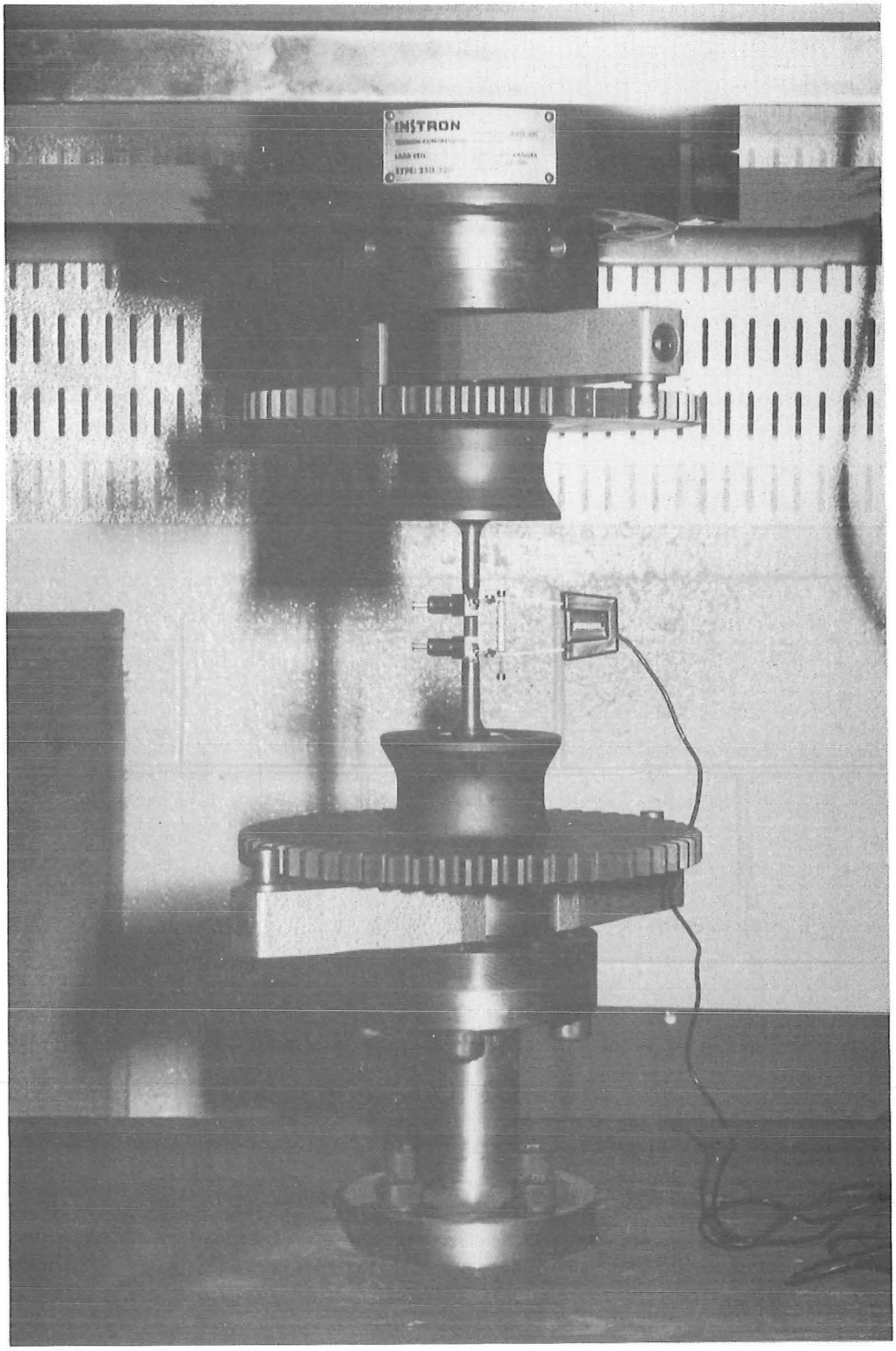

Fig. A2. GRIPPING ARRANGEMENT FOR TENSILE TEST ON FATIGUED SPECIMENS.

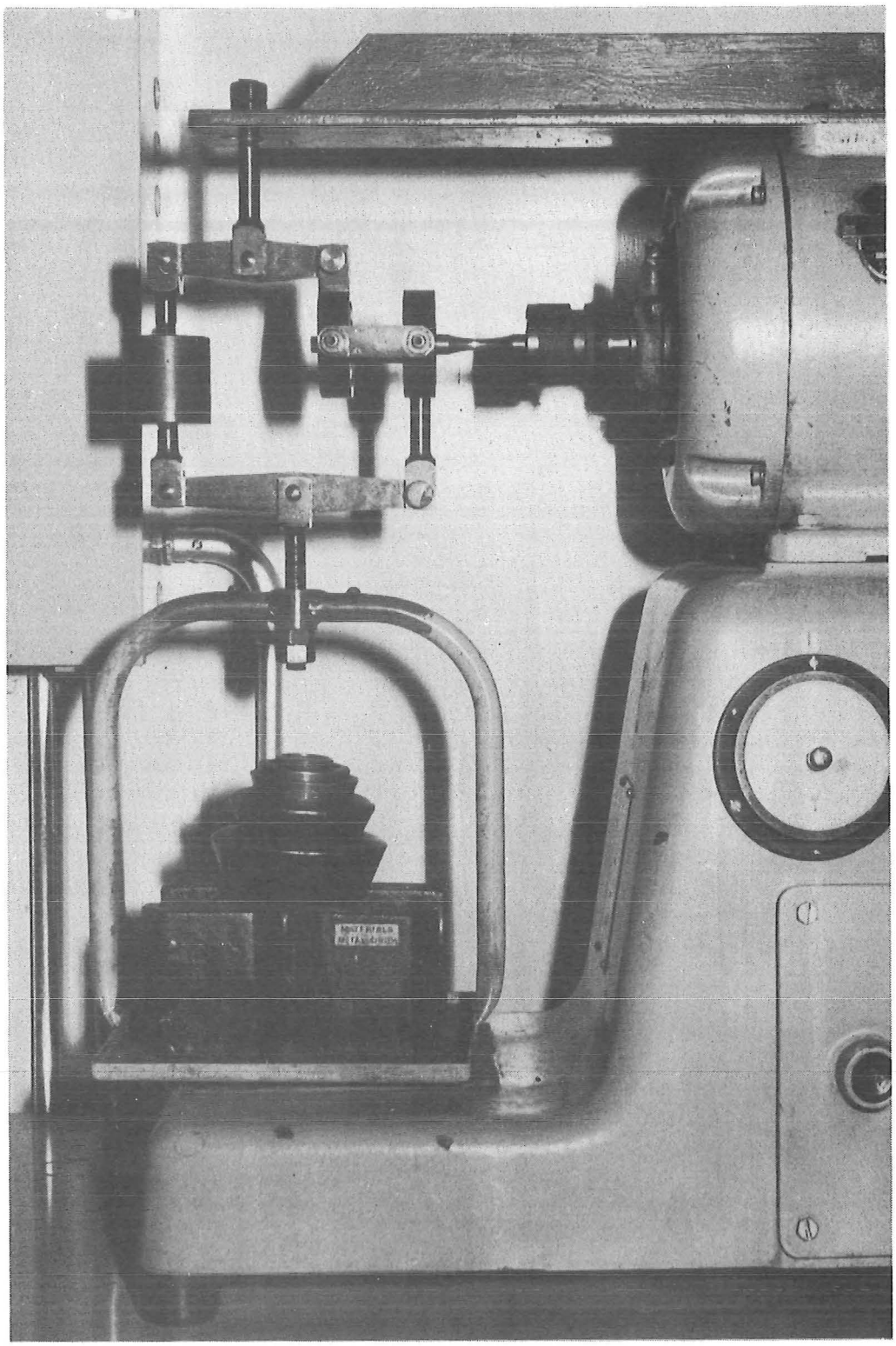

Fig. A3. ROTATING BENDING FATIGUE TEST WITH TWO POINT LOAD-CANTILEVER SYSTEM.

Load application was always carried out after the machine was set in motion, and precaution was taken to ensure that the load was applied slowly.

(d) ROTATING BENDING SPECIMEN PREPARATION:

The rotating bending specimen details are as shown in fig.7.12. Similar polishing procedures as adopted for the direct stress specimens were used with the exception that circumferential polishing was carried out with the specimen held in a rotating bending fatigue machine.

APPENDIX 'F'

DETERMINATION OF FATIGUE LIMITS USING STAIRCASE METHOD.

The most common test procedures used in determining the fatigue strength or fatigue limit of a material are the "Probit" method and the "Staircase" method. In the Probit method, one or more groups of specimens are tested for a fixed number of cycles at various stress levels close to the estimated fatigue strength (limit), a test being stopped if its endurance exceeds the required life. The percentage of failures at each stress level is then plotted against the stress level on a probability paper. The best line is then drawn through the points and the mean fatigue strength (limit) of the sample is the stress corresponding to 50% of failures.

The Probit method generally requires large numbers of specimens. The same results can be obtained more economically using the Staircase method, but the time required may be longer, as the specimens have to be tested one at a time. In this investigation, as only one direct stress fatigue machine was available, the Staircase method was the obvious choice for the direct stress specimens. For the rotating bending specimens, although four dual-ended rotating bending testing machines were available, there were eight sets of steels (A1-A5, B1-B3) to be tested, consequently, the more economical Staircase method was again chosen as testing for all eight sets of specimens could be conducted together.

The full details of the Staircase method are given in BS 3518 part 5, and will only be briefly summarised here. In the Staircase method, the first test piece is tested at an

estimated mean value of the fatigue strength (limit). If failure occurs before the required life, the next specimen is tested at one stress increment below the first stress level. If on the other hand, the first specimen survives the required life, then the next specimen is tested at one stress increment above the first stress level. This procedure is repeated for all the specimens to be tested. The results for the analysis in the Staircase method are taken from the first pair of opposite results. The analysis used the less frequent event, that is, if there are more failures than runouts, then the number of runouts is used, and vice versa.

The mean fatigue strength (limit) m is given by

$$m = S_o + d\left(\frac{A}{n} \pm \frac{1}{2}\right) \qquad \text{eqn B.1}$$

where S_o = lowest stress

d = stress increment

n = total of less frequent events = $\sum_{i=o}^{z} n_i$

$A = \sum_{i=o}^{z} i n_i$

n_i = number of the less frequent events at i-th stress above S_o

i = coded stress level (i = o for S_o)

z = number of stress levels above S_o

$+\frac{1}{2}$ is used if the less frequent event is a runout, and

$-\frac{1}{2}$ is used if the less frequent event is a failure.

The estimated standard deviation S is given by

$$S = 1.62\, d\left[\frac{B \sum_{i=o}^{z} n_i - A^2}{n^2} + 0.029\right] \qquad \text{eqn B.2}$$

where $B = \sum i^2 n_i$

The stress increment should be kept as small as possible, as the smaller the stress increment, the greater is the reliability of the results.

As only sixteen specimens were produced for each set of the experimental steels in this investigation, the mean fatigue limit m was calculated from the modified Staircase equation

$$m = \frac{C}{n} \qquad \text{eqn B.3}$$

where C = sum of stresses used on the last (n-1) tests, plus the stress that would have been used on the next test if it had been run;

n = total number of specimens starting with the first pair of opposite results.

The Staircase results from both the direct stress and rotating bending tests for the eight sets of experimental steels are shown in figs.B.1-B.8.

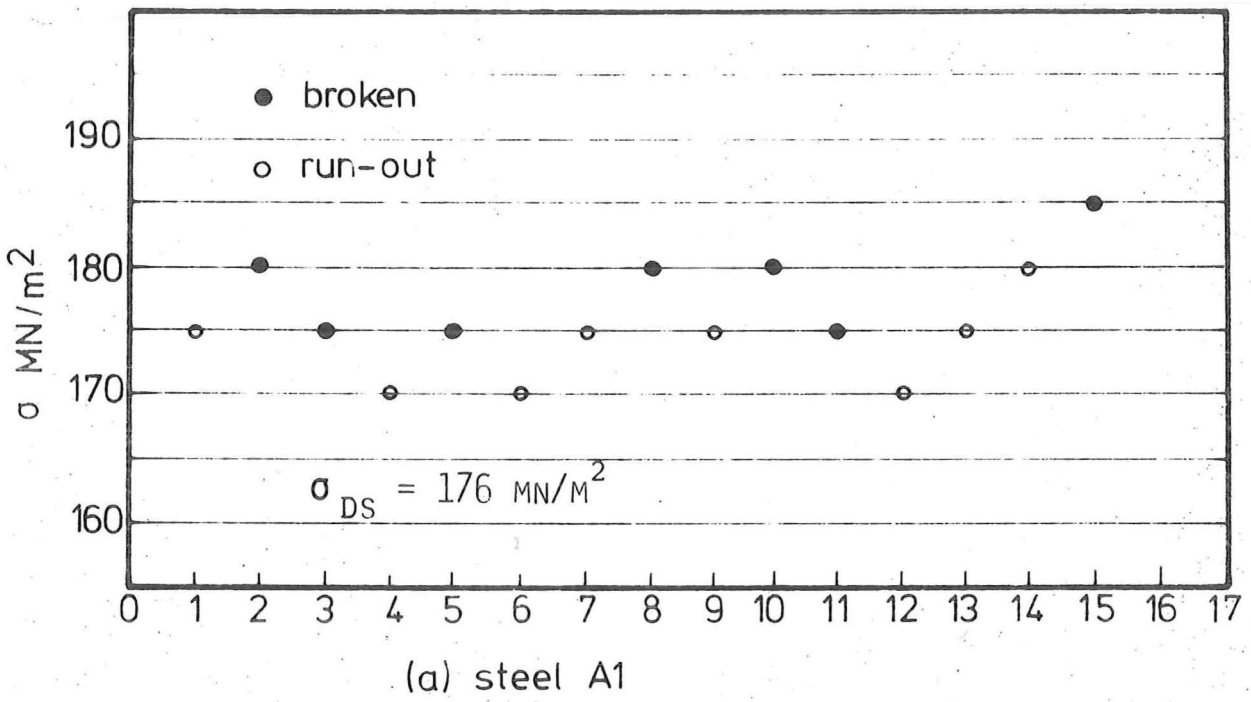

(a) steel A1

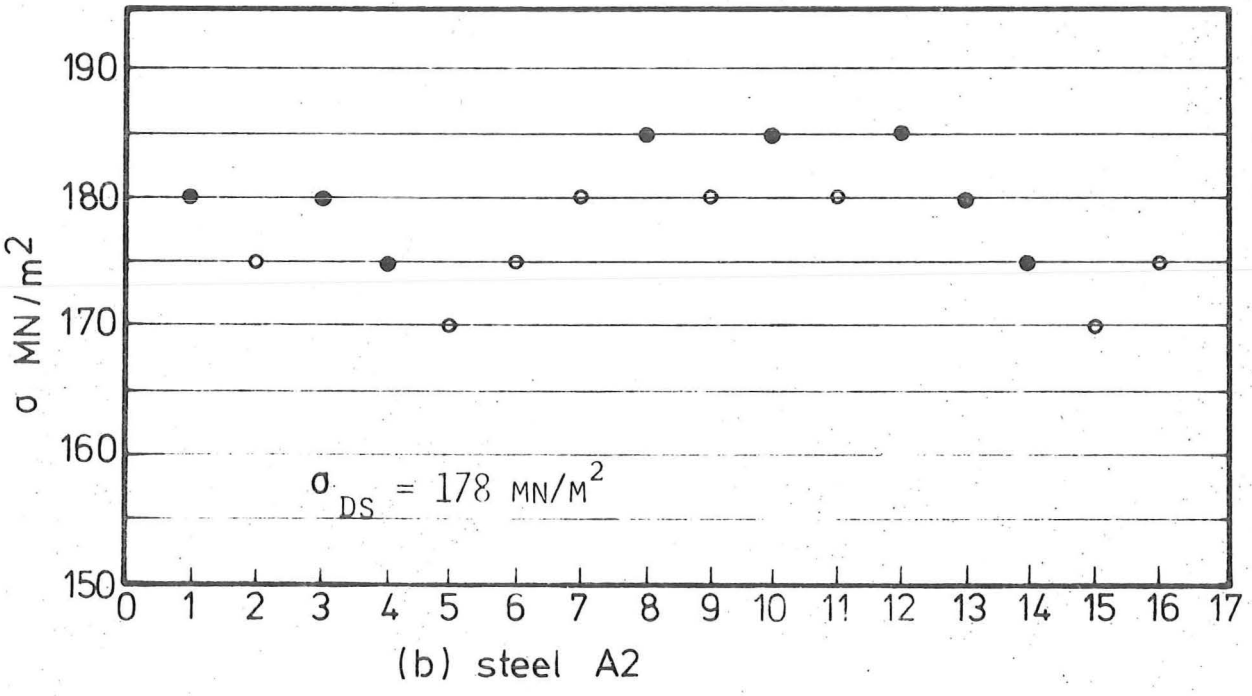

(b) steel A2

Fig. B.1 STAIRCASE RESULTS (DIRECT STRESS)

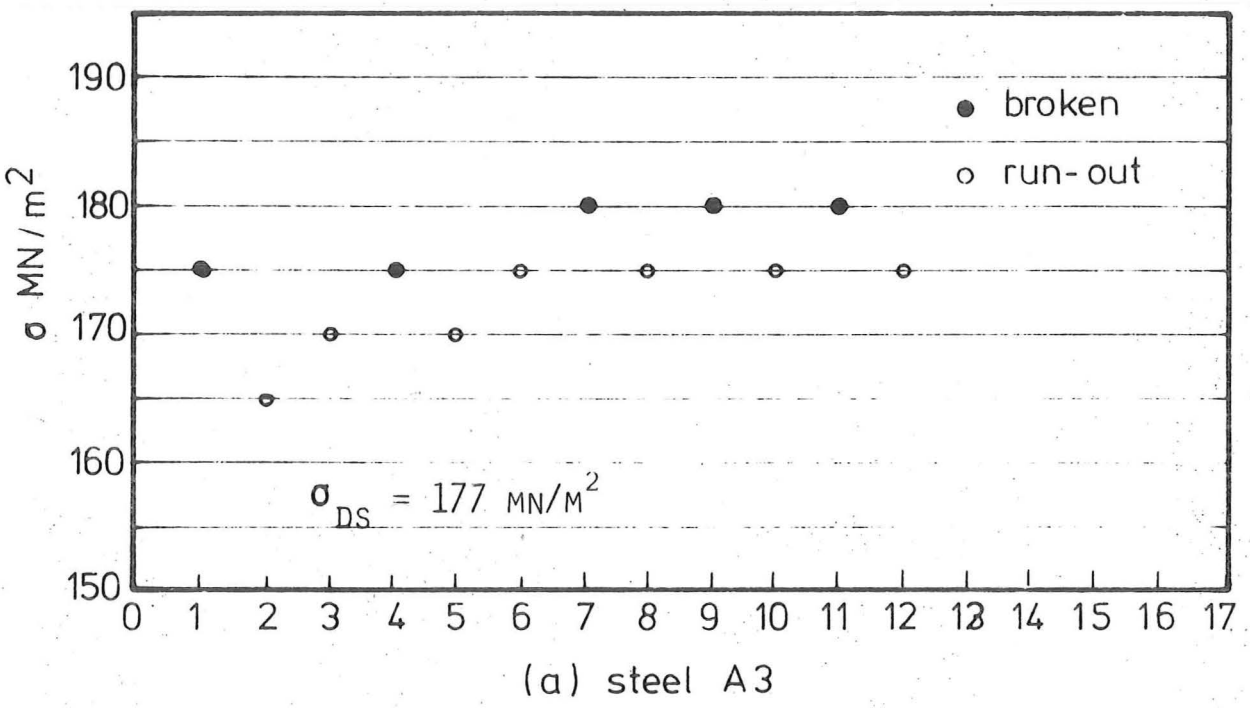

(a) steel A3

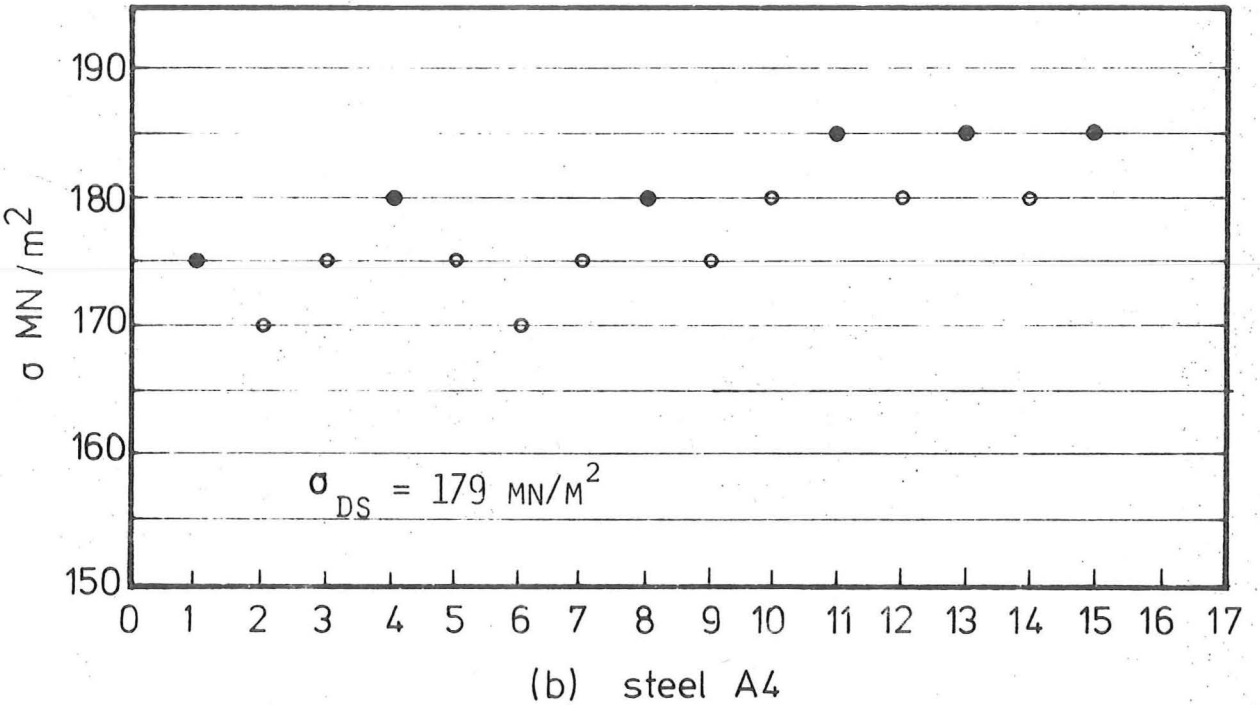

(b) steel A4

Fig. B.2 STAIRCASE RESULTS (DIRECT STRESS)

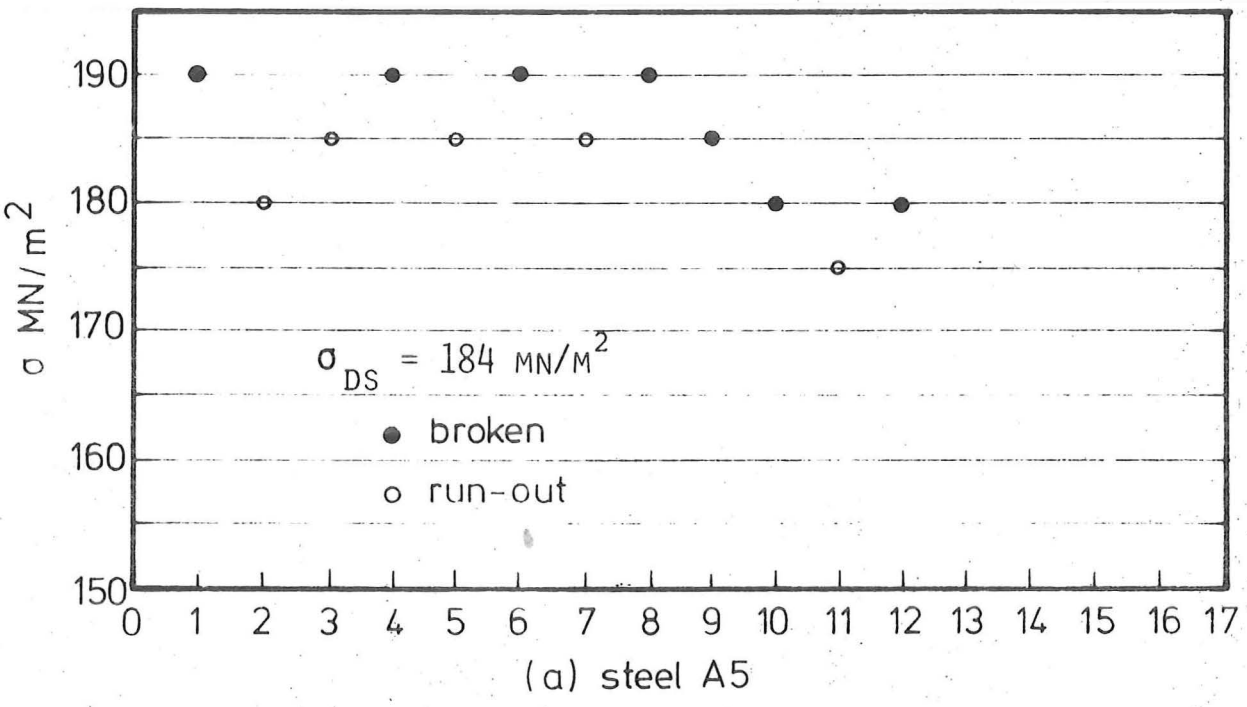

(a) steel A5

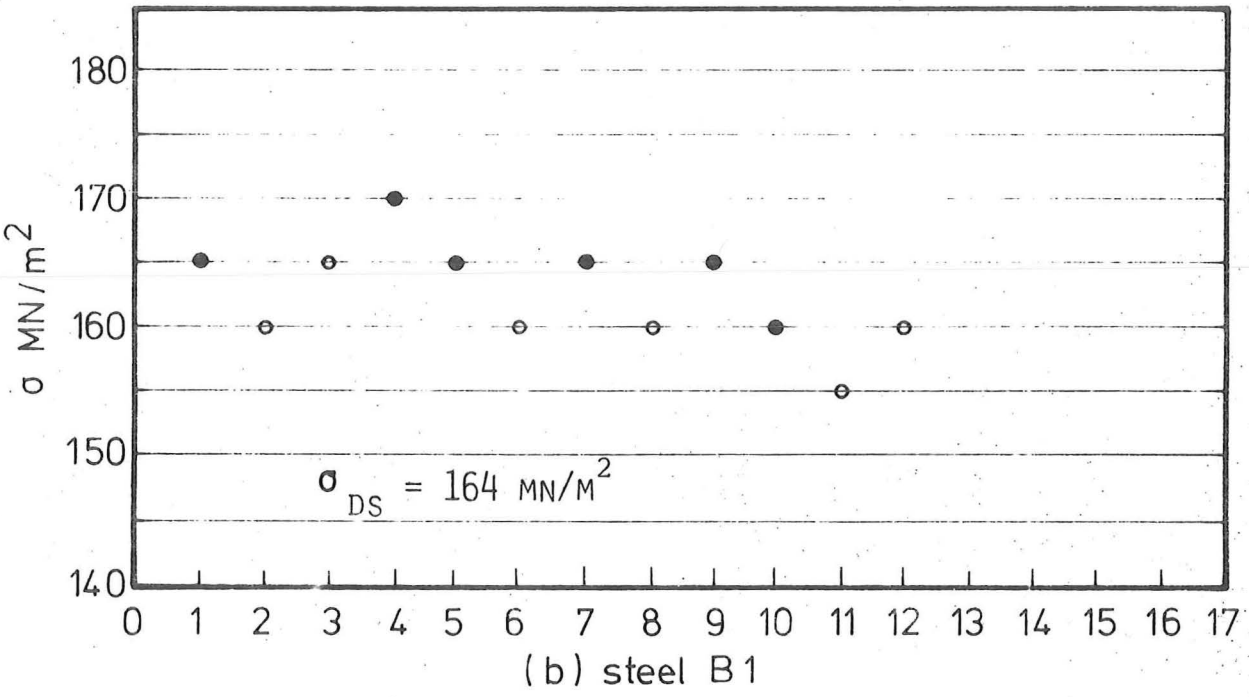

(b) steel B1

Fig. B.3 STAIRCASE RESULTS (DIRECT STRESS)

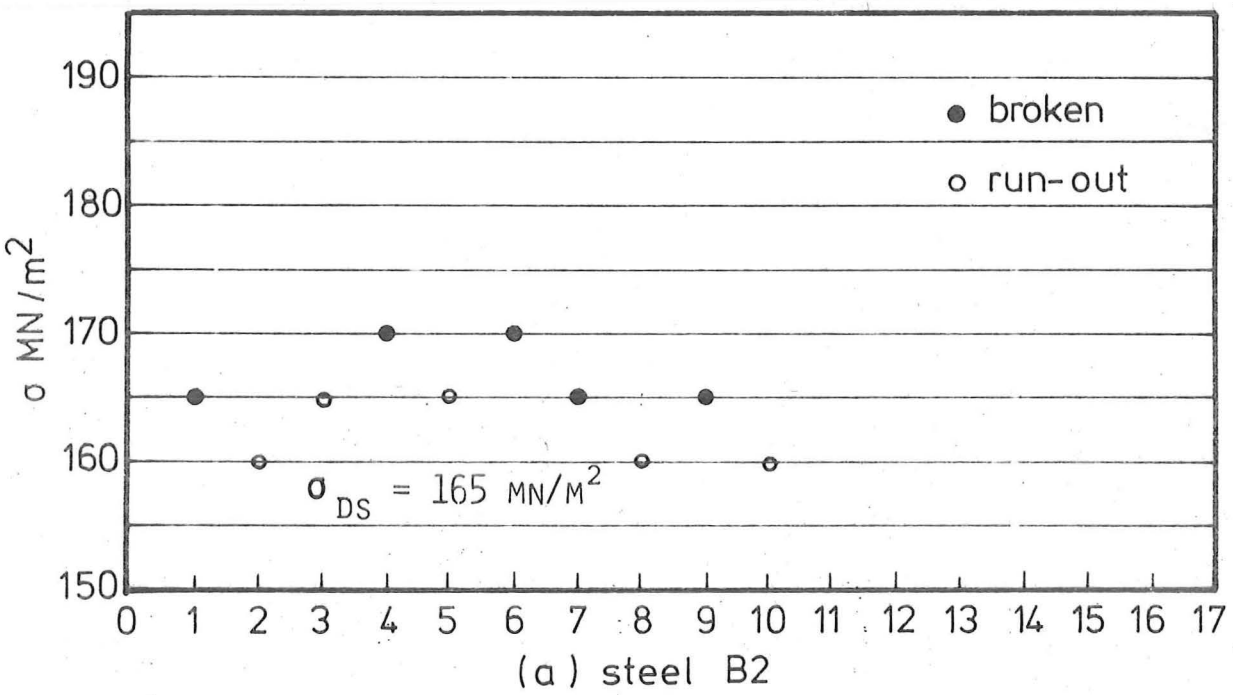

(a) steel B2

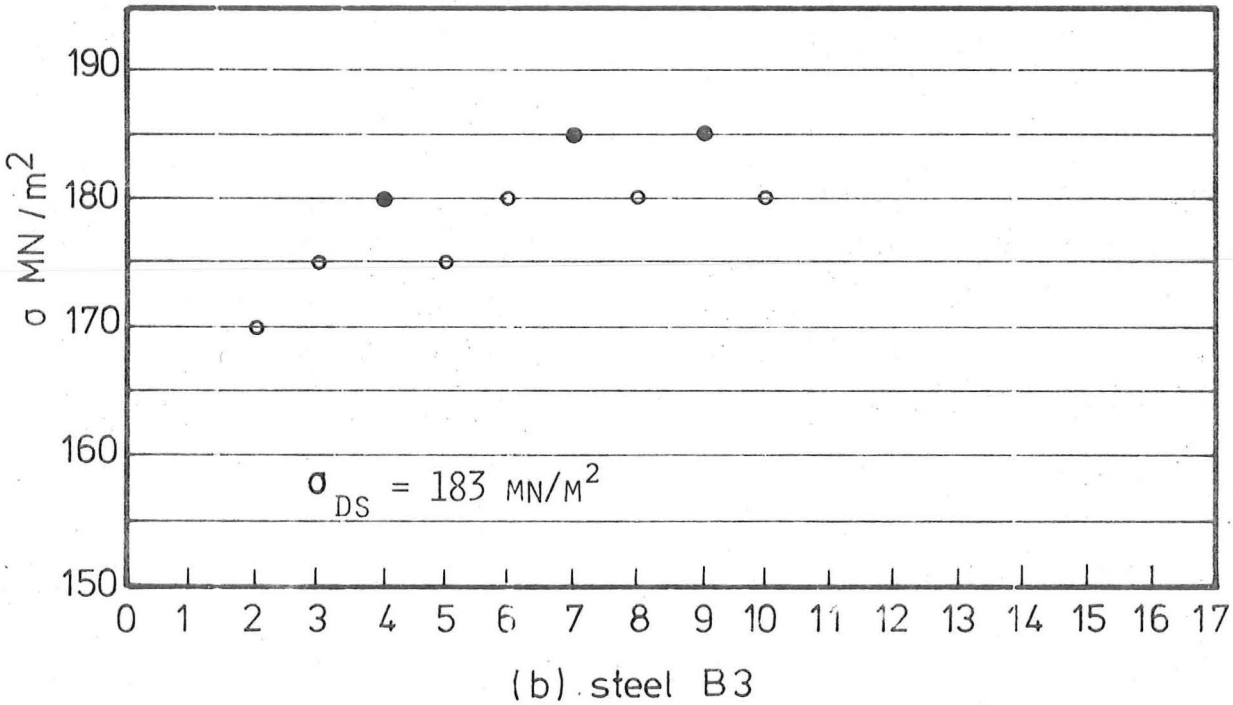

(b) steel B3

Fig. B4 STAIRCASE RESULTS (DIRECT STRESS)

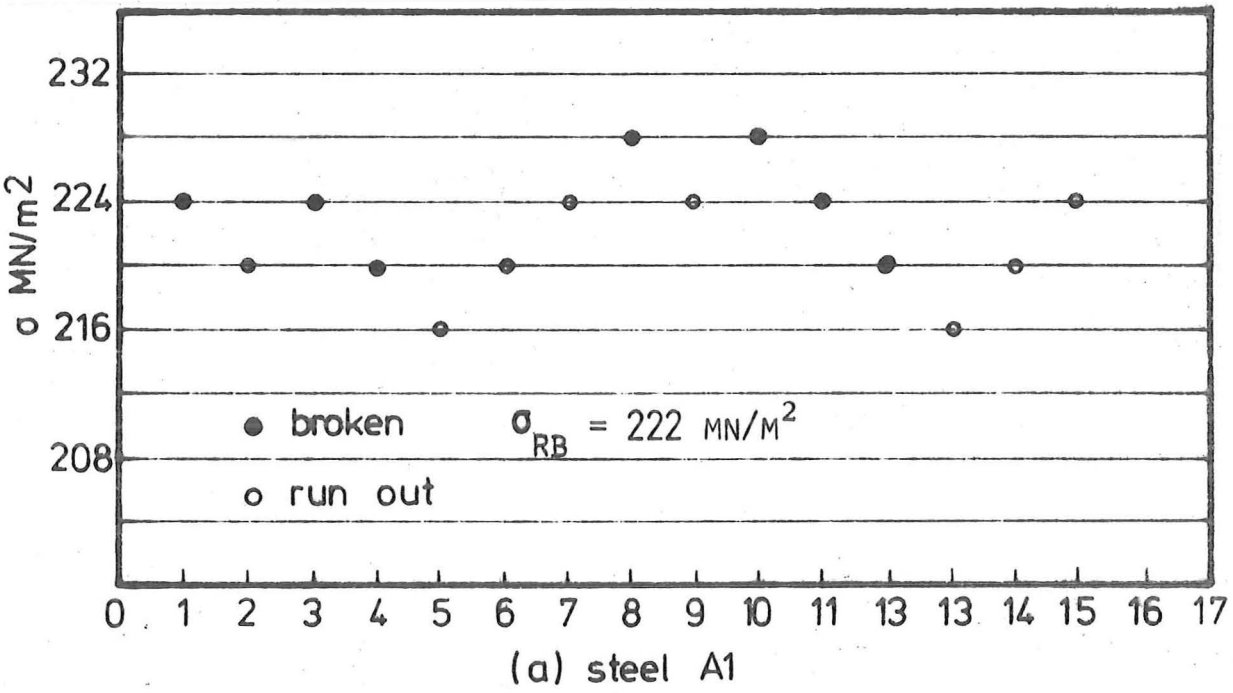

(a) steel A1

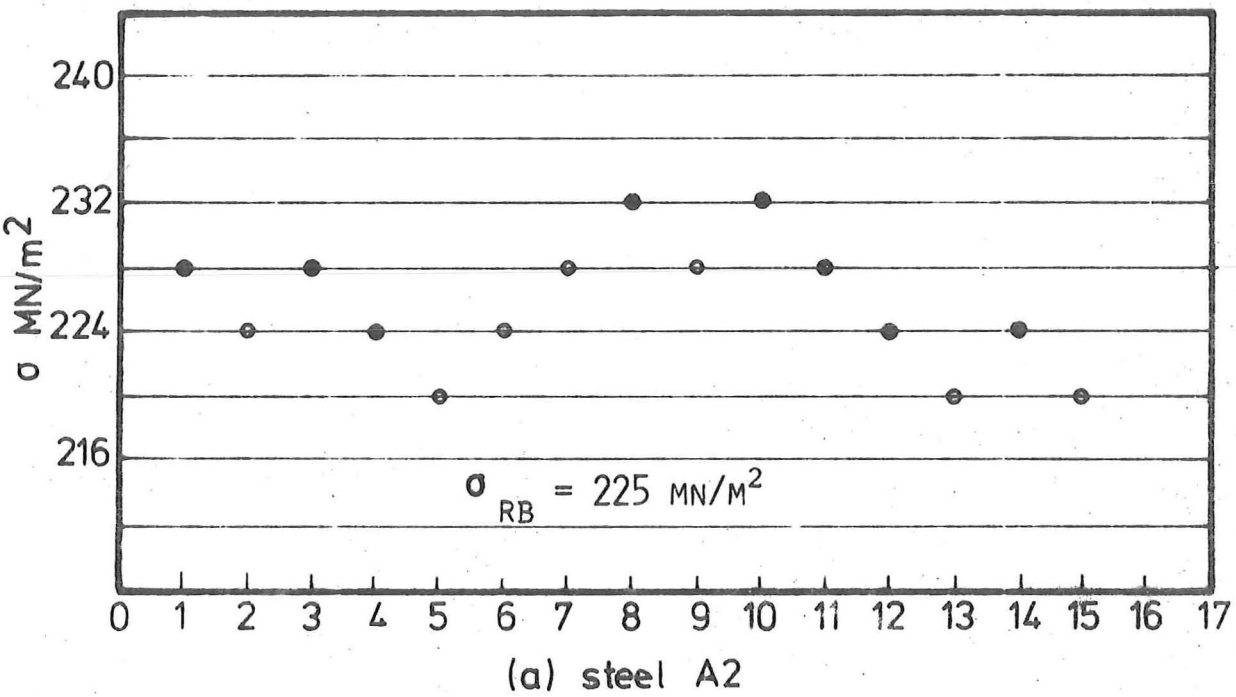

(a) steel A2

Fig. B5 STAIRCASE RESULTS (ROTATING BENDING)

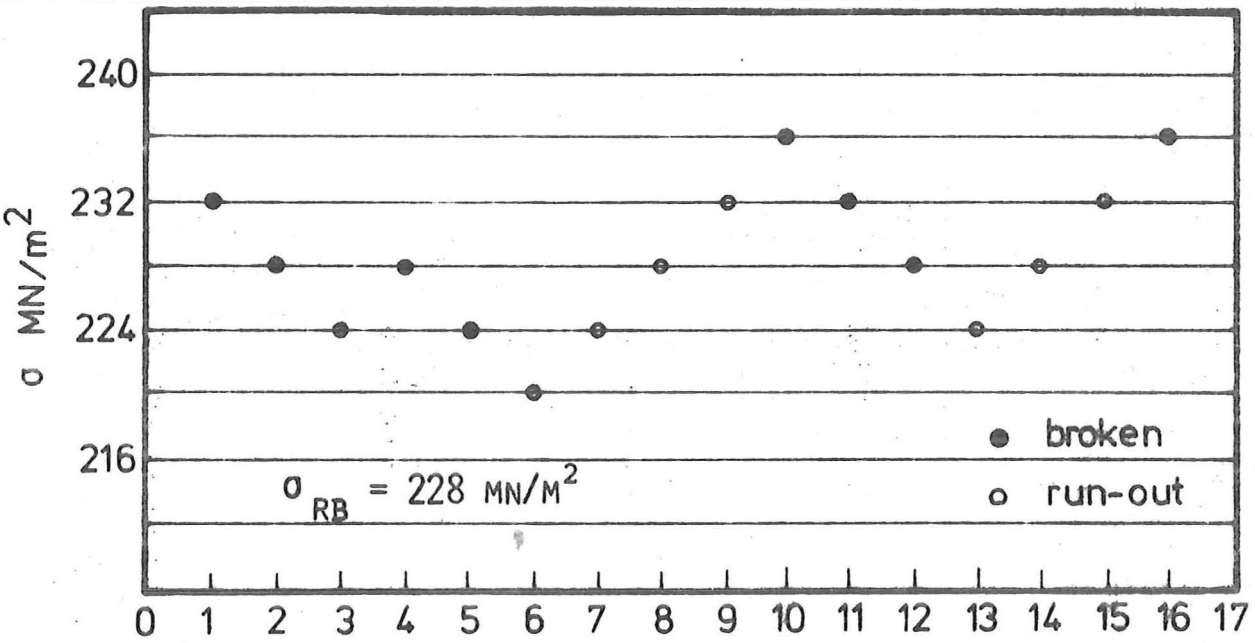

(a) steel A3

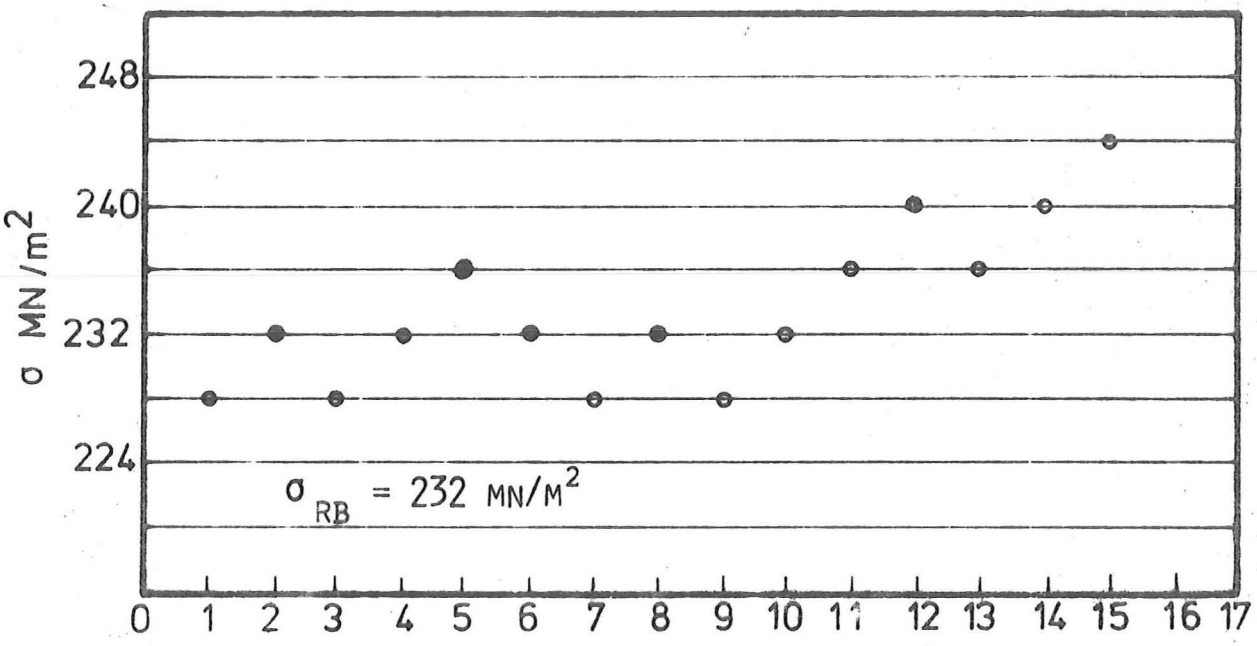

(b) steel A4

Fig. B.6 STAIRCASE RESULTS (ROTATING BENDING)

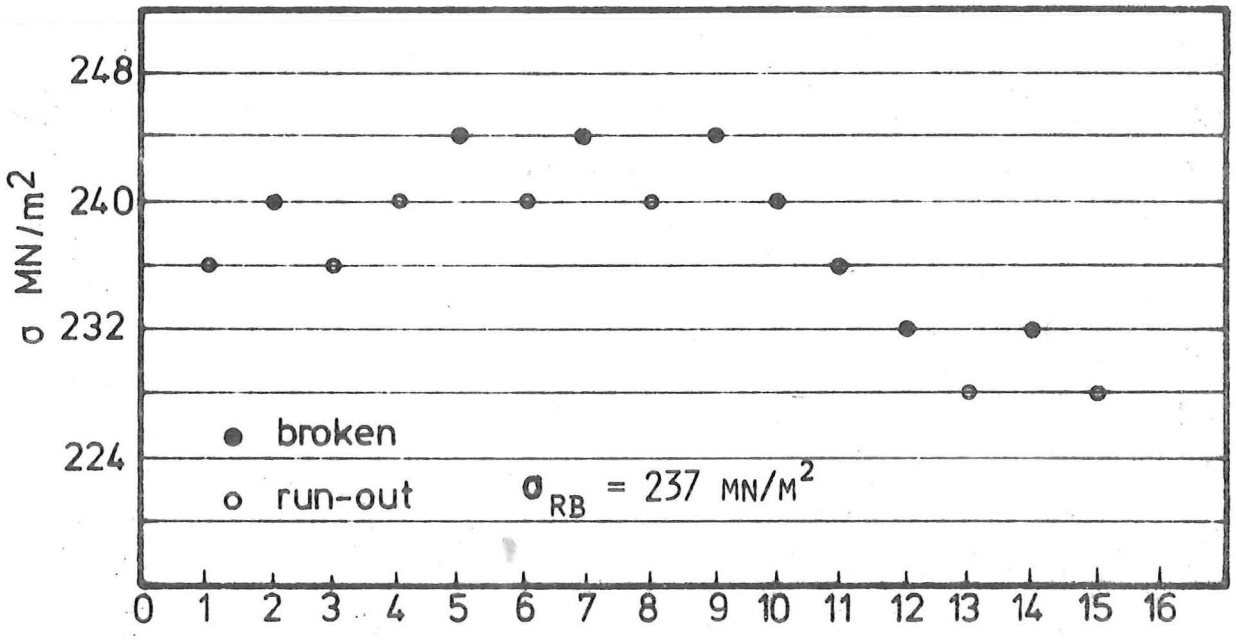

(a) steel A5

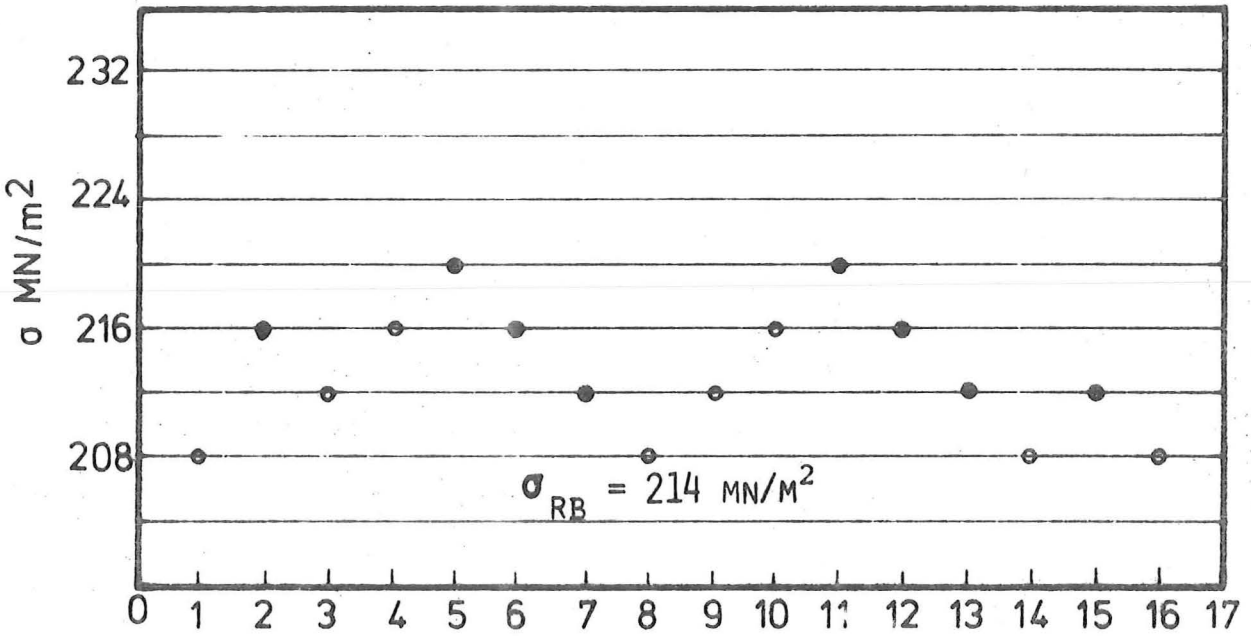

(b) steel B 1

Fig. B.7 STAIRCASE RESULTS (ROTATING BENDING)

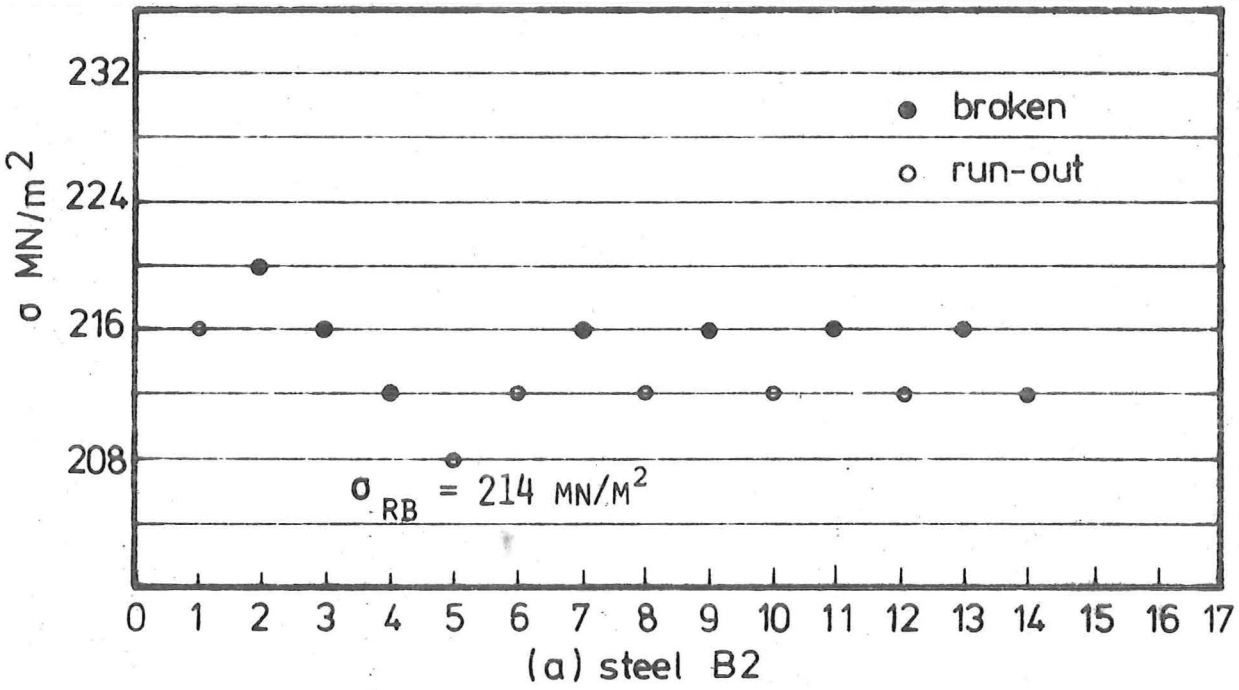

(a) steel B2

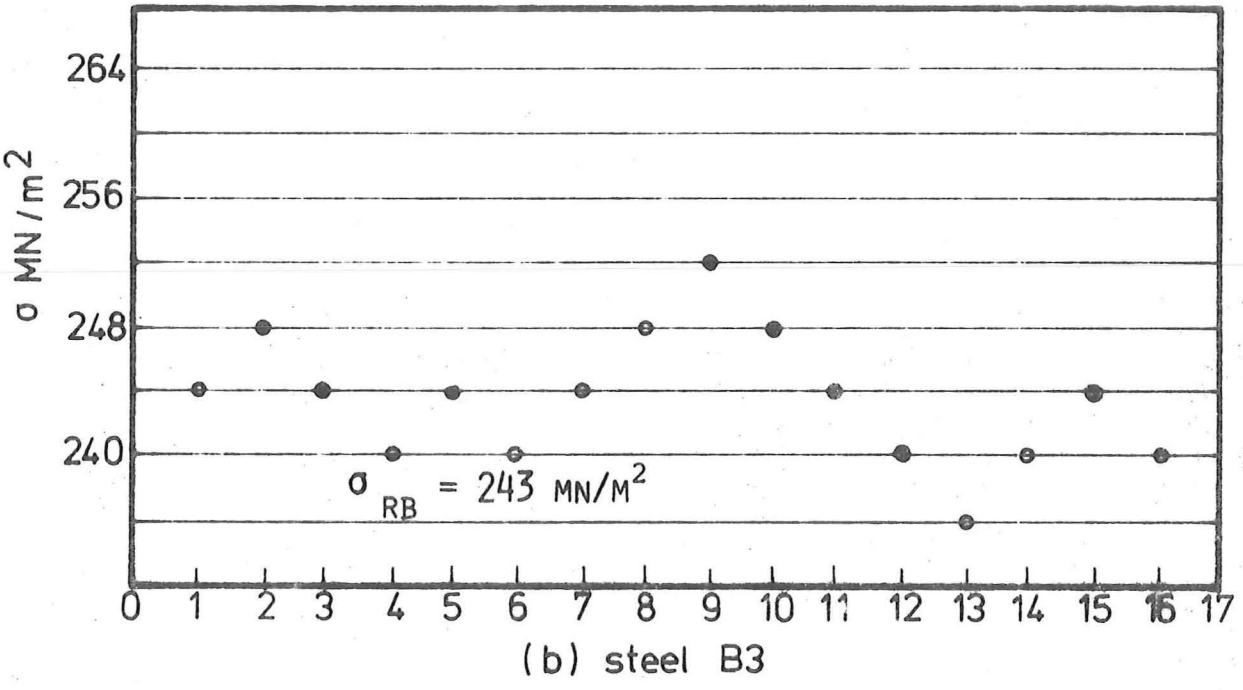

(b) steel B3

Fig. B.8. STAIRCASE RESULTS (ROTATING BENDING)

APPENDIX 'C'

DETERMINATION OF NITROGEN IN STEEL.

The total nitrogen content in steel is considered to be made up of two parts:-

(i) Acid-insoluble nitrides, and

(ii) Acid-soluble nitrides, which consist mainly of aluminium nitride and interstitial nitrogen.

It is assumed that:

$$\%\ N_{\substack{\text{as free}\\\text{interstitial}}} = \%\ N_{\substack{\text{as soluble}\\\text{nitrides}}} - \%\ AlN$$

The procedure is summarised diagramatically in fig.C.1.

(a) METHOD FOR DETERMINING SOLUBLE AND INSOLUBLE NITRIDES:

3.5 gm of steel sample (in the form of drillings) is dissolved in about 40-50 ml of 18% sulphuric acid. The mixture is heated over a steam bath to aid the decomposition of metal. After cooling, 2 ml of barium chloride is added, and separation of the soluble and insoluble parts is carried out by centrifuging. (Barium chloride is added to improve the separation.)

The soluble part is siphoned off and 10 ml of concentrated sulphuric acid is added to the insoluble nitrides. Heat is added until complete dissolution of the 'insoluble' nitrides.

The soluble and 'insoluble' solutions are then separately steam distilled with 40-50 ml of sodium hydroxide and about 40 ml of ammonia free distilled water. The distillation apparatus is as shown in fig.C.2. The distillate is collected in 10 ml of boric acid solution. 2 ml of Nessler reagent is added to the distillates and the solutions are adjusted to

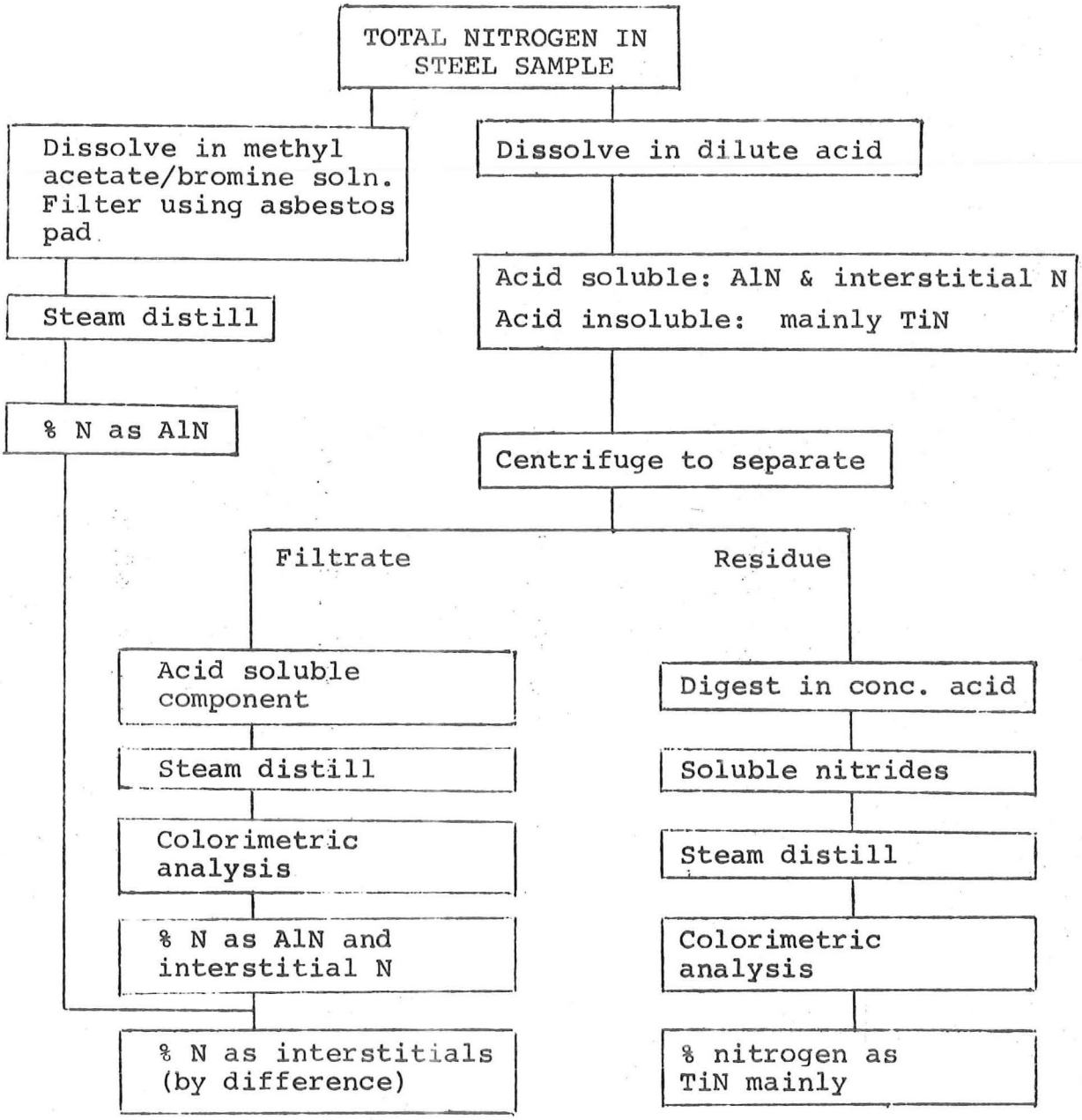

Fig.C.1: Format for nitrogen analysis of steel.

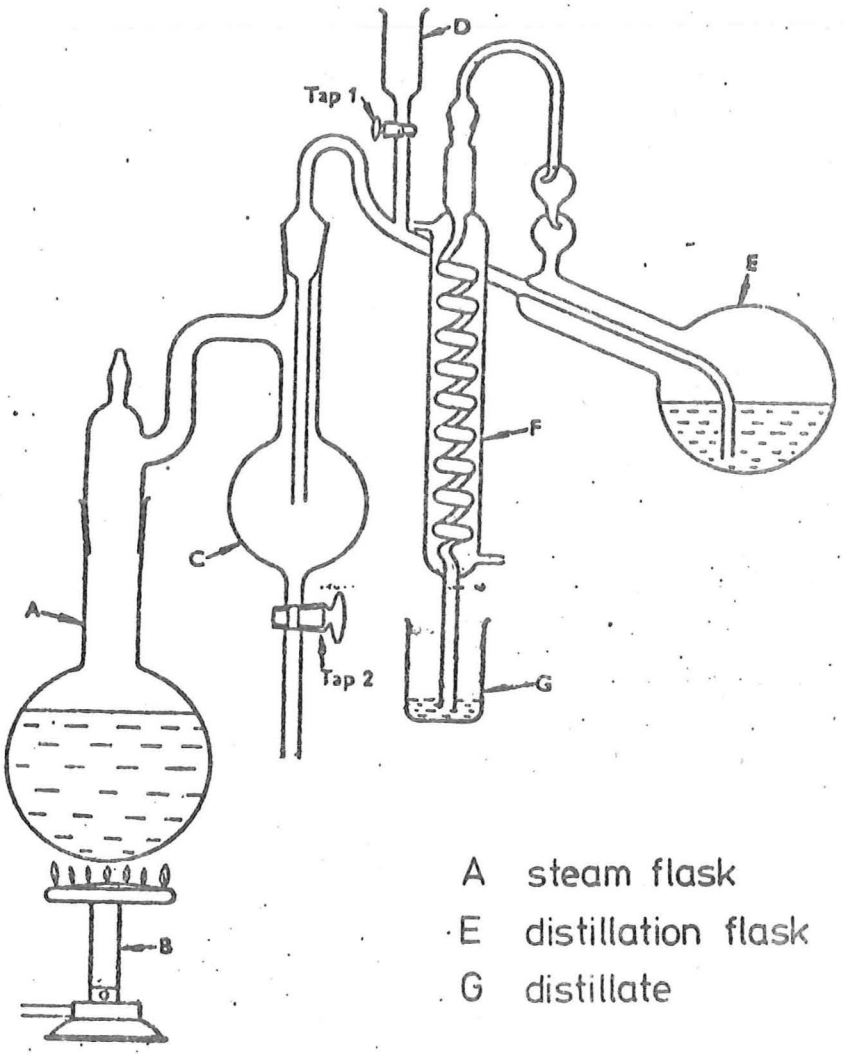

Fig. C.2. STEAM DISTILLATION APPARATUS

equal volume by adding ammonia free distilled water. The amount of nitrogen present in these solutions may then be determined using colorimetric examination, and the actual nitrogen level obtained from the calibration curve prepared using standard nitrogen solutions. The interstitial (or active) nitrogen is then given by the difference between the nitrogen in soluble nitrides and the nitrogen combined as aluminium nitride.

(b) METHOD OF DETERMINING THE ALUMINIUM NITRIDE:

3.5 gm of steel sample (in the form of drillings) is dissolved in 50 ml of Methyl-Acetate plus 10 ml of Bromine. The mixture is dissolved with the aid of a small flame. Aluminium nitride which is not soluble in these solutions is filtered off using an asbestos pad. The pad is washed using Methyl-Acetate and then dried. The dried pad is then put into the distillation flask (E in fig.C.2) and the nitrogen combined as AlN is obtained by steam distillation and determined using colorimetry.

The accuracy of these analyses is in the order of $\pm$ 0.0005%.

(c) GENERAL PRECAUTION:

(i) Care must be taken to ensure that decomposition of steel samples and the centrifuging separation process is complete.

(ii) Every precaution against contamination with extraneous ammonia must be taken.

(iii) Blank determination should be carried out with each batch of tests to ensure that nitrogen does not come from any other sources other than the steel sample.